A NOVEL SYNTHESIS AND THERMODYNAMIC INVESTIGATION OF UMoO$_6$

UNE NOUVELLE SYNTHÈSE ET UNE ENQUÊTE THERMODYNAMIQUE DE UMoO$_6$

A Thesis Submitted to the Division of Graduate Studies
of the Royal Military College of Canada
by

Robert Aaron Barry, rmc, BSc, RCN
Acting Sub-Lieutenant

In Partial Fulfillment of the Requirements for the Degree of
Master of Science in Chemistry and Chemical Engineering with a Specialty in
Nuclear Science and Engineering

June 2015

Acknowledgements

Abstract

The Royal Military College Thermodynamic Fuel Model (RMC-TFM) has a history of setting boundary conditions for complete kinetic and fuel behaviour models. This thesis improved the RMC-TFM by refining our understanding of $UMoO_6$ and the UO_3-MoO_3 phase diagram. A novel, aqueous synthesis method was developed to produce high purity $UMoO_6$. A $C_p(T)$ function (J K^{-1} mol^{-1}) of $223.0844 - 0.1945T(K) + 2.2965x10^{-4}T^2(K) - 2.515493x10^6T^{-2}(K)$ was determined with an associated error of ± 5 % over a temperature range of 343-668 K. A ΔH^o_{trans} of -32 $\pm$ 3 kJ mol^{-1} at 734 $\pm$ 32 K was found and the *meta*-stable form of $UMoO_6$ was added to the RMC-TFM. A ΔH^o_{decomp} of 82 $\pm$ 10 kJ mol^{-1} at a T_{decomp} of 1205 $\pm$ 10 K was determined and used to calculate $\Delta H^o_{f, 298 K}$ = -1972 $\pm$ 13 kJ mol^{-1}. Finally, the UO_3-MoO_3 phase diagram was used to refine and select the thermodynamic values for inclusion in the RMC-TFM and the results compared against the original benchmarking CT experiments.

Résumé

Le modèle thermodynamique de combustible nucléaire du Collège militaire royal du Canada (MTCN-CMRC) est utilisé pour fixer des conditions aux limites pour les modèles complets de cinétique et de comportement du combustible. Cette thèse a amélioré le MTCN-CMRC en affinant notre compréhension de $UMoO_6$ et le diagramme de phase de UO_3-MoO_3. Une nouvelle méthode de synthèse aqueuse a été développée pour la production de $UMoO_6$ à haute pureté. Une fonction pour la capacité de chaleur spécifique ($J\ K^{-1}\ mol^{-1}$) a été déterminée comme étant $223.0844 - 0.1945T(K) + 2.2965 \times 10^{-4}T^2(K) - 2.515493 \times 10^6 T^{-2}(K)$ avec une erreur associée de $\pm 5\ \%$ par rapport à une gamme de température de 343-668 K. Une enthalpie de transition, ΔH^o_{trans}, de 32 ± 3 kJ mol^{-1} à 734 ± 32 K a été trouvé et le produit $UMoO_6$ *méta*-stable a été ajouté au MTCN-CMRC. Une $\Delta H^o_{décomp}$ de 82 ± 10 kJ mol^{-1} à une $T_{décomp}$ de 1205 ± 10 K a été déterminée et utilisée pour calculer ΔH^o_f , $_{298\ K} = 1972 \pm 13$ kJ mol^{-1}. Enfin, le diagramme de phase de UO_3-MoO_3 a été utilisé pour affiner et sélectionner les valeurs thermodynamiques pour inclusion dans le MTCN-CMRC et les résultats ont été comparés aux expériences originales de CT.

Table of Contents

List of Tables

List of Figures

xiii

List of Symbols, Abbreviations, Acronyms, and Nomenclature

μ	Partial molar Gibbs energy
Å	Angstrom
β	Beta particle
λ	Wavelength
θ	Angle between incident and diffracted X-rays
a	Thermodynamic activity
a b c	Unit cell parameters a, b, and c
ACR	Advanced CANDU® Reactor
AECL	Atomic Energy of Canada Limited
Al_2O_3	Aluminium oxide
Ar	Argon
atm	Atmospheres of pressure
Ba	Barium
$BiPO_4$	Bismuth(III) phosphate
CANDU®	CANada Deuterium Uranium Reactor
CCDC	Cambridge Crystallographic Data Centre
Ce	Cerium
Ci	Curie
cm	Centimetre
CNSC	Canadian Nuclear Safety Commission
C_p	Specific heat capacity at constant pressure
Cs	Caesium
CSD	Cambridge Structural Database
CT	Coulombic titration
C_V	Specific heat capacity at constant volume
d	Interplanar spacing
D_2O	Deuterium oxide (heavy water)
D calc	Calculated density
DSC	Differential scanning calorimetry
DTA	Differential thermal analysis
EDX	Energy dispersive X-ray spectroscopy
emf	Electromotive force
F_{ooo}	Structure factor
g	Gram
G	Gibbs Free Energy

GA	Gravimetric analysis
GoF	Goodness of fit
GWd ton^{-1}	Gigawatt days per ton
h	Hour
H	Enthalpy
H_2	Hydrogen
H_2O	Water
HNO_3	Nitric acid
^{131}I	Iodine-131 isotope
ICDD	International Centre for Diffraction Data
ICP-MS	Inductively coupled plasma mass spectrometry
IR	Infrared spectroscopy
J	Joule
K	Kelvin
k_b	Boltzmann constant
kg	Kilogram
kJ	Kilojoule
kV	Kilovolt
L	Litre
La	Lanthanum
LOCA	Loss of coolant accident
LEU-fp	Low enriched uranium fission product model
M	Molar concentration (mol L^{-1})
mg	Milligram
min	Minute
mL	Millilitre
mmol	Millimole
MPa	Mega pascal
mol	Mole
Mo	Molybdenum
MoO_2	Molybdenum dioxide
MoO_3	Molybdenum trioxide
MW_e	Electric megawatt
mW	Milliwatt
n	Number of planes
n	Neutron
N^o	Avogadro's number

Na_2MoO_4	Sodium molybdate
Nd	Neodymium
nm	Nanometres
Np	Neptunium
NSERC	Natural Science and Engineering Research Council of Canada
O_2	Diatomic oxygen (naturally occurring form)
OP&P	Operating Policies & Principles
P	Pressure
Pd	Palladium
pO$_2$	Partial pressure of oxygen or oxygen potential
ppm	Parts per million
psi	Pounds per square inch
Pu	Plutonium
^{239}Pu	Plutonium-239 isotope
P-XRD	Powder X-ray diffraction
q	Heat
R	Gas constant
R$_1$	R indices
*w*R$_2$	R indices
Rh	Rhodium
R int	Independent reflections
RMC	Royal Military College of Canada
RMC-TFM	Royal Military College of Canada Thermodynamic Fuel Model
Ru	Ruthenium
s	Second
S	Entropy
SC-XRD	Single-crystal X-ray diffraction
SEM	Scanning electron microscopy
SIMFUEL	Simulated nuclear fuel
Sr	Strontium
STP	Standard Temperature and Pressure
T	Temperature
TGA	Thermogravimetric analysis
Th	Thorium
^{230}Th	Thorium-230 isotope
U	Internal energy
U	Uranium

^{233}U	Uranium-233 isotope
^{234}U	Uranium-234 isotope
^{235}U	Uranium-235 isotope
^{238}U	Uranium-238 isotope
^{239}U	Uranium-239 isotope
$UMoO_6$	Uranium molybdenum oxide compound
UNENE	University Network of Excellence in Nuclear Engineering
UNS	Unspecified
UO_2	Uranium(IV) dioxide
$UO_2(NO_3)_2$	Uranyl nitrate
UO_3	Uranium(VI) trioxide
U_3O_8	Triuranium octoxide
UK	United Kingdom
USA	United States of America
V	Volume
w	Work
W	Watt
x	Molar fraction
Z	Number of chemical formula units per unit cell
Zircaloy-4	Zirconium alloy
Zr	Zirconium
ZrO_2	Zirconium(IV) dioxide

1.   Introduction

Nuclear reactor development in Canada started in 1944 and nuclear energy now accounts for over 15 % of the electricity generated in Canada and over 50 % of the electricity generated in Ontario [1]. The safe and continued operation of nuclear power in Canada is dependent on past, present, and future study. The impetus for studying the thermodynamic properties of nuclear fuel is further described in this section. The history of this type of study at the RMC is presented along with the development of the need for this thesis. Finally, the objectives of this thesis to fulfill the requirements of the RMC-TFM are stated.

1.1   Impetus

A nuclear fuel element undergoing fission contains a multitude of different chemical elements and compounds at a variety of high temperatures and pressures. This complex chemical system, known as nuclear fuel chemistry, is necessary to understand and model fully in order to predict fuel behaviour and material properties for regular operating conditions, accident conditions, and defective fuel failure scenarios. Also, such understanding and models can be applied to new fuel design, fuel reprocessing, and short- and long-term fuel disposal. Computer models are best suited for this purpose due to their low costs and versatility.

Fuel chemistry plays roles of varying significance on fuel behaviour and material properties, which are dependent on the environmental conditions to which the fuel is exposed. Examples of fuel behaviour and material properties affected by fuel chemistry include oxygen potential, thermal expansion, thermal conductivity, density, heat capacity, melting temperature, neutron absorption, fission gas release, and stress corrosion cracking [2]. The effects of fuel chemistry on these behaviours and material properties are significant during normal operating conditions and become more important when fuel is defective or during accident conditions.

During accident conditions, such as a loss of coolant accident (LOCA), reactor temperatures can rise much higher than normal operating conditions, affecting the fuel chemistry. At a sheathing surface temperature of 1073 K, fuel rods begin to swell and may burst and release volatile fission and activation products into the primary coolant system. At 1173 K, the exothermic reaction between the zirconium (Zr) in the Zircaloy-4 sheathing and steam begins and the temperature heating rate increases. Between 1573-1773 K, the Uranium dioxide (UO_2) fuel will react with

the Zircaloy-4 sheathing and vapourize some fission and activation products. Finally, between 2673-2923 K, UO_2-Zr mixtures melt and even the less volatile fission and activation products have to be considered for vapourization [3].

In the case of defective fuel failures, the sheathing of the fuel element is breached, the heavy water (D_2O) coolant penetrates the fuel sheathing, and the fuel and fission and activation products can be subject to oxidation. While defects occur in less than 0.1 % of CANDU® fuel bundles [4], the oxidation can have an effect on fuel behaviour and material properties. For example, in extreme circumstances thermal conductivity is lowered, which can lead to fuel centreline melting [5]. Also, defective fuels result in the release of some fission and activation products into the primary coolant system, affecting coolant chemistry and increasing its radioactivity, posing an increased health risk to some energy workers in the nuclear power plant [6].

Fuel reprocessing extracts specific elements and compounds from spent nuclear fuel. Originally, it was developed to extract the unused plutonium (Pu) bred from the neutron capture of fertile ^{238}U to create nuclear weapons by nuclear weapons states like the USA, France, and the UK. Today, Pu is commonly extracted for further use in reactors, specifically fast reactors, as a significant amount of fission and activation products remain in the UO_2 fuel matrix. Reprocessing methods are normally chemical processes such as precipitation, solvent extraction, and ion exchange, and have a dependence on the oxidation states of elements in order to separate them from the fuel. One example of a reprocessing method employs Bismuth phosphate ($BiPO_4$) to selectively precipitate Pu(IV) and not Pu(VI) or U(VI) [7]. An understanding of fuel chemistry facilitates the reprocessing of spent fuel.

Fuel chemistry plays a role in both the short- and long-term disposal of nuclear fuel. The decay heat produced by the fuel and the radioactivity released are a function of the specific isotopes of the elements present. Decay heat, radioactivity, and chemical composition are some of the factors that influence the design of disposal solutions and the length of containment time. The interaction of the fuel with proposed containment materials, the interaction of the fuel with ground water, and other possible materials that could breach the containment must be considered as part of a disposal proposal [8].

The above examples of the importance of nuclear fuel chemistry span almost all phases of the nuclear fuel cycle. This demonstrates the requirement for the Canadian nuclear industry to attempt to fully understand fuel chemistry in order to maximize safety margins, energy production, and efficient operation. Computer modelling is one effective means that has been utilized to meet this requirement by simulating in-core fuel behaviour, as shown in Ref. [9-15]. Assisting in the development of these large models is a solid understanding of the chemical stability of a nuclear fuel system under different conditions. The chemical stabilities generated by a thermodynamic fuel model that can adequately predict fuel phase stability, such as the RMC-TFM [5], can be fed into larger models for in-core fuel behaviour as they set some boundary conditions.

1.2   History of the RMC-TFM

In Canada, computer codes have a long history in the nuclear industry. There has been steady progress in the development of codes to predict fuel behaviour and material properties under different conditions. The following is a brief history of the RMC-TFM, a model partly designed to assist in the prediction of fuel defect conditions.

Ewart *et al.* was one of the first to develop a code for mixed oxide fuel in 1984, but did not consider fuel oxidation [16]. B.J. Lewis *et al.* started work on a fuel oxidation model in 1990 [12]. In 1997, the University of California at Berkeley established a relationship between steam and hydrogen reactions and fuel oxidation within the fuel-to-sheath gap [17]. In 2002, B.J. Lewis *et al.* developed a new fuel oxidation model [9].

In 2006, J.D. Higgs completed his doctoral thesis at the RMC, under the supervision of B.J. Lewis and W.T. Thompson, which expanded the previous fuel oxidation model to predict fuel oxidation behaviour in operating defective elements using a method that depended on fuel oxidation kinetics, interstitial oxygen diffusion, and heat transfer [18]. Higgs' work was assisted by boundary conditions provided by a preliminary version of the RMC-TFM, which was developed by many contributors under the direction of W.T. Thompson. In 2009, E.C. Corcoran, also under the supervision of B.J. Lewis and W.T. Thompson, published her doctoral thesis that further expanded and experimentally benchmarked the RMC-TFM [19].

In its current state, the RMC-TFM can predict fuel chemical stabilities under normal operating conditions, accident conditions, and primarily oxidizing fuel defect conditions, using the principle of Gibbs Energy Minimization (Section 2.4.2). Several complete fuel oxidation models have been created using the thermodynamic boundary conditions set by various versions of RMC-TFM [9-15]. For these fuel oxidation models, the RMC-TFM has been used to predict the nature (*e.g.*, phase stability) and quantities of compounds formed given the fission product inventory and environmental conditions.

1.3 Thesis Context within the RMC-TFM

The need for this thesis developed out of the latest work completed with the RMC-TFM by E.C. Corcoran. She expanded the RMC-TFM and performed validation redox benchmarking experiments. These experiments showed the model under-predicted oxidation in SIMFUEL samples (details of the experiments can be found in Section 2.5.2). Three modes were used to bring the model in line with experimental results, the latter two of which required additional experimental validation, thus creating the requirement for this thesis.

Corcoran conducted the validation redox experiments by reducing samples of pure UO_2 and SIMFUEL with a baseline oxygen partial pressure (pO_2) and then oxidized the samples at a variety of pO_2's in a coulombic titration (CT) apparatus [19]. The amount of oxygen acquired by the sample was measured and it was determined that the RMC-TFM predicted oxygen acquisition well for pure UO_2, but under-predicted the amount of acquired oxygen for SIMFUEL samples.

Corcoran postulated three modes that may account for increased oxygen acquisition by the SIMFUEL. In Mode I, the solubility of MoO_2 in UO_2 decreases at the temperatures required for the reduction phase, resulting in the MoO_2 being forced into the metallic Mo phase. Upon the oxidation phase, the Mo metal re-oxidizes to become MoO_2 again, resulting in more oxygen acquisition by the sample than predicted. Mode II involves the hyper-stoichiometric phase of molybdenum dioxide (MoO_{2+x}). Previous versions of the RMC-TFM did not account for this phase, possibly explaining the under-prediction of oxygen acquisition. Mode III describes the UO_2 fuel combining with Mo to form U-Mo-O compounds, namely $UMoO_6$. $UMoO_6$ acquires one mole of O_2 when formed from MoO_2 and UO_2, allowing for a significant amount of oxygen acquisition.

For Mode I, the solubility of MoO_2 in UO_2 was modelled using the work of Kleykamp [20]. However, it was postulated that MoO_2 solubility in UO_2 would be less at the lower temperatures used in the CT experiments of Ref. [19]. A function of MoO_2 solubility in UO_2 with respect to temperature was fitted to respect the experimental findings of Kleykamp at high temperatures, but also allow for less MoO_2 solubility in UO_2 at the lower temperatures used in the CT experiments. The result was a significant increase in the predicted oxygen acquisition of the samples, but not enough to account for all the oxygen acquisition.

For Mode II, the hyper-stoichiometry of MoO_2 to MoO_{2+x} predicted by Zador [21] and later published by Brewer in his Mo-O binary phase diagram [22] was included in the model. This change had a negligible effect on the RMC-TFM prediction of the oxidation of fuel as this region and the deviation from ideal stoichiometry are both relatively small. Part of this thesis was focused on experimentation of this non-stoichiometric region of MoO_2 in order to validate the findings of Zador and consequently the predictions of the RMC-TFM. This aspect of the project was relatively unfruitful, but is included in Appendix A.

For Mode III, $UMoO_6$ was added to the RMC-TFM using the thermodynamic data from Dash *et al.* [23] and Dharwadkar *et al.* [24]. The production of $UMoO_6$ acquires one mole of O_2 from the surrounding environment if made from one mole each of the starting reactants MoO_2 and UO_2. The addition of $UMoO_6$ to the model brought the oxidation predictions of the model in line within the uncertainties of the validation experiments. This thesis focused on the $UMoO_6$ compound, its synthesis, the experimental determination of its thermodynamic data, and selection of data for inclusion in the RMC-TFM.

1.4   Objectives of the Research

The objective of this thesis was to improve the RMC-TFM by refining our understanding of $UMoO_6$ and the UO_3-MoO_3 phase diagram. This involved many sub-tasks, which included:

    i)   Creation of a novel, aqueous synthesis method that produces $UMoO_6$ of high quality and purity, paired with thorough characterization of the product material.

ii)   Experimental measurements of the thermodynamic properties (*e.g.*, C_p, ΔH°_{trans}, ΔH°_{decomp}, and T_{decomp}) of $UMoO_6$ and comparison of measurements to available literature data.

iii)   Calculation of the $\Delta H^\circ_{f, 298\,K}$ of $UMoO_6$ from the experimental measurements and comparison to available literature data.

iv)   Evaluation of all available thermodynamic data for $UMoO_6$, both measured and from literature, to select the most appropriate data for use in the RMC-TFM via the assessment of the UO_3-MoO_3 phase diagram.

v)   Assess the effect of data changes on the RMC-TFM prediction of the benchmarking CT experiments.

Section 4 details the results and discussion of each sub-task in pursuit of the main objective of this thesis.

2.   Background

The aim of this section is to provide all background knowledge relevant to this thesis. First, Section 2.1 describes CANDU® technology, including the physical configuration of the reactor, nuclear fission and breeding, and defective fuels. This gives context to the complex system being modelled by the RMC-TFM. Section 2.2 reviews the thermodynamic properties used in this thesis. Section 2.3 presents the work previously completed on $UMoO_6$ in the literature. Section 2.4 describes FACTSage [25], the thermodynamic computing program that computes chemical stabilities based on the RMC-TFM. Finally, Section 2.5 further describes the RMC-TFM and its relation to this thesis.

2.1   CANDU® Technology

A nuclear fuel is a complex chemical system which is modelled by the RMC-TFM. This section provides context to this system by presenting the aspects of CANDU® technology relevant to this thesis.

2.1.1   *Reactor Design*

In a CANDU® reactor, 28-37 ceramic natural UO_2 fuel pellets are loaded into Zircaloy-4 tubes, backfilled with helium gas and sealed to form fuel elements. Fuel bundles are made from the assembly of 37 or 43 fuel elements, depending on the CANDU® reactor design. A 700 MW_e CANDU®-6 reactor uses 37 element fuel bundles, 12 fuel bundles per fuel channel and has 380 fuel channels in the Calandria, or reactor core. Therefore, 4560 fuel bundles, or over 168 000 fuel elements or over 5 million fuel pellets, are present in the reactor during operation [26]. A basic visual representation of the components of a CANDU® reactor can be seen in Figure 1.
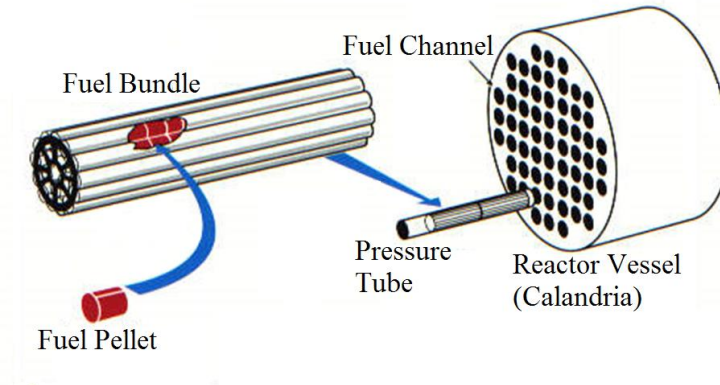
Figure 1: Visual representation of the components of a CANDU®, adapted from [27]

Heavy water (D_2O) is used as both the moderator and coolant in CANDU®. It is pumped directly over the fuel bundles under high pressure of 9.89 to 11.05 MPa to prevent it from boiling, removing the heat to later be used to drive a heat exchanger, create steam, turn turbines, and create electrical power [26]. The thin, collapsible Zircaloy-4 sheathing protects the fuel from direct contact with the D_2O coolant while absorbing few neutrons and promoting good thermal conductivity [28]. A cross section of a fuel element can be seen in Figure 2.

2.1.2   *Nuclear Fission and Breeding*

As described in Section 2.1.1, the UO_2 pellets are placed in Zircaloy-4 sheathing, backfilled with helium gas, sealed, and assembled into fuel bundles. Figure 2 shows a cross section of a fresh UO_2 fuel element inside a pressure tube with coolant flowing over the sheathing.
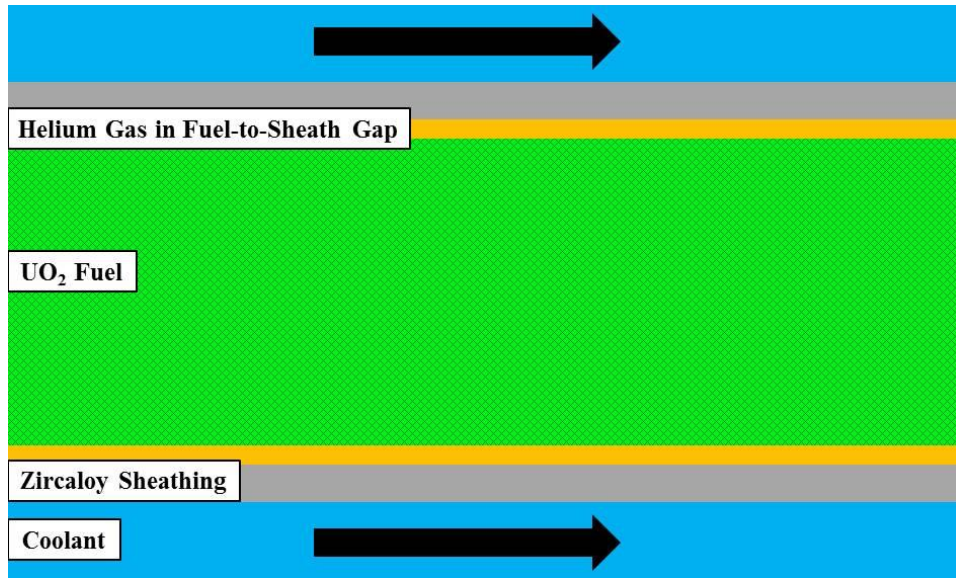
Figure 2: Cross section of a fresh fuel element

When fission is initiated, the fresh UO_2 fuel matrix (where the U is comprised of 99 % ^{238}U, 0.711 % ^{235}U and trace ^{234}U [29]) is bombarded with neutrons. These neutrons are "slowed" (thermalized) by the D_2O moderator. Some ^{235}U atoms undergo fission when the atom absorbs a thermal neutron and splits into one large and one small fission product, releasing heat and more neutrons, Equation 1. Some ^{238}U atoms absorb neutrons and decay to form activation products in a process known as breeding. ^{234}U generally alpha decays to Thorium, specifically ^{230}Th.

$$^{235}_{92}U + ^{1}_{0}n \rightarrow large\ fission\ product + small\ fission\ product + (2 - 3\ )^{1}_{0}n + heat$$ Equation 1
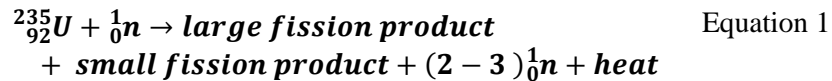
Fissile materials (such as ^{235}U) are directly capable of fission when thermal neutrons are absorbed. In the right conditions, they can sustain a nuclear chain reaction as they produce more neutrons during fission than they absorb. The neutrons released during fission can be thermalized by the moderator and absorbed by other fissile atoms, which fission and sustain the nuclear reaction. To maintain criticality, the correct moderation to thermalize the neutrons and the correct geometry to minimize neutron loss by absorption or leakage are required. Criticality is the sustainment of the nuclear chain reaction by the system alone with no other neutron sources.

Fertile materials (such as ^{238}U) are not directly fissile, but can become fissile through the absorption of a neutron and two subsequent beta decays [30], as seen in Equation 2.

$$^{238}_{92}U + ^{1}_{0}n \rightarrow ^{239}_{92}U \rightarrow ^{239}_{93}Np + ^{0}_{-1}\beta \rightarrow ^{239}_{94}Pu + ^{0}_{-1}\beta \qquad \text{Equation 2}$$
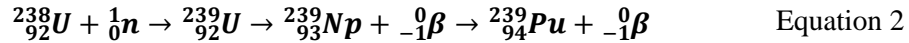
^{239}U, ^{239}Np, and ^{239}Pu are known as activation products as they are formed from the absorption of a neutron and subsequent decays, but are not formed from the splitting of an atom like fission products. The conversion of fertile material into fissile material is termed breeding. Breeding is important in CANDU® fuel as the ^{235}U is the initial fissile material at reactor start, but fertile ^{238}U converted to fissile ^{239}Pu sustains the criticality of the reactor and accounts for the majority of the fission in CANDU® [31]. This is because CANDU® reactors operate using natural uranium and thus initially only 0.711 % of the fuel is fissile ^{235}U and over 99 % of the fuel is the fertile ^{238}U isotope [26] and must be bred to be fissile and possibly undergo fission.

Fissile ^{233}U, ^{235}U, and ^{239}Pu (bred from fertile ^{238}U) undergo fission in CANDU® reactors. As described earlier, fission results in one large fission product and one small fission product. A bimodal distribution of fission products is found when plotting the probability of formation of a fission product by the molecular mass of that fission product, as seen in Figure 3. The distribution of fission products is a function of the fissile isotope and the speed of the neutrons causing the fission.
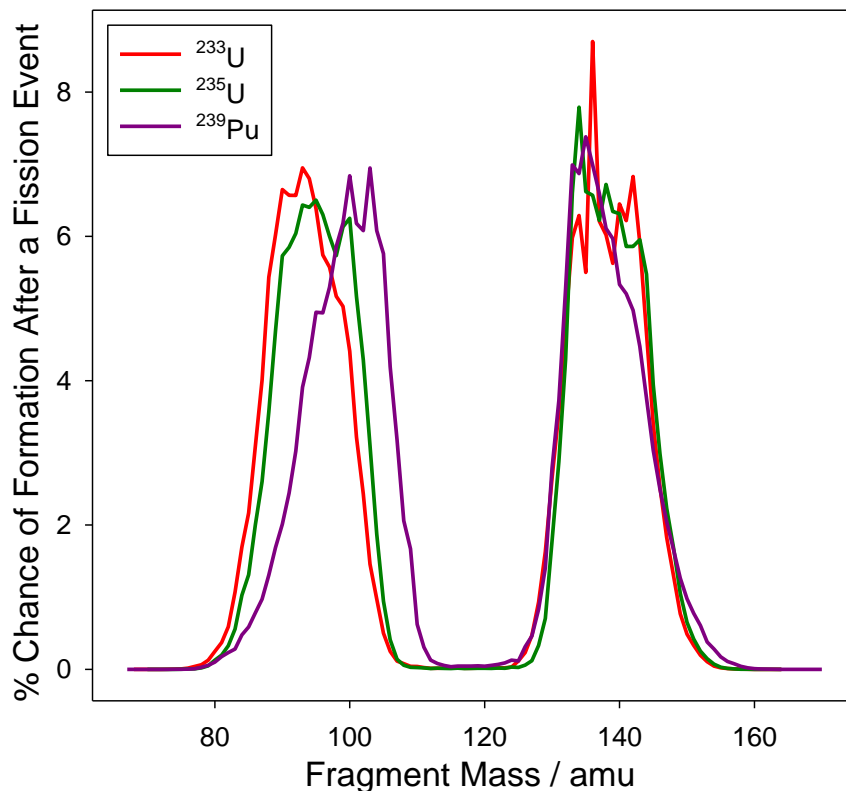
Figure 3: Fission product distributions of ^{233}U, ^{235}U, and ^{239}Pu from thermal neutrons, adapted from [32]

After fission and breeding have commenced, the fresh UO_2 fuel matrix becomes mixed with fission and activation products that can precipitate from the fuel matrix as oxides (oxide precipitates) or in metallic form (metallic precipitates), remain dissolved in the fuel matrix as oxides (soluble oxides) or in metallic form (noble metal inclusions), or become a gas which can slowly accumulate in the helium gas within the fuel-to-sheath gap [33]. The degree to which UO_2 fuel has been converted to fission or activation products is known as burnup and is measured in units of fraction of fuel atoms that underwent fission (fission per initial metal atom as a percentage) or in actual energy released per mass of initial fuel in gigawatt days per metric ton (GWd ton^{-1}).

The new mixture of UO_2 and fission and activation products spans a significant portion of the periodic table, Figure 4. It can be noted that Mo can be found as a noble metal inclusion or a soluble oxide.

Figure 4: Chemical state of nuclear fuel fission and activation products, adapted from [34]

As per the design specifications, the first form of radioactive material containment is the UO_2 fuel matrix. Fission and activation products can remain dissolved in the UO_2 fuel matrix, captured within grain boundaries, or within fuel matrix inclusions. Also, the Zircaloy-4 sheathing encloses the helium gas (that contains some gaseous fission products) around the fuel and prevents the fuel from direct contact with the D_2O coolant, reducing fuel oxidation. This is seen in Figure 5 and Table 1.
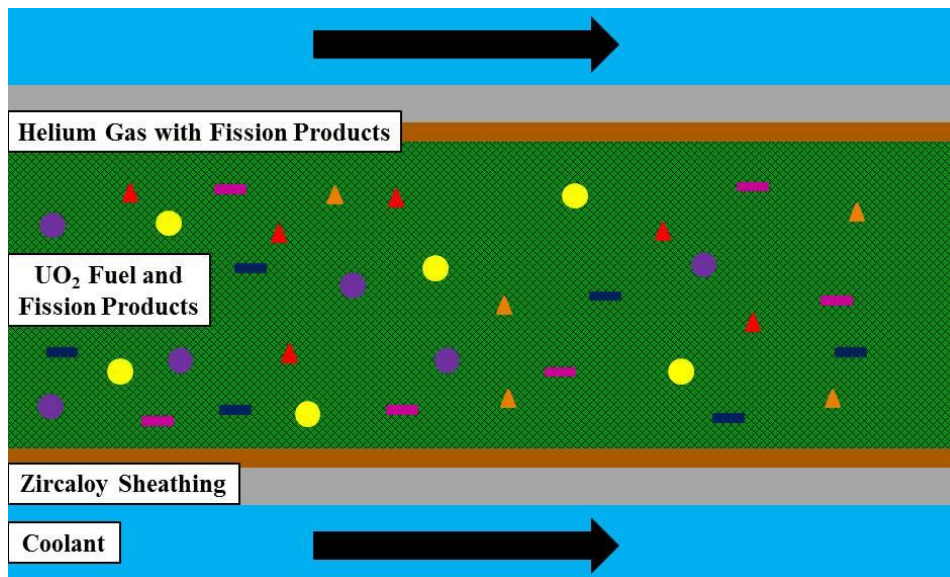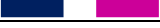
Figure 5: Cross section of a fuel element undergoing fission

Table 1: Legend for Figure 5

Symbol	Significance
● ●	Metallic Precipitates
▲ ▲	Noble Metal Inclusions
▬ ▬	Oxide Precipitates
▬▬▬	Helium Gas and Gaseous Fission Products
▨▨▨	Oxide Matrix (with Soluble Fission Products)

In this complex system, it is difficult to predict the states and amounts of each compound in the system without a chemical stability model or more expensive specialized post irradiation analysis. The RMC-TFM is capable of predicting the chemical stability of this complex system at equilibrium given the initial product inventory (*i.e.*, the fission and activation products predicted for a specific burnup) and environmental conditions such as the temperature and pressure of the system.

2.1.3 Defective Fuel

The complex chemical system described above can be significantly affected when the fuel sheathing becomes defective. A fuel defect occurs when a breach in the sheathing allows the heavy water coolant to make contact with the fuel. Generally, the coolant flashes to steam and oxidizes the Zircaloy-4 sheathing, producing hydrogen and creating a H_2/H_2O gas mixture in the fuel-to-sheath gap. The H_2/H_2O gas mixture comes in direct contact with the fuel and can oxidize the UO_2 fuel, causing it to become hyper-stoichiometric (Equation 3). The oxygen can then diffuse interstitially through the fuel matrix. Similarly, the H_2/H_2O mixture can oxidize fission and activation products. The extent of fuel oxidation is directly related to the fuel burnup (*i.e.,* the fuel chemical composition) and the $H_2{:}H_2O$ ratio (dependent on the size of the breach and temperature) [5]. The $H_2{:}H_2O$ ratio is generally represented by an oxygen potential (pO_2) and the relationship between the two is explained in Appendix B.

$$UO_2 + xH_2O \rightarrow UO_{2+x} + xH_2 \qquad \text{Equation 3}$$
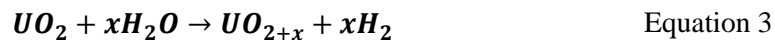
In addition to fuel oxidation, the helium back fill gas, gaseous fission products, and some oxide and metallic precipitates can escape into the coolant as a result of a fuel defect [18].

Figure 6 illustrates a breach in the Zircaloy-4 sheathing of a defective fuel and Figure 7 shows the release of the helium gas, gaseous fission products, and some oxide and metallic precipitates as the coolant flashes to steam in the fuel-to-sheath gap.
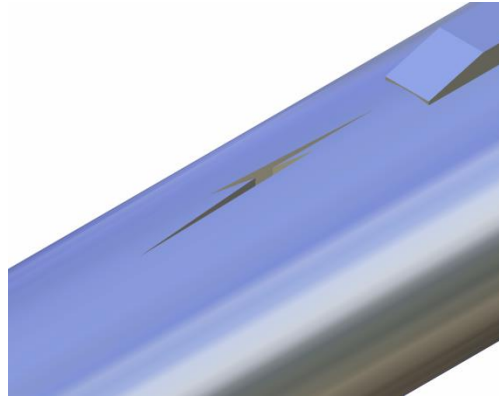
Figure 6: Computer generated image of the surface of a defective fuel element [10]
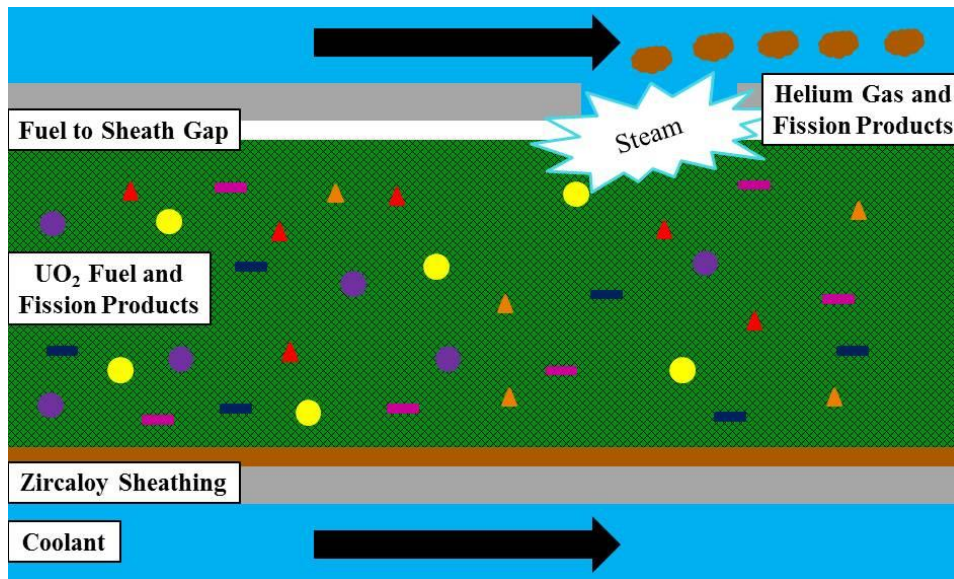
Figure 7: Cross section of a defective fuel element

Although the fuel defect rate is low in CANDU® reactors, being less than 0.1 % per fuel bundle, it equates to one fuel defect per reactor per year [4]. Hence, almost every nuclear reactor will have an instance of defective fuel element over its lifetime. Fuel defects can normally be attributed to one of the following [35]:

i)   Manufacturing flaws such as incomplete endcap welds, porous endcap bar stock, insufficient volume, excess hydrogen gas within the element, and fretting through the sheath from endcap weld flashings.

ii)   Operational defects such as sheath fretting due to debris from the coolant, stress corrosion cracking of the sheath due to power ramps (both normal and abnormal operation), bundle disassembly due to resonant vibration in acoustically active channels, and mechanical damage due to abnormal fuelling.

Fuel material properties are specific to the chemical state of the fuel, such as temperature gradient, thermal conductivity, matrix stress gradient, vapour pressure, creep strength, diffusion coefficient, grain size, grain restructuring, and crack patterns. When the fuel is oxidized, its material properties can change. One very important change is a decrease in the thermal conductivity of the fuel, which in extreme circumstances can lead to fuel centre line melting [5]. Centre line melting is when the centre of the fuel begins to melt as a result of the heat generated through fission not being dissipated at a sufficient rate [36].

Also important, defective fuels can result in some fission and activation products being released into the primary coolant, thus affecting coolant chemistry, increasing its activity (sometimes called radioactivity) and potentially posing an increased health risk to some on-site nuclear energy workers [6]. If the activity of the coolant in the primary heat transport system is increased to a level above that mandated in the Operating Policies & Principles (OP&P) in the licence administered by the Canadian Nuclear Safety Commission (CNSC), and the level is not reduced below the limit within 24 hours, the reactor must be shut down. The activity of iodine-131 (^{131}I) is normally measured and used to represent the activity of the entire coolant due to the health hazard ^{131}I poses to plant workers [37]. The permissible limits of ^{131}I are shown below in Table 3 [38]. The shutdown limit is associated with the flow rate of the purification system of the primary heat transport system (as ^{131}I is removed by filtration and generally not left to accumulate). Defective fuels should be removed immediately upon detection and location to prevent energy and financial loss and maintain plant safety margins [5].

Table 2: OP&P shutdown limits of ^{131}I in the primary heat transport system [38]

Flow Rate (kg s^{-1})	^{131}I Shutdown Limit (µCi kg^{-1})
0	700
2.5	120
5.0	60
10.0	32
15.0	20
20.0	16

The RMC-TFM can be used to predict the chemical stability of the fuel under normal operating conditions, but specializes in its ability to predict chemical stability in the oxidative conditions created in off-normal conditions, which include defective fuel failures. As such, the RMC-TFM can be used to produce some of the boundary conditions required by other kinetic fuel behaviour models [9-13] to predict the behaviour of the fuel under defect conditions. Therefore, the maintenance and improvement activities of the RMC-TFM, such as the activities of this thesis, are important to the Canadian nuclear industry and advance our predictive computational toolset for nuclear fuel behaviour.

2.2 Thermodynamics Overview

The RMC-TFM is a database of thermodynamic information that is used to predict fuel chemical stability under equilibrium conditions by applying the first principles of Gibbs' energy minimization (Section 2.4.2). Within this section, an overview of the fundamental thermodynamic values that make up the RMC-TFM is provided. These values include enthalpy (H), heat capacity (C_p), and entropy (S), and by extension, Gibbs free energy (G). Also, the effect of mixing phases on the thermodynamic properties of a system is presented.

2.2.1 Enthalpy

Enthalpy (H) represents the total energy of a thermodynamic system. It is defined in terms of internal energy (U), pressure (P), and volume (V), as seen in Equation 4.

$$H = U + PV$$
<div align="right">Equation 4</div>

U can be thought of as the energy required to create a system. It is related to heat (q) and work (w) by Equation 5.

$$U = q - w \qquad \qquad \text{Equation 5}$$

PV can be thought of as the energy required to create room for that system by establishing its pressure and volume. Enthalpy represents the total energy of the system [39].

It should be noted that *H* cannot be measured directly and its absolute value is often not relevant to thermodynamic study. Generally, only changes in enthalpy (ΔH) from a reference point are measured and used. ΔH is a state value meaning it is independent of the steps between the initial and final states. By definition, an exothermic process is performed when $\Delta H < 0$ and an endothermic process when $\Delta H > 0$.

Enthalpy of reaction (ΔH_{RXN}) is defined as the energy required for a given chemical reaction to proceed from reactants to products. Hess's law states that a change in enthalpy is independent of the pathway between the initial and final states, as seen in Equation 6.

$$\Delta H_{RXN} = \Sigma \Delta H_{f,products} - \Sigma \Delta H_{f,reactants} \qquad \text{Equation 6}$$

The standard enthalpy of formation (ΔH^{o}_{f}) of a compound is defined as the energy required to create one mole of that compound from its constituent elements in their most stable states at STP (Standard Temperature and Pressure). ΔH^{o}_{f} of elements in their most stable form are assigned a value of zero by convention (as a reference point is required) [39].

2.2.2 *Molar Heat Capacity*

Molar heat capacity (*C*) is the energy required to raise the temperature of 1 mol of substance by 1 K. It can be defined as a differential of the change in heat over the change in temperature (*T*) seen in Equation 7. It is normally expressed in J mol^{-1} K^{-1}.

$$C = \frac{dq}{dT} \qquad \qquad \text{Equation 7}$$

However, *dq* is dependent on the process, leading to molar heat capacity at constant volume (C_V) and constant pressure (C_p). Only C_p will be used in this thesis. It is obtained by applying a constant pressure to Equation 7,

$$C_P = \frac{dq_P}{dT}$$

Equation 8

The relationship between ΔH and C_p is important as it is used by the FACTSage program. This relationship is built by taking the partial derivatives of Equations 4 and 5 with respect to V at constant P to obtain

$$dH_P = dq_P$$

Equation 9

Thus, Equation 8 can be extended to include

$$C_P = \frac{dq_P}{dT} = \frac{dH_P}{dT}$$

Equation 10

and

$$\Delta H_P = \int_{T_1}^{T_2} C_p dT$$

Equation 11

A complete proof can be found in Appendix C. Because ΔH^o at 298 K (ΔH^o_{298K}) is most often reported in the literature, Equation 11 can be modified to give ΔH^o for any given temperature (ΔH^o_T) [39].

$$\Delta H^o_T = \Delta H^o_{298K} + \int_{298K}^{T} C_p dT$$

Equation 12

2.2.3 Entropy

Entropy (S) is used to account for the preferred direction of energy flow (*i.e.*, (i) heat flowing into or out of the system; (ii) work being done on or by the system). This section further defines entropy using the second law of thermodynamics, shows the relationship between ΔS and C_p, and finally refines this relationship as the third law of thermodynamics gives meaning to the absolute value of S.

2.2.3.1 Entropy and the Second Law of Thermodynamics

S can be thought of as the degree of disorder or dispersal of energy. It is observed that gases disperse in a vacuum and heat transfers from high temperatures to lower temperatures. Thus, the second law of thermodynamics is an observation that, in a thermodynamic process, the sum of the entropies of systems participating

increases. Additionally, if a system becomes more ordered, the energy required for that change must come from the surroundings.

If the process is completely reversible,

$$\Delta S_{universe} = \Delta S_{system} + \Delta S_{surroundings} = 0$$

<div align="right">Equation 13</div>

If the process is natural and irreversible,

$$\Delta S_{universe} = \Delta S_{system} + \Delta S_{surroundings} > 0$$

<div align="right">Equation 14</div>

There are three constituents to consider, the system of interest, the area surrounding the system, and the universe. The universe is the summation of both the system and the surroundings. It is a volume so large that any change in volume or energy is small in comparison to the total volume of the universe. Because $\Delta S_{universe}$ must be equal to or greater than zero, over time the universe, as a whole, progresses towards a more disordered state [39].
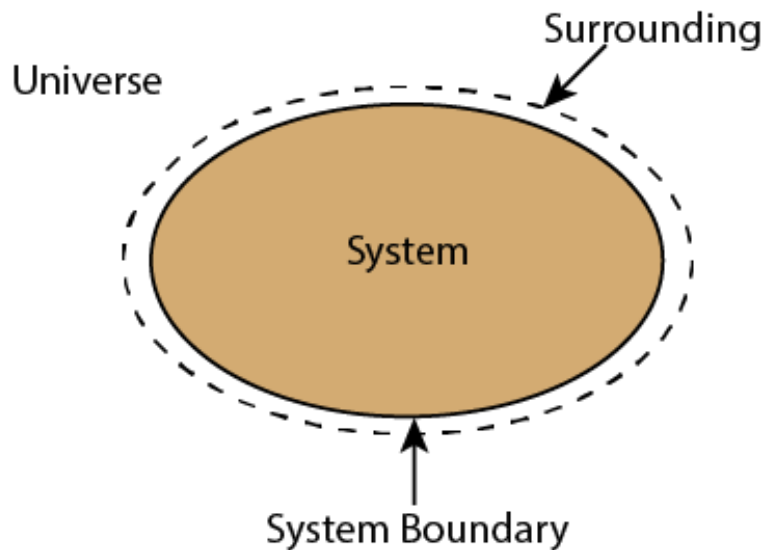
<div align="center">**Figure 8: Visual representation of entropy constituents [40]**</div>

A small change in S is defined as the thermal energy added to the system (q) by the surroundings during a reversible process divided by the temperature of the system and surroundings, Equation 15 [41].

$$dS = \frac{dq_{rev}}{T}$$

<div align="right">Equation 15</div>

2.2.3.2 *Entropy and Heat Capacity*

The relationship between entropy and heat capacity can be found by rearranging Equation 15 and substituting Equation 9 to obtain

$$dH = TdS$$

Equation 16

With Equation 10, this rearranges to,

$$dS = \frac{C_P}{T} dT$$

$$\Delta S = \int_{T_1}^{T_2} \frac{C_P}{T} dT$$

Equation 17

2.2.3.3 *Entropy and the Third Law of Thermodynamics*

At absolute zero temperature, a solid is in its ground state or the lowest possible U. Vibrational energy of the ground state exists and U is not zero. As long as the system exists, the same conclusions can be drawn for H using Equation 4. Because the absolute values of U and H are arbitrary, only changes in U and H are measured and used in thermodynamics. Unlike U and H, S is sometimes expressed as an absolute value at given conditions. This is because $S = 0$ is not arbitrary, but rather has significant meaning. The third law of thermodynamics states "*all truly perfect crystals at absolute zero temperature have zero entropy*" [39]. At absolute zero, a crystal is free of defects, has no translational or angular energy, and its atoms are in the ground state. This is the greatest possible order for matter and thus $S = 0$.

The reason $S = 0$ comes from the *fundamental assumption of statistical thermodynamics*, Equation 18.

$$S = k_B \ln \Omega$$

Equation 18

where k_B is the Boltzmann constant and Ω is the number of microstates. At absolute zero, $\Omega = 1$ and thus $S = 0$ [41]. It can be difficult to determine the number of microstates in a system, thus Equation 17 is adapted under the condition $S = 0$ when $T = 0$ to give Equation 19.

$$S_T^o = \int_0^T \frac{C_P}{T} dT$$

Equation 19

Similar to $\Delta H^o{}_{298K}$, $S^o{}_{298K}$ is most often reported in the literature. S^o_T can then be calculated using

$$S^o_T = S^o_{298K} + \int_{298K}^{T} \frac{C_p}{T} dT$$

Hess's law can also be applied to entropies, however absolute values are used.

$$\Delta S_f = \Sigma S_{products} - \Sigma S_{reactants}$$

2.2.4 Gibbs Free Energy

Gibbs free energy is a term used to define the total useful energy of a system. Mathematically, it is the internal energy of the system (U), plus a small amount of work (PV) required to create room for the system minus a small amount of energy (TS) obtained from the environment when creating the system.

$$G = U - TS + PV$$

Substituting in Equation 4 for a change in Gibbs free energy at constant pressure

$$\Delta G = \Delta H - T\Delta S$$

Equation 23 is very useful in thermodynamics as it can be easily solved for most processes. ΔH^o and S^o values for most compounds have been well researched and literature values accepted [39]. $C_p(T)$ functions are also often published in the literature and thus ΔG can be solved at different temperatures using Equations 12 and 20. As a function of ΔH and S, ΔG is also temperature dependent.

Equation 23 shows the temperature dependence of G. The pressure dependence can be shown by taking the first derivative of Equation 22 with respect to pressure, Equation 24.

$$dG = VdP$$

If the ideal gas law ($PV = nRT$) is substituted for one mole of gas

$$dG = \frac{RT}{P} dP$$

$$\Delta G = RT \ln\left(\frac{P_2}{P_1}\right)$$

<div align="right">Equation 25</div>

Equation 26 can be used to define ΔG at some pressure (P) relative to ΔG^o (*i.e.*, when pressure is 1 atm) [41].

$$\Delta G = \Delta G^o + RT \ln(P)$$

<div align="right">Equation 26</div>

Because G is a function of H, it also cannot be measured directly and its absolute value is often not relevant to thermodynamic study. Generally, only changes in Gibbs free energy (ΔG) from a reference point are measured and used.

Gibbs energy of formation (ΔG_f) is the amount of useful energy that must be put into a system to form one mole of product from its most stable elemental parts. Hess's law can be applied to Gibbs free energy.

$$\Delta G_{RXN} = \sum \Delta G_{f,products} - \sum \Delta G_{f,reactants}$$

<div align="right">Equation 27</div>

Because ΔG represents the total useful energy of a system, it gives insight into the stability and favourability of a system [42]. Equation 28 is an important relationship for thermodynamics. Its derivation can be found in Appendix C.

$$\Delta G_{P,T,system} < 0$$

<div align="right">Equation 28</div>

Equation 28 is for spontaneous isobaric and isothermal processes. In general, systems with a negative ΔG are thermodynamically favoured and will proceed in the direction indicated, $\Delta G = 0$ corresponds to a system at equilibrium, and a positive ΔG is thermodynamically disfavoured and will proceed in the reverse of the indicated direction. This can be seen in Figure 9.
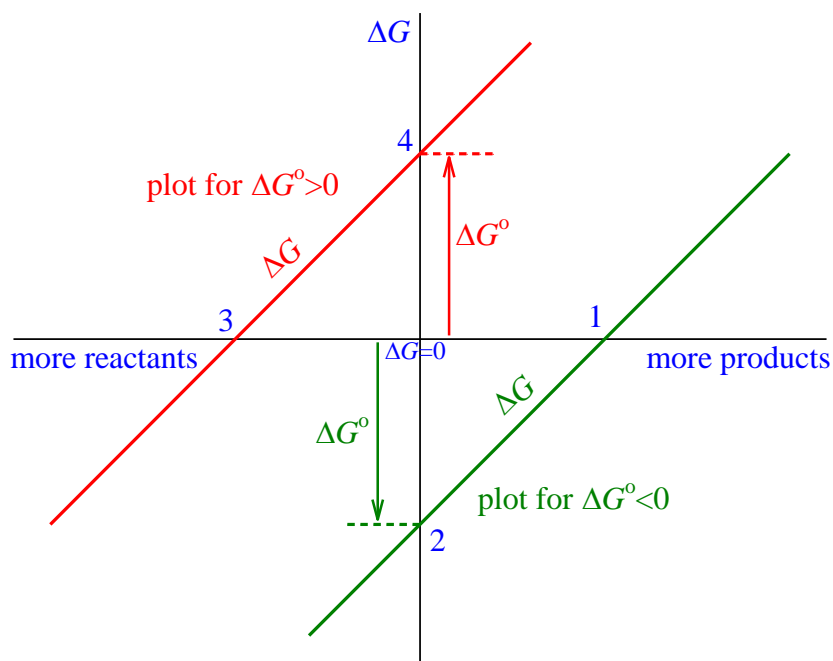
Figure 9: Visual representation of ∆G, adapted from [43]

In Figure 9, the green solid line represents the G of a given chemical reaction written as reactants $\rightarrow$ products. Point 1 represents the reactants:products ratio at equilibrium. This is the point where $\Delta G_{RXN} = 0$ and the reaction does not proceed in either direction. If the ratio of reactants:products is at point 2, ΔG_{RXN} is negative and the reaction progresses to the right, towards point 1, with an equilibrium that is more product-favoured. In this case, the reaction proceeds in the direction written and reactants become products as $\Delta G_{RXN} < 0$.

The solid red line represents the G of a different chemical reaction. Point 3 represents the ratio of reactants to products that corresponds to equilibrium as $\Delta G_{RXN} = 0$. If the ratio of reactants to products is at point 4, ΔG_{RXN} is positive and the reaction progresses to the left, towards point 3, with an equilibrium that favours reactants. In this case, the reaction proceeds in the opposite direction written and products become reactants as $\Delta G_{RXN} > 0$.

2.2.5   *Mixing of Phases*

Mixing occurs when two or more phases form a homogenous new phase, but do not combine chemically. When mixing occurs, the thermodynamic values of the system experience a change. This phenomenon is explained using the example of a fictitious liquid solution of elements A and B.

If A and B are completely immiscible (no mixing occurs), the Gibbs energy of the A-B liquid solution (G_l) would simply be a weighted average of the two phases, Equation 29, represented by the black dashed line in Figure 10 [44].

$$G_l = G_A^o X_A + G_B^o X_B$$ Equation 29

where X_A and X_B are the molar fractions of A and B in the liquid, respectively, and G_A^o and G_B^o are the Gibbs energy of formation under standard conditions of A and B for the liquid phase, respectively.

If both A and B are partially or completely miscible, the Gibbs energy of the liquid system is affected by the mixing. G_l is the Gibbs free energy curve of the liquid solution of A and B, represented in Figure 10 by the curved solid black line. The difference in Gibbs free energy between the miscible and immiscible solutions is known as Gibbs energy of mixing (ΔG_{mix}). ΔG_{mix} is a function of both enthalpy of mixing (ΔH_{mix}) and entropy of mixing (ΔS_{mix}), Equation 30.

$$\Delta G_{mix} = \Delta H_{mix} - T\Delta S_{mix}$$ Equation 30
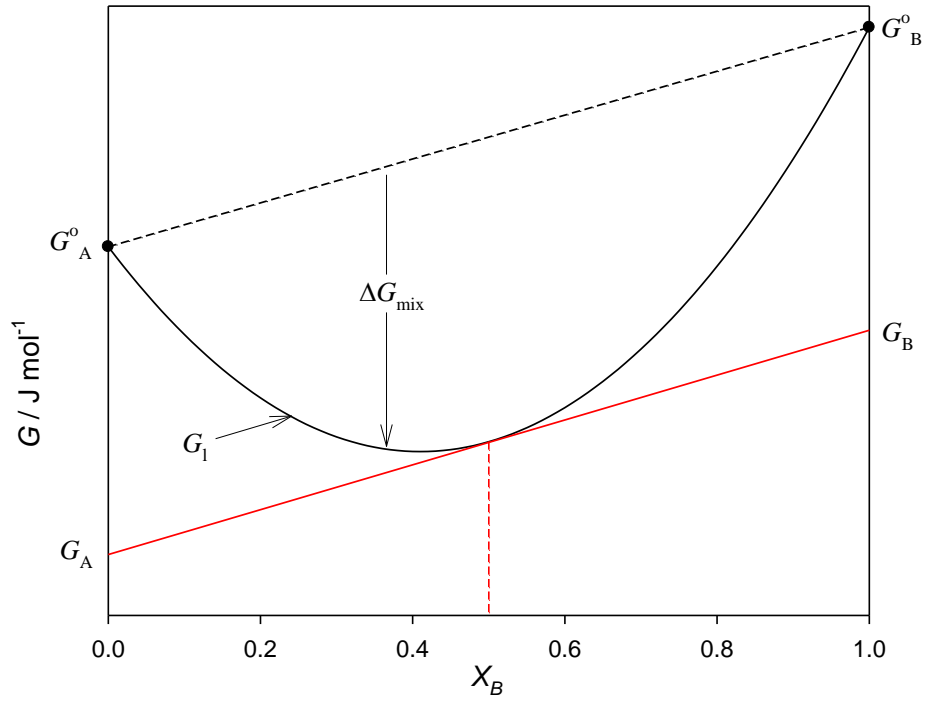
Figure 10: The Gibbs free energy curve of a liquid solution of A-B (G_l) at an arbitrary temperature, T

Figure 10 represents the Gibbs free energy curve at a single temperature, T. ΔG_{mix} is a function of composition, temperature, and pressure. Figure 11 represents the ΔG_{mix} of the A-B mixture at various temperatures. A similar diagram can be made for varying pressure.
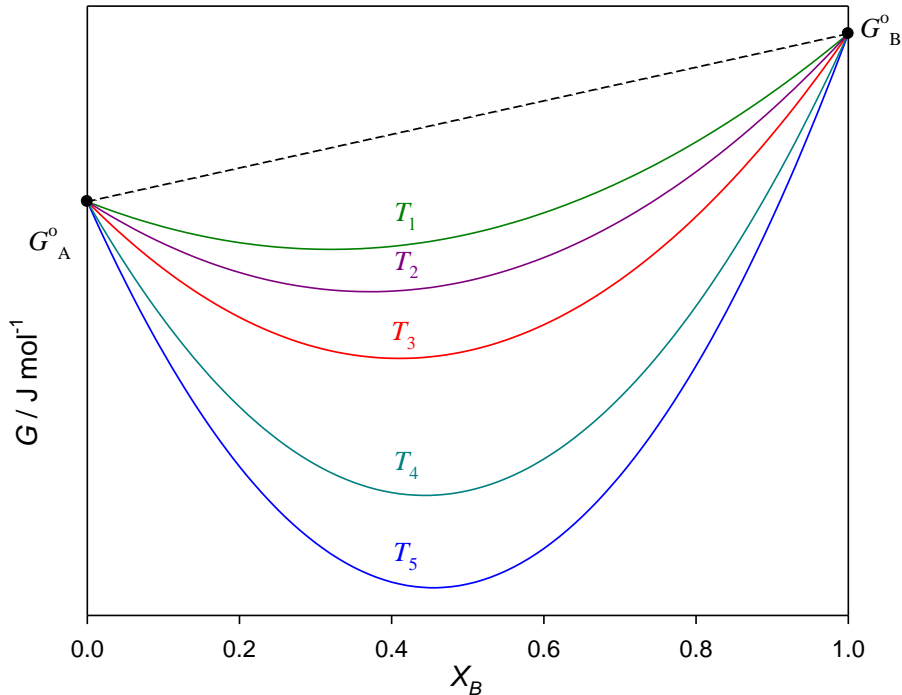
Figure 11: The Gibbs free energy curves of liquid solution A-B at various arbitrary temperatures, T_1, T_2, T_3, T_4, and T_5

In an ideal solution, the A and B atoms are nearly alike, have nearly identical radii, and have nearly identical electronic structures. Under this assumption, there is no change in bonding energy or volume upon mixing and thus $\Delta H_{\text{mix}}^{\text{ideal}} = 0$ [44].

For ideal $\Delta S_{\text{mix}}^{\text{ideal}}$, Equation 18 is used. Ω (the microstate) is assumed to be only a function of the configuration of the atoms in the mixture due to random mixing and no other factors, such as temperature, pressure, and chemical gradients. Since the configurational entropy (S_{config}) of pure A and B are both zero, ΔS_{config} is equal to S_{config}. Additionally, because of the assumption of only random mixing affecting the entropy, $\Delta S_{\text{mix}}^{\text{ideal}} = \Delta S_{\text{config}} = S_{\text{config}}$.

For the Ω term, a random distribution of A atoms (N_A) and B atoms (N_B) over ($N_A + N_B$) random sites in the liquid is assumed by random mixing. The entropy due to S_{config} (or in this case $\Delta S_{\text{mix}}^{\text{ideal}}$) is then given by Boltzmann's equation, Equation 31.

$$S_{config} = \Delta S_{mix}^{ideal} = k_B \, ln\left(\frac{(N_A + N_B)!}{N_A! \, N_B!}\right)$$

<div align="right">Equation 31</div>

where k_B is the Boltzmann constant [44].

If Stirling's approximation is applied to Equation 31 [44],

$$\Delta S_{mix}^{ideal} = -k_b \, (N_A + N_B) \cdot \left(X_A \, ln\frac{N_A}{N_A + N_B} + X_B \, ln\frac{N_B}{N_A + N_B}\right)$$

<div align="right">Equation 32</div>

For one mole of solution (*i.e.,* $N_A + N_B = N^o$ (Avogadro's number)),

$$\Delta S_{mix}^{ideal} = -R \, (X_A \, ln \, X_A + X_B \, ln \, X_B)$$

<div align="right">Equation 33</div>

as $k_b N^o = R$ [44], $X_A = \frac{N_A}{N_A + N_B}$ and $X_B = \frac{N_B}{N_A + N_B}$.

Since $\Delta H_{mix}^{ideal} = 0$,

$$\Delta G_{mix}^{ideal} = R \, T(X_A \, ln \, X_A + X_B \, ln \, X_B)$$

<div align="right">Equation 34</div>

To determine the value of G_l for any composition, the tangent is taken at the composition of interest (shown in red for $X_B = 0.5$ in Figure 10). Its interceptions of both y-axes are measured (G_A and G_B). G_l is then defined according to Equation 35.

$$G_l = G_A X_A + G_B X_B$$

<div align="right">Equation 35</div>

In reality, the A-B solution is likely not ideal. The difference between a real solution value and its corresponding ideal value is known as an excess parameter, or excess Gibbs energy (G_E). Figure 12 is an example of the difference between ideal and real mixing.

$$G_E = \Delta G_{mix} - \Delta G_{mix}^{ideal}$$

<div align="right">Equation 36</div>
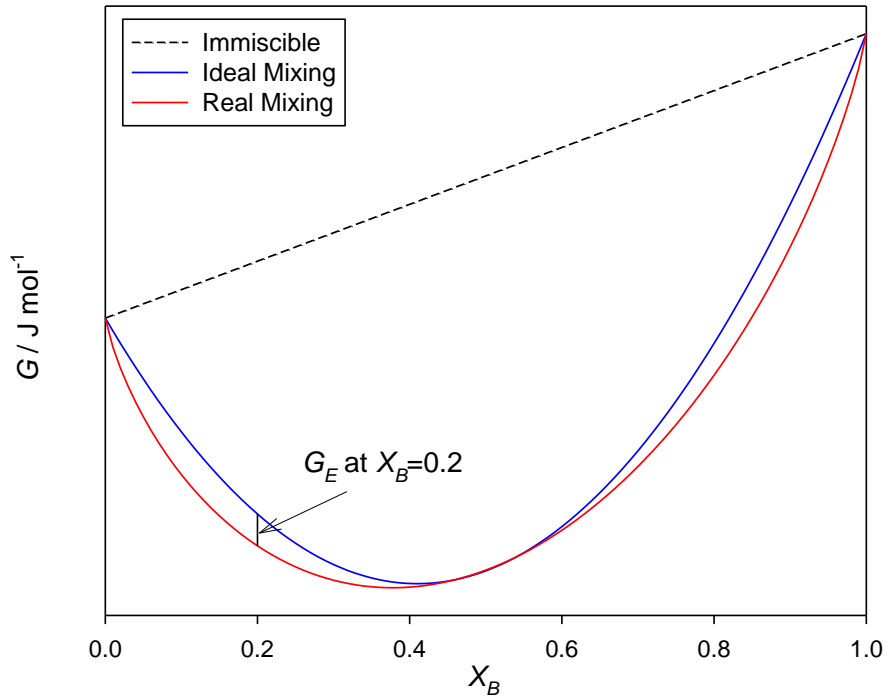
Figure 12: Example of the difference between Gibbs free energy curves of ideal and real mixing

If G_E is positive, the solution is less stable than if it were ideal. Conversely, if G_E is negative, the solution is more stable than if it were ideal [44].

In this thesis, excess parameters are represented by polynomials. G_E is defined according to Equation 37 as a function of composition and temperature.

$$G_E = X_A X_B \left[A + B\,T + C\,\ln T + D\,T^2 + E\,T^3 + F\,T^{-1} \right] \qquad \text{Equation 37}$$

where A, B, C, D, E, and F are coefficients selected to fit the system. In this thesis, only A and B coefficients are used in an attempt to model behaviour in as few terms as possible. This method generally leads to better extrapolations and a more stable model.

A simplistic polynomial function was selected to represent the G_E. Other functions can be selected; however, these functions can have unnecessary deviations from

ideal mixing when extrapolated. Additionally, existing solution data in the RMC-TFM use polynomial functions to represent G_E.

2.3 UMoO$_6$ Data in the Literature

Mo and O$_2$ can react with the UO$_2$ fuel to create U-Mo-O compounds such as UMoO$_5$ [45], UMoO$_6$ [45], U$_2$MoO$_8$ [45], UMo$_2$O$_8$ [45], UMo$_7$O$_{22}$ [46], and UMo$_{10}$O$_{32}$ [46], among others. Molybdenum's high affinity for oxygen makes it of particular interest when studying fuel oxidation. Also, as molybdenum is an abundant fission product, it has a significantly greater effect on fuel oxidation models than many other fission elements. This thesis puts an emphasis on the compound UMoO$_6$ because of its proposed thermodynamic stability and importance in the UO$_3$-MoO$_3$ phase diagram. As described later in Section 2.5.3, UMoO$_6$ was added to the RMC-TFM yet requires further experimental validation.

2.3.1 Synthesis of UMoO$_6$

There are two main synthesis methods, solid state and aqueous, existing in the literature. This sub-section highlights shortcomings of these production methods and the requirement to develop a better synthesis method.

2.3.1.1 Solid State Synthesis of UMoO$_6$

Currently, the literature is dominated by solid state methods for the synthesis of UMoO$_6$, Table 3. These methods generally involve mixing molybdenum (VI) oxide (MoO$_3$) and a uranium oxide (UO$_2$, UO$_3$, or U$_3$O$_8$) and then heating at high temperatures in the presence of air or oxygen [23, 45-56]. High purity starting materials are used to minimize impurities in the final product. However, the volatility of MoO$_3$ above 723 K [57] causes it to be the limiting reagent and leads to significant excess U-oxide(s) in the final product. Some methods attempt to control the reaction stoichiometry by preventing MoO$_3$ volatility. This was attempted by crushing and sintering the reactants into a pellet [45], sealing in an ampoule [46], or accepting the volatility with the addition of excess MoO$_3$ [52]. Ultimately, the reactants are never matched in an ideal stoichiometry on the molecular level and excess reactant to varying degrees is inevitable in the final product.

Table 3: Solid state synthesis methods of UMoO$_6$

Published method	Starting materials		Conditions	
Authors	Uranium	Molybdenum	Temp (K)	Time
Bharadwaj *et al.* [47]	UO$_2$	MoO$_3$	950	21 h
	U$_3$O$_8$^{a}	MoO$_3$	950	21 h
Chattopadhyay *et al.*^{b} [46]	U$_3$O$_8$	MoO$_3$	873	6 h
Dash *et al.* [23]	U$_3$O$_8$	MoO$_3$	773	200 h
Juenke *et al.* [48]	U-O (UNS)	Mo-O (UNS)	1073-1273	UNS
Keskar *et al.* [49]	UO$_2$	MoO$_3$	1073	40 h
	UMoO$_5$^{c}	-	1173	8-10 h
Kovba *et al.* [50]	U$_3$O$_8$	MoO$_3$	UNS	UNS
Misra *et al.*^{d} [51]	UO$_2$	MoO$_3$	673	8 h
			773	8 h
			873	8 h
			1073	1 week
Miyake *et al.*^{e} [45]	UO$_3$	MoO$_3$	923	50 h
Nagai *et al.* [52]	U$_3$O$_8$	MoO$_3$	1043	2 h
Serezhkin *et al.* [53]	U$_3$O$_8$	MoO$_3$	773-823	100 h
Suleimanov *et al.* [54]	UO$_3$	MoO$_3$	823	48 h
Swaminathan *et al.*^{e} [55]	UO$_2$	MoO$_3$	873	48 h
Ustinov *et al.* [56]	U$_3$O$_8$^{a}	MoO$_3$	873-1273	UNS

UNS = unspecified

^{a}U$_3$O$_8$ synthesized by heating UO$_2$ in air

^{b}Compacted and sealed both compounds in an ampoule before heating

^{c}UMoO$_5$ synthesized by heating UO$_{2.00}$ (previously reduced in 7 % H$_2$ in Ar at 1123 K for 4-5 h) and MoO$_3$ in a vacuum sealed ampoule at 1173 K for 14 h

^{d}All heating completed sequentially

^{e}Both compounds pressed into a pellet to minimize MoO$_3$ volatilization during heating

The method used to characterize UMoO$_6$ synthesized by solid state methods is almost exclusively powder X-ray diffraction (P-XRD). P-XRD induces X-rays on a powder sample at a variety of angles. These X-rays diffract when they interact with

a crystallographic plane in the structure and are measured by a detector. By applying Bragg's Law (*i.e.*, nλ = 2$d$sinθ [58]) with the wavelength (λ) of the incident X-ray and the angle (2θ) between the incident X-ray and the diffracted X-ray and *n* being a positive integer, the interplanar spacing (*d*) of the planes can be determined. The result is a spectrum of the intensity of a diffracted X-ray as a function of the angle of the incident X-ray (or *d* spacing). This spectrum is unique to the crystal structure of the powder of interest, similar to a *fingerprint*. P-XRD generally does not measure impurities < 1 %, but impurities can be masked if the angles of intensities are coincident with the material of interest. Such is the case, at 2θ $\cong$ 21°, when comparing $UMoO_6$ and U_3O_8 [47], Figure 13.
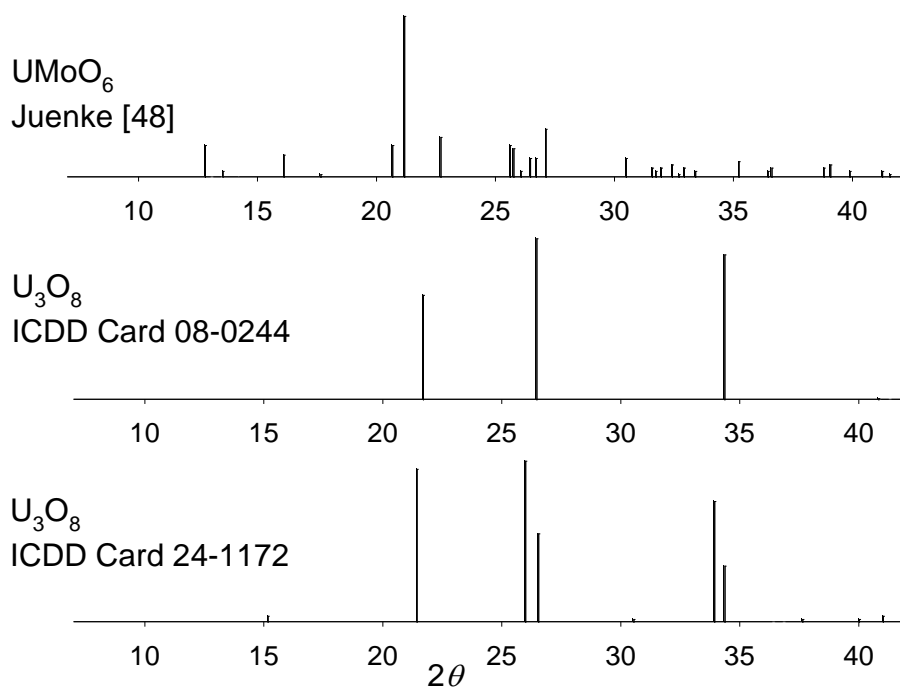
Figure 13: P-XRD of Juenke *et al.* [48] compared to U_3O_8 patterns (ICDD card 08-0244 and ICDD card 24-1172)

Juenke *et al.* [48] established the most common P-XRD reference card used for $UMoO_6$ characterization. The most prominent peak for $UMoO_6$ occurs at 2θ $\cong$ 21°. This can easily mask the 2θ $\approx$ 21° peaks found for U_3O_8 ICDD cards 08-0244 and 24-1172.

Although the P-XRD patterns published in Juenke *et al.* [48], Kovba *et al.* [50], Serezhkin *et al.* [53], and Ustinov *et al.* [56] are in close agreement, the samples are not conclusively characterized beyond P-XRD. It is possible that these solid-state samples contain excess reactant. Elemental analysis and further characterization of the products are needed for conclusive identification of pure $UMoO_6$.

2.3.1.2   Aqueous Synthesis of UMoO$_6$

An alternative approach to the synthesis of $UMoO_6$ is through the reaction of aqueous solutions of uranyl (UO_2^{2+}) and molybdate (MoO_4^{2-}) salts to precipitate $UMoO_6$ from solution, Equation 38. The aqueous synthesis method between these two ions has the inherent ability to match U and Mo 1:1 on a molecular scale. The product is precipitated from solution and the excess reactants and the salt produced by metathesis of the counter-ions remain in solution. Fedoseev *et al.* published a synthesis of $UO_2MoO_4 \cdot 2.75\ H_2O$ by reacting $UO_2(NO_3)_2$ and Na_2MoO_4 at 373 K in minimal water [59], with a P-XRD pattern in ICDD card 44-0034. Serezhkin *et al.* [60] synthesized two separate crystal forms of $UO_2MoO_4 \cdot 2\ H_2O$ (α and β) via the reaction between $UO_2(OH)_2$ and MoO_3 at temperatures above 423 K (ICDD cards 43-0354 and 43-0355). In both cases, however, minimal supporting characterization was performed on the materials. The biggest disadvantage of an aqueous synthesis method is the possibility of the other ions contaminating or becoming part of the final product. Unless comprehensive elemental analysis is completed, one cannot assume a pure product.

$$UO_2^{2+}{}_{(aq)} + MoO_4^{2-}{}_{(aq)} \rightarrow UMoO_{6(s)}$$
<div align="right">Equation 38</div>
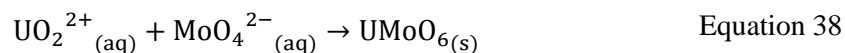
2.3.2   Thermodynamics of UMoO$_6$

Once $UMoO_6$ is synthesized, its thermodynamic properties can be investigated. The stable thermodynamic properties of $UMoO_6$ make it of interest for nuclear study as it is the only U-Mo-O compound thought possible to form in a nuclear fuel [61].

$UMoO_6$ was first studied thermodynamically by the Bhabha Atomic Research Centre by a research group that included Chattopadhyay [46], Dharwadkar [24], and Tripathi [61] in the 1980's. Chattopadhyay *et al.* [46] determined the Gibbs' energy of formation by the emf technique at 1000 K.

$$\Delta G^o_{f,UMoO_6} = -1476 \pm 12 \; kJ \; mol^{-1} \qquad \text{Equation 39}$$

Tripathi *et al.* [61] later performed transpiration measurements of the trimer gaseous species, $(MoO_3)_{3(g)}$, over a two-phase mixture of $UMoO_{6(s)}$ and $MoO_{3(s)}$ and $UMoO_{6(s)}$ and $U_3O_{8(s)}$. Tripathi *et al.* defined a temperature-dependant Gibbs' energy of formation of

$$\Delta G^o_{f,UMoO_6}(kJ \; mol^{-1}) = (-1962 \pm 10) + (0.463 \pm 0.008)T \quad \text{Equation 40}$$

for the temperature range of 1110 K < T < 1250 K. Finally, Dharwadkar *et al.* [24] used thermogravimetric and XRD techniques to measure ΔG_{RXN} for the reaction

$$UMoO_{6(s)} + CaO_{(s)} \rightarrow CaMoO_{4(s)} + \frac{1}{3}U_3O_{8(s)} + \frac{1}{6}O_{2(g)} \qquad \text{Equation 41}$$
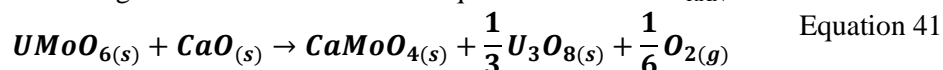
from which they used literature values for the other reactants and products to determine

$$\Delta G^o_{f,UMoO_6}(kJ \; mol^{-1}) = -2095.08 + 0.467T \qquad \text{Equation 42}$$

where the temperature range is 980 K < T < 1210 K.

In 2000, Dash *et al.* [23] used a high-temperature Calvet micro-calorimeter in the temperature range 299 K < T < 1000 K to measure $H^o(T)$-$H^o(298.15 \; K)$ of $UMoO_6$. Dash fit his experimental data with a polynomial function and took the first differential with respect to temperature to determine the heat capacity (*i.e.*, Equation 12). Dash's function is listed in Table 4. Using the experimental $UMoO_6$ $C_p(T)$ function, literature values for the reactants, and the Gibbs free energy values from Dharwadkar *et al.* [24] and Tripathi *et al.* [61], he calculated $\Delta H^o_{f, UMoO_6}$ and $S^o_{f, UMoO_6}$. The values are shown in Table 5. The $\Delta H^o_{f, UMoO_6}$ values that Dash produced from the two datasets were very different. Therefore, Dash used a first principle LeVan calculation [62] to estimate another $\Delta H^o_{f, UMoO_6}$, -1989.6 kJ mol^{-1}, the third value listed in Table 5. As this value was very close to the Tripathi value (-1975.2 ± 12.39 kJ mol^{-1}), Dash preferred the $\Delta H^o_{f, UMoO_6}$ and $S^o_{f, UMoO_6}$ values calculated from Tripathi's data.

In 2010, Suleimanov *et al.* [54] used adiabatic calorimetry to determine low-temperature $C_p(T)$ functions (Table 4) which in turn were used to determine $S^o_{298K, \; UMoO_6} = 192.8 \pm 0.8$ J mol^{-1} K^{-1} using Equation 17. They used HF-solution

calorimetry to obtain $\Delta H^{o}_{f\,298\,K}$ = -1985 ± 8 kJ mol^{-1}. Using the values for $\Delta H^{o}_{f\,298\,K}$, S^{O}_{298K}, and Equation 23, a $\Delta G^{o}_{f\,298\,K}$ was calculated to be -1836 ± 8 kJ mol^{-1}. In addition to these standard thermodynamic values, they determined T_{fusion} = 1212 ± 2 K and $\Delta H_{fusion\,1212\,K}$ = 16 ±1 kJ mol^{-1} using differential thermal analysis (DTA).

Aside from experimental data, the thermodynamic properties of $UMoO_6$ can be calculated starting from the free energy modelled at quasi-harmonic approximation levels and with the assistance of *ab-initio* calculations. These calculations are an approximation based upon theory and periodic table trends. The method used is outlined in [63] and values for $\Delta H^{o}_{f,\,298\,K}$, $S^{o}_{f,\,298\,K}$ (Table 5) and a $C_p(T)$ function (Table 4) were calculated by collaborators at CEA-Saclay using the CASTEP code [64].

Table 4: Coefficients for the UMoO₆ $C_p(T)$ functions of the form of Equation 43 of Suleimanov *et al.* [54], Dash *et al.* [23], and *ab-initio* calculations [65]

Ref.	Temp Range (K)	k_o	k_1	k_2	k_3	k_{-2}
Suleimanov [54]	6.6-13	0.5715	-0.1769	0.01747	0.0004910	-
Suleimanov [54]	13-47	-0.2263	-0.1200	0.02759	-0.0002361	-
Suleimanov [54]	47-300	485.26	-0.895498	2.7658E-3	-3.4699E-06	380734
Dash [23]	299-1000	158.65	0.004288	-0.0002361	-	-1.40770E+06
Ab-initio [65]	0-1000	186.66	0.019090	0.24647E-06	-	-2.79339E+06

*The Suleimanov [54] 47-300 K range $C_p(T)$ function contains the additional terms of $-5238050T^3$ and $3704.84T^{05}$

$$C_p^°(T(K))\ (J\ mol^{-1}K^{-1}) = k_o + k_1T + k_2T^2 + k_3T^3 + k_{-2}T^{-2} \qquad \text{Equation 43}$$

Table 5: Summary of literature thermodynamic values for UMoO₆

Source	$\Delta H^o_{f, 298\ K}$ (kJ mol^{-1})	C_p (298.15 K) (J mol^{-1} K^{-1})	$S^o_{f, 298\ K}$ (J K^{-1} mol^{-1})
Dash (Tripathi [61])	-1975.2 ± 12.39	-	216.3 ± 12.39
Dash (Dharwadkar [24])	-2105.8 ± 12.39	-	202.9 ± 12.39
Dash [23]	-1989.6 (calc.)	155.60 ± 2.80	-
Suleimanov [54]	-1985 ± 8	161.71 ± 0.32	192.8 ± 0.8
Ab-initio [65]	-1845.6 (calc.)	163.12 (calc.)	193.9

Figure 14 plots the ΔG_f of $UMoO_6$ from the literature sources shown above as a function of temperature. The formation of three moles of water is given as a reference point in blue. This allows comparison between plots directly as each reaction is in isolation from one another with the same amount of oxygen. $UMoO_6$ has a more negative ΔG_f (*i.e.*, lower on the Ellingham diagram in Figure 14) than water. Therefore, the formation of $UMoO_6$ is more thermodynamically favoured than water and its formation is favoured in the event of a defective fuel failure and may also be favoured under normal and other reactor conditions.
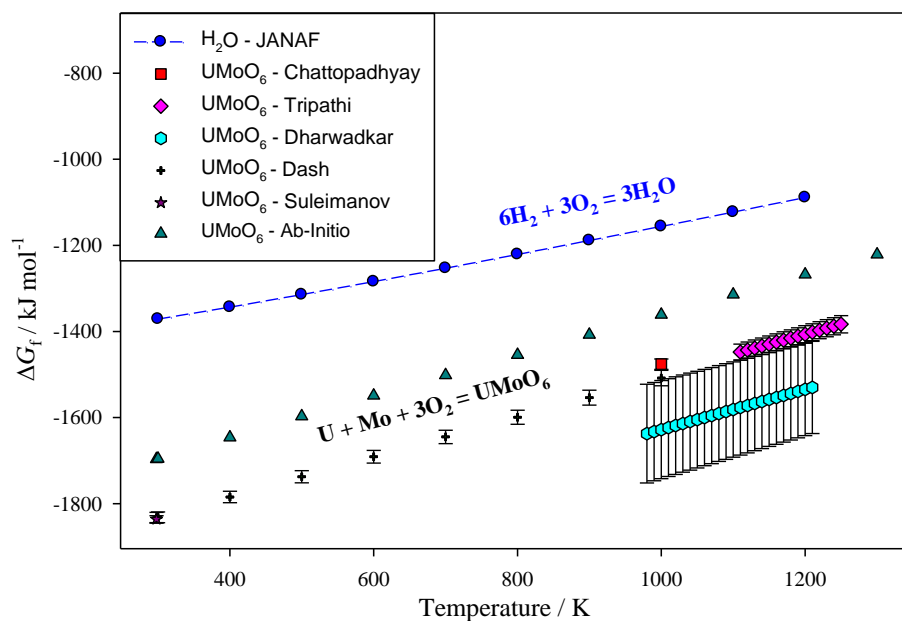
Figure 14: Ellingham diagram illustrating ΔG as a function of temperature for the formation of 3 moles H_2O [66] and 1 mole $UMoO_6$, Chattopadhyay *et al.* [46], Tripathi *et al.* [61], Dharwadkar *et al.* [24], Dash *et al.* [23], Suleimanov *et al.* [54], *Ab-initio* [65] with 3 mol of O_2

2.3.3   *U-Mo-O Phase Diagrams*

Many binary and ternary phase diagrams exist for the U-Mo-O chemical system. Brewer *et al.* developed a Mo-O phase diagram from the thermodynamic data of many sources [22]. Miyake *et al.* investigated $UMoO_6$, $UMoO_5$, U_2MoO_8, and UMo_2O_8 for use in phase diagrams [45]. Chattopadhyay *et al.* investigated the UO_2-MoO_2-O region of the system [46]. Dion *et al.* used U-Mo-O data to investigate the UO_3-MoO_3-Na_2O system [67]. Only Ustinov *et al.* [56] investigated

the UO_3-MoO_3 phase diagram, which is most applicable to this thesis. When assessing the thermodynamic data of $UMoO_6$, the UO_3-MoO_3 phase diagram is useful as $UMoO_6$ forms at $X_{UO_3} = 0.5$ and it has an easily identifiable T_{decomp}. This thesis uses the work of Ustinov $et\ al.$ to refine the selection of thermodynamic variables of $UMoO_6$ for inclusion in the RMC-TFM.

Ustinov $et\ al.$ [56] observed the thermal effects and P-XRD when heating mixtures of U_3O_8 and MoO_3 in air. It was assumed U_3O_8 fully oxidized to UO_3 in the presence of air, however U_3O_8 was discovered by P-XRD in some of the final samples. Ustinov assumed their results represented the UO_3-MoO_3 system, but the U_3O_8 contaminant may have had a significant effect on their results. Further, Ustinov did not consider the gas phase.

Ustinov proposed that a eutectic forms over the MoO_3-rich side of the UO_3-MoO_3 phase diagram at 1013 ± 100 K and a peritectic or small eutectic forms over the UO_3-rich side at 1253 ± 100 K. The Ustinov $et\ al.$ [56] UO_3-MoO_3 binary phase diagram is reproduced in Figure 15 with the experimental data points shown in red. The work of Ustinov was accepted and built upon by Dion [67] while investigating the Na-U-Mo-O system. However, few studies have investigated the UO_3-MoO_3 binary since.
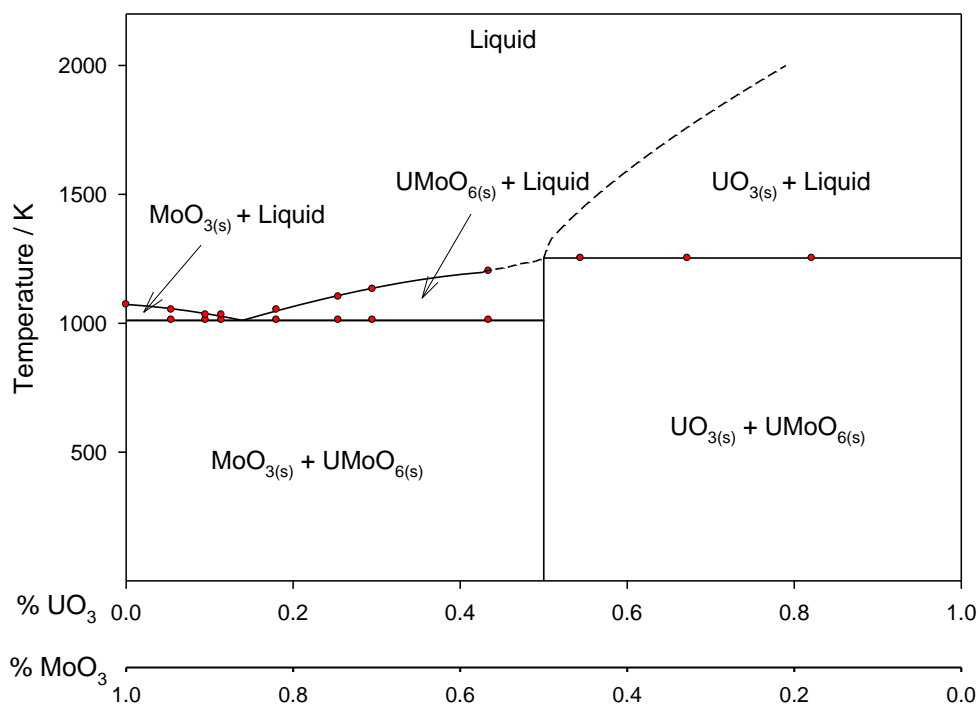
Figure 15: Ustinov *et al.* [56] UO$_3$-MoO$_3$ binary phase diagram with experimental data points shown with red dots

2.4   FACTSage

FACTSage is a fully integrated chemical thermodynamics computing program introduced in 2001 after merging FACT-Win and ChemSage [25]. It calculates and solves chemical thermodynamics problems using the thermodynamic information databases it contains. The RMC-TFM is one such database created from literature data and experimental data collected at the RMC. This section outlines the information required to create a single species data file entry or a solution file, explains how FACTSage computes data using Gibbs energy minimization to construct phase diagrams, and provides a summary of FACTSage capabilities.

2.4.1   Creating Single Species Entries and Solution Files

There are two types of data entries possible in FACTSage. One is single species entries, which are individual chemical elements or compounds. The second type is mixing data entered in the form of a solution file [25]. The RMC-TFM is a

database consisting of many single data species entries and solution files. A listing of the files used herein from the RMC-TFM is given in Appendix D.

Typically, the thermodynamic data required for a single species entry is the $\Delta H^{o}_{f, 298\,K}$ and $S^{o}_{f, 298\,K}$ of the species and its $C_p(T)$ function for a specified temperature range. Multiple $C_p(T)$ functions can be used for multiple temperature ranges if a piece-wise function is more suitable than a single function. When a transition from a complete species entry to a new species is known (for example, $H_2O_{(s)}$ to $H_2O_{(l)}$), ΔH^{o}_{trans} at a specified T can be substituted for $\Delta H^{o}_{f, 298\,K}$ and $S^{o}_{f, 298\,K}$ of the new species, but a new $C_p(T)$ function must be added. FACTSage uses the last value of a $C_p(T)$ function beyond its defined range. FACTSage will also only consider species for which it has thermodynamic information, thus the absence of compounds can change expected results [25].

Solution files can also be added to account for non-ideal mixing as described in Section 2.2.5. If no solution file is entered, ideal mixing is assumed by FACTSage. A solution file is constructed by first selecting the single species files for the two or more species being mixed. Next, a solution model is added to fit the excess Gibbs energy of mixing. All available mixing models in FACTSage are listed in Table 6. In this thesis, only a Kohler/Toop polynomial solution model was used of the form seen in Equation 37. This simple solution model provides an excess Gibbs energy function dependant on temperature and composition.

Table 6: Solution models available in FACTSage [25]

Polynomial (Kohler/Toop)
Wagner Interaction Formalism
Quasi-Chemical
Sublattice (Kohler/Toop)
Pitzer
Polynomial (Muggianu)
Sublattice (Muggianu)
Sublattice (Quasi-Chemical)
Compound Energy Formalism
Compound Energy Formalism with SGTE Format

2.4.2   Gibbs Energy Minimization

With a complete thermodynamic database, FACTSage can determine what species will form at equilibrium by minimizing the Gibbs free energy of the system. First,

the user manually inputs the species present in the system and in what quantities. The user must also define the conditions of the system, such as T and P. Finally, the user selects the thermodynamic databases that will be used in the calculations. FACTSage minimizes the Gibbs free energy of the inputted system using the process below [25].

The ΔG of individual chemical species is determined using Equations 12, 20, and 23:

$$\Delta H_T = \Delta H_{298\ K} + \int_{298K}^{T} C_p dT \qquad \text{Equation 12}$$

$$S_T = S_{298\ K} + \int_{298K}^{T} \frac{C_p}{T} dT \qquad \text{Equation 20}$$

$$\Delta G = \Delta H - T\Delta S \qquad \text{Equation 23}$$

Since $\Delta H_{298\ K}$, $S_{298\ K}$, and $C_p(T)$ of each species is defined by the thermodynamic database, ΔG_T is known for each species entered.

Next, the ΔG_T is expressed as a partial molar Gibbs energy (μ_i)

$$\mu_i = \left(\frac{\delta\ G_i}{\delta\ n_i} \right) \qquad \text{Equation 23}$$

where i is the species and n is the number of moles of that species.

In the case of a species in a real mixture, μ_i is expanded to include an excess mixing term similar to Equation 36.

$$\mu_i = \mu_i^{ideal} + \mu_i^{excess} \qquad \text{Equation 44}$$

Solution files are used to determine the excess Gibbs energy of mixing, which is then used to create the excess partial molar Gibbs energy in Equation 44.

Finally, the G of the system is minimized to determine the species and quantities that form at equilibrium [68].

For an ideal system of s condensed species and a gas (g) mixture of m species, Gibbs energy can be written as

$$G_{T,P} = RT \cdot \sum_{i=1}^{m} n_i^g \left[\left(\frac{\mu^o}{RT} \right)_i^g + ln\ P + ln\ x_i^g \right] + \sum_{i=1}^{s} n_i^c \left(\frac{\mu^o}{RT} \right)_i^c \qquad \text{Equation 45}$$

where n_i^g and n_i^c are the number of moles of species i in the gas (g) and condensed (c) phases, respectively. If the system is non-ideal, an excess mixing term of $(\frac{\mu^{excess}}{RT})_i$ is added to both the gas and condensed phase terms for each species using the solution database. If no solution data is available, an ideal system is assumed.

Equation 45 must be solved under the constraint of mass balance. Mass balance can be defined as

$$\sum_{i=1}^{m} a_{ij}^g n_i^g + \sum_{i=1}^{s} a_{ij}^c n_i^c = b_j, j = 1, \dots, NC \qquad \text{Equation 46}$$

Where $a_{ij}^{g,c}$ is the number of atoms of the jth element in a molecule of species i in the system, b_j is the amount of element j in the system, and NC is the number of different elements in the system [68]. Under the restriction of Equation 46, Equation 45 is solved via the Lagrangian multiplier technique using algorithms unique to FACTSage [25] with the condition to minimize the total Gibbs energy of the system. Once solved, the amounts of each species and their phases at equilibrium under the conditions specified are known.

2.4.3 Phase Diagram Construction

The ability to predict the phases and species that form under equilibrium conditions can be used further to make post processing products, such as phase diagrams. A phase diagram is a diagram that shows the stable phases under equilibrium as a function of temperature, pressure, and elemental composition. By plotting one of these variables for each axis, the stable phases forming under those conditions can be visually shown. It is important to note that phase diagrams only show the stable phases and not the quantities formed. This thesis will focus on phase diagrams that fix pressure and plot stable phases as a function of temperature and elemental composition.

Recall in Section 2.2.5, ΔG_{mix} is the energy difference between miscible and immiscible mixtures and represent the energy of mixing. Recall in Figure 10, the Gibbs free energy curve for a liquid solution of A and B at an arbitrary T and P

was plotted as a function of X_B. Now consider a new solid phase (α) of compounds A and B, Figure 16.
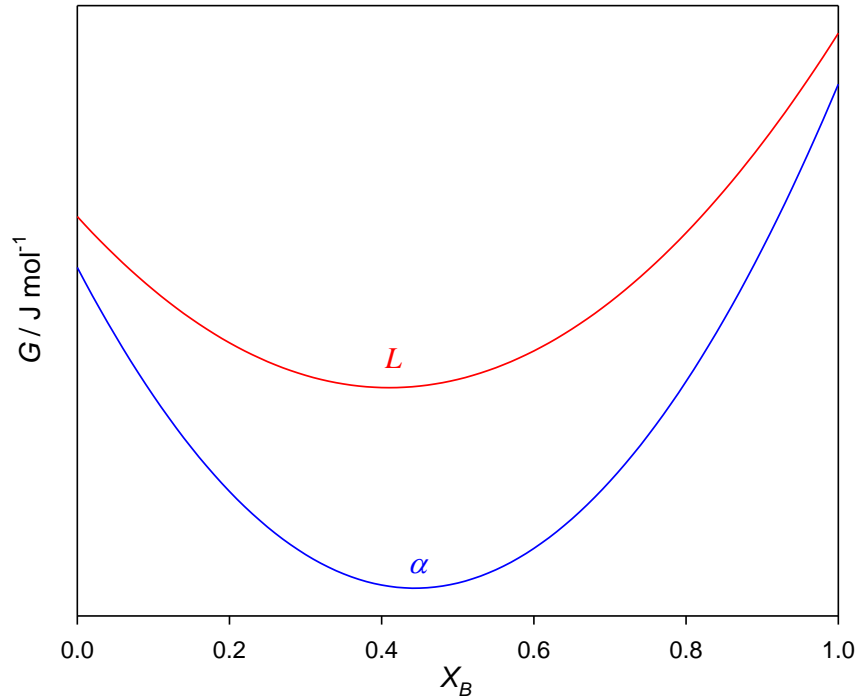
Figure 16: The Gibbs free energy curves of A-B as a liquid solution (*L*) and a solid phase (*α*) at an arbitrary temperature, T_1

At T_1, the α phase is below that of the liquid phase at all compositions of A and B. Therefore, the α phase is favoured to form instead of the liquid phase at all compositions at T_1 [69].

At a given X_B, the amount of energy that the liquid would need to form at T_1 is represented by Equation 47.

$$\mu_L = \mu_L^o + RT\,ln(a)$$ Equation 47

where *a* is the thermodynamic activity. This value is the "effective concentration" of a species in a mixture. It is generally 1 for liquids and solids that form at equilibrium and the effective partial pressure (*i.e.*, fugacity) of gases [39].

If the sample was heated high enough (T_2), the liquid phase curve lowers below the α curve and thus the liquid phase is more favoured to form at all compositions.

There may be a temperature between T_1 and T_2 (*i.e.*, T_3) where the two Gibbs free energy curves cross, Figure 17.
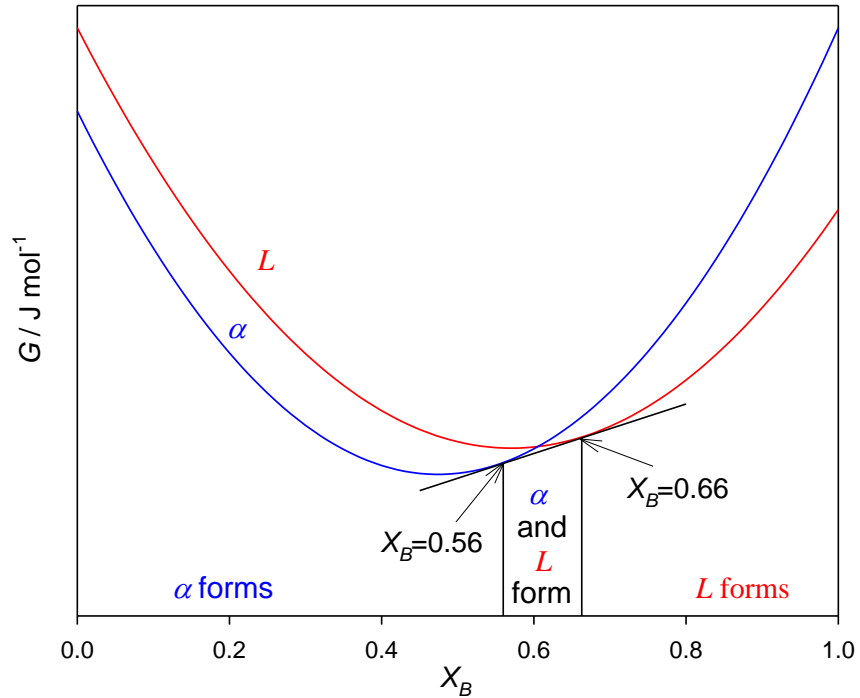
Figure 17: The Gibbs free energy curves of A-B as a liquid solution (L) and a solid phase (α) at an arbitrary temperature, T_3

In this case, the lowest point for a specific range of compositions is a common tangent between the two Gibbs free energy curves. The points where the lowest common tangent (shown in black in Figure 17) touches the two curves mark the composition range where the two phases would form in equilibrium ($X_B = 0.56$ and 0.66 in Figure 17).

The corresponding lines of T_1, T_2 and T_3 on the A-B phase diagram are shown in Figure 18 [69].
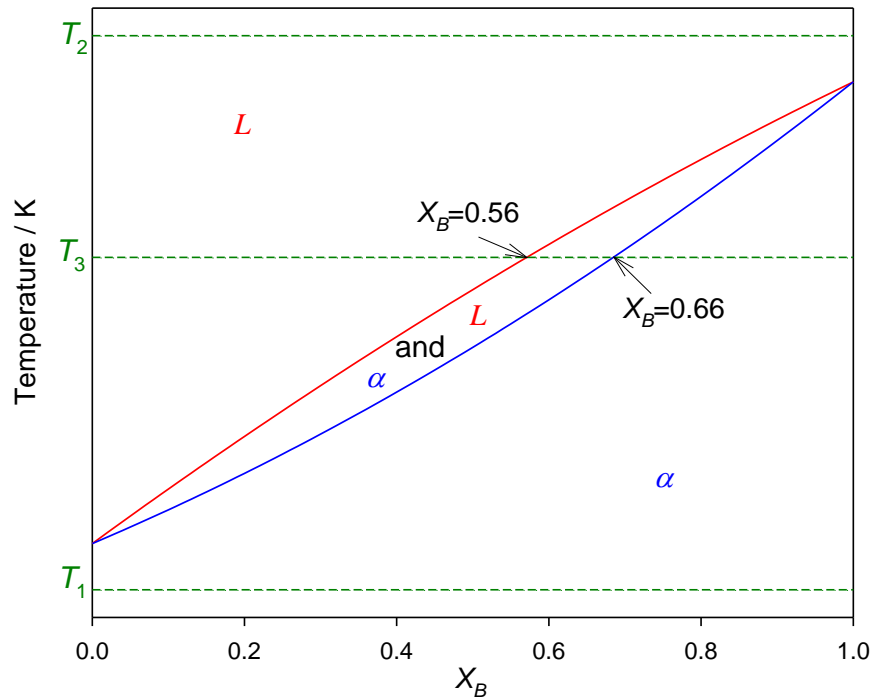
Figure 18: The A-B phase diagram

Depending on the shape of the Gibbs free energy curves at different temperatures, it is possible to have a miscibility gap. A miscibility gap is a region in a phase diagram where a mixture exists as two or more phases. It is the result of concavity in the Gibbs free energy curve, creating a "*hump*", and a lowest common tangent drawn between the two phases. Consider Figures 19 to 22 that show the Gibbs free energy curves for a liquid solution of A and B and a solid curve of phase α (an A-rich phase) and phase β (a B-rich phase) at different temperatures where $T_4 > T_5 > T_6 > T_7$.

At the high temperature of T_4, liquid forms over all compositions, Figure 19.
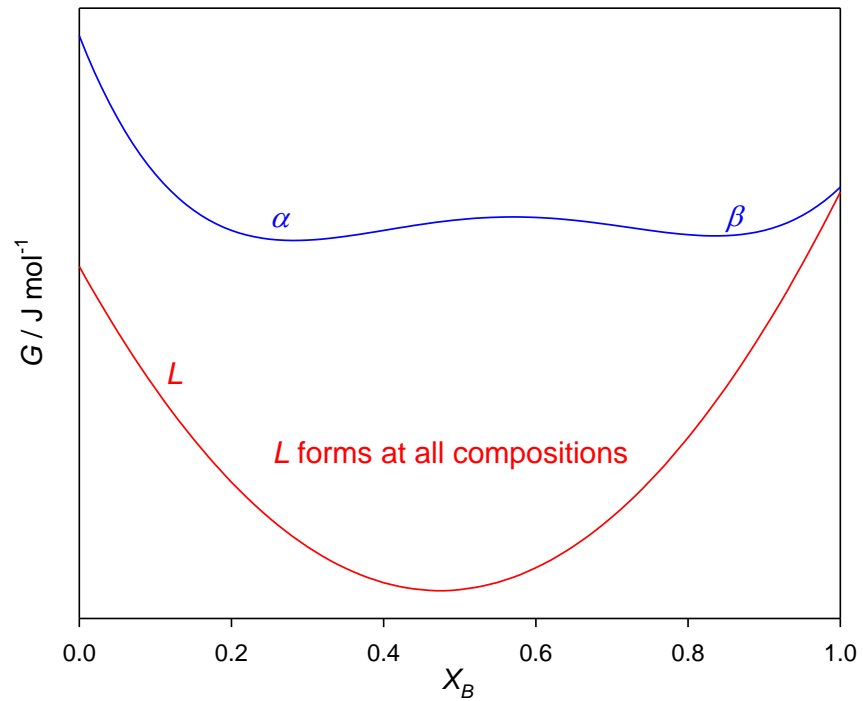
Figure 19: The Gibbs free energy curves of A-B in a liquid solution (*L*) and solid phases (*α* and *β*) at an arbitrary temperature, T_4

At a lower temperature of T_5, all the phases form depending on the composition of the mixture, Figure 20. At some compositions, two phases are stable at equilibrium.
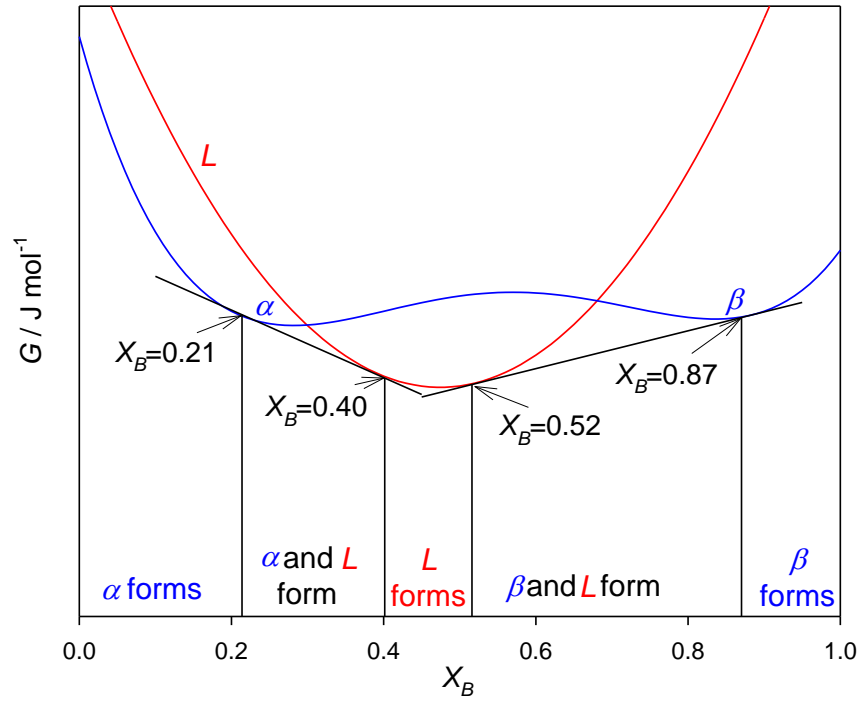
Figure 20: The Gibbs free energy curves of A-B in a liquid solution (*L*) and solid phases (*α* and *β*) at an arbitrary temperature, T_5

Decreasing the temperature again to T_6, the specific temperature of T_6 allows three phases to form at the same time at $X_B = 0.48$, Figure 21.
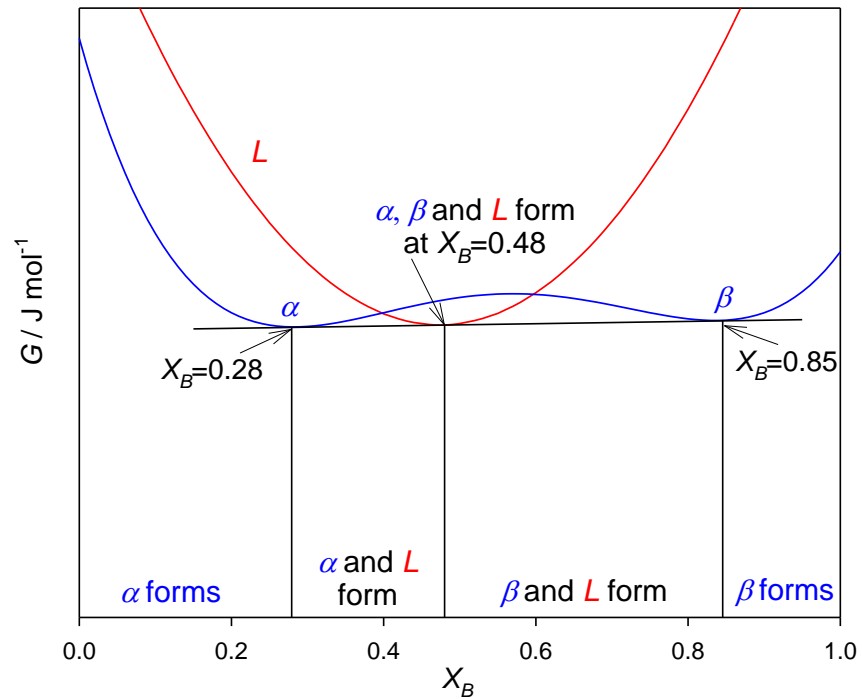
Figure 21: The Gibbs free energy curves of A-B in a liquid solution (*L*) and solid phases (*α* and *β*) at an arbitrary temperature, T_6

When the temperature is cooled further to T_7, only solid phases form at equilibrium, Figure 22.
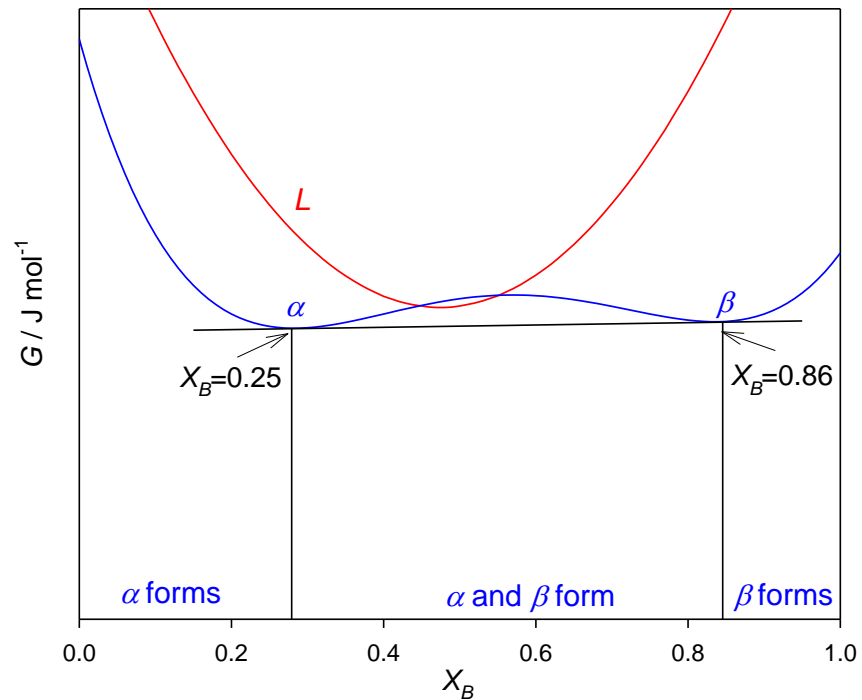
Figure 22: The Gibbs free energy curves of A-B in a liquid solution (*L*) and solid phases (*α* and *β*) at an arbitrary temperature, T_7

Figure 23 is the A-B phase diagram formed from the Gibbs free energy curves of the system (Figures 19 to 22). FACTSage minimizes the Gibbs free energy with this method for the temperature range and compositions specified by the user to create phase diagrams [69].
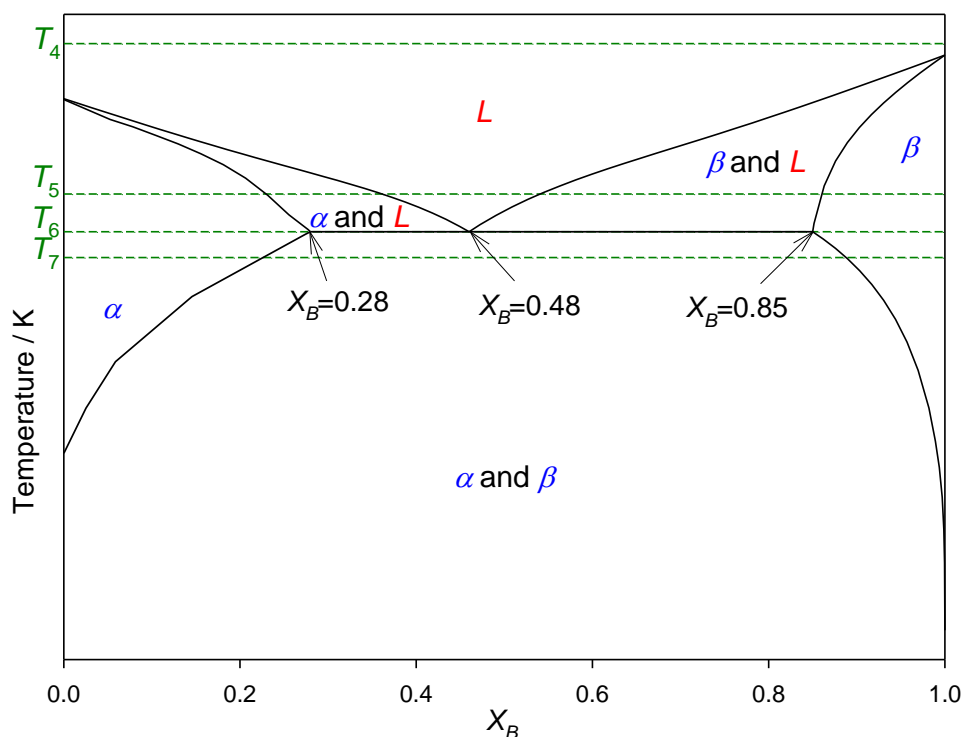
Figure 23: The A-B phase diagram

As FACTSage constructs phase diagrams by constructing the lowest common tangent (Gibbs energy minimization), the Laws of Thermodynamics are respected including thermodynamic first principles such as the Gibbs phase rule, Equation 48.

$$F = C - P + 2 \qquad \text{Equation 48}$$

where F is the number of degrees of freedom, C is the number of components, and P is the number of phases in equilibrium. For a phase diagram that fixes pressure (one degree of freedom) and plots temperature against elemental composition, the condensed phase rule is used, Equation 49 [70].

$$F = C - P + 1 \qquad \text{Equation 49}$$

As an example, consider the imaginary mixture of components A and B that are immiscible as solids and completely miscible as liquids. Figure 24 is a binary phase diagram that fixes pressure at 1 atm and plots the stable phases as a function

of temperature and elemental composition. Fixing the pressure at a different value corresponds to a different phase diagram. In this diagram, $X_A + X_B = 1$.
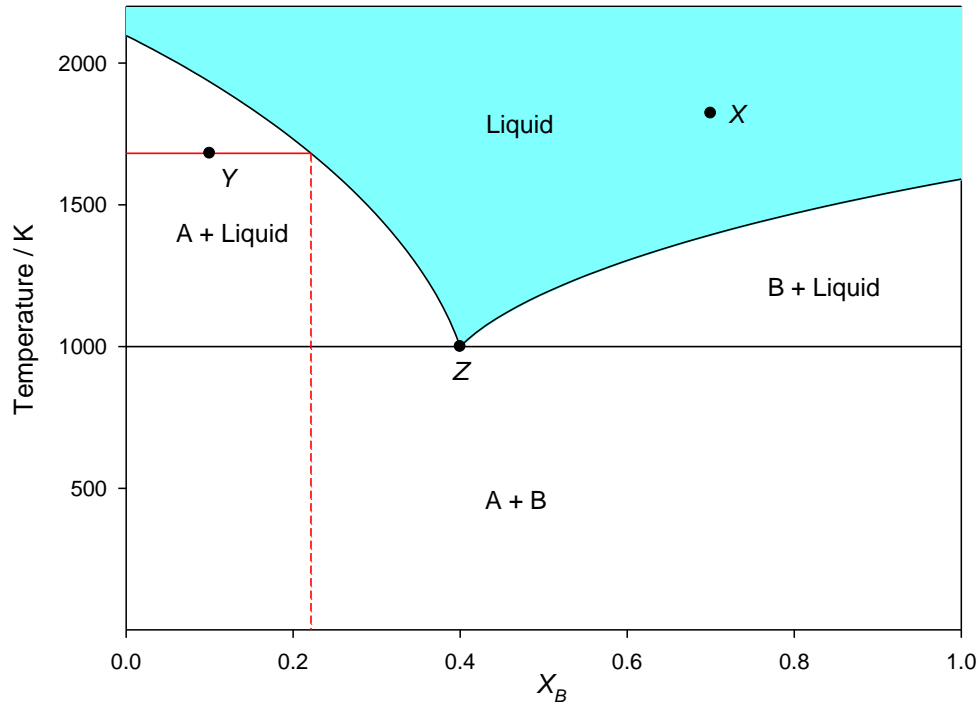
Figure 24: Imaginary binary phase diagram of components A and B

At point X, liquid is the one and only phase ($P = 1$) and the system has two components ($C = 2$), A and B. According to the condensed phase rule, there are two degrees of freedom ($F = 2$). Both temperature and composition may be varied independently and form an area of liquid stability (shown in blue in Figure 24).

At point Y, liquid and solid A comprise the two phases present ($P = 2$) and the system still has two components ($C = 2$). According to the condensed phase rule, there is one degree of freedom. Both temperature and composition may be varied; however, fixing one automatically defines the other. For example, if temperature is fixed at 1680 K (the solid red line in Figure 24), the composition of the liquid phase is fixed at 22 % X_B and the composition of solid A at 0 % X_B. The quantities of solid A and liquid are dependent on the elemental composition selected, but the system has been completely defined.

At point *Z*, solid A, solid B, and liquid are all present ($P = 3$) and the system still has two components ($C = 2$). According to the condensed phase rule, there are zero degrees of freedom. Neither temperature nor composition may be varied. The result is single point of stability where all three phases are present. Changing temperature, composition, or pressure will cause one of the phases to disappear [70].

2.4.4 *FACTSage Summary*

Figure 25 is a flow chart that summarizes the function of FACTSage. $\Delta H_{298\,K}$, $S_{298\,K}$, and $C_p(T)$ of individual chemical species and non-ideal mixing data (solution files) are added to make a thermodynamic database, seen in red, such as the RMC-TFM. The parameters entered by the user are shown in green (constituent components, *T* and *P*). The Gibbs energy minimization conducted by FACTSage that determines the species formed at equilibrium is shown in blue. Also shown are post-processing products that can be made from this data such as phase diagrams or model trends.
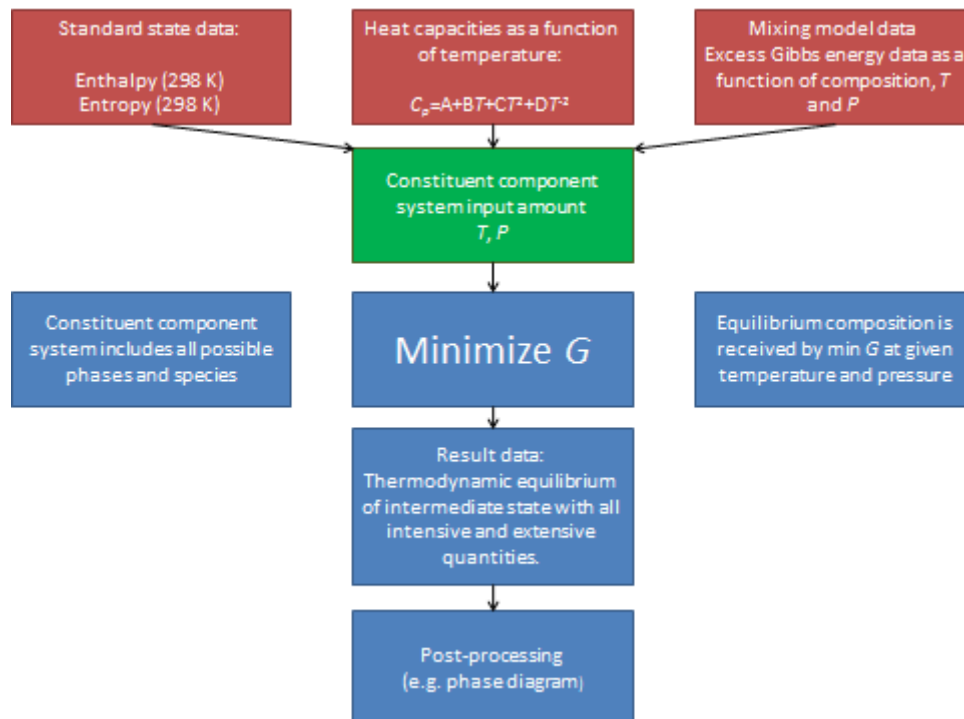
Figure 25: Flowchart of FACTSage function [68]

2.5　　　RMC-TFM

Section 1.3 provided the context of this thesis within the RMC-TFM. This section further details the RMC-TFM. It describes the current state of the model, the validation experiments used to benchmark it, and the modes used to bring the model in line with the experimental data. It highlights the need for this thesis to provide further experimental validation to mode III.

2.5.1　　　*Current State*

The RMC-TFM is used to predict the stable phases that form at equilibrium in a nuclear fuel given initial product inventory and environmental parameters. This thermodynamic fuel model can be used to set the framework (*i.e.*, some of the boundary conditions) for more complete kinetic models. It was designed for defective fuel modelling, meaning it has thermodynamic information for a variety of oxides that may form under these conditions and is suited to model higher temperatures in a defective fuel.

The most current use of the model was in Ref. [19], which developed a lightly-enriched uranium fission product model (LEU-fp) from the complete RMC-TFM. LEU fuel was chosen to expand the RMC-TFM towards modeling ACR-1000 fuel. The LEU-fp model is capable of predicting the phase proportions and oxidation for 23 of the most abundant elements, fission products, and activation products in a nuclear fuel[*].

As discussed in Section 2.1.2, the fuel matrix is comprised of fresh UO_2. As such, the LEU-fp model uses the U-O binary system as its base. Complete thermodynamic information on the UO_2 fuel matrix is used in the model, including the non-stoichiometric region of $UO_{2\pm x}$, and other U-O compounds possibly found in the fuel matrix such as UO_3, U_3O_8, U_3O_7, and U_4O_9. Inside this fuel matrix, the LEU-fp model accounts for five different types of fission product phases:

1) An oxide matrix with soluble fission product phase;
2) A complex oxide precipitate or grey phase;
3) A gas phase;
4) A noble metal inclusions or white phase; and
5) A rhombohedral and additional oxide phase.

---

[*] U, Zr, Mo, Ce, Ru, Sr, Ba, La, Nd, Pd, Rh, Cs, Pu, Xe, Np, Y, Tc, Pr, Rb, Te, I, H, and O

The phases of the fission and activation products are a function of their thermodynamic information as well as their solubility within the UO_2 fuel matrix. An example input and output of the model can be found in Appendix E. The initial product inventory is entered along with the environmental parameters of *T* and *P*. The model determines which species form at equilibrium, in what quantities, and in which phase type.

2.5.2   *Coulombic Titration Experiments*

As discussed by Corcoran [19], the LEU-fp model has been benchmarked by a number of key CT (coulombic titration) experiments at AECL Chalk River Laboratories (now Canadian Nuclear Laboratories). These experiments involved measuring the amount of oxygen absorbed by UO_2 and SIMFUEL samples at fixed oxygen partial pressures (pO_2) and temperatures.

The UO_2 samples used were pure UO_2 ceramic powders similar to those used in nuclear fuel. SIMFUELs were UO_2 ceramic powders that were infused with non-radioactive oxides that represent the fission products present at a certain burnup [71]. Therefore, SIMFUELs are designed to represent a fuel at a given burnup and are ideal for experimentation because of their low reactivity when compared to spent nuclear fuel. Also, the amount of fission products infused within is known. Two SIMFUELs, SIMFUEL 1 and 2, were used in the LEU-fp validation experiments. The composition of each type of SIMFUEL is found in Table 7. It is important to note that SIMFUEL 1 contains a higher quantity of Mo than SIMFUEL 2.

Table 7. Composition of SIMFUEL samples (in ppm) [72].

Element	SIMFUEL 1		SIMFUEL 2	
	ppm	±	ppm	±
Ba	9	2	1000	100
Ce	7	1	2700	300
Cs	0.11	0.03	-	-
La	3.5	0.7	900	200
Mo	900	100	180	40
Nd	18	4	4500	500
Pd	700	50	260	50
Rh	50	20	50	10
Ru	280	30	13	6
Sr	5	1	1600	200
U	890000	40000	880000	40000
Zr	7	1	2200	200

*Note: SIMFUEL 1 is referred to as 4-Additive and SIMFUEL 2 is referred to as 11-Additive in [19]

Figure 26 shows a schematic of the CT experimental setup from Ref. [19]. Note, the CT experiments were not completed by this thesis, but are important to the final model evaluation of this thesis.

As discussed in Ref. [19], a fuel sample of known mass and temperature was subjected to a carrier gas comprised of 2000 ppm H_2 in Ar that flowed through the system. Two CT cells that both control and measure the pO_2 of the carrier gas were located upstream and downstream (additional information about the CT cells can be found in Appendix B).
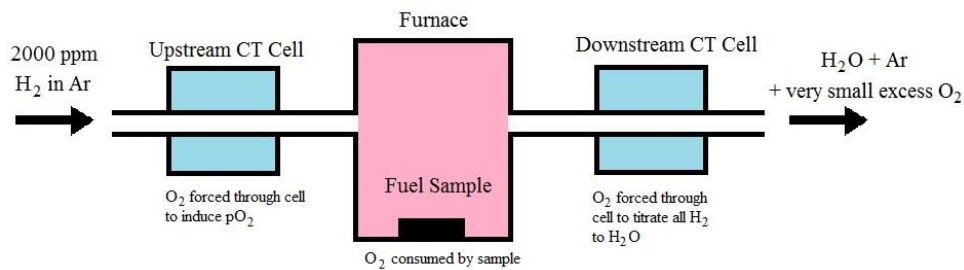
Figure 26: Schematic of the CT experimental setup [19]

Each CT experiment consisted of two phases, the reduction phase and oxidation phase. For the reduction phase, the upstream CT cell confirmed a low pO_2 in the carrier gas (*i.e.,* ~10^{-19} at 1273 K) flowed over the fuel samples. The low pO_2 removed any oxygen that may have absorbed or adsorbed on to the fuel sample during storage. The downstream CT cell passed a current, in the form of O^{2-} ions, to convert the remaining H_2 content in the carrier gas to H_2O vapour. If the sample released oxygen, the downstream CT cell passed a current that was less than the baseline current (*i.e.,* less than 26750 µA). Therefore, integration of downstream CT cell current that was below the baseline current condition yielded a direct measurement of the oxygen released by the sample.

In the oxidation phase, the upstream CT cell passed a current of 25000 µA to induce a high known pO_2 to the carrier gas (*i.e.,* ~10^{-12} atm at 1173 K or ~10^{-10} atm at 1273 K). As the carrier gas was allowed to flow over the sample, the sample absorbed oxygen from the carrier gas. The downstream CT cell passed enough current to titrate all the remaining H_2 in the carrier gas to H_2O vapour (*i.e.,* a baseline current of 1750 µA). If the fuel sample absorbed oxygen, the current in the downstream cell was above the baseline current condition. Therefore, integration of downstream CT cell current that was above baseline current yielded a direct measurement of the oxygen absorbed by the sample.

As discussed in Ref. [19], the CT experimentation on UO_2 samples matched well with the LEU-fp model predictions. This can be attributed to the extensive experimental and modelling research conducted on UO_2. However, the model did not match well with the SIMFUEL samples. The amount of oxygen absorbed was under-predicted, as seen in Table 8.

Table 8: Comparison of LEU-fp model to CT results for SIMFUEL samples, adapted from [19]

Run	SIMFUEL Sample	Temperature (K)	CT Measured O_2 Absorption (μmol)	LEU-fp Predicted O_2 Absorption (μmol)
1	SIMFUEL 1	1173.15	44 ± 6	15.16
2	SIMFUEL 1	1273.15	56 ± 10	23.42
3	SIMFUEL 2	1173.15	40 ± 8	27.10
4	SIMFUEL 2	1273.15	46 ± 15	29.59

2.5.3   *New Modes to Correct Oxygen Under-Prediction*

Corcoran [19] considered three modes, which could account for the under-prediction of oxygen absorption in the model. They are all related to molybdenum because of its ability to buffer oxygen and significant accumulation in a nuclear fuel.

I. MoO_2 becomes less soluble in the UO_2 matrix at the temperature conditions of the experiment. Therefore, before the experiment begins, some MoO_2 is reduced to the noble metal phase and then reabsorbs oxygen as the oxidizing conditions of the experiment commence.

II.   There exists a region of hyper-stoichiometry (MoO_{2+x}) that could account for increased oxygen absorption [21-22].

III. Mo could oxidize in the presence of U to form the compound $UMoO_6$ described in Section 2.3.

In Mode I, the solubility of MoO_2 in UO_2 was originally fit to respect the work of Kleykamp [20]. To update to this mode, the solubility of MoO_2 in UO_2 was decreased at the lower temperatures of the CT experiments, but still respected the findings of Kleykemp [20] at high temperatures. This alteration to the model nearly doubled the amount of predicted oxygen absorbed by the SIMFUEL, but still fell short of the full amount absorbed during experimentation.

Mode II updated using the non-stoichiometric region of MoO_2 in the Mo-O binary phase diagram predicted by Zador [21] and published by Brewer [22]. The LEU-fp model incorporated MoO_{2+x} similar to the way it incorporated the non-stoichiometry of UO_2, where a solution file with corresponding excess parameters is made such that

$$(1 - x)MoO_2 + (x)MoO_3 \rightarrow MoO_{2+x} \qquad \text{Equation 50}$$
$$(hyper - stoichiometry)$$

$$(1 - x)MoO_2 + (x)MoO \rightarrow MoO_{2-x} \qquad \text{Equation 51}$$
$$(hypo - stoichiometry)$$
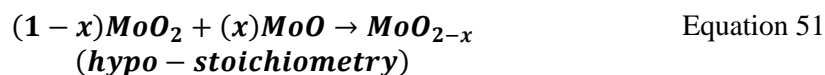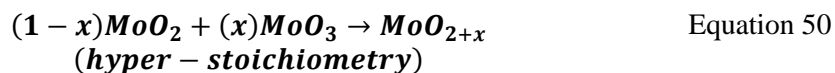
In addition to the non-stoichiometric region of MoO_2, the compounds Mo_4O_{11} and Mo_9O_{26} were included, as well as the gaseous species Mo_3O_9, Mo_4O_{12}, Mo_5O_{15}, Mo_2O_6, MoO_2, and MoO. All these Mo-O compounds were used to model the Mo-O system. The result was a negligible addition of absorbed oxygen predicted by the model as most of the Mo-O compounds added are not very stable or favoured in nuclear fuel conditions and the non-stoichiometry of $MoO_{2\pm x}$ did not account for a very large absorption of oxygen. The full oxidation of MoO_2 to MoO_3 was not considered, as the pO_2 in nuclear fuel was not high enough to stabilize the MoO_3 phase. Part of the focus of this thesis was to experimentally validate the work of Zador [21] to ensure the known stoichiometric region is small enough to have a negligible effect on the model. The results of this work are presented in Appendix A as the results were inconclusive due to a lack of sensitivity of available equipment.

Finally, Mode III incorporated $UMoO_6$ into the fuel model. $UMoO_6$ was chosen as it is the only U-Mo-O compound thought to form in a nuclear fuel, it is thermodynamically stable, and it absorbs a significant amount of oxygen during its formation if formed from the starting reactants MoO_2 and UO_2. Additionally, only $UMoO_6$ had ΔH^o_f, S^o_f, and C_p data available in the literature. $UMoO_6$ was added to the model based on literature values of Dash *et al.* [23] and Dharwadkar *et al.* [24] and the result was a LEU-fp model prediction within the uncertainty of the CT SIMFUEL experiments, as seen in Table 9.

Table 9: Comparison of updated LEU-fp model to CT results for SIMFUEL samples [19]

Run	SIMFUEL Sample	Temperature (K)	CT Measured O_2 Absorption (μmol)	LEU-fp Predicted O_2 Absorption (μmol)
1	SIMFUEL 1	1173.15	44 ± 6	42 ± 4
2	SIMFUEL 1	1273.15	56 ± 10	52 ± 4
3	SIMFUEL 2	1173.15	40 ± 8	33 ± 4
4	SIMFUEL 2	1273.15	46 ± 15	34 ± 4

The main focus of this thesis was to experimentally verify the thermodynamic values used in Mode III. While the addition of $UMoO_6$ to the model conveniently brings the predicted model values in line with the experimental validation, its thermodynamic values require further validation. As explained in Section 2.3, Dash *et al.*'s [23] and Dharwadkar *et al.*'s [24] samples, among many other literature data, may have been contaminated by excess U-oxide in the sample from solid state synthesis. Additional thermodynamic investigation was required to ensure the thermodynamic values determined in [23] and [24] and used in the RMC-TFM are correct. It is possible that other U-Mo-O ternary oxides are forming such as $UMoO_5$ [45], $UMoO_6$ [45], U_2MoO_8 [45], UMo_2O_8 [45], UMo_7O_{22} [46], and $UMo_{10}O_{32}$ [46], among others, but thermodynamic data required for inclusion in the RMC-TFM are lacking in the literature (*i.e.,* ΔH^o_f, S^o_f, and C_p). Investigation into these other U-Mo-O ternary oxides is outside the scope of this thesis, but may be considered for future work.

3.   Scope and Methodology

The project goal of improving the RMC-TFM by refining our understanding of the $UMoO_6$ compound and the UO_3-MoO_3 phase diagram was achieved in part through experimentation. The methods used in these experiments are discussed below. Section 3.1 describes the novel three-step aqueous synthesis of $UMoO_6$ developed in this thesis. The characterization methods used to conclusively identify the sample as $UMoO_6$ are discussed in Section 3.2. Section 3.3 describes the method used to determine C_p, ASTM E1269-11. Finally, Section 3.4 discusses the decomposition experiments completed to obtain ΔH^o_{trans} and ΔH^o_{decomp} and the four different methods used to determine T_{decomp}.

3.1   <u>Novel Aqueous Synthesis of $UMoO_6$</u>

$UMoO_6$ cannot be purchased from a chemical manufacturer and had to be synthesized in order to be studied. For the reasons stated in Section 2.3.1.1, solid state synthesis was deemed to be unacceptable because of possible reactant contamination. Instead, $UMoO_6$ was synthesized via a novel aqueous synthesis method and fully characterized. This is the first pure $UMoO_6$ to be synthesized and characterized in great detail. In the first step, a Na-U-Mo-O intermediate ($Na_2[(UO_2)_6(MoO_4)_7(H_2O)_2]\cdot9H_2O$, compound **1**) was prepared via wet chemistry. $UMoO_6\cdot1.84H_2O$ (compound **2**) was then created after refluxing in excess $UO_2(NO_3)_2$, followed by extended drying to obtain the final product of $UMoO_6$ (compound **3**).

3.1.1   *Preparation of $Na_2[(UO_2)_6(MoO_4)_7(H_2O)_2]$ $9H_2O$ (Compound 1)*

A solution of 1.99 mmol (481.8 mg) of $Na_2MoO_4\cdot2$ H_2O (Anachemia) was made by dissolving in ~20 mL of distilled water. It was pipetted slowly into a stirring solution of 1.99 mmol (1000.1 mg) of $UO_2(NO_3)_2\cdot6$ H_2O (British Drug Houses Ltd.) in ~20 mL of distilled water at room temperature. A bright yellow precipitate formed immediately and the solution was allowed to stir for 24 h at room temperature. The precipitate was subsequently collected via centrifugation, washed twice with distilled water and dried overnight at 393 K (88.7 % yield, based on the determined formulation $Na_2[(UO_2)_6(MoO_4)_7(H_2O)_2]\cdot9H_2O$). This compound is hereinafter referred to as compound **1**.

3.1.2   *Preparation of $UMoO_6 \cdot 1.84\ H_2O$ (Compound 2)*

A solution of excess $UO_2(NO_3)_2$ was prepared by dissolving 288.2 mg (0.5740 mmol) of $UO_2(NO_3)_2 \cdot 6\ H_2O$ in ~20 mL of distilled water (28.7 mmol L^{-1}). Compound **1** (192.2 mg, 0.0614 mmol) was suspended in ~20 mL of this solution. The sample was refluxed for seven days at 378 K, filtered using a water aspirator and Buchner funnel with filter paper, and washed twice with distilled water. The solid was yellow, but visibly paler in colour than compound **1** and less crystalline. It was allowed to dry in air for four days (87.2 % yield based on anhydrous sample).

3.1.3   *Preparation of $UMoO_6$ (Compound 3)*

Compound **2** was dried for 14 h at 773 K under a stream of argon using a thermogravimetric analyzer and differential scanning calorimeter (TGA/DSC) described later in Section 3.2.1.5. Masses of ~150 mg were continually monitored until a stable mass was achieved.

3.2   <u>Product Characterization</u>

The defining feature of this $UMoO_6$ novel synthesis method over other methods published in the literature is the complete characterization of the sample. While P-XRD is generally the sole characterization method reported in other preparations, this method widened the scope to include a variety of characterization methods for both the $UMoO_6$ final product and the intermediates.

3.2.1   *Characterization of Compound 1*
                             $Na_2[(UO_2)_6(MoO_4)_7(H_2O)_2]\ 9H_2O$

Scanning Electron Microscopy (SEM), Energy-dispersive X-ray Spectroscopy (EDX), Inductively Coupled Plasma Mass Spectrometry (ICP-MS), Infrared Spectroscopy (IR), Single Crystal X-ray Diffraction (SC-XRD), Thermogravimetric Analysis (TGA), and Powder X-ray Diffraction (P-XRD) were conducted on compound **1** for a complete characterization. Sections 3.2.1.1 to 3.2.1.6 describe the methods used in each of these characterization methods.

3.2.1.1 Scanning Electron Microscopy (SEM) and Energy-dispersive X-ray Spectroscopy (EDX)

Samples were mounted on adhesive carbon discs for scanning electron microscopy (SEM) and energy-dispersive X-ray spectroscopy (EDX). The instrument used was a Philips XL-30CP tungsten filament scanning electron microscope and energy-dispersive X-ray spectrometer using an accelerating voltage of 25 kV for the electron beam and a scattered electron detector. The SEM was used to provide images of the sample enlarged by up to 6500x. This scale of magnification was possible because of the significant metal content, and therefore high conductivity, of the samples tested. EDX provided an elemental analysis of the surface of the samples. As EDX is a surface analysis technique, the elemental composition provided reflects only the surface of the sample and not the bulk of the sample. Additionally, secondary electron scattering that occurs naturally in EDX causes relatively larger background noise and thusly less accurate elemental quantification. As a result, it provided an accurate representation of the elements present or not present in a material, but the exact quantities were subject to healthy skepticism. ICP-MS provided a better bulk elemental analysis.

3.2.1.2 Inductively Coupled Plasma Mass Spectrometry (ICP-MS)

Sample preparation for ICP-MS was conducted by dissolving a known mass (~10 mg) of sample in a known volume of 2.0 % nitric acid stock solution. The stock solution was made by diluting concentrated nitric acid (Fisher Scientific, Optima purity) in distilled deionized water twice-processed through a reverse osmosis filtration system. The sample was then diluted 2000 times with more stock solution. Oxygen and hydrogen content could not be measured by ICP-MS because the stock solution (required to dissolve the sample) contained water. The instrument used was a PerkinElmer SCIEX ELAN DRC II ICP-MS. The ICP-MS measured the presence and concentration of Na, U, and Mo in the sample (not O and H) in order to determine the Na:U:Mo ratios. ICP-MS was used to provide a better indication of the bulk non-oxygen content of the samples.

3.2.1.3 Infrared Spectroscopy (IR)

Sample preparation for IR was conducted by mixing a small amount of sample (~2 mg) with ~100 mg of dry KBr powder (Sigma-Aldrich). The sample was well mixed and ground in a mortar and pestle and then pressed into a ~1 cm pellet at

100 psi. The instrument used was a PerkinElmer Spectrum 65 Fourier transform infrared spectrometer. The IR spectrum was compared with others in the literature to identify some of the chemical bonds in the compound.

3.2.1.4 *Single Crystal X-ray Diffraction (SC-XRD)*

SC-XRD data were collected with a Bruker AXS KAPPA single-crystal X-ray diffractometer at the University of Ottawa (Mo Kα radiation, wavelength 0.71073 Å, APEX II CCD detector) on a single crystal mounted on a thin glass fiber using paraffin oil and cooled to 200 K under a stream of nitrogen gas. Raw data collection and processing were performed with the APEX II software package from BRUKER AXS [73]. Data were collected with a sequence of 0.3° ω scans at 0, 90, 180, and 270° in φ. Initial unit cell parameters were determined from 60 data frames collected at the different sections of the Ewald sphere. Semi-empirical absorption corrections based on equivalent reflections were applied [74]. Solutions in the non-centrosymmetric chiral space group yielded chemically reasonable and computationally stable results of refinement. The Flack parameter for the chiral structure was refined to 0.095(5). The structures were solved by direct methods, completed with difference Fourier synthesis, and refined with full-matrix least-squares procedures based on F^2. Residual electron density peaks located in geometrically acceptable positions were refined as partially-occupied water solvent molecules. Placement of hydrogen atoms were assumed from the positions providing reasonably configured hydrogen bonds to other oxygen atoms in the core structure. Remaining large residual electron density peaks might be explained by the presence of additional partially-occupied and disordered water solvent molecules present in the lattice. Partially-occupied sodium cations and partially-occupied water solvent molecules were refined with isotropic sets of thermal motion parameters. For refinement of all other atoms in the structure, anisotropic sets of thermal motion coefficients were used. After initial placement, all hydrogen atoms were treated as idealized contributions during the refinement. All scattering factors are contained in several versions of the SHELXTL program library, with the latest version used being v.6.12 [75].

3.2.1.5 *Thermogravimetric Analysis (TGA)*

A SETARAM SETSYS Evolution 24 thermogravimetric analyzer and differential scanning calorimeter (TGA/DSC) was used to investigate the amount of water and impurities in compound **1**. The sample was stabilized for 1 h at room temperature,

heated to 873 K using a heating ramp rate of 20 K min^{-1}, held for 4 h at 873 K and cooled to room temperature for a 1 h hold. The entire sequence was conducted under an ultra-high purity argon (Air Liquide Canada Inc.) environment. The decomposition of the sample was monitored by continually measuring the sample mass to determine the amount of water and other impurities and the temperatures at which they volatilized.

3.2.1.6 Powder X-ray Diffraction (P-XRD)

Powder X-ray diffraction (P-XRD) of solid samples was performed on a Thermo/ARL Scintag X1 X-ray diffractometer and/or an Olympus BTX Profiler X-ray diffraction and X-ray fluorescence analyzer, both using Cu K-α radiation (wavelength = 0.154 nm) and 30 min scanning cycles. The pattern of intensity as a function of peak angles (θ) were used as *pseudo fingerprints* to compare against known samples in published databases.

3.2.2 Characterization of Compound 2 ($UMoO_6 \cdot 1.84\ H_2O$)

SEM, EDX, ICP-MS, IR, TGA, and P-XRD were conducted on compound **2** using the same methods as described above for compound **1**. Unfortunately, the crystals produced after refluxing were too small to conduct SC-XRD. Additionally, Gravimetric Analysis (GA) was used to determine the quantity of oxygen in compound **2**.

3.2.2.1 Gravimetric Analysis (GA)

GA was conducted on compound **2** (pre-dried in a vacuum oven at 393 K for 7 days) using the oxine method published in [76]. A known mass of ~200 mg of dry sample was dissolved in concentrated nitric acid. The solution was titrated to methyl red using 10 M sodium hydroxide (Caledon) and diluted to 100 mL with distilled water. 5 g of ammonium acetate (Merck) was dissolved in the solution and it was heated to boiling. A 4 % oxine reagent (4 g of oxine (AnalaR) dissolved in 8.5 mL of warm glacial acetic acid (Caledon) diluted to 100 mL with distilled water) was added dropwise with stirring until no new precipitation occurred, and a further 5 mL added. The solution was cooled to 313 K, filtered with a water aspirator, and further dried with a vacuum oven for 48 h at 393 K. The precipitate contained all the uranium and molybdenum as $UO_2(C_9H_6ON)_2 \cdot C_9H_7ON$ and $MoO_2(C_9H_6ON)_2$, respectively. Using the U:Mo ratios determined by ICP-MS, the mass of U and Mo in the original oxide could be determined. The difference was

assumed to be oxygen as it was the only other element present in the original compound.

3.2.3 *Characterization of Compound 3 (UMoO$_6$)*

SEM, EDX, and P-XRD were conducted on compound **3** using the same methods previously described.

3.3 The Specific Heat (C_p) of UMoO$_6$

The C_p of UMoO$_6$ (compound **3**) was determined using the method published in ASTM E1269-11 [77]. The instrument used was a TA Instruments model Q20 Differential Scanning Calorimeter (DSC). Calibration was conducted using an indium standard reference material prior to experimentation. For this experiment, an empty or "reference" crucible made of aluminum of known mass was placed onto one of the two crucible holders of the DSC. A second aluminium crucible of known mass was filled with a known amount of material of interest to make the "test" crucible and placed on the other crucible holder. For one run, the system was brought to isothermal conditions at 323 K and held for 10 min, heated at a ramp rate of 20 K min^{-1} to 673 K and held isothermally for 10 min then cooled, all under a nitrogen flow of 50 mL min^{-1} (Air Liquide Canada Inc.). The DSC measured and recorded the difference in heat flow between the reference crucible and the test crucible as a function of temperature and time. Each run was repeated four times with the same reference and test crucibles and averaged to make a test.

In order to determine C_p, three tests or a "triplicate" system was required. This consisted of a blank, standard, and UMoO$_6$ sample test. Each test in the triplicate was the average of four repeated runs and an example is presented in Figure 27. A blank test used an empty crucible as the test crucible. The standard reference material selected was Al$_2$O$_3$ because of its well-defined C_p and its similarity in physical form to UMoO$_6$ as an oxide powder. The UMoO$_6$ sample was dried *in situ* in the DSC for 1 h at 673 K prior to the start of experimentation. The triplicate formed a graph similar to Figure 27 when plotted together. The same reference crucible was used for all three tests (12 runs total).
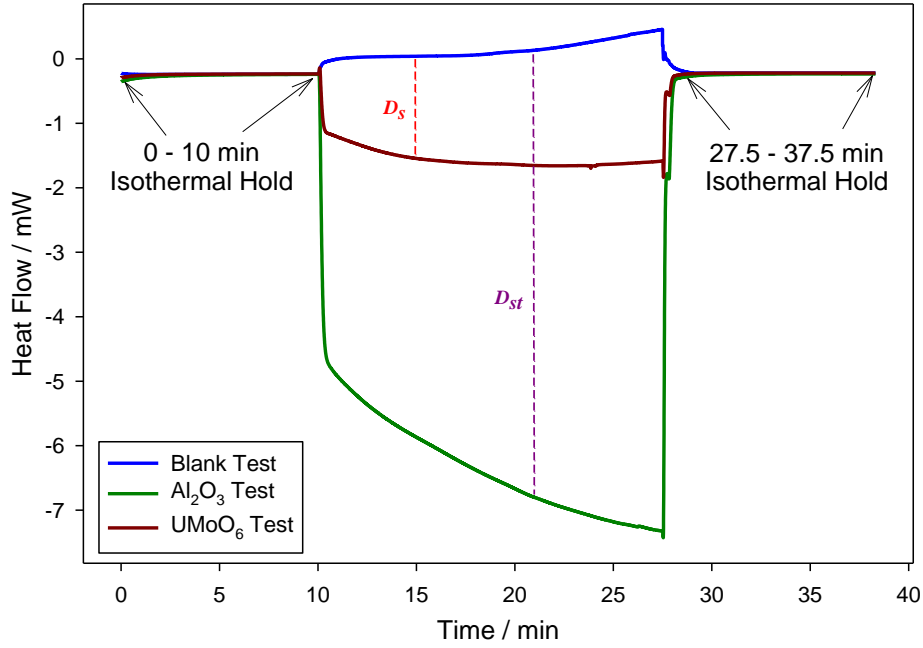
Figure 27: Idealized plot of a triplicate consisting of a blank, Al$_2$O$_3$, and UMoO$_6$ showing heat flow as a function of time

The C_p of UMoO$_6$ was calculated according to Equation 52:

$$C_{p(s)} = \frac{60 \cdot E \cdot D_s}{W_s \cdot b} - \frac{\Delta W \cdot C_{p(c)}}{W_s} \qquad \text{Equation 52}$$

where:

$C_{p(s)}$ is the C_p of the UMoO$_6$ sample in J g^{-1} K^{-1};

D_s is the vertical displacement between the DSC heat flow curves of the blank test and the UMoO$_6$ test at a given temperature in mW (seen in red in Figure 27);

W_s is the mass of UMoO$_6$ in mg;

b is the heating rate in K min^{-1};

ΔW is the difference in mass between the reference crucible and the crucible containing UMoO$_6$ sample in mg; and

$C_{p(c)}$ is the C_p of the crucible material (aluminium) in J g^{-1} K^{-1}.

E is a sensitivity coefficient defined according to Equation 53:

$$E = \left(\frac{b}{(60 \cdot D_{st})}\right) \cdot \left(W_{ST} \cdot C_{p(st)} + \Delta W \cdot C_{p(c)}\right) \qquad \text{Equation 53}$$

where:

D_{st} is the vertical displacement between the DSC heat flow curves of the blank test and the standard test (Al_2O_3) at a given temperature in mW (seen in violet in Figure 27);

W_{st} is the mass of Al_2O_3 in mg;

$C_{p(st)}$ is the C_p of Al_2O_3 in J g^{-1} K^{-1}; and

ΔW is the difference in mass between the reference crucible and the crucible containing Al_2O_3 in mg.

Figure 27 is an idealized graph for the purpose of explaining the theory of this method. The isothermal holds (*i.e.,* between 0-10 min and 27.5-37.5 min) have coinciding heat flow values in all three tests of the triplicate near 0 mW. Under real experimental conditions, the heat flow values during the isothermal holds of each test in the triplicate almost never coincide, Figure 28. Typically, they coincide or nearly coincide for the first isothermal hold at 323 K, but a large difference is found during the higher isothermal hold at 673 K. Non-coinciding heat flow values during isothermal holds are due to changes in sample mass, change in heating rate, or differences in the specific heat capacities of the crucibles [78]. Since a constant mass was measured before and after each run and the heating rate kept constant at 20 K min^{-1}, the non-coinciding isothermal holds are a result of different heat capacities between the different test samples. This is expected as any given quantity of Al_2O_3 is likely to have a different heat capacity than any given quantity of $UMoO_6$, both of which have higher heat capacities than air contained in an empty blank crucible.

To overcome these non-coinciding heat flow values during isothermal holds, a baseline is drawn in a straight line from the stable end of the first isothermal hold to the stable end of the second isothermal hold for each thermalgram, Figure 28. The distance between the thermalgram and its baseline are measured and the real distance between any two thermalgrams is then the addition of the two thermalgram-baseline distances in question [79]. For example, in Figure 28, $D_s = d_1 + d_2$.
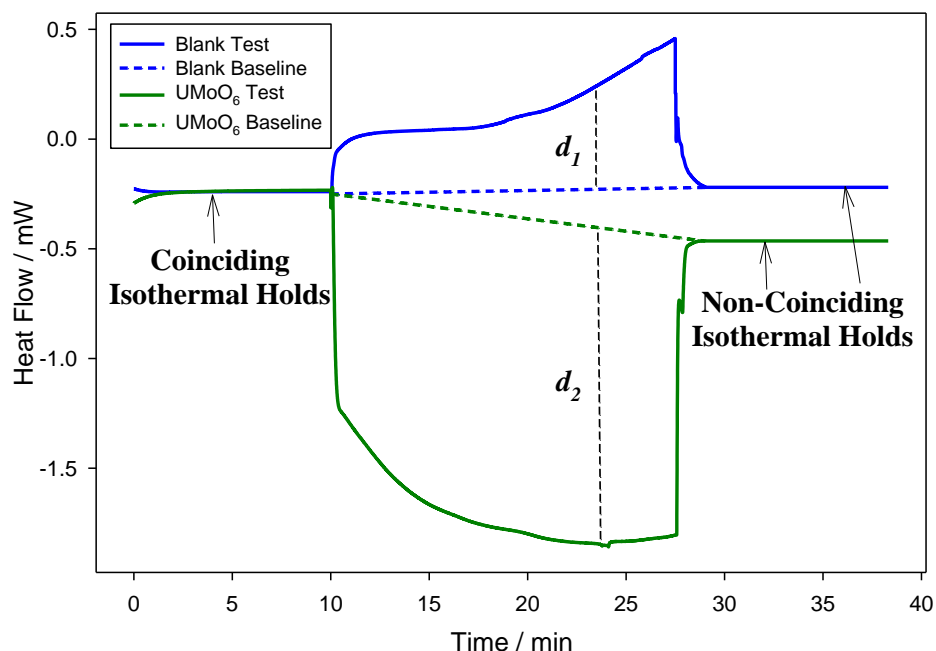
Figure 28: Corrected baseline for non-coinciding isothermal holds

One test (the average of four replicate runs) was completed for a blank and for the standard reference material, Al_2O_3. One test on aluminium metal and MoO_3 powder was completed to determine their respective C_p's for quality assurance of the test method, Appendix F, and gives an accuracy of ± 5 %. Three tests were completed on completely dry $UMoO_6$ (compound **3**). Three tests were completed on wet $UMoO_6$ (compound **2**) and damp $UMoO_6$ (compound **2**) each and the results included in Appendix G.

3.4   Decomposition Experiments

Decomposition experiments were used to determine the ΔH^o_{trans}, ΔH^o_{decomp} and T_{decomp} of $UMoO_6$ using the same TGA/DSC described in Section 3.2.1.5. A sample of compound **2** (~75 mg) was dried *in situ* in the TGA/DSC at 393 K for 24 h until a stable mass was achieved and then cooled to 293 K. It was then heated to 1473 K at a heating rate of 10 K min^{-1} and held for 1 h. The sample began to decompose during the heating ramp and continued to lose mass during the 1473 K isothermal hold. Finally, the sample was cooled to room temperature. The entire run was completed under an argon (Air Liquide Canada Inc.) flow of 100 mL min^{-1} and the mass and heat flow continually measured. A blank run was required to account for

mass changes due to buoyancy during heating and heat flow differences due to system geometry and mass differences in the two crucibles. A blank run had an identical heating program and used the two empty crucibles, which were then used for the $UMoO_6$ run. Blank runs were completed prior to their corresponding $UMoO_6$ run and subsequently subtracted.

The decomposition tests included:
- Five tests on samples dried for 24 h at 393 K
- One test on a sample dried for 14 h at 673 K
- One test on a sample dried for 14 h at 773 K

3.4.1 Enthalpy of Transition (ΔH^o_{trans}) and Decomposition (ΔH^o_{decomp})

The ΔH^o_{trans} and ΔH^o_{decomp} values were determined by integrating their corresponding peaks in the DSC heat flow data. As the heat flow data was measured in watts (W or J s^{-1}), integrating the peak over time returned a value in joules (J). This quantity of heat was divided by the number of moles of substance to obtain a value in J mol^{-1}. The baseline for integration was drawn directly across both ends of the peak, Figure 29. The total area under the curve to the drawn baseline was determined by the Calisto software (details on how the software works can be found in Appendix H). An uncertainty of two standard deviations of the dataset was accepted.
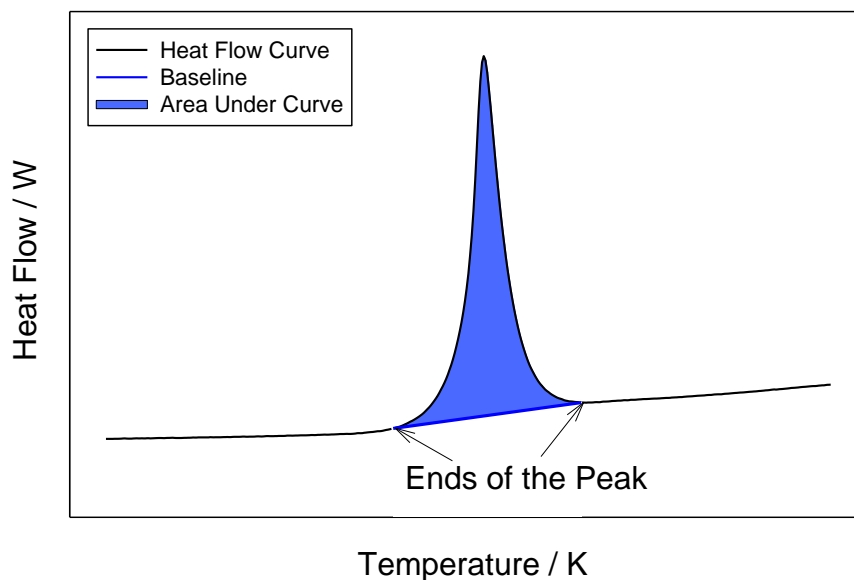
Figure 29: The integration of the heat flow curve to determine ΔH^o_{trans} and ΔH^o_{decomp}

3.4.2   Decomposition Temperature (T_{decomp})

The T_{decomp} was determined using four different methods:

      1) first change in mass

      2) 5 % of decomposition by mass

      3) onset temperature from DSC curve using Calisto software

      4) onset temperature from DSC curve by manual determination

<u>Method 1: First change in mass</u>

This method is described in ASTM E2550-11 [80]. The initial stable mass was established as the baseline condition. The temperature at the first deviation from the baseline in either the mass data or the first derivative of the mass data was assumed to be T_{decomp}. This method was subjective to human error and repeatability, and thus the uncertainty was dependent on the person conducting the analysis. An uncertainty of two standard deviations of the dataset was accepted.
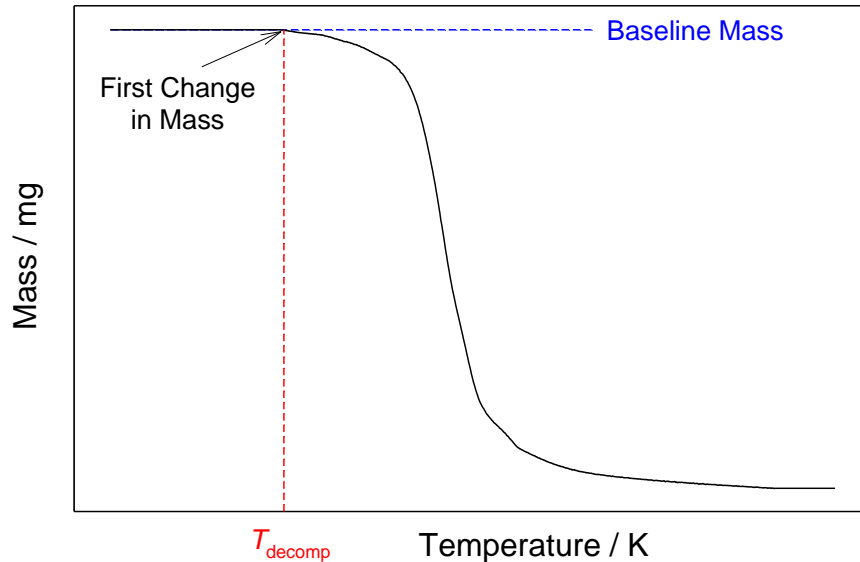
Figure 30: First change in mass method of T_{decomp} determination

Method 2: 5 % of decomposition by mass

This method is described in ASTM E1641-13 [81]. A failure criterion of a 5 % mass loss was selected to define the decomposition temperature. Under this criterion, the initial and final masses of the sample were identified. The temperature when the sample had undergone a loss of 5 % of its total mass was the T_{decomp}. This method was less subjective than method 1 as the user-selected values, initial and final mass, were easily identifiable. An uncertainty of two standard deviations of the dataset was accepted.
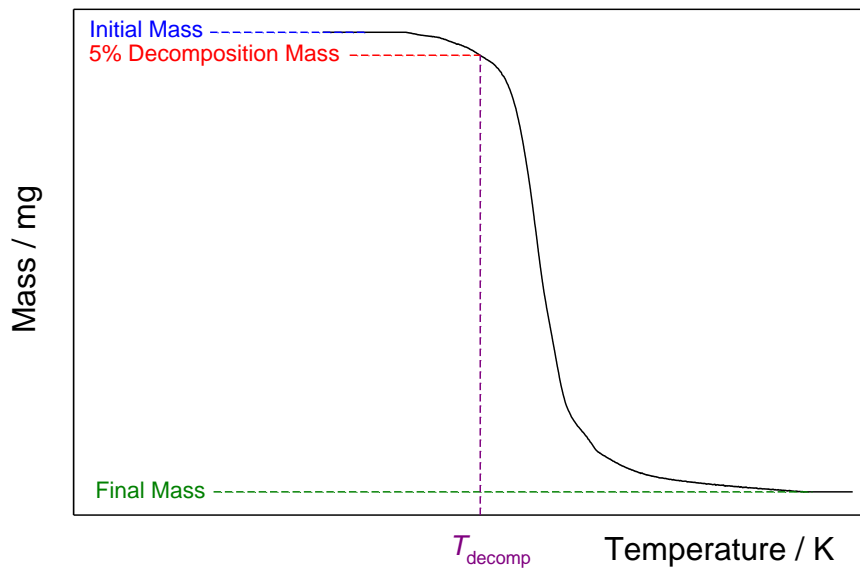
Figure 31: 5 % decomposition by mass method of T_{decomp} determination

Method 3: Onset Temperature from DSC Curve using Calisto Software

This method is described in ASTM D3418-12 [82] and ASTM E2160-04 [83]. The DSC heat flow curve was used to determine T_{decomp} instead of the mass data. First, the Calisto software extrapolated a baseline from the stable DSC heat flow curve prior to the decomposition peak (red, Figure 32). Next, the Calisto software extrapolated a tangent from the point of maximum rate of change of the heat flow (blue, Figure 32). The temperature at the intersection of these two lines was the T_{decomp}. An uncertainty of two standard deviations of the dataset was accepted.
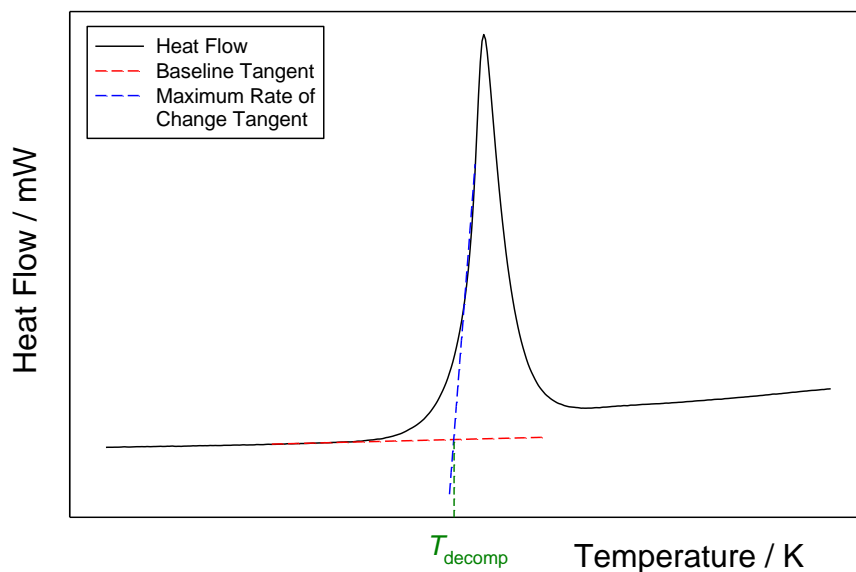
Figure 32: The intersection of the baseline tangent and maximum rate of change tangent to determine T_{decomp} via heat flow

This method exploited the advantage of heat flow data collection by the TGA/DSC. Both methods 1 and 2 relied on change in mass, which is an effect caused by decomposition rather than the decomposition itself. Measuring changes in heat flow is a direct measurement of decomposition; however, the temperature at the peak in the curve does not correspond to the T_{decomp}. This is because the thermocouples used to measure the heat flow of the sample were not directly immersed in the sample and were therefore subject to a temporal delay (*i.e.*, for any change in temperature of the sample, there was a delay in the measurement of the subsequent heat flow change). By using the intersection of the two tangent lines, this method extrapolated the temporal delay in the DSC heat flow curve backwards in time to account for this delay [82-83].

Method 4: Onset temperature from DSC curve by manual determination

This method was identical to method 3 except the baseline and maximum rate of change tangent lines were manually drawn by the user instead of by the Calisto software. Again, an uncertainty of two standard deviations of the dataset was accepted. This method was advantageous when the Calisto software had difficulty

determining the baseline. As will be shown in Section 4.2.4, this method was the method of choice for this thesis.

3.5   <u>Exemption Quantities</u>

It should be noted that for this thesis, any sample that contained radioactive materials (*i.e.*, containing U) was kept under exemption quantities unless within the SLOWPOKE-2 facility. These exemption quantities were calculated using the limits set by the CNSC [84], Table 1. The exemption quantity calculation methodology can be found in Appendix I. Additionally, safety precautions approved by the RMC radiation officer were followed, Appendix J.

Table 10: Maximum mass under exemption quantity for select radioactive compounds

Compound	Maximum Mass (g)
$UMoO_6$	0.712
UO_2	0.447
$UO_2(NO_3)_2 \cdot 6H_2O$	0.831

4. **Results and Discussion**

This section highlights the achievement of the five sub-tasks listed in Section 1.4. Namely; $UMoO_6$ synthesis and characterization; measurement of C_p, ΔH^o_{trans}, ΔH^o_{decomp}, and T_{decomp}; $\Delta H^o_{f, 298 K}$ calculation; evaluation and selection of data via the UO_3-MoO_3 binary phase diagram; and assessing the effect of data changes on the RMC-TFM prediction of the benchmarking CT experiments.

As discussed in Section 2.3.1, a method for producing pure $UMoO_6$, free of U-oxide and Mo-oxide reactants and other impurities, must be investigated. Therefore, Section 4.1 discusses a novel, aqueous synthesis method developed to produce high purity $UMoO_6$. It describes three compounds made en route to the final product, high purity $UMoO_6$, and validates this synthesis via a series of characterization methods.

Section 4.2 showcases the thermodynamic properties collected for newly synthesized $UMoO_6$. This includes a $C_p(T)$ function (J K^{-1} mol^{-1}) of $223.0844 - 0.1945T(K) + 2.2965 \times 10^{-4}T^2(K) - 2.515493 \times 10^6 T^{-2}(K)$ with an associated error of $\pm 5 \%$ over a temperature range of 343-668 K, a ΔH^o_{trans} of -32 $\pm$3 kJ mol^{-1} at 734 $\pm$ 32 K, a ΔH^o_{decomp} of 82 $\pm$ 10 kJ mol^{-1}, and a T_{decomp} of 1205 $\pm$ 10 K. While the methods used to determine these data were described in Section 3, this section discusses the challenges experienced collecting these data, the calculation of uncertainty ranges, and the limitations of these data. Finally, a comparison of these data is made against literature.

Section 4.3 discusses the method used to calculate the $UMoO_6$ $\Delta H^o_{f, 298 K}$ of -1972 $\pm$ 13 kJ mol^{-1} using the experimental values for C_p, ΔH^o_{decomp} and T_{decomp} and a series of potential decomposition reactions. Also, this section discusses the method used to obtain the uncertainty ranges and makes a comparison against literature values.

Section 4.4 discusses the evaluation of all thermodynamic data for $UMoO_6$ selected for inclusion in the RMC-TFM via the assessment of the UO_3-MoO_3 phase diagram. Finally, Section 4.5 evaluates the effect of changing thermodynamic data in the RMC-TFM on its ability to predict the oxidation in the CT experiments.

4.1   <u>UMoO$_6$ Synthesis and Characterization</u>

A three step, novel, aqueous synthesis method was established to create high purity UMoO$_6$ for further testing. Mixing aqueous solutions of Na$_2$MoO$_4$ and UO$_2$(NO$_3$)$_2$ resulted in the formation of Na$_2$[(UO$_2$)$_6$(MoO$_4$)$_7$(H$_2$O)$_2$]·9 H$_2$O (compound **1**). Refluxing compound **1** in excess UO$_2$(NO$_3$)$_2$ lead to UMoO$_6$·1.84 H$_2$O (compound **2**). Drying compound **2** at 773 K for 14 h at 1 atm resulted in completely dry UMoO$_6$ (compound **3**), which had a structure similar to UMoO$_6$ compounds described in the literature. The characterization methods used to identify these compounds are described below. This high purity compound is necessary in order to investigate its thermodynamic properties for the RMC-TFM and ensure U-oxide and Mo-oxide contaminants in the solid state literature methods did not affect their data.

4.1.1   *Characterization of Compound **1***
                   Na$_2$[(UO$_2$)$_6$(MoO$_4$)$_7$(H$_2$O)$_2$] ·9 H$_2$O

Mixing Na$_2$MoO$_4$ and UO$_2$(NO$_3$)$_2$ resulted in the formation of Na$_2$[(UO$_2$)$_6$(MoO$_4$)$_7$(H$_2$O)$_2$]·9H$_2$O (compound **1**). This identification was made after conducting SEM, EDX, ICP-MS, IR, SC-XRD, TGA, and P-XRD. A conventional photograph is displayed in Figure 33 showing the bright yellow microcrystalline nature of compound **1**.

Figure 33: Conventional photograph of compound 1

4.1.1.1 Scanning Electron Microscopy (SEM) and Energy-dispersive X-ray Spectroscopy (EDX)

Examination of compound **1** using SEM showed small crystal formations, which were approximately 150 μm in length, Figure 34. There is a consistent plate-like appearance to each crystal resembling an elongated octagon.
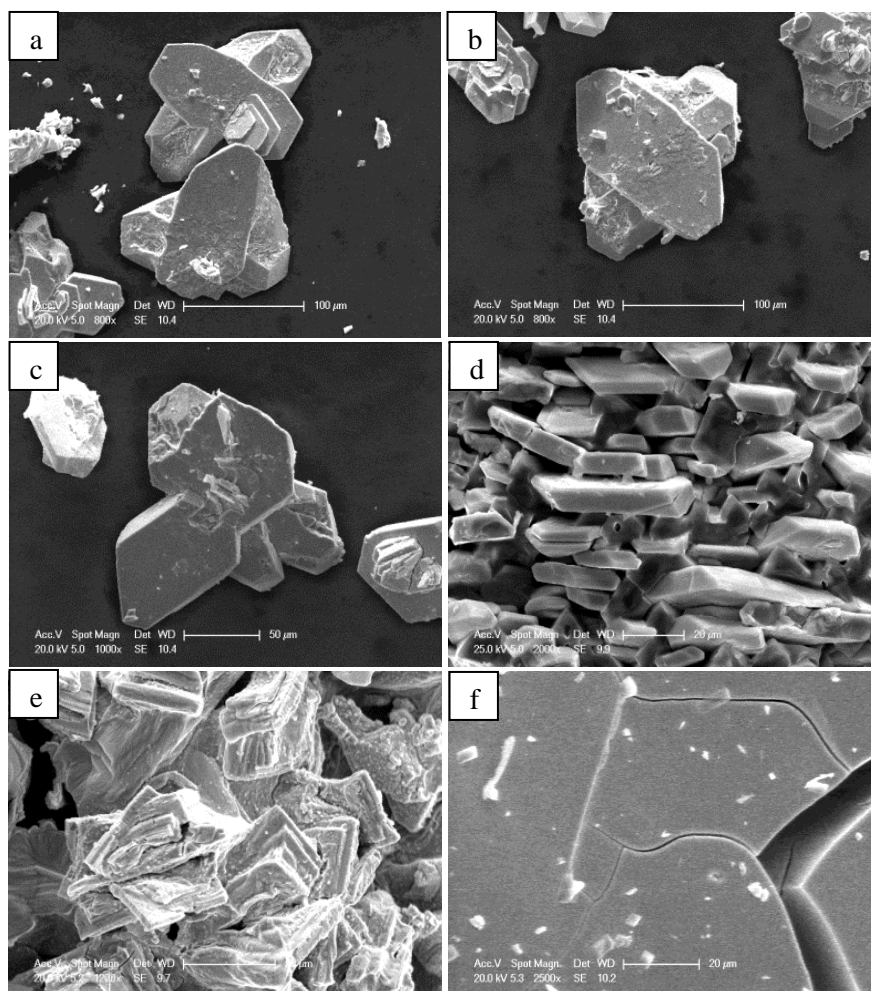
Figure 34: SEM of compound 1 showing the ~150 μm crystals at a=800x, b=800x, c=1000x, d=2000x, 1200x, and f=2500x magnification

EDX was conducted over a variety of spots on different crystal surfaces. The results reveal an elemental composition of U, Mo, O, and Na. The homogeneity of the crystals suggests that Na is part of the crystal structure itself and not an

impurity. As displayed in Table 11, U and Mo appear in near stoichiometric ratios with a smaller amount of Na. A Na:U:Mo ratio of 2:9:8 was determined. The crystal appears oxygen-deficient with 62 % O content by atoms when calculated by difference compared to 75 % expected in $UMoO_6$. Recall from Section 3.2.1.1 that EDX is a surface analysis tool and has relatively large secondary electron scattering and oxygen content is difficult to quantify accurately. However, results ultimately suggest the formation of a Na-U-Mo oxide.

Table 11: EDX results of compound 1

Element	Average Atom % With O Determined by Difference	$UMoO_6$ Theoretical Atom %
Na	4 ± 2	0
Mo	16 ± 4	12.5
U	18 ± 4	12.5
O	62 ± 2	75

4.1.1.2   *Inductively Coupled Plasma Mass Spectrometry (ICP-MS)*

ICP-MS yielded a Na:U:Mo ratio of 3:7:8. This agrees well with the Na:U:Mo ratio of 2:9:8 determined by EDX. Both methods indicate near stoichiometric ratios of U:Mo and a small concentration of Na, likely to be part of the crystal structure itself.

4.1.1.3   *Infrared Spectroscopy (IR)*

The IR spectrum of compound **1** is rather sparse, Figure 35, typical of a metal oxide. The large bowing peak around 3500 cm^{-1} indicates the presence of water in the material (blue, Figure 35). The strong peaks at 1650 cm^{-1} and below 1000 cm^{-1} resemble the characteristic 1640 cm^{-1} and 965 cm^{-1} peaks of the mineral Iriginite, $(UO_2)(Mo_2O_7) \cdot 3H_2O$, as well as the peaks at 1650 cm^{-1} and 944 cm^{-1} for the mineral Calcurmolite, $Ca_2(UO_2)_3Mo_2O_{11} \cdot nH_2O$ [85] (red and green, Figure 35). The presence of these peaks indicates that the product is most likely not a mixture of starting materials, but rather some form of U-Mo oxide.
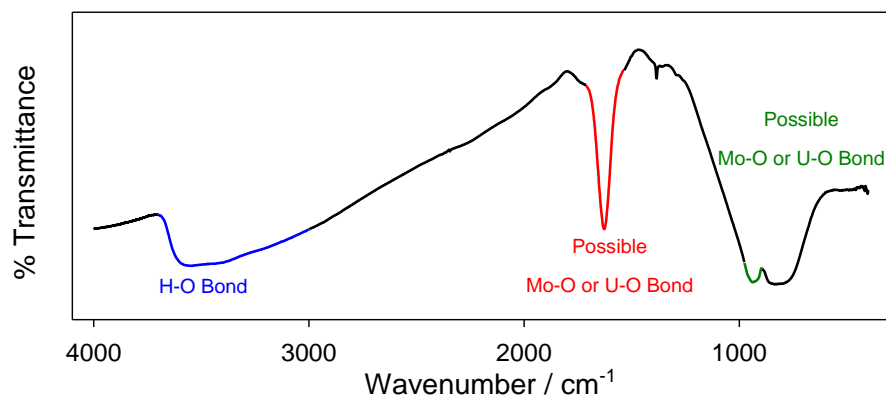
Figure 35: IR spectrum of compound 1

4.1.1.4   *Single Crystal X-ray Diffraction (SC-XRD)*

The crystals grown were large enough to perform SC-XRD, resulting in the definitive structural determination and atomic formulation of the product being $Na_8(UO_2)_{24}(MoO_4)_{28}(H_2O)_8$ per unit cell (*i.e.*, four $Na_2[(UO_2)_6(MoO_4)_7(H_2O)_2]$ units in a unit cell, $Z = 4$). Compound **1** crystallizes in the orthorhombic space group *C222₁* and displays an extended U-Mo-O network. Unit cell parameters can be found in Table 12. Although there are three crystallographically distinct U atoms and four Mo atoms, all atoms display virtually identical positions in the crystal structure. Each U atom adopts a pentagonal bipyramidal geometry, Figure 36, with all seven bonds to oxygen atoms. The axial positions are either occupied by terminal oxygen atoms (U1-O2 and U3-O19) or by oxygen atoms bonded to terminal sodium atoms (U1-O1-Na3, U2-O11-Na3, U2-O12-Na2, and U3-O20-Na2). The average U-O bond length of these terminal oxygen atoms is ~1.78 Å). The equatorial oxygen atoms (U-O$_{av}$ = ~2.38 Å) bridge to tetrahedral Mo atoms (Mo-O$_{av}$ = ~1.75 Å), creating a network of U-O-Mo planes visible along the *a* axis (Figure 37). The only exception is the equatorial O21 of U3 that is a water molecule. As two U3 are present in the empirical formula, these water represent the two H_2O molecules in the empirical formula. The remaining H_2O are present in the voids of the crystal structure and are loosely bonded to the oxygen in the crystal to varying degrees by hydrogen bonding. Atomic coordinates and select bond lengths and angles are listed in Appendix K.

Table 12: Crystallographic data and refinement parameters for compound 1

a (Å)	12.4947(6)
b (Å)	18.7181(10)
c (Å)	22.6721(11)
V (Å^3)	5302.5(5)
Space group	C 2 2 2$_1$
F$_{ooo}$	4872
μ (mm^{-1})	19.948
Z	4
D calc (Mg/m^3)	3.557
Crystal size (mm)	0.110 x 0.090 x 0.030
Radiation	Mo Kα
R int	0.0666
R$_1$	0.0516
wR$_2$	0.1215
R$_1$ (all data)	0.0663
wR$_2$ (all data)	0.1279
GoF	1.008
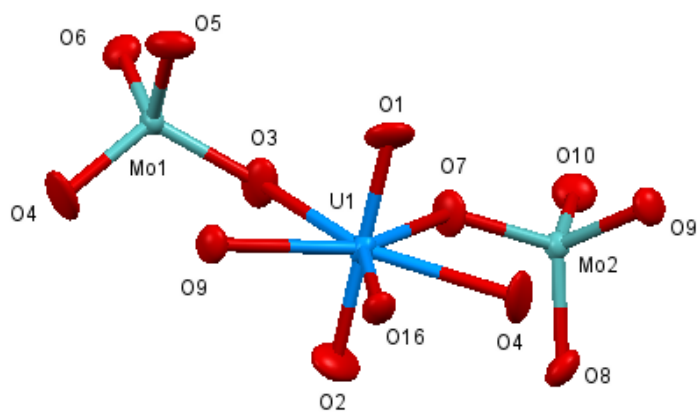
Figure 36: Partial plot of compound 1 showing the geometry of U (blue) and Mo (teal) with thermal ellipsoids drawn at the 50 % probability level

Through bridging oxygen atoms (red), the extended solid is generated, consisting of alternating pentagonal bipyramidal uranyl and tetrahedral molybdate units. Figures 37 and 38 show the extended structure and include the interstitial Na ions (purple).
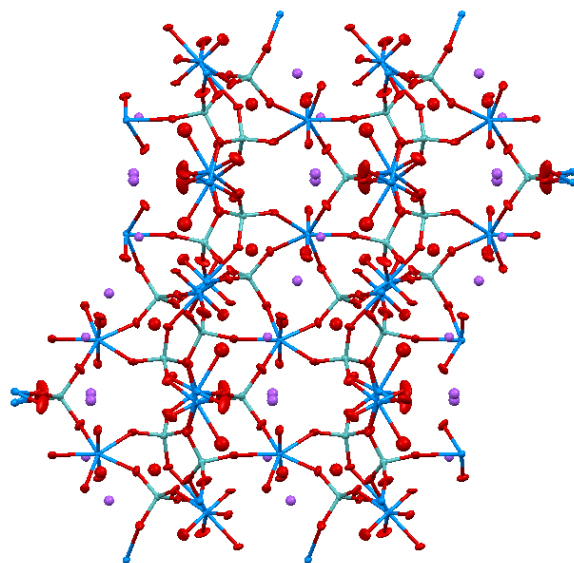
Figure 37: Thermal ellipsoid plot of compound 1 (50 % probability) as viewed down the *a* axis with hydrogen atoms and connections between molecules of water (oxygen in red) and Na ions (purple) omitted for clarity
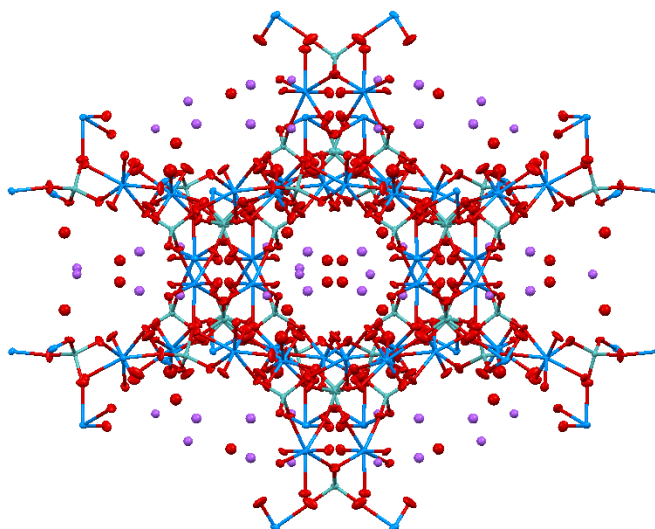
Figure 38: Thermal ellipsoid plot of compound 1 (50 % probability) as viewed down the *c* axis with hydrogen atoms and connections between molecules of water (oxygen in red) and Na ions (purple) omitted for clarity

The Na ions are incorporated in the structure by interaction with the oxygen atoms at the exterior of the highly bridged network. Although the Na ions display severe disorder and partially occupy several positions in the network, the relative stoichiometry could still be determined to include two Na^+ for every six UO_2^{2+} and seven MoO_4^{2-} units, resulting in an electrically neutral formula. This Na:U:Mo ratio of 2:6:7 agrees well with ICP-MS (3:7:8). Although the EDX measurement of 2:9:8 predicts more U than Mo, SC-XRD and ICP-MS are more accurate and consider the entire crystal, as opposed to the surface-only technique of EDX. Additionally, the Na:U:Mo ratio determined by ICP-MS and SC-XRD are within the error margins of EDX.

As shown in Figure 38 above, the 3D structure consists of void spaces. These pores contain water molecules from the aqueous preparation (as concluded by IR spectroscopy). Due to the small size of the crystals and severe disorder and vibration encountered with individual solvent molecules, the solvent molecules were not refined during the structural determination. Instead, mass loss during TGA was used to quantify the amount of water present in the sample.

The SC-XRD data collected were added to the Cambridge Structural Database (CSD) as number CSD-429044 and the Cambridge Crystallographic Data Centre (CCDC) as number CCDC-1037785.

The SC-XRD data were used to simulate the complete P-XRD pattern of compound **1**, Figure 39. This figure is relevant to the discussion in Section 4.1.1.6.
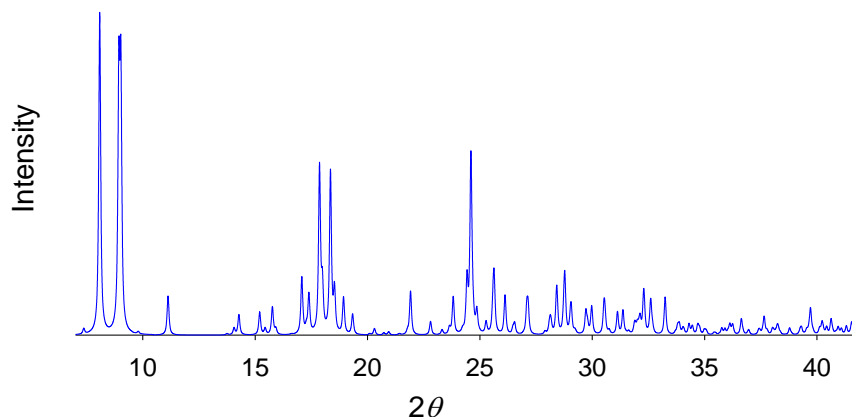
Figure 39: Simulated P-XRD pattern of compound 1 from SC-XRD

4.1.1.5   Thermogravimetric Analysis (TGA)

SC-XRD established the empirical formula of compound **1** and the void spaces were shown to contain water from the IR analysis. In order to quantify the amount of water in compound **1**, TGA was conducted on the product. Figure 40 displays the mass loss as a function of temperature. The initial mass loss of 5.62 % (shown in green in Figure 40) occurred by 531 ± 2 K and corresponds to 9 H_2O molecules per empirical formula unit. The remaining mass loss to 6.74 % total (shown in blue in Figure 40) occurred during the temperature ramp and a stable mass was achieved during the 873 ± 2 K temperature hold. This mass loss corresponds to 2 H_2O molecules per formula unit and likely correlates to H_2O bound to U in the framework. The assumption of all mass loss attributed to water loss was validated by IR showing H-O bonds and EDX and ICP-MS showing no indication of other impurities. All mass loss corresponds to 11 H_2O for each $Na_2(UO_2)_6(MoO_4)_7$ unit. As 2 H_2O are part of the framework, this gives an overall formula of $Na_2[(UO_2)_6(MoO_4)_7(H_2O)_2]\cdot 9\ H_2O$.
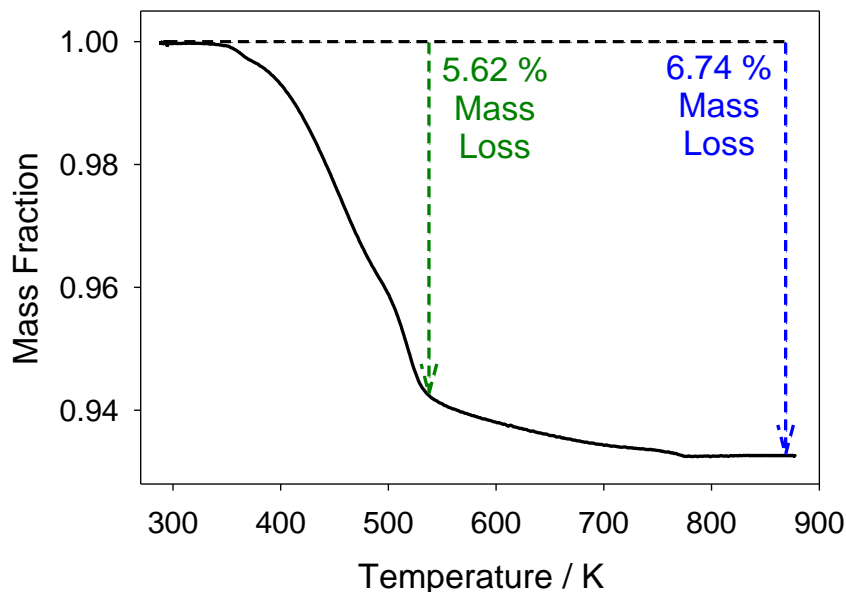
Figure 40: Mass loss as a function of temperature in compound 1

4.1.1.6 *Powder X-ray Diffraction (P-XRD)*

P-XRD analysis was performed on compound **1**, Figure 41. The simulated P-XRD pattern matches well with the experimental P-XRD pattern, indicating that the single crystal chosen for analysis is representative of the bulk material. The common peak angles are 2θ = 8.5, 9.4, 18.3, 18.9, 22.3, 25.0, and 29.2°. A thorough visual analysis was completed with literature P-XRD data and a computational comparison made with Powdercell [86] using literature SC-XRD data. Both analyses determined that compound **1** contains no starting reactants, U-species, Mo-species, or various other mixed U-Mo or Na-U-Mo oxide species. A complete list of P-XRD patterns checked visually and SC-XRD patterns checked with Powdercell can be found in Tables 14 and 15, respectively. The compound **1** P-XRD pattern bears some resemblance to the Fedoseev *et al.* ICDD card 44-0034 [59], identifying it as $UO_2MoO_4 \cdot 2.75H_2O$. Recall from Section 2.3.1.2 that Fedoseev [59] used an aqueous synthesis method with Na as a counter ion in one of the starting reactants. As no elemental analysis was conducted in [59], it is possible that Na is also present in their sample and they may have indeed synthesized **1** and not $UMoO_6$ as reported. The ideal standard for $UMoO_6$ in the literature is Juenke *et al.* [48].
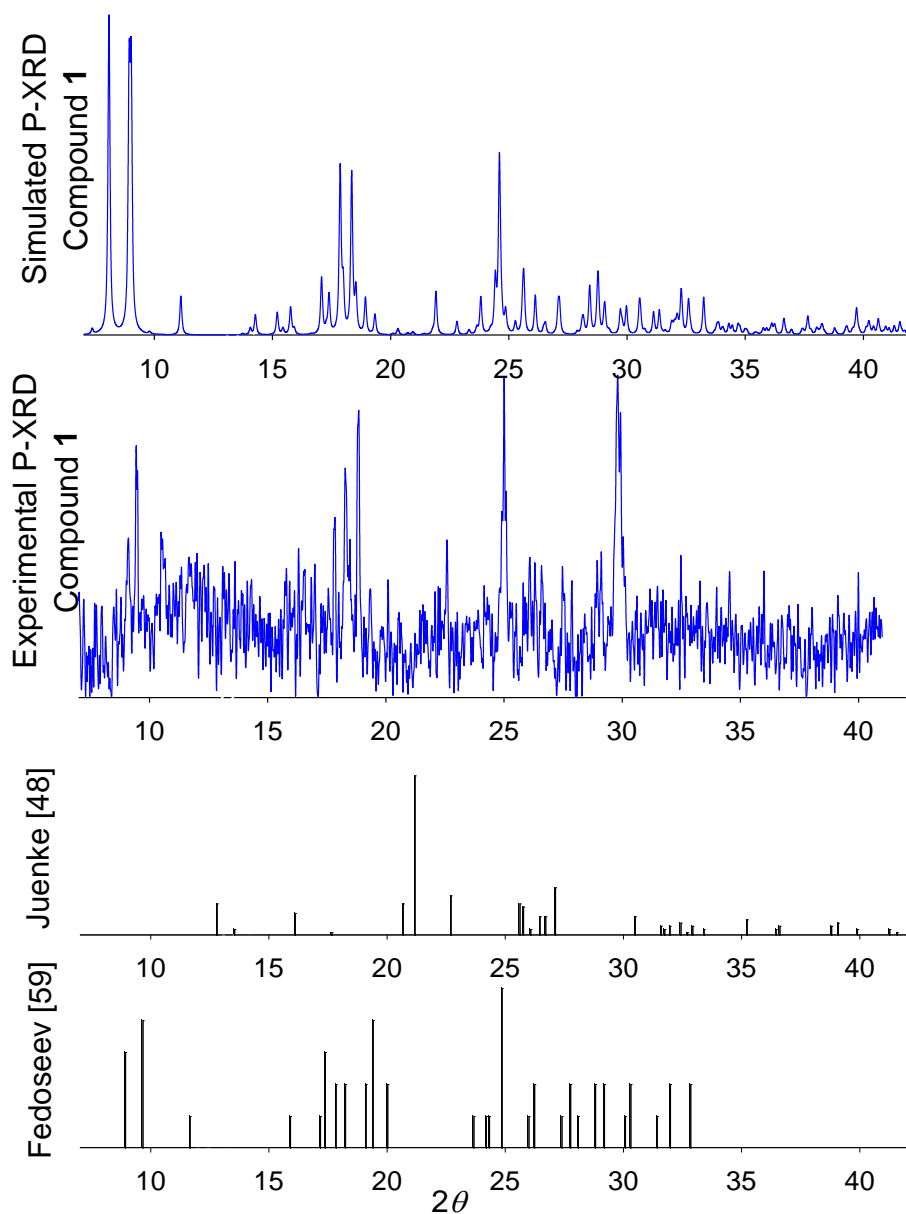
Figure 41: P-XRD results of compound 1

The synthesis of compound **1** was the first of a three step process to synthesize high purity $UMoO_6$. Since compound **1** contained Na within its crystal structure, a reflux in excess $UO_2(NO_3)_2$ was attempted to drive the reaction towards completion and exchange the Na^+ ions for UO_2^{2+}. The result is compound **2**.

4.1.2　　　　　　Characterization of Compound **2** ($UMoO_6 \cdot 1.84\ H_2O$)

Compound **1** was refluxed in excess $UO_2(NO_3)_2$ to remove the Na from the crystal structure to form compound **2** ($UMoO_6 \cdot 1.84\ H_2O$). Characterization of compound **2** was conducted by SEM, EDX, ICP-MS, IR, TGA, P-XRD, and GA. A conventional photograph is displayed in Figure 42 showing the loss of crystallinity and paler yellow colour after the reflux. Because of this loss of crystallinity, SC-XRD was unable to be conducted, but a conclusive characterization was made by the methods described below.
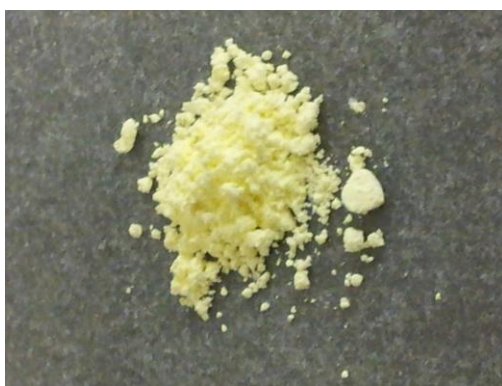
Figure 42: Conventional photograph of compound 2

4.1.2.1　　　　　　Scanning Electron Microscopy (SEM) and
　　　　　　　　　　　Energy-dispersive X-ray Spectroscopy (EDX)

Examination of compound **2** using SEM showed a loss of crystallinity and the formation of a pale yellow powder, Figure 43.
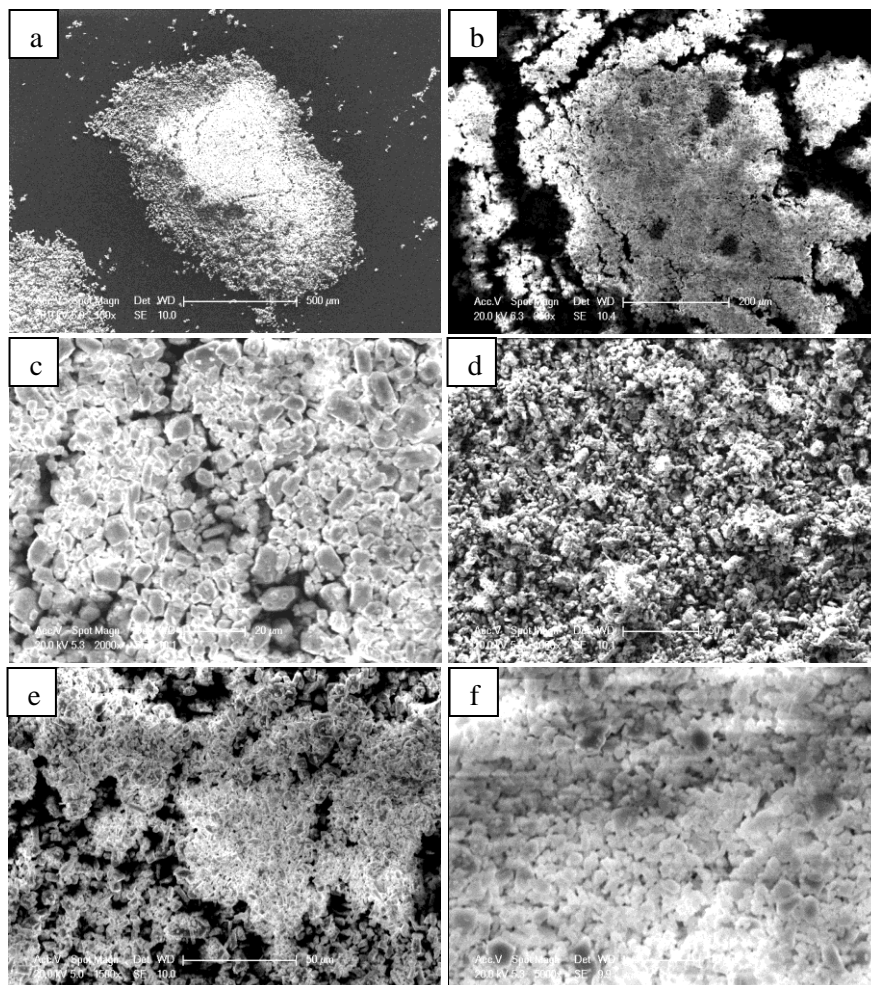
Figure 43: SEM of compound 2 showing the ~5 µm crystals at a=150x, b=350x, c=2000x, d=1000x, 1500x, and f=5000x magnification

EDX was conducted over a variety of spots on compound **2**. As Table 13 indicates, the elemental composition includes U, Mo, and O. However, Na was not observed in this sample. Importantly, the U:Mo ratio is approximately 1:1, as anticipated for the formation of $UMoO_6$. Oxygen, although difficult to measure accurately with EDX, was calculated as both an element and by difference, Table 13, giving an O content by atom of 79.8 % and 63.5 %, respectively. These values span the 75 % O content of $UMoO_6$, however a more accurate O content determination is made with GA (Section 4.1.2.6).

Table 13: EDX results of compound 2

Element	Average Atom % O as Element	Average Atom % O by Difference	$UMoO_6$ Theoretical Atom %
Na	0	0	0
Mo	10.5 ± 0.1	18.8 ± 0.3	12.5
U	9.7 ± 0.3	17.7 ± 0.3	12.5
O	79.8 ± 0.3	63.5 ± 0.1	75

4.1.2.2 Inductively Coupled Plasma Mass Spectrometry (ICP-MS)

ICP-MS was conducted and a Na:U:Mo ratio of 3:49:50 was found. This agrees well with an absence of Na determined by EDX. As Na is difficult to fully remove from the distilled water used to make the nitric acid stock solution for ICP-MS, its presence in almost any ICP-MS analysis is not unexpected. It is also possible that residual Na was left on compound **2** after washing. Although no longer present in the crystal structure, residual Na would appear during ICP-MS analyses. It is evident that nearly all, if not all, of the Na present in compound **1** is no longer present after refluxing to form compound **2**.

4.1.2.3 Infrared Spectroscopy (IR)

The IR spectrum of compound **2** closely resembles that of compound **1**, Figure 44. It too has a large bowing peak around 3500 cm^{-1} indicating the presence of water (blue, Figure 44). It also has strong peaks at 1650 cm^{-1} and below 1000 cm$_{-1}$ (red and green, Figure 44).
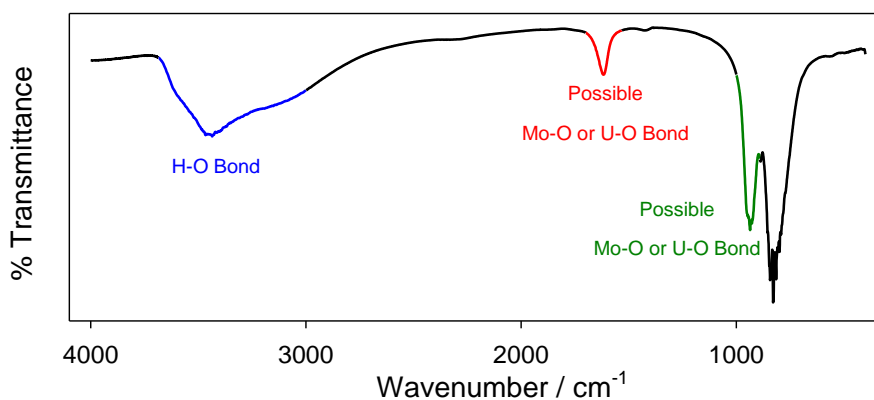
Figure 44: IR spectrum of compound 2

4.1.2.4   *Thermogravimetric Analysis (TGA)*

TGA performed on compound **2** exhibits the same trends as compound **1**, Figure 45, corresponding to a mass loss of 7.15 %. If the final product is $UMoO_6$ and all mass loss is attributed to water, this corresponds to a formula of $UMoO_6 \cdot 1.84\ H_2O$.
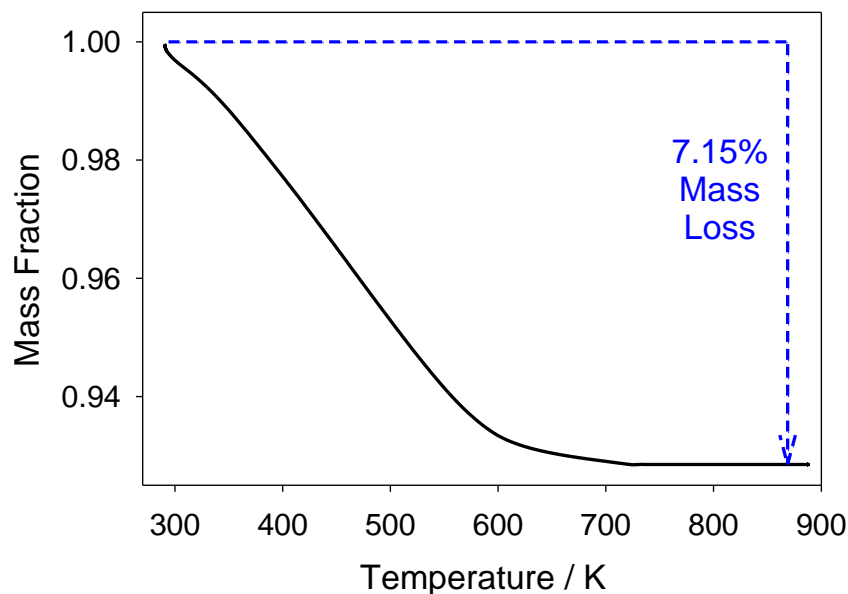
Figure 45: Mass loss as a function of temperature in compound 2

4.1.2.5   *Powder X-ray Diffraction (P-XRD)*

P-XRD analysis performed on compound **2** is shown in Figure 46. The pattern is visually different from compound **1**, indicating a change in crystal structure and not solely a replacement of Na^+ by UO_2^{2+} in the same positions. The P-XRD pattern is visually different from the solid state method of Juenke *et al.* [48] and aqueous method of Fedoseev *et al.* [59].
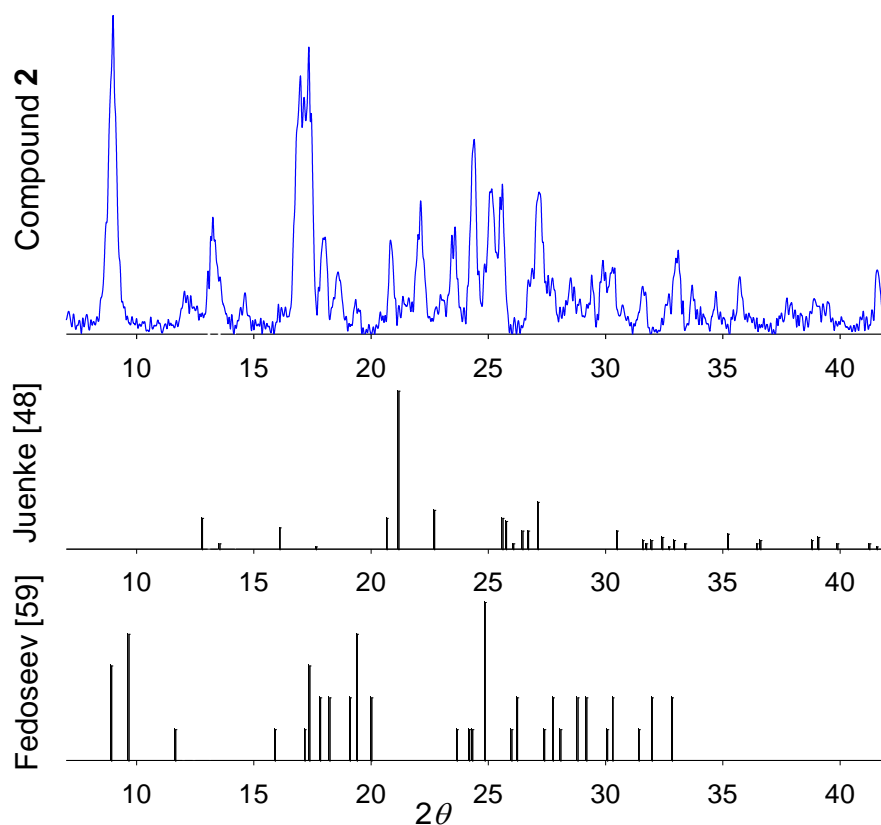
Figure 46: P-XRD results of compound 2

As with the P-XRD pattern of compound **1**, a thorough visual analysis with literature P-XRD data and a computational comparison via Powdercell [86] using literature SC-XRD data were made. Both analyses determined that compound **2** also contains no starting reactants, U-species, Mo-species, or various other mixed U-Mo or Na-U-Mo oxide species, Tables 14 and 15. This novel P-XRD pattern, different from Juenke *et al.* [48] and Fedoseev *et al.* [59], indicates a new structural form of $UMoO_6$.

Table 14: List of P-XRD patterns not matching compound 1 or 2

Compound	Ref.
Na_2MoO_4	[87],[88],[89],[90],[91]
$UO_2(NO_3)_2\ 6H_2O$	[92]
Mo	[93],[94]
MoO_2	[95]
MoO_3	[96],[97],[98],[99],[100]
U	[101]
UO_2	[102],[103],[104]
UO_3	[105],[106],[107]
U_3O_8	[108],[109]
UO_2MoO_4	[110],[111],[112]
Umohoite ($UO_2MoO_4\ 2H_2O$)	[113]
Umohoite ($UO_2MoO_4\ 4H_2O$)	[114],[115]
α - $UMoO_6\ 2H_2O$	[116]
β - $UMoO_6\ 2H_2O$	[117]
$UO_2MoO_4\ 2.75H_2O$	[118]
$UMoO_5$	[119],[120]
$U(MoO_4)_2\ H_2O$	[121]
α - $Na_2UMo_2O_{10}$	[67]
β - $Na_2UMo_2O_{10}$	[67]
$Na_2U(MoO_4)_3$	[122]
$Na_2U_3Mo_4O_{22}$	[123],[124]
$Na_2U_3Mo_9O_{37}$	[124]
$Na_4U(MoO_4)_4$	[122]
$Na_4U_3Mo_2O_{17}$	[124]
$Na_6UMo_4O_{18}$	[124], [125]
$Na_8U_3Mo_5O_{28}$	[126]
$Na_6U_2Mo_4O_{21}$	[124]

Table 15: List of SC-XRD patterns not matching compound 1 or 2 either in singular or any possible mixture

Compound	Ref.
Na_2MoO_4	[127]
$UO_2(NO_3)_2\ 3H_2O$	[128]
MoO_2	[129]
MoO_3	[130]
UO_2	[131]
$\alpha\text{-}UO_3$	[132]
$\alpha\text{-}U_3O_8$	[133]
$\beta\text{-}U_3O_8$	[133]
UO_2MoO_4	[134]
$UMoO_5$	[135]
UMo_2O_8	[136],[137]
UMo_5O_{16} Mon	[138]
UMo_5O_{16} Orth	[138], [139]
$U_{0.75}Mo_5O_{16}$	[138]
U_2MoO_8	[140]
$U_3Mo_{20}O_{64}$	[141]
UMo_4O_{14}	[142]
Umohoite (UO_2MoO_4) $2H_2O$)	[143]
Umohoite ($UMoO_6$ $4H_2O$)	[144]
Iriginite ($UO_2Mo_2O_7$ $3H_2O$)	[145]
$(UO_2)Mo_2O_7(H_2O)_2$	[146]
$Na_2(UO_2)(MoO_4)_2$	[147]
$Na_2(UO_2)(MoO_4)_2(H_2O)_4$	[148]
$Na_6(UO_2)(MoO_4)_4$	[149]
$Na_6(UO_2)_2O(MoO_4)_4$	[149]
$Cs_2(UO_2)_2(MoO_4)_3$	[150]
$Cs_2(UO_2)O(MoO_4)$	[151]
$Cs_6(UO_2)_2(MoO_4)_3(MoO_5)$	[152]

4.1.2.6 *Gravimetric Analysis (GA)*

The reaction of UO_2^{2+} and MoO_4^{2-} ions should yield $UMoO_6$. Both metals are in the +6 oxidation state, the highest achievable for both U and Mo. There is no indication or reason for the oxidation state of either metal to change or for oxygen to be lost in the reaction. This theory is supported by EDX data (Section 4.1.2.1), specifying an O content by atom of 79.8 % and 63.5 % when O is calculated as an element and by difference, respectively.

GA provided a more accurate measurement of O content. Starting with a sample of known mass (pre-dried in a vacuum oven at 393 K for 7 days), GA was conducted using the method described in Section 3.2.2.1 to give the combined mass of Mo and U in the sample. Assuming a 1:1 U:Mo ratio determined by EDX and ICP-MS, the difference in mass was assumed to be oxygen as no other elements were present in EDX or ICP-MS analysis. The result was six O atoms per U or Mo atom and the identification of compound **2** as $UMoO_6$. This accurate measurement of O content provides the final piece of characterization evidence to conclusively identify the new compound as $UMoO_6 \cdot 1.84\ H_2O$.

The synthesis of compound **2** was the second of a three step process towards $UMoO_6$. Compound **2** contained water within its crystal structure and did not match the ideal published pattern of Juenke *et al.* [48]. It was discovered that heating compound **2** to 773 K for 14 h at 1 atm resulted in a colour change from yellow to green. As discussed later in Section 4.2.2, an exothermic peak in the DSC heat flow at 734 ± 32 K indicated a transition from a *meta*-stable form of $UMoO_6$ (compound **2**) to the more stable form reported in the literature. This transition is the third and final step for synthesizing $UMoO_6$ (compound **3**).

4.1.3   *Characterization of Compound **3** ($UMoO_6$)*

As compound **2** was dried at 773 K for 14 h at 1 atm, all water was driven off prior to an exothermic DSC heat peak at 734 ± 32 K believed to be a transition of *meta*-stable $UMoO_6$ (compound **2**) to the stable $UMoO_6$ reported in the literature [48] (compound **3**). This characterization was completed by SEM, EDX, and P-XRD. A conventional photograph is displayed in Figure 47 showing the green colour that occurred after water loss and transition from compound **2**.

Figure 47: Conventional photograph of compound 3

4.1.3.1　　　　*Scanning Electron Microscopy (SEM) and*
　　　　　　　　　Energy-dispersive X-ray Spectroscopy (EDX)

Examination of compound **3** using SEM displayed long rectangular prism-shaped crystals approximately 10 µm in length, Figure 48. These crystals were too small for SC-XRD to be conducted, but a conclusive characterization was made by the methods described below. As the water was removed from the crystal structure of compound **2** and the heat of drying caused the crystal structure to collapse and reform, compound **3** formed. This crystal structure change was accompanied by the visual colour change from yellow to green.
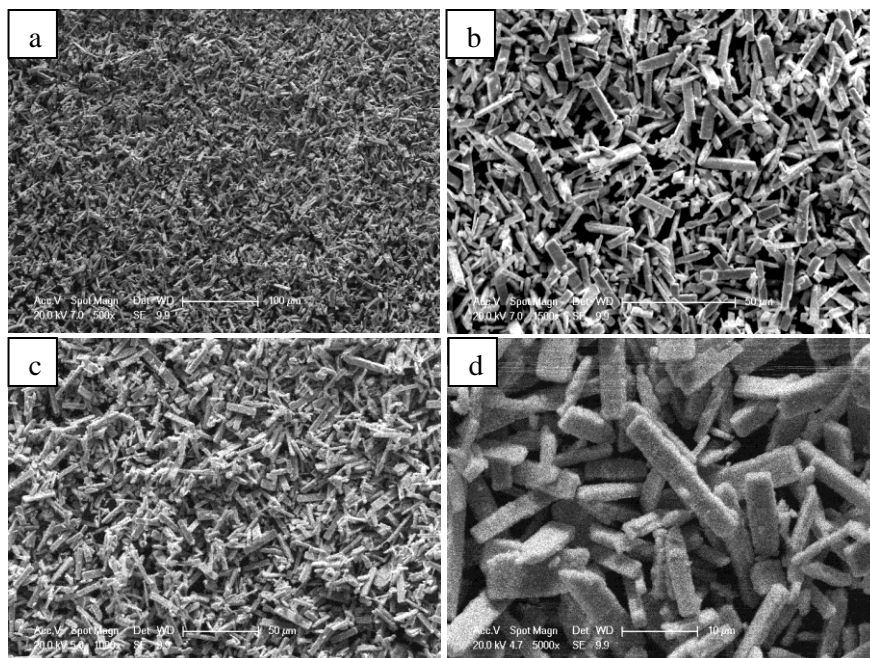
Figure 48: SEM of compound 3 showing the ~10 µm crystals at a=500x, b=1500x, c=1000x, and d=5000x magnification

EDX was conducted over a variety of spots on compound **3**. Na continued to not be observed and the elemental composition includes U, Mo, and O, similar to compound **2**. The U:Mo ratio is still approximately 1:1, as anticipated for the formation of $UMoO_6$. Oxygen was calculated as both an element and by difference, Table 16, giving O content by atom of 76.8 % and 63.5 %, respectively.

Table 16: EDX results of compound 3

Element	Average Atom % O as Element	Average Atom % O by Difference	$UMoO_6$ Theoretical Atom %
Na	0	0	0
Mo	11.9 ± 1.1	18.7 ± 0.1	12.5
U	11.3 ± 0.9	17.8 ± 0.1	12.5
O	76.8 ± 2.0	63.5 ± 0.1	75

4.1.3.2   Powder X-ray Diffraction (P-XRD)

P-XRD conducted on compound **3** shows a visual match to the product of the solid-state synthesis method of Juenke *et al.* [48], Figure 49, confirming the exothermic heat peak at 734 ± 32 K corresponded to a transition of *meta*-stable

94/134

$UMoO_6$ (compound **2**) to the stable $UMoO_6$ reported in the literature (compound **3**). This process was exothermic as heat was released en route to a more stable compound. The aqueous synthesis process described produces $UMoO_6$ with the same P-XRD pattern as that reported in the literature, but does not include the U-oxide and Mo-oxide reactant impurities of a solid-state synthesis method, most likely resulting in a higher purity product.
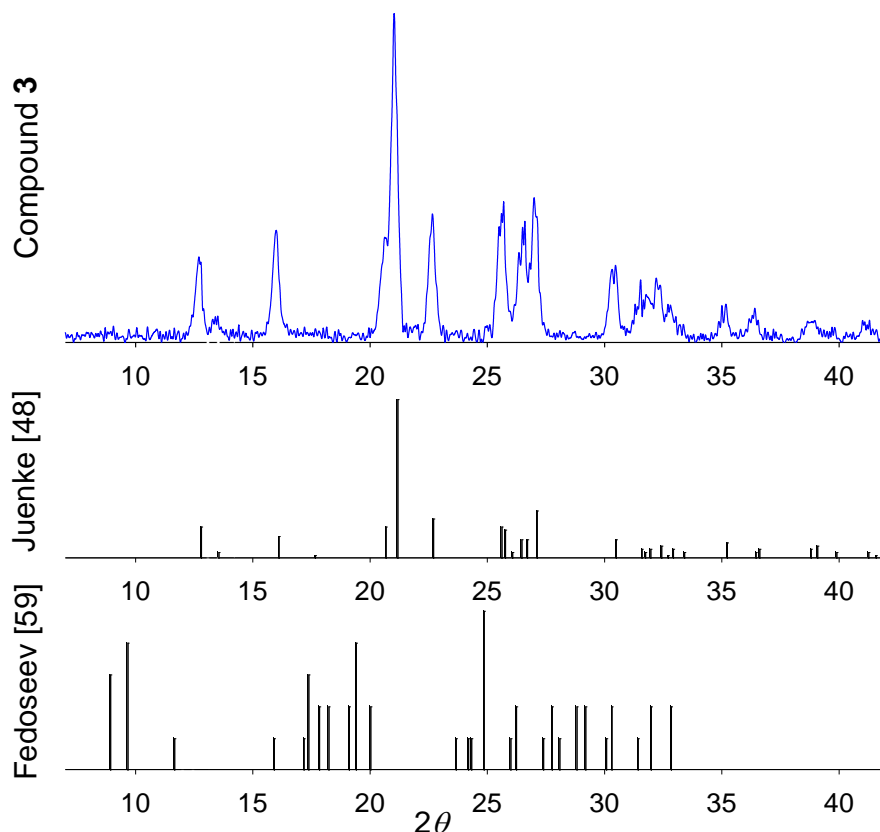
Figure 49: P-XRD results of compound 3

4.1.4   Summary

Mixing Na_2MoO_4 and $UO_2(NO_3)_2$ in a water solution resulted in the formation of compound **1**. This compound was added to the CSD as number CSD-429044 and the CCDC as CCDC-1037785. The similar powder pattern to Fedoseev *et al.* [59] suggests [59] may not be $UMoO_6$ as reported and instead have Na incorporated in the sample. Refluxing compound **1** in excess $UO_2(NO_3)_2$ removed the Na present in its crystal structure, but caused a loss of crystallinity. P-XRD of compound **2**

found a unique *meta*-stable structure for $UMoO_6$. Drying compound **2** at 773 K for 14 h at 1 atm removed all water and a phase transition from *meta*-stable compound **2** to compound **3** occurred at 734 ± 32 K. The crystal structure of compound **3** had the same crystal structure as the accepted $UMoO_6$ structure of Juenke *et al.* [48]. A manuscript is under review for the synthesis described herein [153]. As compound **1** did not have any U-oxide or Mo-oxide contaminants, it is believe that both successors also did not contain these contaminants, which was confirmed by P-XRD. A P-XRD comparison of compound **3** with Juenke *et al.* [48] confirmed a pure $UMoO_6$ product was synthesized, which could be used to obtain the thermodynamic properties of C_p, ΔH^o_{trans}, ΔH^o_{decomp}, T_{decomp}, and $\Delta H^o_{f, 298 K}$ through calculations.

4.2 Thermodynamic Properties

Once the high purity $UMoO_6$ was synthesized, some of its thermodynamic properties could be determined. In Section 4.2.1, the C_p of fully dry $UMoO_6$ (compound **3**) is determined and compared against literature values, after which, in Section 4.2.2, a transition between *meta*-stable $UMoO_6$ and literature $UMoO_6$ [48] is identified and quantified as ΔH^o_{trans} by integrating the corresponding peak in the DSC heat flow curve. In Section 4.2.3, a ΔH^o_{decomp} is quantified by the same method. Finally, in Section 4.2.4, a T_{decomp} is determined by four different methods and one value selected.

4.2.1 The Specific Heat Capacity (C_p) of $UMoO_6$

The heat capacity of compound **3** (*i.e.*, dried for 14 h at 773 K at 1 atm and characterized to be $UMoO_6$ described in the literature [48]) was determined. Although C_p data was collected for wet and damp compound **2** (Appendix G), only the C_p data for compound **3** was considered for addition to the RMC-TFM as only dry $UMoO_6$ is believed to form in nuclear fuels due to the high temperature environment. Three replicate samples produced a $C_p(T)$ function (J K^{-1} mol^{-1}) of $223.0844 - 0.1945T(K) + 2.2965 \times 10^{-4}T^2(K) - 2.515493 \times 10^6 T^{-2}(K)$ with an associated error of ± 5 % over a temperature range of 343-668 K, Figure 50. This function was determined by fitting experimental data points using the residual sum of squares regression of Sigmaplot [154]. In the literature, Dash *et al.* [23] found a $C_p(T)$ function by measuring the enthalpy increments using high-temperature Calvet micro-calorimetry and this is used as a baseline for comparison. The Dash *et al.* method, published in Ref. [155], shows a ± 2 % error in the H_T-$H_{298 K}$

enthalpy increment measurements and a ± 2% error in the fit function integrated to obtain the $C_p(T)$ function. A conservative overall error of ± 5 % is assumed for the work of Dash *et al.* [23].
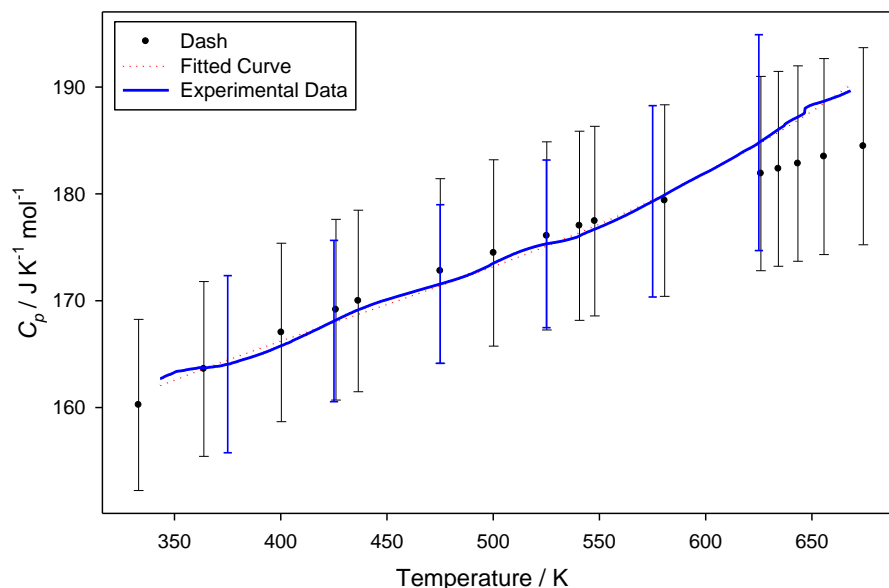
Figure 50: Specific heat capacity of dry UMoO$_6$ in relation to Dash *et al.* [23]

The $C_p(T)$ function is very close to that of Dash *et al.* [23], but departs at the high end of the valid temperature range. This departure can be explained by a phenomenon that likely occurred during the execution of the method described in Section 3.3. The DSC heating rate likely slowed as it approached the top of the programmed temperature range. This test method demands a constant heating rate as a slowing heating rate gives more time for heat to flow into the sample over the duration of the non-constant heat rate. The greater amount of heat during the non-constant heating rate caused a higher C_p to be determined. As a result of this C_p departure at the top of the temperature range, a large deviation from Dash [23] is found when the fitted $C_p(T)$ function is extrapolated to the high temperatures required by the RMC-TFM, Figure 51. This trend becomes important in Section 4.3 when the $C_p(T)$ function is required to determine $\Delta H^o_{f, 298\,K}$. Overall, the $C_p(T)$ function of Dash *et al.* [23] is likely to be a better representation of the C_p of UMoO$_6$ as it has a larger experimental temperature range, 299-1000 K; while the $C_p(T)$ function determined in this thesis is limited to between 343-668 K and must be extrapolated beyond.
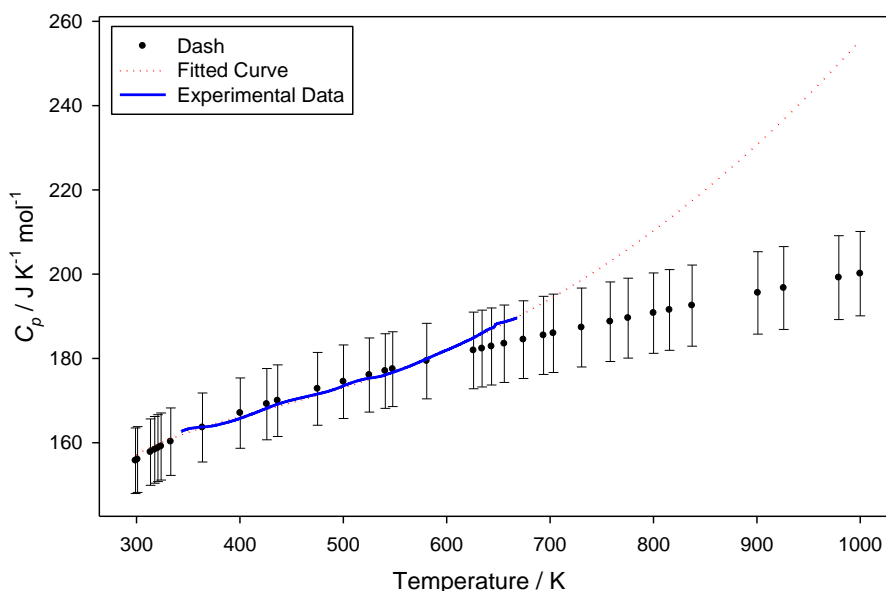
Figure 51: Extrapolated $C_p(T)$ function of dry UMoO$_6$ compared to the literature values of Dash *et al.* [23]

While the $C_p(T)$ function determined by this thesis may be less accurate at the top of the temperature range, the lower temperature range is in line with literature. Recall that Suleimanov *et al.* [54] determined a low temperature $C_p(T)$ piecewise function (6.6 K to 300 K) for UMoO$_6$ and *ab-initio* [65] calculations described in Section 2.3.2 can be used to predict the C_p of compounds. A comparison can be made at the temperature 298.15 K, Table 17, showing the C_p at 298.15 K determined by this thesis lies above Dash [23] and below Suleimanov [54] and *ab-initio* calculations [65]. The Suleimanov *et al.* [54] method of adiabatic calorimetry is generally considered a better method for determining low temperature C_p, and the Dash *et al.* [23] method of high-temperature Calvet micro-calorimetry better for determining high temperature C_p. The C_p determined by this thesis lies between the two experimental values determined in the literature and thus breeds confidence in the result. The C_p determined by *ab-initio* calculations [65] is in line with experimental values, but is only an estimate based on vibrational harmonics.

Table 17: Comparison of the C_p of UMoO$_6$ at 298.15 K

Source	C_p at 298.15 K (J K^{-1} mol^{-1})
This Thesis	157.21 ± 7.86
Dash *et al.* [23]	155.60 ± 7.78
Suleimanov *et al.* [54]	161.71 ± 1.86
Ab-initio [65]	160.94

To best evaluate the C_p of UMoO$_6$ over all temperature ranges, the $C_p(T)$ functions of Suleimanov *et al.* [54], Dash *et al.* [23], *ab-initio* calculations, and this thesis (fitted from experimental data using residual sum of squares regression of Sigmaplot) are plotted over their respective valid temperature ranges in Figure 52. The coefficients for their $C_p(T)$ functions of the form of Equation 43 are listed in Table 18.

$$C_p^\circ(T(K)) \ (J \ mol^{-1}K^{-1}) = k_o + k_1T + k_2T^2 + k_3T^3 + k_{-2}T^{-2} \quad \text{Equation 43}$$

Table 18: Coefficients for the UMoO$_6$ $C_p(T)$ functions of the form of Equation 43 of Suleimanov *et al.* [54], Dash *et al.* [23], *ab-initio* calculation [65], and this thesis

Ref.	Temp Range (K)	k_o	k_1	k_2	k_3	k_{-2}
Suleimanov [54]	6.6-13	0.5715	-0.1769	0.01747	0.0004910	-
Suleimanov [54]	13-47	-0.2263	-0.1200	0.02759	-0.0002361	-
Suleimanov [54]	47-300	485.26	-0.895498	2.7658E-3	-3.4699E-06	380734
Dash [23]	299-1000	158.65	0.004288	-0.0002361	-	-1.40770E+06
Ab-initio [65]	0-1000	186.66	0.019090	0.24647E-06	-	-2.79339E+06
This thesis	343-668	223.0844	-0.1945	2.2965E-04	-	-2.515493E+06

*The Suleimanov [54] 47-300 K range $C_p(T)$ function contains the additional terms of -5238050T^3 and 3704.84T^{05}
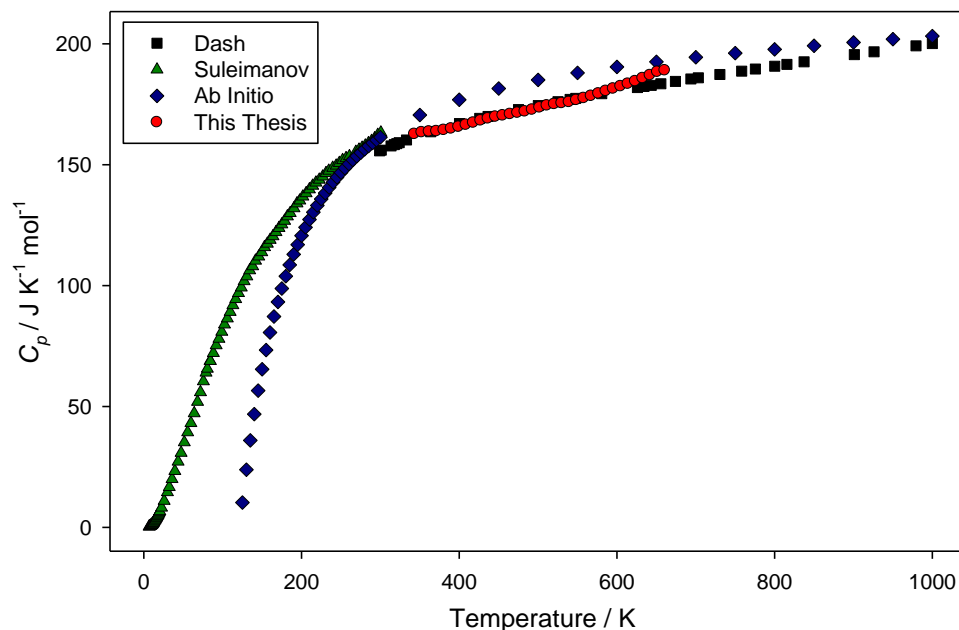
Figure 52: $C_p(T)$ **functions of this thesis (fitted), Dash** *et al.* **[23], Suleimanov** *et al.* **[54], and** *ab-initio* **calculations [65]**

The complete temperature range of C_p values in Figure 52 shows that the Suleimanov *et al.* [54] function is bound by the condition that the limit of C_p is zero as temperature approaches zero. This boundary condition likely makes the Suleimanov *et al.* [54] function a better fit at low temperatures. While the *ab-initio* calculations [65] provide the largest temperature range, they under-predict the C_p at low temperatures and over-predict at high temperatures when compared to experimentally determined values. As *ab-initio* calculations are based on internal vibrational harmonics in the material, they are purely an estimate and experimental data holds greater weight. The higher temperature $C_p(T)$ function determined by this thesis provides very high C_p values when extrapolated to higher temperatures. By default, Dash *et al.* [23] is the best $C_p(T)$ function to represent the high temperature region. Thus, from all available data, the C_p of $UMoO_6$ is best represented by a two part piecewise function, the Suleimanov *et al.* [54] piecewise function for the low temperature range 6.6 K to 300 K and the Dash *et al.*[23] function for the high temperature range 300-1000 K, Table 19. It will hereon be referred to as the literature piecewise $C_p(T)$ function.

Table 19: The literature piecewise $C_p(T)$ function

Temperature Range (K)	Source	Function (J K^{-1} mol^{-1}) T in K
6.6-13	[54]	$0.5715 - 0.1769T + 0.01747T^2 + 0.0004910T^3$
13-47	[54]	$-0.2263 - 0.1200T + 0.02759T^2 - 0.0002361T^3$
47-300	[54]	$485.26 - 5238050T^{-3} + 380734T^{-2} - 3704.84T^{-0.5} -0.895498T + 2.7658\text{E-}3T^2 -3.4699\text{E-}6T^3$
300-1000	[23]	$158.65 + 4.288\text{E-}2T - 14.077\text{E5}T^{-2}$

4.2.2   *Enthalpy of Transition ($\Delta H^o{}_{trans}$)*

As described in Section 3.4, decomposition experiments were conducted on compound **2**. The first event to occur was water loss as the sample was heated. All change in mass due to water loss occurred prior to 673 K and a stable mass was observed at temperatures beyond this point (until the final decomposition). At 734 ± 32 K, a large exothermic peak in the DSC heat flow data occurred and the mass remained constant, identified in Figure 53 as the transition peak. This is believed to be the exothermic transition between the *meta*-stable compound **2** and stable compound **3** as no mass loss occurred and a change in crystal structure was observed via P-XRD described in Section 4.1.

By integrating the area under the DSC heat flow peak, the heat released during the transition was quantified as $\Delta H^o{}_{trans}$ of -32 ± 3 kJ mol^{-1}. The *meta*-stable compound was added to the RMC-TFM with this transition energy used as the amount of energy released en route to the more stable form. Because the *meta*-stable form requires more heat to form than the stable form reported in the literature [48], it is unlikely to form in a nuclear fuel. However, it is included in the RMC-TFM for completeness.
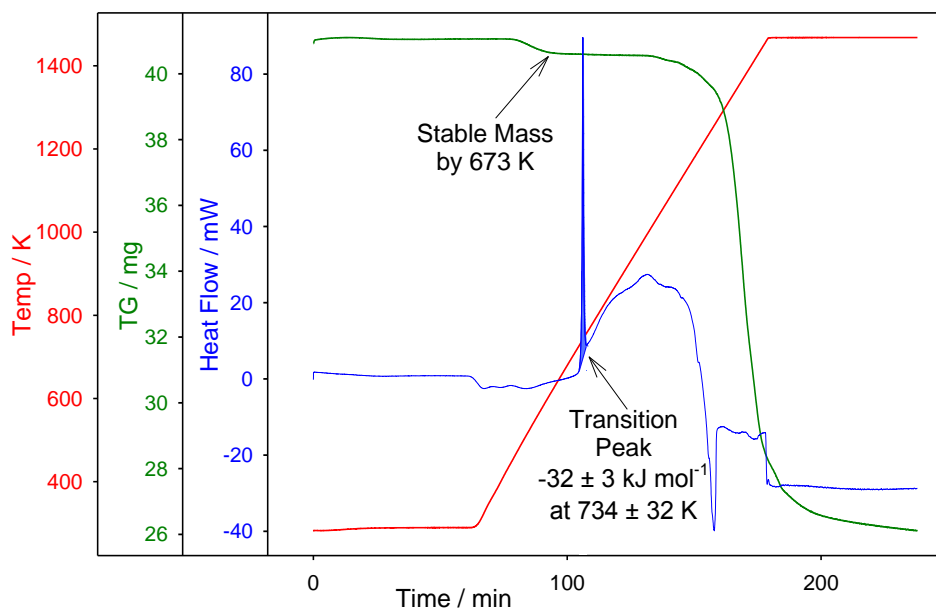
Figure 53: 734 ± 32 K exothermic transition peak in DSC heat flow data

4.2.3   Enthalpy of Decomposition (ΔH^o_{decomp})

After the exothermic peak at 734 ± 32 K, a stable mass continued to be observed until endothermic decomposition occurred at 1205 ± 10 K, Figure 54. The determination of T_{decomp} is described in the next section. By integrating the area under the endothermic peak in the DSC heat flow data, the enthalpy of decomposition was determined to be $\Delta H^o_{decomp} = 82 \pm 10$ kJ mol^{-1}. This value combined with T_{decomp} becomes significant to determine $\Delta H^o_{f, 298 K}$ in Section 4.3.
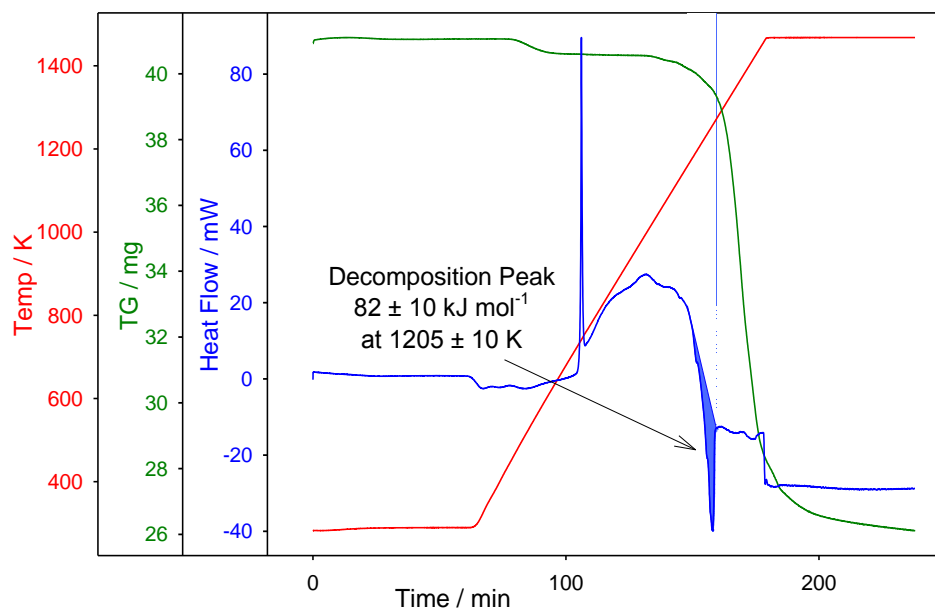
Figure 54: 82 ± 10 kJ mol^{-1} endothermic decomposition peak in DSC heat flow data

4.2.4 *Decomposition Temperature (T_{decomp})*

The temperature of the 82 ± 10 kJ mol^{-1} decomposition peak was determined via four different methods: (i) first change in mass; (ii) 5 % of decomposition by mass; (iii) onset temperature from the DSC curve using Calisto software; and (iv) onset temperature from DSC curve by manual determination, Table 20. The fourth method, *onset temperature from the DSC curve by manual determination*, was determined to be the most accurate, giving a value of $T_{decomp} = 1205 \pm 10$ K. This was the temperature used in the RMC-TFM and combined with ΔH^{o}_{decomp} to obtain $\Delta H^{o}_{f, 298 K}$ in Section 4.3.

Table 20: Decomposition temperature of $UMoO_6$ via different methods

Number	Method	Decomposition Temperature (K)
1	First Change in Mass	1023 ± 25
2	5 % of Decomposition by Mass	1196 ± 37
3	Onset Temperature from DSC Curve using Calisto Software	1220 ± 18
4	Onset Temperature from DSC Curve by Manual Determination	1205 ± 10

Method 1, *first change in mass*, relied on human repeatability in identifying the first deviation from the baseline. This proved to be a very subjective method as the result of 1023 ± 25 K is much lower than the other methods and has a high associated error due to poor human repeatability. Method 2, *5 % decomposition by mass*, is a method generally reserved for compounds more complex than solid oxides like $UMoO_6$, specifically polymers. As a result, the T_{decomp} of 1196 ± 37 K found is in line with other methods, but produced the highest associated error. It is possible the 5 % decomposition failure criterion is not as applicable to solid oxides as it is to polymers. Method 3, *onset temperature from the DSC curve using Calisto software*, had a T_{decomp} within error of the above methods, however it appears the computer algorithm used to select the baseline tangent is variable with the given dataset. Based on various replicate experiments, a human user produces a more consistent tangent from which the integration is made. Ultimately, Method 4, *onset temperature from the DSC curve by manual determination*, produced the most precise value of 1205 ± 10 K and was selected for further use in Section 4.3 to determine $\Delta H^o_{f, 298 K}$.

A T_{decomp} of 1205 ± 10 K compares with literature values shown in Table 21. The experimental findings of Suleimanov *et al.* [54] are closest to the results of this thesis. While the Suleimanov *et al.* [54] paper defines the thermal event in the DTA as the fusion of solid $UMoO_6$ to liquid, the corresponding TG shows a significant mass loss. This suggests a decomposition of solid $UMoO_6$ either directly to a gaseous phase or to a liquid phase that immediately vapourizes to a gaseous form. The findings of Suleimanov *et al.* [54] may be closest to this study because their results actually reflect a mass loss rather than a true fusion reaction, similar to this thesis. Ustinov *et al.* [56] heated samples in air, thus allowing the U_3O_8 to oxidize to UO_3, but U_3O_8 in the sample determined by P-XRD suggests this reaction did not go to completion. This U_3O_8 contamination, coupled with a likely inaccurate thermo recorder method from the 1970`s, allows for significant

error in the measured temperature. Serezhkin *et al.* [60] likely sealed samples in quartz ampoules [156], not allowing any mass to escape, but possibly increased the pressure inside the crucible to keep the $UMoO_6$ in a liquid form and not allow it to vapourize. This would account for a higher melting temperature at higher pressures. Ultimately, the results of this thesis and Suleimanov *et al.* [54] are most recent and best reflect an open system at 1 atm from which to model the UO_3-MoO_3 phase diagram.

Table 21: Comparison of literature decomposition temperatures of $UMoO_6$

Reaction	Ref.	Temperature (K)
$UMoO_{6(s)} \rightarrow UMoO_{6(l)}$	Ustinov *et al.* [56]	1253 ± 10
$UMoO_{6(s)} \rightarrow UMoO_{6(l)}$	Suleimanov *et al.* [54]	1212 ± 2
$UMoO_{6(s)} \rightarrow UMoO_{6(l)}$	Serezhkin *et al.* [60]	1283
$UMoO_{6(s)} \rightarrow$ U-oxide + gas	This study	1205 ± 10

4.2.5   Summary

Using the newly synthesized $UMoO_6$, its thermodynamic properties of C_p, ΔH^o_{trans}, ΔH^o_{decomp}, and T_{decomp} were found experimentally. The $C_p(T)$ function (J K^{-1} mol^{-1}) of fully dry $UMoO_6$ was determined to be $223.0844 - 0.1945T(K) + 2.2965 \times 10^{-4}T^2(K) - 2.515493 \times 10^6 T^{-2}(K)$ with an associated error of ± 5 % over a temperature range of 343-668 K. An exothermic peak in the DSC heat flow data at 734 ± 32 K was identified as the transition between *meta*-stable $UMoO_6$ (compound **2**) and $UMoO_6$ (compound **3**). Integration of the transition peak determined $\Delta H^o_{trans} = -32 \pm 3$ kJ mol^{-1}. Both $C_p(T)$ and ΔH^o_{trans} were added to the RMC-TFM as a *meta*-stable $UMoO_6$ species. Integrating the endothermic peak in the DSC heat flow data during sample decomposition provided the ΔH^o_{decomp} of 82 ± 10 kJ mol^{-1}. The *onset temperature from the DSC curve by manual determination* method provided the most accurate T_{decomp} at 1205 ± 10 K. As these thermodynamic data are in line with most literature, it appears the U-oxide and Mo-oxide contaminants in solid state methods did not significantly affect the literature data. Both ΔH^o_{decomp} and T_{decomp} are used in Section 4.3 to calculate $\Delta H^o_{f, 298 K}$. The selection of thermodynamic values to include in the $UMoO_6$ species data file of the RMC-TFM are then selected in Section 4.4.

4.3   Decomposition Reactions

In Section 4.2, the ΔH^o_{decomp} of 82 ± 10 kJ mol^{-1} and T_{decomp} of 1205 ± 10 K of $UMoO_6$ were determined experimentally. The enthalpy of formation for $UMoO_6$ ($\Delta H^o_{f, 298 K}$) can be calculated using these two values, a $UMoO_6$ $C_p(T)$ function, the decomposition reaction, and the known $\Delta H^o_{f, 298 K}$ and $C_p(T)$ values for the products of the decomposition reaction. However, the chemical species of the products in the decomposition reaction are unknown as there was no downstream gas analysis capability for the TGA/DSC. Instead, the decomposition reaction needed to be estimated theoretically based on observations made during the decomposition experiments.

It was observed that some oxide remained in the reaction crucible after decomposition and some oxide crystals formed in a cooler part of the furnace chamber, likely re-condensing after volatilizing from the reaction crucible as a gas. EDX analysis determined the material left in the crucible after decomposition to be a U-oxide free of Mo and the oxide crystal formation in the cooler furnace chamber to be a Mo-oxide. EDX suggested UO_2 and MoO_3, however, as EDX is a surface analysis tool, the stoichiometries of these oxides may be inaccurate. It is therefore only fair to conclude that solid U-oxide was present in the crucible after decomposition and Mo-oxide volatilized out of the crucible and re-condensed in the cooler sections of the furnace chamber.

It can therefore be assumed the decomposition reaction had the form:

$$UMoO_{6\,(s)} \rightarrow U - oxide_{(s)} + Mo - oxide_{(g)} \qquad \text{Equation 54}$$
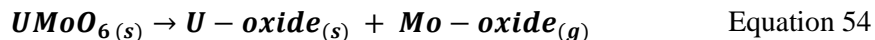
It is possible oxygen may also have been a product to balance any oxygen deficit caused during decomposition. It is also possible that a mixture of U-oxides or Mo-oxides was generated.

Once a decomposition reaction is assumed, $\Delta H^o_{f, UMoO_6}$ at the experimentally determined T_{decomp} can be predicted using Hess's law and the experimentally determined ΔH^o_{decomp}.

$$\Delta H^o_{decomp} = \Sigma \Delta H^o_{f,products} - \Sigma \Delta H^o_{f,reactants} \qquad \text{Equation 55}$$

Applying the assumed decomposition reaction, Equation 54

$$\Delta H^o_{decomp} = \Delta H^o_{f,U-oxide} + \Delta H^o_{f,Mo-oxide} - \Delta H^o_{f,UMoO_6}$$

$$\Delta H^o_{f,UMoO_6} = \Delta H^o_{f,U-oxide} + \Delta H^o_{f,Mo-oxide} - \Delta H^o_{decomp} \qquad \text{Equation 56}$$

where literature values are used for $\Delta H^o_{\text{f, U-oxide}}$ and $\Delta H^o_{\text{f, Mo-oxide}}$. Finally, $\Delta H^o_{\text{f, 298 K, UMoO}_6}$ is found from $\Delta H^o_{\text{f, UMoO}_6}$ at T_{decomp} using $C_p(T)$ and Equation 12.

$$\Delta H^o{}_T = \Delta H^o_{298K} + \int_{298K}^{T} C_p(T)dT \qquad \text{Equation 12}$$

For this thesis, ten possible decomposition reactions were proposed. Reactions 1-4 are generalized hypothesises based upon four common U-oxides, $MoO_{3(g)}$ volatilizing and $O_{2(g)}$ used to balance the chemical equation. Reactions 5-8 are hypotheses based on four common U-oxides and the branching ratio postulated by Tripathi *et al.* [61] for the MoO_3 polymeric gas species. Reaction 9 is the RMC-TFM decomposition prediction with only Mo gases allowed to form and reaction 10 is the RMC-TFM decomposition prediction with all possible species allowed to form, Table 22.

Table 22: Different decomposition of $UMoO_6$ reactions

#	Assumed Decomposition Reaction
1	$UMoO_{6(s)} \rightarrow UO_{3(s)} + MoO_{3(g)}$
2	$UMoO_{6(s)} \rightarrow UO_{2(s)} + MoO_{3(g)} + 1/2\ O_{2(g)}$
3	$UMoO_{6(s)} \rightarrow 1/3\ U_3O_{8(s)} + MoO_{3(g)} + 1/6\ O_{2(g)}$
4	$UMoO_{6(s)} \rightarrow 1/4\ U_4O_{9(s)} + MoO_{3(g)} + 3/8\ O_{2(g)}$
5	$UMoO_{6(s)} \rightarrow UO_{3(s)} + 3/50\ Mo_3O_{9(g)} + 4/50\ Mo_4O_{12(g)} + 5/50\ Mo_5O_{15(g)}$
6	$UMoO_{6(s)} \rightarrow UO_{2(s)} + 3/50\ Mo_3O_{9(g)} + 4/50\ Mo_4O_{12(g)} + 5/50\ Mo_5O_{15(g)} + 1/2\ O_{2(g)}$
7	$UMoO_{6(s)} \rightarrow 1/3\ U_3O_{8(s)} + 3/50\ Mo_3O_{9(g)} + 4/50\ Mo_4O_{12(g)} + 5/50\ Mo_5O_{15(g)} + 1/6\ O_{2(g)}$
8	$UMoO_{6(s)} \rightarrow 1/4\ U_4O_{9(s)} + 3/50\ Mo_3O_{9(g)} + 4/50\ Mo_4O_{12(g)} + 5/50\ Mo_5O_{15(g)} + 3/8\ O_{2(g)}$
9	$UMoO_{6(s)} \rightarrow 1/3\ U_3O_{8(s)} + 0.1666642\ O_{2(g)} + 0.15513164\ Mo_4O_{12(g)} + 0.06684396\ Mo_3O_{9(g)} + 0.0357654\ Mo_5O_{15(g)}$
10	$UMoO_{6(s)} \rightarrow 1/3\ U_3O_{8(s)} + 0.99349\ MoO_{3(l)} + 0.166664\ O_{2(g)} + 0.001011601\ Mo_3O_{9(g)} + 0.000790136\ Mo_4O_{12(g)} + 0.000061306\ Mo_5O_{15(g)} + 0.000002564\ Mo_2O_{6(g)}$

$\Delta H^o_{\text{f, 298 K}}$ of $UMoO_6$ was determined for all ten of the Table 22 reactions. $\Delta H^o_{\text{decomp}}$ = 82 ± 10 kJ mol^{-1} and T_{decomp} = 1205 ± 10 K were used for all calculations. Two

sets of literature values were used, the pre-existing RMC-TFM [19] and Cordfunke *et al.* [157]. Both the literature piecewise $C_p(T)$ function and the experimentally determined $C_p(T)$ of this thesis were used for a total of four $\Delta H^o_{f, 298 K}$ of $UMoO_6$ values for each decomposition reaction. The results are presented in Table 23.

Table 23: $\Delta H^o_{f, 298 K}$ of $UMoO_6$ using RMC-TFM or Cordfunke *et al.* [157] literature values and the literature piecewise $C_p(T)$ function or this thesis $C_p(T)$ function

Rxn #	$\Delta H^o_{f, 298 K}$ (kJ mol^{-1}) RMC-TFM Literature Values This Thesis $C_p(T)$	$\Delta H^o_{f, 298 K}$ (kJ mol^{-1}) RMC-TFM Literature Values Literature $C_p(T)$	$\Delta H^o_{f, 298 K}$ (kJ mol^{-1}) Cordfunke Literature Values This Thesis $C_p(T)$	$\Delta H^o_{f, 298 K}$ (kJ mol^{-1}) Cordfunke Literature Values Literature $C_p(T)$
1	-1697 ±42	-1672 ±34	-1708 ± 41	-1683 ± 33
2	-950 ± 42	-924 ± 34	-1428 ± 42	-1402 ± 34
3	-1663 ± 41	-1638 ± 33	-1672 ± 40	-1646 ± 32
4	-1596 ± 41	-1570 ± 33	-1611 ± 41	-1585 ± 33
5	-1981 ± 31	-1955 ± 23	-1978 ± 31	-1952 ± 23
6	-1233 ± 31	-1207 ± 23	-1697 ± 31	-1671 ± 23
7	-1946 ± 30	-1921 ± 22	-1941 ± 30	-1916 ± 22
8	-1879 ± 30	-1854 ± 21	-1880 ± 31	-1855 ± 23
9	-1949 ± 31	-1924 ± 22	-1943 ± 31	-1918 ± 23
10	-1998 ± 21	**-1972 ± 13**	-1992 ± 21	-1967 ± 13

Four factors are used to determine the error associated with $\Delta H^o_{f, 298 K}$ for $UMoO_6$, the experimental ΔH^o_{decomp} error, the error of each literature thermodynamic datum of the products ($\Delta H^o_{f, 298 K}$ and C_p), and the error of the $C_p(T)$ function used for $UMoO_6$. The $\Delta H^o_{f, 298 K}$ of $UMoO_6$ values calculated using the literature piecewise $C_p(T)$ function have lower errors as the literature piecewise $C_p(T)$ function has a lower error than the $C_p(T)$ determined experimentally by this thesis.

The $\Delta H^o_{f, 298 K}$ for $UMoO_6$ selected was -1972 ± 13 kJ mol^{-1}. It was calculated using decomposition reaction 10 (predicted by the RMC-TFM), RMC-TFM literature values, and the literature piecewise $C_p(T)$ function. It was selected for four reasons.

1) The thermodynamic data of the RMC-TFM are slightly more current than that of Cordfunke *et al.*

2) The literature piecewise $C_p(T)$ function, as explained in Section 4.2.1, is more precise at the T_{decomp} than the $C_p(T)$ function determined by this thesis.

3) Reaction 10 is in line with experimental observations and is based upon thermodynamic data already in the model, allowing easy integration. Reactions 1-4 do not account for polymeric MoO_3 gas species, reactions 5-8 have a rigid decomposition ratio for the MoO_3 gas species, and reaction 9 does not allow for liquids to form.

4) The value of -1972 $\pm$ 13 kJ mol^{-1} compares well with that of Tripathi *et al.* [61] -1975.2 $\pm$ 12.39 kJ mol^{-1} and Suleimanov *et al.* [54] -1985 $\pm$ 8 kJ mol^{-1}.

This thesis produced a $C_p(T)$ function and a $\Delta H^o_{f, 298 K}$ for $UMoO_6$, but other literature values exist as well. The final selection of thermodynamic values to be added to the $UMoO_6$ data file of the RMC-TFM is made in Section 4.4 using the UO_3-MoO_3 binary phase diagram to justify these decisions.

4.4 Selection of Thermodynamic Data for $UMoO_6$ in the RMC-TFM

As literature $UMoO_6$ thermodynamic data also exists, a selection had to be made as to which data to include for $UMoO_6$ in the RMC-TFM. The selection was based on the assessment of the UO_3-MoO_3 binary phase diagram. While many binary and ternary phase diagrams exist for the U-Mo-O chemical system [22], [45], [46], [67], the UO_3-MoO_3 phase diagram was most applicable when assessing the effects of $UMoO_6$. In this diagram, $UMoO_6$ forms, has an easily identifiable T_{decomp}, and experimental data for this system exist in the literature.

To summarize $UMoO_6$ thermodynamic values from both this thesis and the literature, Table 5 lists the possible thermodynamic values of $\Delta H^o_{f, 298 K}$, S^o_f, and $C_p(298.15 K)$ to be included for $UMoO_6$ in the RMC-TFM. Recall from Section 2.4 that these three thermodynamic values complete the necessary information for a single species entry in FACTSage, the program currently used for the RMC-TFM.

Table 24: Comparison of this thesis and literature thermodynamic values for UMoO$_6$

Source	$\Delta H^o_{f,\,298\,K}$ (kJ mol^{-1})	C_p (298.15 K) (J mol^{-1} K^{-1})	$S^o_{f,\,298\,K}$ (J K^{-1} mol^{-1})
This Thesis	-1972 ± 13	157.21 ± 7.86	-
Dash (Tripathi [61])	-1975.2 ± 12.39	-	216.3 ± 12.39
Dash (Dharwadkar [24])	-2105.8 ± 12.39	-	202.9 ± 12.39
Dash [23]	-1989.6 (calc.)	155.60 ± 2.80	-
Suleimanov [54]	-1985 ± 8	161.71 ± 0.32	192.8 ± 0.8
Ab-initio [65]	-1845.6 (calc.)	163.12 (calc.)	193.9

*Note: $\Delta H^o_{f,\,298\,K}$ and $S^o_{f,\,298\,K}$ of Dharwadkar and Tripathi were determined from their $\Delta G^o_{f,\,298\,K}$ by Dash using his C_p (Section 2.3.2)

Recall from Section 2.3.3 that Ustinov *et al.* [56] investigated the UO$_3$-MoO$_3$ system by observing the thermal effects and P-XRD of heating mixtures of U$_3$O$_8$ and MoO$_3$ in air. Figure 15 has been replicated from Section 2.3.3 below. They assumed the U$_3$O$_8$ fully oxidized to UO$_3$, however U$_3$O$_8$ was discovered in some of the final samples by P-XRD. Ustinov assumed their results were accurate for the UO$_3$-MoO$_3$ system and no longer considered U$_3$O$_8$, but the U$_3$O$_8$ contaminant may be significant. Ustinov discovered that a eutectic forms over the MoO$_{3(s)}$+UMoO$_{6(s)}$ region and a peritectic or small eutectic forms over the UO$_{3(s)}$+UMoO$_{6(s)}$ region. The Ustinov *et al.* [56] UO$_3$-MoO$_3$ binary phase diagram is reproduced in Figure 15 with the experimental data points shown in red. For these data points an error of ± 100 K is assumed because of the possible inaccuracies of the thermo-recorder experimental method from the 1970's and the U$_3$O$_8$ contamination. Ustinov's phase diagram was accepted and used by Dion [67] while investigating the Na-U-Mo-O system. However, few studies have been completed to confirm the UO$_3$-MoO$_3$ binary since.
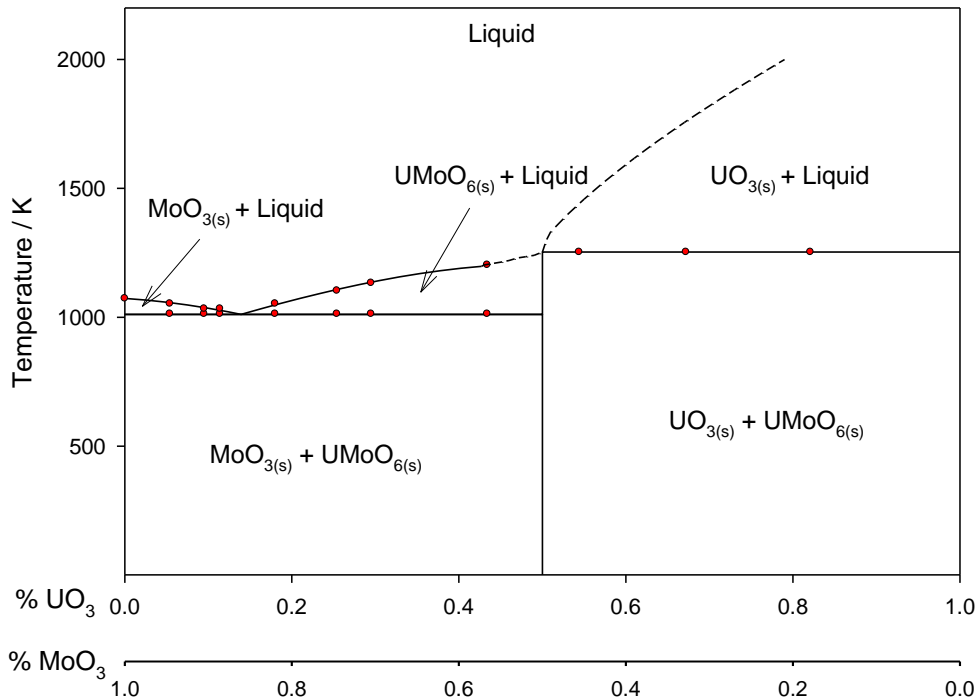
Figure 15: Ustinov _et al._ [56] UO₃-MoO₃ binary phase diagram with experimental data points shown with red dots (replicate of Figure 15 produced in Section 2.3.3)

As a starting point for comparison, the UO_3-MoO_3 phase diagram was calculated using data from the RMC-TFM after the three mode updates by Corcoran [19]. It originally used literature data similar to Dharwadkar _et al._ [24] ($\Delta H^o_{f, 298 K}$ = -2105.0952 kJ mol^{-1} and $S^o_{f, 298 K}$ = 206.179 J K^{-1} mol^{-1}), the Dash _et al._ [23] $C_p(T)$ function, and a constant excess mixing parameter ($UO_{3(l)}$-$MoO_{3(l)}$) of -218 500 J. These values were selected to cause the formation of $UMoO_6$ at the oxidizing condition for the CT experiments, thus bringing the RMC-TFM into alignment with CT results by increasing the number of moles of oxygen absorbed by the sample.

However, the use of Dharwadkar _et al._'s $\Delta H^o_{f, 298 K}$ may not have been the best choice, discounted by Dash _et al._ [23] because it differed from other experimental measurements (-1975 ± 12 kJ mol^{-1}) and theoretical calculations (-1989.6 kJ mol-1), Table 24. Further, the original model produced a very high T_{decomp} of 2190 K. The eutectic that forms over the $UO_{3(s)}$+$UMoO_{6(s)}$ region is too UO_3-rich with respect the experimental findings of Ustinov _et al._ [56] (_i.e._, first

liquid at $X_{UO_3} \cong 0.7$ vs. $X_{UO_3} \cong 0.5$). Finally, the $UO_{3(s)}$ liquidus line is at 2067 K compared to the 1253 K line of Ustinov *et al.* [56].
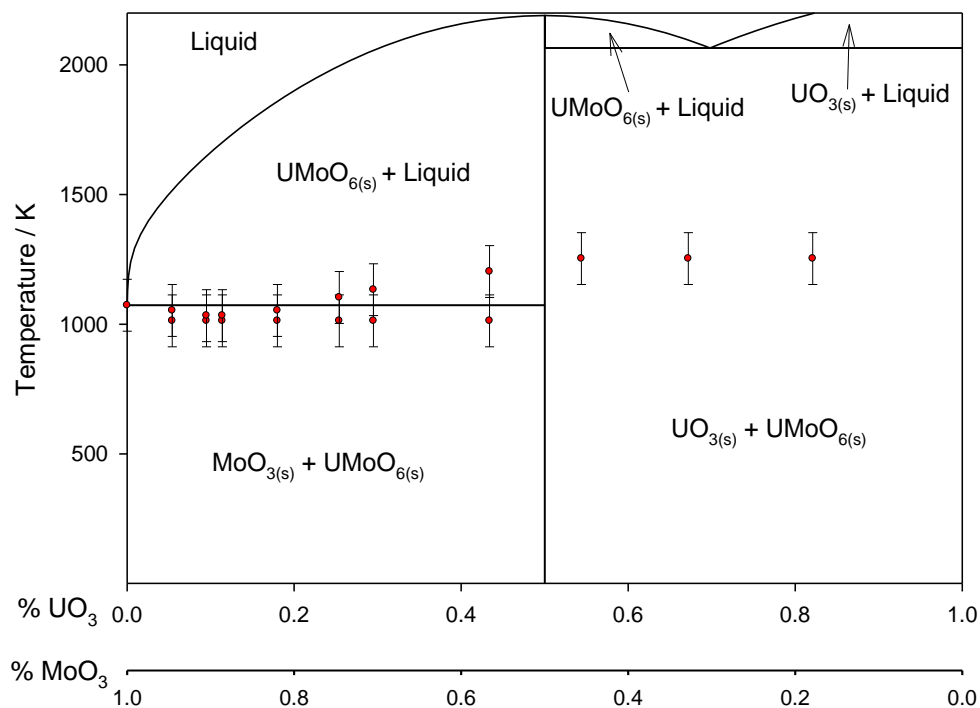
Figure 55: UO_3-MoO_3 phase diagram calculated using RMC-TFM data after the three mode updates by Corcoran [19] with Ustinov *et al.* [56] experimental data points shown in red

As suggested by Corcoran [19], additional experimental data on $UMoO_6$ and re-assessment of the UO_3-MoO_3 diagram was necessary (as clearly evident in a comparison between Figures 15 and 55). Recall from Section 2.4, updating the $UMoO_6$ compound file requires $\Delta H^o_{f, 298 K}$, $S^o_{f, 298 K}$, and $C_p(T)$ functions. Additionally, the UO_3-MoO_3 solution file requires fitting such that $UMoO_6$ decomposes at the T_{decomp} determined by this thesis (1205 ± 10 K) and the $MoO_{3(s)}$ liquidus line forms at 1013 K, as determined by Ustinov *et al* [56].

Recall in Section 4.2.1 that the literature piecewise $C_p(T)$ function was selected as the best representation for $UMoO_6$ (Table 19). While the $C_p(T)$ function produced through this thesis is close in agreement at lower temperatures, the literature piecewise $C_p(T)$ function provides a larger valid temperature range. Also, the

literature piecewise $C_p(T)$ function is based on experimental data, unlike the calculated *ab-initio* $C_p(T)$ function. As a result, the literature piecewise $C_p(T)$ function was selected for inclusion in the RMC-TFM.

Table 24 lists several $S^o_{f, 298 K}$ that could be included in the RMC-TFM. $S^o_{f, 298 K}$ is found by integrating the $C_p(T)$ function over temperature from 0-298 K (Equation 19). The Dash *et al.* [23] $C_p(T)$ function is valid for the temperature range 299-1000 K and has to be extrapolated to lower temperatures in order to determine $S^o_{f, 298 K}$. The *ab-initio* calculations are valid in the temperature range 0-298 K and beyond, but are not bound by the condition of $C_p = 0$ J K^{-1} mol^{-1} when $T = 0$. The Suleimanov *et al.* [54] $C_p(T)$ function is valid for the temperature range 6.6-300 K and is bound by this condition. While the two $S^o_{f, 298 K}$ values determined by low temperature $C_p(T)$ functions are in close agreement (*ab-initio* of 193.90 J K^{-1} mol^{-1} and Suleimanov *et al.* of 192.8 ± 0.8 J K^{-1} mol^{-1}), the Suleimanov *et al.* value is selected for inclusion in the RMC-TFM because it is bound by the condition $C_p = 0$ J K^{-1} mol^{-1} when $T = 0$ and is based on experimental data rather than a calculated estimate.

With a $S^o_{f, 298 K}$ and $C_p(T)$ function selected, only a $\Delta H^o_{f, 298 K}$ was required to completely update the $UMoO_6$ compound in the RMC-TFM. In Table 5, the Dharwadkar *et al.* [24] value of -2105.8 ± 12.39 kJ mol^{-1} was determined by Dash *et al.* [23] to be too low and was discarded. Similarly, the value determined by *ab-initio* calculations, -1845.639 kJ mol^{-1}, is too high. As the majority of the $\Delta H^o_{f, 298 K}$ values lie between -1972 and -1989.6 kJ mol^{-1}, the true value was assumed to be in this region.

Figure 10 is the UO_3-MoO_3 phase diagram calculated from $\Delta H^o_{f, 298 K} = -1972$ kJ mol^{-1}, $S^o_{f, 298 K} = 192.8$ J K^{-1} mol^{-1}, and the literature piecewise $C_p(T)$ function. A two term excess mixing parameter ($UO_{3(l)}$-$MoO_{3(l)}$) of $-397925+225T$(K) J causes $UMoO_6$ to decompose at the T_{decomp} determined by this thesis (1205 ± 10K) and the $MoO_{3(s)}$ liquidus line to form at 1013 K, as determined by Ustinov [56].
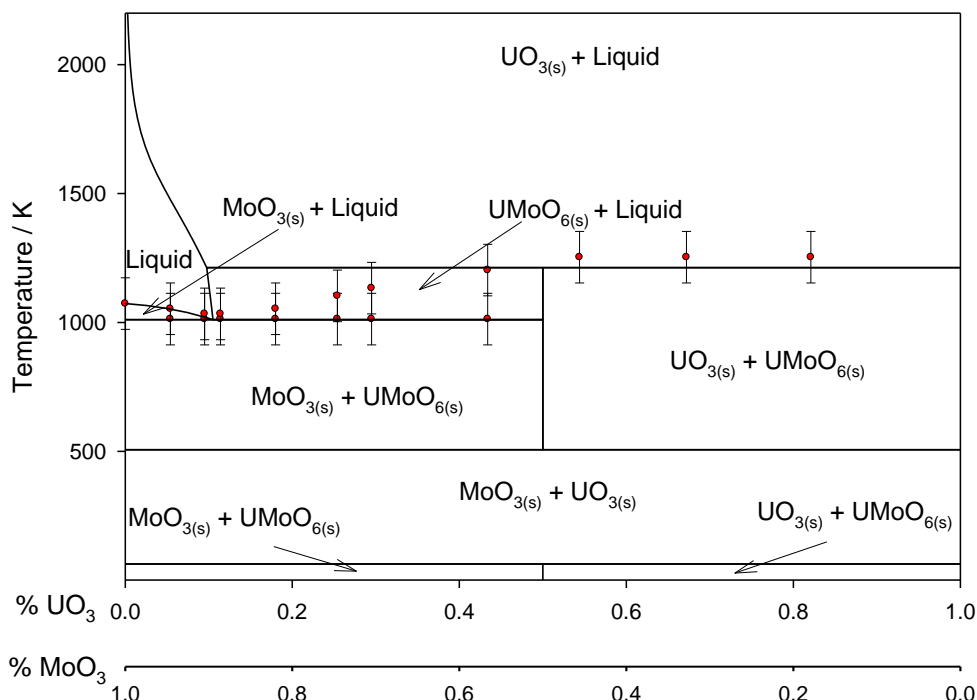
Figure 56: UO₃-MoO₃ phase diagram calculated using $\Delta H^o_{f, 298\ K}$ = -1972 kJ mol⁻¹, $S^o_{f, 298\ K}$ = 192.8 J K⁻¹ mol⁻¹, the literature piecewise $C_p(T)$ function, and an excess mixing parameter (UO₃₍l₎-MoO₃₍l₎) of -397925+225*T*(K) J with Ustinov *et al.* [56] experimental data points shown in red

This nonsensical diagram has a $UO_{3(s)}$ + $MoO_{3(s)}$ band, between 68 and 508 K, where $UMoO_{6(s)}$ does not form. This is a result of the large $\Delta H^o_{f, 298\ K}$ = -1972 kJ mol⁻¹ selected. The $\Delta H^o_{f, 298\ K}$ of $UMoO_6$ must be more negative in order to stabilize it from ambient conditions to the decomposition temperature. To determine a more appropriate $\Delta H^o_{f, 298\ K}$, the maximum activity (*a*) of $UMoO_6$ in the $UO_{3(s)}$ + $MoO_{3(s)}$ band was determined. Using Equation 47, it was determined that -5.6 kJ mol⁻¹ should be added to the $\Delta H^o_{f, 298\ K}$ to stabilize the compound. The $\Delta H^o_{f, 298\ K}$ was set to -1977.6 kJ mol⁻¹, the two term excess mixing parameter (UO₃₍l₎-MoO₃₍l₎) set to -225250+50*T*(K) J to cause $UMoO_6$ to decompose at the T_{decomp} determined by this thesis and $MoO_{3(s)}$ liquidus to form at 1013 K, and the results presented in Figure 57. Further, a $\Delta H^o_{f, 298\ K}$ value of -1977.6 kJ mol⁻¹ is reasonable as it lies between the experimentally obtained number of Tripathi *et al.* [61] (-1975.2 ± 12.39 kJ mol⁻¹) and Suleimanov *et al.* [54] (-1985 ± 8 kJ mol⁻¹).
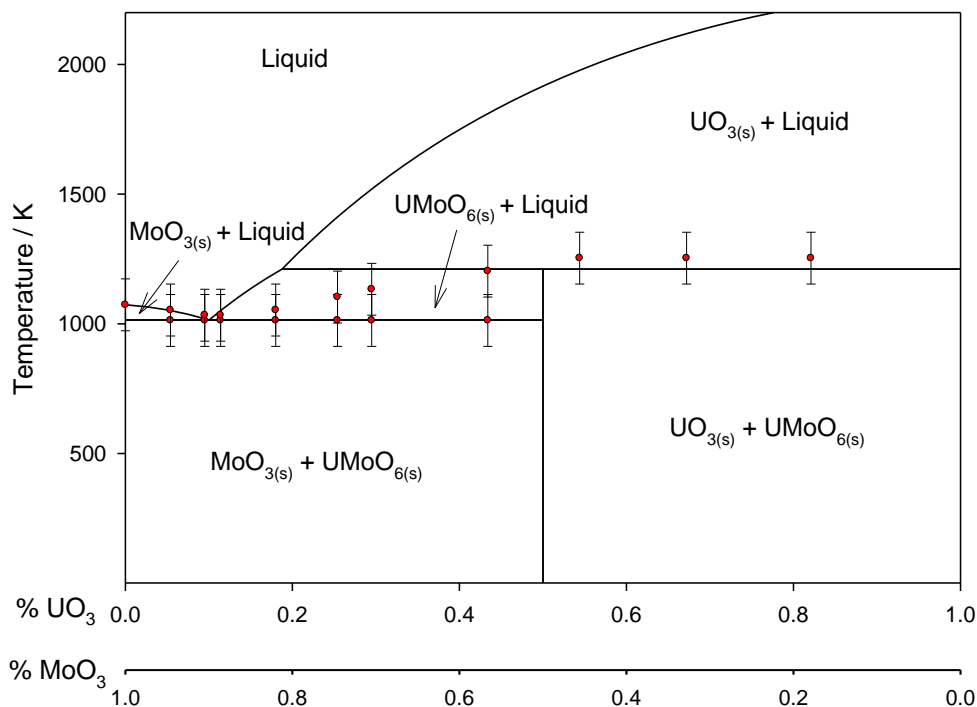
Figure 57: UO$_3$-MoO$_3$ phase diagram calculated using $\Delta H^o_{f, 298\ K}$ = -1977.6 kJ mol^{-1}, $S^o_{f, 298\ K}$ = 192.8 J K^{-1} mol^{-1}, the literature piecewise $C_p(T)$ function, and an excess mixing parameter (UO$_{3(l)}$-MoO$_{3(l)}$) of -225250+50T(K) J with Ustinov *et al.* [56] experimental data points shown in red

Figure 57 respects the experimental findings of Ustinov *et al.* [56]. Both the liquidus lines for UO$_{3(s)}$ and MoO$_{3(s)}$ are within experimental error. The eutectic over the MoO$_3$-rich region forms at 10.2 % UO$_3$, in line with Ustinov *et al,*, and the melting point of pure MoO$_3$ is also well-matched. The UMoO$_6$-Liquid region of the eutectic does not agree well with Ustinov *et al.*, however, this may be explained by the exclusion of the gaseous species in this phase diagram and by Ustinov *et al.* assuming U$_3$O$_8$ fully oxidized to UO$_3$. The disagreement coincides with greater UO$_3$ content. Ultimately, the values in Table 25 were the ones selected for inclusion in the RMC-TFM.

Table 25: Thermodynamic values selected for the $UMoO_6$ data file in the RMC-TFM

Variable	Source	Value
$\Delta H^o_{f, 298\ K}$	This thesis	-1977.6 kJ mol^{-1}
$S^o_{f, 298\ K}$	Suleimanov [54]	198.2 J K^{-1} mol^{-1}
$C_p(T)$	Dash [23] and Suleimanov [54]	see Table 19
Excess parameter ($UO_{3(l)}$-$MoO_{3(l)}$)	This thesis	-225250+50T(K) J

Table 26 lists the invariant points of interest between the UO_3-MoO_3 phase diagram determined by this thesis (Figure 57) and the literature. A comparison of T_{decomp} has already been described in Section 4.2.4. The temperatures of both the reaction of (1) $UMoO_{6(s)}$ + $MoO_{3(s)}$ $\rightarrow$ liquid; and (2) $UMoO_{6(s)}$ +$UO_{3(s)}$ $\rightarrow$ $UO_{3(s)}$ + liquid are lower in the phase diagram determined by this thesis than that of Ustinov *et al.* [56], but within the uncertainty range. This may be explained by the U_3O_8 contamination and a likely inaccurate thermo-recorder method from the 1970's.

Table 26: Invariant Points of Interest

Invariant Reaction	Temperature (K)	As depicted in Figure 57 (K)
$UMoO_{6(s)}$ +$MoO_{3(s)}$ $\rightarrow$ liquid	1013 ± 100 Ustinov [56]	1013
$UMoO_{6(s)}$ +$UO_{3(s)}$ $\rightarrow$ $UO_{3(s)}$ + liquid	1253 ± 100 Ustinov [56]	1205
$UMoO_{6(s)}$ $\rightarrow$ liquid	1253 ± 10 Ustinov [56]	1205
	1212 ± 2 Suleimanov [54]	
	1283 Serezhkin [53]	
	1205 ± 10 [this thesis]	

Ustinov *et al.* [56] only considered condensed phases (*i.e.,* liquids and solids) in his UO_3-MoO_3 phase diagram. As a result, it does not respect the U-O binary phase diagram along the line $X_O = 0.75$ (*i.e.*, UO_3) or the Mo-O binary along the line $X_O = 0.75$. As gas is not considered, U_3O_8 and MoO_2 do not form in this diagram as they are known to form in the U-O and Mo-O binary phase diagrams. In order to form U_3O_8 and MoO_2, gaseous species need to be considered.

Currently, no open source thermodynamic literature exists on the gas mixture of the UO_3-MoO_3 phase diagram. Figure 58 was constructed using the thermodynamic data from Table 25 and assumed ideal mixing of the metal and oxide gaseous species of U, Mo, and O, which include the polymeric MoO_3 gas species in the RMC-TFM.

This preliminary phase diagram below does not include any ternary U-Mo-O gaseous species as no data exists. As such, Figure 58 is only a preliminary assessment to guide further experimental work. This figure should not be considered valid as further experiments and thermodynamic assessment are required. However, the $X_{MoO_3} = 1$ line respects the $X_O = 0.75$ line of the Mo-O phase diagram and the $X_{UO_3} = 1$ line respects the $X_O = 0.75$ line of the U-O phase diagram.
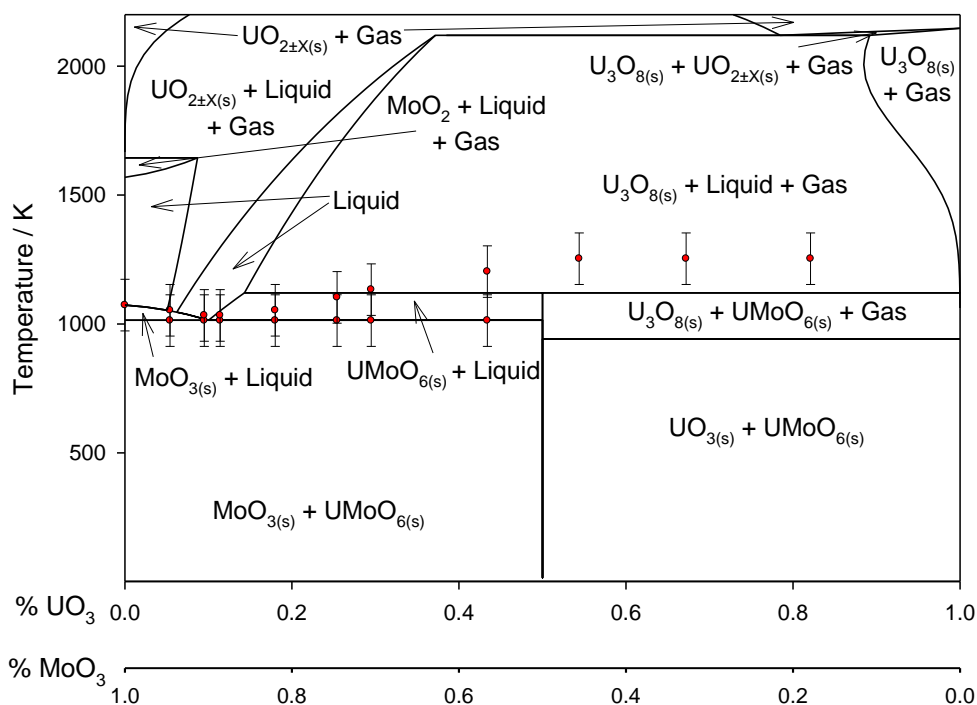
Figure 58: UO_3-MoO_3 phase diagram calculated from the values in Table 25 and gases added and Ustinov *et al.* [56] experimental data points shown in red

4.5   Effect on the RMC-TFM Prediction of the CT Experiments

Recall from Section 2.5.2 that CT experiments were completed to benchmark the RMC-TFM with three samples (UO_2, SIMFUEL 1, and SIMFUEL 2). Initially, the RMC-TFM predicted oxidation well for UO_2, but under-predicted for SIMFUEL samples. The SIMFUEL 1 samples had a large Mo content (approximately 900 ppm) and the SIMFUEL 2 samples had a lower Mo content (approximately 180 ppm). Three correction modes were applied that brought the model in line with experimental results. These modes were all focused on molybdenum because of its ability to buffer oxygen. Ultimately, thermodynamic properties for $UMoO_6$ were selected to force its formation for the oxidation conditions of the CT experiments. The thermodynamic properties selected by Corcoran [19] were within published uncertainty ranges, but she recommended further studies be completed to assess $UMoO_6$ and the UO_3-MoO_3 phase diagram.

This thesis completed the assessment on $UMoO_6$ and found thermodynamic properties that made it less stable than the values used by Corcoran [19]. Table 27 lists the $\Delta G^o_{f, 298 K}$ of $UMoO_6$ as calculated using the $\Delta H^o_{f, 298 K}$ and $S^o_{f, 298 K}$ data from the RMC-TFM both before and after this thesis update. As $\Delta G^o_{f, 298 K}$ is a measure of formation stability, the increased $\Delta G^o_{f, 298 K}$ suggested by this thesis indicates that the $UMoO_6$ species is less stable than previously suggested.

Table 27: Thermodynamic values for $UMoO_6$ in various RMC-TFM versions

Update	$\Delta H^o_{f, 298 K}$ (kJ mol^{-1})	$S^o_{f, 298 K}$ (J K^{-1} mol^{-1})	$\Delta G^o_{f, 298 K}$ (kJ mol^{-1})
Before ([19])	-2105.0952	206.179	-2167
After (this thesis)	-1977.6	198.2	-2037

As a result of this decrease in $UMoO_6$ stability, the model now predicts $UMoO_6$ does not form under the oxidation conditions of the CT experiment. This corresponds to a decrease in oxygen absorption, affecting the SIMFUEL 1 samples, Table 28. The UO_2 and SIMFUEL 2 samples remain unchanged, as the model before this thesis update also predicted $UMoO_6$ would not form under these conditions.

Table 28: CT Experiments and Predictions[*]

Sample	Temperature (K)	Measured O_2 Absorption (μmol)	Predicted O_2 Absorption Before This Thesis Update (μmol)	Predicted O_2 Absorption After This Thesis Update (μm)
UO_2	1273.15	19 ± 2	18.2 ± 0.8	18.2 ± 0.8
SIMFUEL 1	1173.15	44 ± 6	41.3 ± 0.5	27.2 ± 0.5
SIMFUEL 1	1273.15	56 ± 10	51.1 ± 0.8	37.1 ± 0.8
SIMFUEL 2	1173.15	40 ± 8	38.6 ± 0.4	38.6 ± 0.4
SIMFUEL 2	1273.15	46 ± 15	46.4 ± 0.7	46.4 ± 0.7

[*]Note: Values listed are not an exact match to Table 8 as FACTSage [25] was used verse FACT [158] in Ref [19] and the database has been modified by other assessments completed at the RMC

The updated RMC-TFM predicts the correct oxygen absorption for UO_2 and SIMFUEL 2 samples, but under-predicts for SIMFUEL 1 samples. This thesis suggests $UMoO_6$ does not cause the oxygen absorption for the SIMFUEL 1 samples. However, it is likely another or multiple other U-Mo-O ternary compounds are forming and causing the increase in oxygen acquisition. For example, Chattopadhyay *et al*. [46] proposed a ternary diagram at 1000 K that showed the coexistence of six solid ternary oxide compounds ($UMoO_6$, $UMoO_5$, U_2MoO_8, UMo_2O_8, UMo_7O_{22}, and $UMo_{10}O_{32}$). Corcoran [19] did not include the other ternary oxide compounds as no data for $\Delta H^o_{f, 298 K}$, $S^o_{f, 298 K}$ and C_p exist in the literature.

It is suggested that other ternary oxides be investigated in the same manner as $UMoO_6$ in this thesis. Also, as the data provided by *ab-initio* calculations for $UMoO_6$ were close to experimental data of this thesis and of other studies, it is suggested that *ab-initio* studies be completed for $UMoO_5$ [45], U_2MoO_8 [45], UMo_2O_8 [45], UMo_7O_{22} [46], and $UMo_{10}O_{32}$ [46], if no experimental studies are possible.

4.6 <u>Summary</u>

The objective of this thesis was achieved as the RMC-TFM was improved by refining our understanding of $UMoO_6$ and the UO_3-MoO_3 phase diagram. This was accomplished by completing the five sub-tasks listed in Section 1.4. A novel, aqueous synthesis method was developed to produce high purity $UMoO_6$, free of

U-oxide and Mo-oxide reactants and other impurities. The three step process produced high purity $UMoO_6$ validated by a series of characterization methods. Thermodynamic properties of the newly synthesized $UMoO_6$ were collected including a $C_p(T)$ function (J K^{-1} mol^{-1}) of $223.0844 - 0.1945T$(K) $+ 2.2965 \times 10^{-4}T^2$(K) $- 2.515493 \times 10^6 T^{-2}$(K) with an associated error of ± 5 % over a temperature range of 343-668 K, a ΔH^o_{trans} of -32 ± 3 kJ mol^{-1} at 734 ± 32 K, a ΔH^o_{decomp} of 82 ± 10 kJ mol^{-1}, and a T_{decomp} of 1205 ± 10 K.

The experimental values of ΔH^o_{decomp} and T_{decomp}, the literature piecewise $C_p(T)$ function, and a decomposition reaction based on experimental observations were used to calculate the $UMoO_6$ $\Delta H^o_{f, 298\,K}$ of -1972 ± 13 kJ mol^{-1}. The selection of $UMoO_6$ thermodynamic data for inclusion in the RMC-TFM was made through the assessment of the UO_3-MoO_3 phase diagram.

A new assessment of the CT experiments with the updated $UMoO_6$ compound from this thesis was completed and it was determined $UMoO_6$ does not form under the oxidizing conditions of the CT experiments. Therefore, the updated version of the RMC-TFM under-predicts SIMFUEL 1 oxygen absorption.

Future work is required to investigate other potential U-Mo-O ternary oxides that could account for the SIMFUEL 1 oxygen absorption. The refinement of our understanding of the $UMoO_6$ compound and the UO_3-MoO_3 phase diagram achieved by this thesis is significant, but future work is required. Suggested activities to improve the RMC-TFM are outlined in Section 5.

5.　　　　　　Recommendations for Future Work

Due to time constraints and equipment limitations and availability, some work was unable to be completed and is recommended for consideration in the future. The C_p of $UMoO_6$ could be determined by other methods described below. The UO_3-MoO_3 binary phase diagrams can be refined by revisiting the work of Ustinov *et al.* [56] using modern methods, completing enthalpy of mixing experiments, and investigating the gaseous phases of this diagram. The phase diagram investigation can be expanded to include binary and ternary phases. The investigation into other U-Mo-O ternary oxides could be made to account for the under-prediction of oxidation in the SIMFUEL 1 samples of the CT experiments. Finally, MoO_2 non-stoichiometry can be further investigated and a full set of recommendations is listed in Appendix A.

In Section 4.2.1, it was shown that the ASTM E1269-11 [77] method conducted using the experimental setup at the RMC produced a departure from literature C_p of $UMoO_6$ at high temperatures. It is recommended to repeat the C_p of $UMoO_6$ using a different C_p determining method. Calorimetry is recommended and a variety of methods could prove suitable. Heat pulse calorimetry applies a known quantity of heat in the form of a pulse and the corresponding temperature change is measured as described in [159]. Relaxation calorimetry relates the thermal conductance of the link between the platform and thermal reservoir in the experimental setup with relation time, described in [160]. The dual slope method in calorimetry directly compares heating and cooling rates without needing to measure the thermal conductance between the sample and the bath [161]. Alternating current calorimetry measures oscillations in heat capacity with oscillations in heating [162]. In addition to these calorimetry methods, the method used by Dash *et al*. [23] could be repeated to ensure consistency where enthalpy increments are measured, a function is fit to the data, and the first derivative is taken to produce the $C_p(T)$ function [155]. A different $C_p(T)$ function will have a significant effect on the model as C_p affects the temperature-dependence of $\Delta H^o_{f, 298 K}$ and $S^o_{f, 298 K}$.

The UO_3-MoO_3 binary phase diagram could be further refined. This would start with repeating the work of Ustinov *et al*. [56] using modern equipment. Monitoring the thermal events of UO_3-MoO_3 mixtures with modern DSC or DTA would provide less uncertainty in the temperature measurements and would confirm or deny Ustinov's assumption of U_3O_8 fully oxidizing to UO_3 in air. Next, enthalpy of mixing experiments between UO_3 and MoO_3 liquids could be completed by the

process described in [163]. This data and the T_{decomp} of $UMoO_6$ could be used to fit a more robust excess mixing function for the UO_3-MoO_3 solution file. Finally, the gas phase for the UO_3-MoO_3 phase diagram could be better refined by using a Knudsen or effusion cell to collect better thermodynamic information on U and Mo gas species [164]. Their excess mixing parameters could also be better refined than assuming ideal mixing. Together, the work described above would provide a stronger and more complete UO_3-MoO_3 binary phase diagram.

The investigation of phase diagrams could be expanded to include other binary and ternary diagrams. $UMoO_6$ could form in other U-oxide Mo-oxide binary phase diagrams and affect their results. Dion *et al.* [67] studied the ternary MoO_3-UO_3-Na_2O system. The modified UO_3-MoO_3 binary phase diagram produced from this thesis would impact the MoO_3-UO_3-Na_2O ternary phase diagram. This effect and other ternary systems could be further investigated.

To account for the under-prediction of SIMFUEL 1 samples in the CT experiments, other U-Mo-O ternary oxides could be investigated using the same methods conducted in this thesis for $UMoO_6$. It is possible that other U-Mo-O ternary oxides are forming, such as $UMoO_5$ [45], U_2MoO_8 [45], UMo_2O_8 [45], UMo_7O_{22} [46], and $UMo_{10}O_{32}$ [46], among others.

Finally, the investigation into the non-stoichiometry of MoO_2 was not very fruitful and should be investigated further. The work completed on this system in this thesis is outlined in Appendix A in which a complete list of future recommendations is outlined.

6.   Conclusions

This thesis improved the RMC-TFM by refining our understanding of $UMoO_6$ and the UO_3-MoO_3 phase diagram. The following contributions were made:

- A novel, aqueous synthesis method was developed to produce high purity $UMoO_6$, free of U-oxide and Mo-oxide reactants and other impurities;
- A $C_p(T)$ function (J K^{-1} mol^{-1}) of $223.0844 – 0.1945T(K) + 2.2965 \times 10^{-4}T^2(K) – 2.515493 \times 10^6 T^{-2}(K)$ with an associated error of ± 5 % over a temperature range of 343-668 K was determined;
- A ΔH^o_{trans} of -32 ± 3 kJ mol^{-1} at 734 ± 32 K was determined and this *meta*-stable form of $UMoO_6$ added to the RMC-TFM;
- A ΔH^o_{decomp} of 82 ± 10 kJ mol^{-1} at a T_{decomp} of 1205 ± 10 K was determined;
- The $\Delta H^o_{f, 298 K, UMoO_6}$ was calculated to be -1972 ± 13 kJ mol^{-1};
- The UO_3-MoO_3 phase diagram was used to refine and select the thermodynamic values for inclusion in the RMC-TFM; and
- A list of future recommendations was made to improve the RMC-TFM moving forward

References

[1]   http://www.world-nuclear.org/info/Country-Profiles/Countries-A-F/Canada--Nuclear-Power/ Last accessed: 1 June 2015.

[2]   P. Van Uffelen, R.J.M. Konings, C. Vitanza, and J. Tulenko, "Analysis of Reactor Fuel Rod Behavior", Handbook of Nuclear Engineering, Springer Science and Business Media, New York (2010) 1519-1627.

[3]   P.E. Potter, "High Temperature Chemistry for the Analyses of Accidents in Nuclear Reactors", IUPAC Pure and Applied Chemistry, Vol. 60 (1988) 323-340.

[4]   R.D. MacDonald, M.R. Floyd, B.J. Lewis, A.M. Manzer, and P.T. Truant, "Detecting, Locating and Identifying Failed Fuel in Canadian Power Reactors," AECL-9714, Atomic Energy of Canada Limited (1990).

[5]   J.D. Higgs, B.J. Lewis, W.T. Thompson, and Z. He, "A Conceptual Model for the Fuel Oxidation of Defective Fuel", Journal of Nuclear Materials, Vol. 366 (2007) 99-128.

[6]   B.J. Lewis, R.D. MacDonald, N.V. Ivanoff, and F.C. Iglesias, "Fuel Performance and Fission Product Release Studies for Defective Fuel Elements", Nuclear Technology Vol. 103 (1993) 220-245.

[7]   D.D. Sood and S.K. Patil, "Chemistry of Nuclear Fuel Reprocessing: Current Status", Journal of Radioanalytical and Nuclear Chemistry, Vol. 203 (1996) 547-573.

[8]   D.R. Wiles, "The Chemistry of Nuclear Fuel Waste Disposal", Polytechnic International Press, Montreal, (2002).

[9]   B.J. Lewis, B. Szpunar, and F.C. Iglesias, "Fuel Oxidation and Thermal Conductivity Model for Operating Defective Fuel Rods", Journal of Nuclear Materials, Vol. 306 (2002) 30-43.

[10] El-Jaby, "A Model for Predicting Coolant Activity Behaviour for Fuel-Failure Monitoring Analysis", PhD Thesis, Royal Military College of Canada (2009).

[11] K. Shaheen, "A Semi-empirical Oxidation Model for Defective Nuclear Fuel", MASc Thesis, Royal Military College of Canada (2007).

[12] A. Prudil, B.J. Lewis, P.K. Chan, and J.J. Baschuk, "Development ans Testing of the FAST Fuel Performance Code: Normal Operating Conditions (Part 1)", Nuclear Engineering and Design, Vol. 282 (2015) 158-168.

[13] A. Prudil, B.J. Lewis, P.K. Chan, J.J. Baschuk, and D. Wowk, "Development and Testing of the FAST Fuel Performance Code: Transient Conditions (Part 2)", Nuclear Engineering and Design, Vol. 282 (2015) 169-177.

[14] B.J. Lewis, F.C. Iglesias, D.S. Cox, and E. Gheorghiu, "A Model for Fission-Gas Release and Fuel Oxidation Behaviour for Defective UO_2 Fuel Elements", Nuclear Technologies, Vol. 92 (1990) 353-362.

[15] G. Bruni, B.J. Lewis, and W.T. Thompson, "Framework Model for Hydrogen Redistribution in Zircaloy Sheathing", Journal of Nuclear Materials, Vol. 409 (2011) 33-39

[16] E. Ewart, K. Lassmann, H. Matzke, L. Manes, and A. Saunders, "Oxygen Potential Measurements in Irradiated Mixed Oxide Fuel", Journal of Nuclear Materials, Vol. 124 (1984) 44-55.

[17] University of California, Berkeley, "Chemistry of Defective Light Water Reactor Fuel", D.R. Olander, W. Wang, Y.S. Kim, C. Li, and K. Lim, Electric Power Research Institute Report TR-107074 (1997).

[18] J.D. Higgs, "Modelling Oxidation Behaviour in Operating Defective Nuclear Reactor Fuel Elements", PhD Thesis, Royal Military College of Canada (2006).

[19] E.C. Corcoran, "Thermochemical Modelling of Advanced CANDU Reactor Fuel", PhD Thesis, Royal Military College of Canada (2009).

[20] H. Kleykamp, "The Solubility of Selected Fission Products in UO_2 and $(U,Pu)O_2$", Journal of Nuclear Materials, Vol. 206 (1993) 82-86.

[21] S. Zador and C.B. Alcock, "Thermodynamic Study of $MoO_{2\pm x}$ with Small Deviation from Stoichiometry", Journal of Chemical Thermodynamics, Vol. 2 (1970) 9-16.

[22] L. Brewer, R.H. Lampreaux, "Mo-O Binary", Materials Research Division of Lawrence Berkeley Laboratory, Reprinted in the American Society of Materials, "Mo-O Phase Diagram", Bulletin of Alloy Phase Diagrams, Vol. 1&2, (1980) 85-89.

[23] S. Dash, K. Jayanthi, Z. Singh, N.D. Dahale, S. C. Parida, V.S. Iyer, "Calorimetric Studies on Uranium Molybdate", Journal of Alloys and Compounds, Vol. 296 (2000) 166-169.

[24] S. R. Dharwadkar, "Standard Free Energy of Formation of UMoO6 by Thermogravimetry" Journal of Material Science (1986) 1003-1006.

[25] http://www.factsage.com/ Last accessed: 1 June 2015.

[26] http://www.candu.com/site/media/Parent/EC6%20Technical%20Summary_2012-04.pdf Last accessed: 1 June 2015.

[27] http://www.cameco.com/common/images/content/u101/fuel_bundle.gif Last accessed: 1 June 2015.

[28] http://www.iaea.org/NuclearPower/Downloadable/aris/2013/4.ACR1000.pdf Last accessed: 1 June 2015.

[29] J.R. Lamarsh, "Introduction to Nuclear Engineering – 2nd Edition", Addison Wesley, Canada (1983).

[30] A.M. Weinberg, "Breeder Reactors", Scientific American (1959) 82-94.

[31] P. Chan, "Part 2 – Fuel Production", CCE 533 Lecture Notes, Royal Military College of Canada (2013) UNENE.

[32] http://www.doitpoms.ac.uk/tlplib/nuclear_materials/nuclear_processes.php

[33] E.C. Corcoran, B.J. Lewis, W.T. Thompson, J. Mouris, and Z. He, "Controlled Oxidation Experiments of Simulated Irradiated UO_2 Fuel in Relation to Thermochemical Modelling", Journal of Nuclear Materials, Vol. 414 (2011) 73-82.

[34] H. Kleykamp, "The Chemical State of the Fission Products in Oxide Fuels", Journal of Nuclear Materials, Vol. 131 (1985) 221-246.

[35] S. Wenhui, and A.M. Manzer, "Design and Performance of Fuel for Qinshan Phase III Nuclear Power Plant", China Journal of Nuclear Power Engineering, Vol. 20, Iss. 6, 1-17.

[36] W.J. Garland, "Fuel – Coolant Heat Transfer", McMaster University, Hamilton (2004).

[37] https://canteach.candu.org/Content%20Library/20032104.pdf Last accessed: 1 June 2015.

[38] Direct Liaising with Ernest Lu, Bruce Power, Ontario Power Generation.

[39] A.P.H. Peters, "Concise Chemical Thermodynamics", CRC Press, New York (2010).

[40] http://nptel.iitm.ac.in/courses/112103016/module1/lec1/2.html Last accessed: 1 June 2015.

[41] D.R. Gaskell, "Introduction to the Thermodynamics of Materials – Fifth Edition", Taylor and Francis Group, New York (2008).

[42] Franzen, "Lecture 13 – Gibbs Free Energy and Chemical Potential", Chemistry 433 Lecture Notes, NC State University, Winter 2013.

[43] http://www.chem1.com/acad/webtext/thermeq/TE4.html#FGAS Last accessed: 1 June 2015.

[44] A.D. Pelton, "Thermodynamics and Phase Diagrams of Materials", Centre de Recherche en Calcul Thermochimique, Wiley-VCH Verlag GmbH & Co., École Polytechnique, Montreal, Canada (2006).

[45] C. Miyake, M. Matsumura and K. Taniguchi, "Mutual Oxidation States of Uranium and Molybdenum in U-Mo-O Ternary Oxides", Journal of the Less-Common Metals, Vol. 163 (1990) 133-141.

[46] G. Chattopadhyay, S.N. Tripathi, and A.S. Kerkar, "Thermodynamic Investigations in the System U-Mo-O", Journal of the American Ceramic Society, Vol. 67 (1984) 610-614.

[47] S.R. Bharadwaj, M.S. Chandrasekharaiah, and S.R. Dharwadkar, "On the Solid State Synthesis of $UMoO_6$", Journal of Materials Science Letters, Vol. 6 (1984) 840-842.

[48] E.F. Juenke and S.F. Bartram, "Crystallographic Data on UO_2WO_4 and UO_2MoO_4", Acta Crystallographica, Vol 17 (1964) 618.

[49] M. Keskar, N.D. Dahale, and K. Krishnan, "Thermal Expansion Studies on $UMoO_5$, $UMoO_6$, $Na_2U(MoO_4)_3$ and $Na_4U(MoO_4)_4$", Journal of Nuclear Materials, Vol. 393 (2009) 328-332.

[50] L.M. Kovba, V.K. Trunov, and A.I. Grigor'ev, "Investigation of Anhydrous Uranyl Salts UO_2EO_4 (E = s, Cr, Mo, W)", Journal of Structural Chemistry, Vol. 6 (1965) 883-884.

[51] N.L. Misra, K.L. Chawla, V. Venugopal, N.C. Jayadevan, and D.D. Sood, "X-ray and Thermal Studies on Cs-U-Mo-O System", Journal of Nuclear Materials, Vol. 226 (1995) 120-127.

[52] T. Nagai, N. Sato, S. Kitawaki, A. Uehara, T. Fujii, H. Yamana, and M. Myochin, "Synthesis and Investigation of Uranyl Molybdate UO_2MoO_4", Journal of Nuclear Materials, Vol. 433 (2013) 397–403.

[53] V.N. Serezhkin, L.M. Kovba, and V.K. Trunov, "The Structure of UO_2MoO_4". Radiokhimiya, Vol. 13 (1971) 659.

[54] E.V. Suleimanov, A.V. Golubev, E.V. Alekseev, C.A. Geiger, W. Depmeier, and V.G. Krivovichev, "A Calorimetric and Thermodynamic Investigation of Uranyl Molybdate UO_2MoO_4", Journal of Chemical Thermodynamics, Vol. 42 (2010) 873–878.

[55] K. Swaminathan. N. Mallika and O. M. Sreedharan, "Oxygen Potential in the System $UMoO_6/UMoO_5$ by the Solid Oxide Electrolyte Emf Method", Journal of American Ceramics Society, Vol. 70 (1987) C-168-C-170.

[56] O.A. Ustinov, M.A. Andrianov, N.T. Chebotarev, and G.P. Novoselov, "The System MoO_3-UO_3", Soviet Atomic Energy, Vol. 34 (1973) 203-205.

[57] L. Northcott, "Metallurgy of the Rarer Metals: Molybdenum", Butterworths Scientific Publications, London, (1956) 157.

[58] B. Greenburg, "Bragg's Law with Refraction", Acta Crystallographica, Vol. A45 (1989) 238-241.

[59] A. Fedoseev, N. Budantseva, A. Yusov, and M. Grigor'ev, "New Molybdates of Hexavalent Actinides", Radiokhimiya, Vol. 5 (1990) 14-18.

[60] V.N. Serezhkin, L.M. Kovba, and V.K. Trunov, "Study of the System $UO_3-MoO_3-H_2O$." Radiokhimiya, Vol. 15 (1973) 282-285.

[61] S.N. Tripathi, G. Chattopadhyay, A.S. Kerkar, and M.S. Chandrasekharaiah, "Thermodynamic Stability of $UMoO_6$ by the Transpiration Method", Journal of the American Ceramic Society, Vol. 68 (1985) 232-235.

[62] M. Le Van, Bulletin de la Société Chimique de France, Vol. 2 (1972) 579.

[63] J. L. Fleche, "Thermodynamical functions for crystals with large unit cells such as zircon, coffinite, fluorapatite, and iodoapatite from calculations," Phys. Rev. B, Vol. 65 Iss. 24 (2002) 245-116.

[64] S. J. Clark, M. D. Segall, C. J. Pickard, P. J. Hasnip, M. I. J. Probert, K. Refson, and M. C. Payne, "First principles methods using CASTEP," Z. Für Krist., 220 5–6 (2005) 567–570.

[65] Private Communication, J.-L. Fletch to E.C. Corcoran, CEA-Saclay, 14 November 2014.

[66] D.R. Stull and H. Prophet, "JANAF Thermochemical Table," Second Edition, National Bureau of Standards (971).

[67] C. Dion and A. Noel, "Étude et Interprétation de la ligne UO_2MoO_4-Na_2MoO_4 dans le cadre du système UO_3-MoO_3-Na_2O", Bulletin de la Société Chimique de France, Vol. 9-10 (1981) I-371-I-376.

[68] P. Koukkari, "Introduction to Constrained Gibbs Energy Methods in Process and Materials Research", VTT Technology 160 (2014).

[69] F.C. Cambell, "Phase Diagrams: Understanding the Basics", The Materials Information Society, Ohio, (2012) 41-72.

[70] M. Zhao, L. Song, and X. Fan, "The Boundary Theory of Phase Diagrams and Its Application", Science Press Beijing, New York, (2011) 3-28.

[71] P.G. Lucuta, R.A. Verrall, H. Matzke, and B.J. Palmer, "Microstructural Features of SIMFUEL - Simulated High-Burnup UO_2-Based Nuclear Fuel", Journal of Nuclear Materials 178 (1991) 48-60.

[72] Private Communication, J. Mouris to E.C. Corcoran, AECL-CRL, March 2007.

[73] APEX Software Suite v.2012; Bruker AXS: Madison, WI (2005).

[74] R.H. Blessing, "An Empirical Correction for Absorption Anisotrophy", Acta Crystallographica, Vol. A51 (1995) 33-38.

[75] G.M. Sheldrick, "A Short History of SHELX", Acta Crystallographica, Vol. A64 (2008) 112-122.

[76] A.I. Vogel, "A Text-book of Quantitative Inorganic Analysis. Theory and Practice", Second Edition, Longmans Green and Co., Toronto (1951).

[77] ASTM E1269-11, "Standard Test Method for Determining Specific Heat Capacity by Differential Scanning Calorimetry"

[78] L.C. Thomas, "Interpreting Unexpected Events and Transitions in DSC Results", TA Instruments, TA039.

[79] T.M.V.R. de Barros, R.C. Santos, A.C. Fernandes, and M.E. Minas da Picdadc, "Accuracy and Precision of Heat Capacity Measurements Using a Heat Flux Differential Scanning Calorimeter", Thermochimica Acta, Vol. 269/270 (1995) 51-60.

[80] ASTM E2550-11, "Standard Test Method for Thermal Stability by Thermogravimetry"

[81] ASTM E1641-13, "Standard Test Method for Decomposition Kinetics by Thermogravimetry Using the Ozawa/Flynn/Wall Method"

[82] ASTM D3418-12, "Standard Test Method for Transition Temperatures and Enthalpies of Fusion and Crystallization of Polymers by Differential Scanning Calorimetry"

[83] ASTM E2160-04, "Standard Test Method for Heat of Reaction of Thermally Reactive Materials by Differential Scanning Calorimetry"

[84] Canadian Nuclear Safety Commission Radiation Safety Data Sheet, Uranium, revised 19 September 2011.

[85] N.V. Chukanov, "Infrared spectra of mineral species", Springer Geochemistry/Mineralogy, New York, 2014.

[86] http://www.ccp14.ac.uk/ccp/web-mirrors/powdcell/a_v/v_1/powder/e_cell.html

[87] ICDD Card 12-0773 - Unspecified reference

[88] ICDD Card 20-1130 - C.W.F.T. Pistorius, "Phase Diagrams od Sodium Tungstate and Sodium Molybdate to 45 kbar", Journal of Chemical Physics, Vol. 44 (1966) 4532-4537.

[89] ICDD Card 26-0966 - Technisch physische dienst 1974

[90] ICDD Card 26-0967 - Technisch physische dienst 1974

[91] ICDD Card 26-0968 - Technisch physische dienst 1974

[92] ICDD Card 27-0936 - P.T. Moseley and C.J. Seabrook, "Some Observations on the Isothermal Dehydration of Uranyl (VI) Nitrate Hexahydrate Above Room Temperature", Journal of the Chemical Society, Dalton Transactions, Vol. 10 (1973) 1115-1120.

[93] ICDD Card 04-0809 - H.E. Swanson and E. Tatge, "Standard X-ray Diffraction Patterns", National Bureau of Standards Circular, Vol. 539, 1 (1953).

[94] ICDD Card 42-1120 - Unspecified reference

[95] ICDD Card 32-0671 - Unspecified reference

[96] ICDD Card 05-0508 - H.E. Swanson, R.K. Fuyat and G.M. Ugrinic, "Standard X-ray Diffraction Patterns", National Bureau of Standards Circular, Vol. 539, Vol. 3 (1954).

[97] ICDD Card 09-0209 - Unspecified reference

[98] ICDD Card 21-0569 - Unspecified reference

[99] ICDD Card 35-0609 - Unspecified reference

[100] ICDD Card 37-1445 - Unspecified reference

[101] ICDD Card 11-0628 - Unspecified reference

[102] ICDD Card 05-0550 - H.E. Swanson, R.K. Fuyat and G.M. Ugrinic, "Standard X-ray Diffraction Patterns", National Bureau of Standards Circular 539, Vol. 3 (1954).

[103] ICDD Card 36-0089 - Unspecified reference

[104] ICDD Card 41-1422 - Unspecified reference

[105] ICDD Card 12-0043 - Unspecified reference

[106] ICDD Card 15-0201 - Unspecified reference

[107] ICDD Card 22-1079 - Unspecified reference

[108] ICDD Card 08-0244 - S.M. Siegel, "The Biochemistry of Ligin Formation", Physiologia Plantarium, Vol. 8 (1955) 20-32.

[109] ICDD Card 24-1172 - K. Aykan and A.W. Sleight, "Characterization of Mixed Uranium Antimony Oxides $USbO_5$ and USb_3O_{10}", Journal of the American Ceramic Society, Vol. 53 (1970) 427-431.

[110] ICDD Card 16-0842 - E.F. Juenke and S.F. Bartram, "Crystallographic Data on UO_2WO_4 and UO_2MoO_4", Acta Crystallographica, Vol. 17 (1964) 618.

[111] O.A. Ustinov, M.A. Andrianov, N.T. Chebotarev, and G.P. Novoselov, "The System MoO_3-UO_3", Soviet Atomic Energy, Vol. 34 (1973) 203-205.

[112] L.M. Kovba, V.K. Trunov, and A.I. Grigor'ev, "Investigation of Anhydrous Uranyl Salts UO_2EO_4 (E = s, Cr, Mo, W)", Journal of Structural Chemistry, Vol. 6 (1965) 883-884.

[113] ICDD Card 12-0693 – S.R. Kamhi, "An X-ray Study of Umohoite", The American Mineralogist, Vol. 44 (1959) 920-925.

[114] ICDD Card 11-0375 – R.G. Coleman and D.E. Appleman, "Umohoite from the Lucky MC Mine, Wyoming", The American Mineralogist, Vol. 42 (1957) 657-660.

[115] ICDD Card 12-0778 – P.K. Hamilton and P.F. Kerr, "Umohoite from Cameron, Arizona", The American Mineralogist, Vol. 44 (1959) 1248-1260.

[116] ICDD Card 43-0354 - V.N. Serezhkin, L.M. Kovba, and V.K. Trunov, "Study of the System UO_3-MoO_3-H_2O." Radiokhimiya, Vol. 15 (1973) 282-285.

[117] ICDD Card 43-0355 - V.N. Serezhkin, L.M. Kovba, and V.K. Trunov, "Study of the System UO_3-MoO_3-H_2O." Radiokhimiya, Vol. 15 (1973) 282-285.

[118] ICDD Card 44-0034 - A. Fedoseev, N. Budantseva, A. Yusov, and M. Grigor'ev, "New Molybdates of Hexavalent Actinides", Radiokhimiya, Vol. 5 (1990) 14-18.

[119] ICDD Card 38-0093 – S.R. Bharadwaj, S.R. Dharwadkar, and M.S. Chandrasekharaiah, "Thermogravimetric Study of Some Uranium Molybdates", Thermochimica Acta, Vol. 79 (1984) 377-382.

[120] ICDD Card 43-0115 - Unspecified reference

[121] ICDD Card 13-0046 - Unspecified reference

[122] N.D. Dahale, M. Keskar, N.K. Kulkarni, and K.D. Singh Mudher, "Structural and Thermal Studies on $Na_2U(MoO_4)_3$ and $Na_4U(MoO_4)_4$", Journal of Alloys and Compounds, Vol. 440 (2007) 145-149.

[123] ICDD Card 35-0350 – C. Dion and A. Noel, "Étude et Interprétation du diagramme Na_2MoO_4-UO_3 dans le cadre du système ternaire UO_3-MoO_3-

Na$_2$O", Bulletin de la Société Chimique de France, Vol. 5-6 (1980) I-185-I-192.

[124] E.V. Suleimanov, N.G. Chernorukov, A.V. Golubev, and E.A. Medina, "Thermochemistry of Sodium Uranomolybdates Formed in the System Na$_2$O-UO$_3$-MoO$_3$", Radiokhimiya, Vol. 49 (2007) 25-28.

[125] ICDD Card 32-1131 – C. Dion, A. Noel and J. Laureyns, "Contribution à l'étude du système UO$_3$-MoO$_3$-Na$_2$O. Étude du domaine Na$_2$U$_2$O$_7$-Na$_2$Mo$_2$O$_7$-Na$_2$O", Bulletin de la Société Chimique de France, Vol. 11-12 (1977) 1115-1120.

[126] ICDD Card 32-1132 – C. Dion, A. Noel and J. Laureyns, "Contribution à l'étude du système UO$_3$-MoO$_3$-Na$_2$O. Étude du domaine Na$_2$U$_2$O$_7$-Na$_2$Mo$_2$O$_7$-Na$_2$O", Bulletin de la Société Chimique de France, Vol. 11-12 (1977) 1115-1120.

[127] R.W.G. Wyckoff, "The Structure of Crystals", Interscience Publishers, New York, Vol. 1 (1953) 76.

[128] K.A. Hughes and P.C. Burns, "Uranyl Dinitrate Trihydrate UO$_2$(NO$_3$)$_2$(H$_2$O)$_3$", Acta Crystallographica C, Vol. C59 (2003) I-7-I-8.

[129] R.W.G. Wyckoff, "The Structure of Crystals", Interscience Publishers, New York, Vol. 1 (1963) 239.

[130] N. Wooster, Z.Kristallogr.Mineral.Petrogr.Abt, Vol. 80 (1931) 504.

[131] J. Thewlis, "An X-Ray Powder Study of β-Uranium", Acta Crystallographica, Vol. 5 (1952) 790-794.

[132] S. Siegel and H.R. Hoekstra, "An Examination of the Symmetry of Alpha Uranium Trioxide", Inorganic Nuclear Chemistry Letters, Vol. 7 (1971) 497-504.

[133] B.O. Loopstra, "The Structure of β-U$_3$O$_8$", Acta Crystallographica B, Vol. B26 (1970) 656-657.

[134] V.N. Serezhkin, V.K. Trunov, L.G. Makarevich, "Refined Crystal Structure of Uranyl Molybdates", Kristallografija, Vol. 25 (1980) 858-860.

[135] O.G. D'Yachenko, V.V. Tabachenko, R. Tali, L.M. Kovba, B.O. Marinder, and M. Sundberg, "Structure of UMoO$_5$ Studied by Single-Crystal X-Ray diffraction and High-Resolution Transmission Electron Microscopy", Acta Crystallographica B, Vol. B52 (1996) 961-965.

[136] T.L. Cremers. P.G. Eller, R.A. Penneman, and C.C. Herrick, "Orthorhombic Uranium (IV) Molybdenum (VI) Oxide, UMo$_2$O$_8$", Acta Crystallographica C, Vol. C39 (1983) 1163-1165.

[137] S.V. Krivovichev and P.C. Burns, "γ-UMo$_2$O$_8$ as a New Polymorph of Uranium Dimolybdate Containing Tetravalent Uranium", Doklady Physics, Vol. 49 (2004) 76-77.

[138] V.V Tabachenko, O.G. D'Yachenko, and M.R. Sundberg, "The Crystal Structures of UMo$_5$O$_{16}$ and U$_{0.75}$Mo$_5$O$_{16}$ Studies by X-ray Diffraction and

High-Resolution Electron Microscopy, European Journal of Solid State and Inorganic Chemistry, Vol. 32 (1995) 1137-1149.

[139] V.N. Serezhkin, L.M. Kovba, and V.K. Trunov, "Crystal Strcutre of the Binary Oxide γ-$U_3Mo_{20}O_{64}$", Zhurnal Strukturnoi Khimii, Vol. 14 (1973) 742-744.

[140] V.N. Serezhkin, L.M. Kovba, and V.K. Trunov, "Crystal Structure of U_2MoO_8", Kristallografica, Vol. 18 (1973) 514-517.

[141] V.N. Serezhkin, L.M. Kovba, and V.K. Trunov, "Structure of the Double Oxide α-$U_3Mo_{20}O_{64}$", Kristallografica, Vol. 18 (1973) 961-965.

[142] N.D. Zakharov, E. Pippel, R. Hillebrand, and P. Werner, "Structure of UMo_4O_{14}", Progress in Nuclear Energy, Vol. 57 (2012) 150-154.

[143] S.V. Krivovichev and P.C. Burns, "Crystal Chemistry of Uranyl Molybdates. 1. The Structure and Formula of Umohoite", The Canadian Mineralogist, Vol. 38 (2000) 717-726.

[144] E.S. Makarov and L.I. Anikina, "Crystal Structure of Umohoite $(UMoO_6(H_2O)_2 \, 2H_2O)$", Geochemistry, Vol. 1 (1963) 14-21.

[145] S.V. Krivovichev and P.C. Burns, "Crystal Chemistry of Uranyl Molybdates. 2. The Structure and Formula of Iriginite", The Canadian Mineralogist, Vol. 38 (2000) 847-851.

[146] S.V. Krivovichev and P.C. Burns, "Crystal Chemistry of Uranyl Molybdates. 7. An Iriginite-Type Sheet of Polyhedra in the Structure of $[(UO_2)Mo_2O_7(H_2O)_2]$", The Canadian Mineralogist, Vol. 40 (2002) 1571-1577.

[147] S.V. Krivovichev, "Crystal Chemistry of Uranyl Molybdates. 5. Topologically Distinct Uranyl Dimolybdate Sheets in the Structures of $Na_2[(UO_2)(MoO_4)_2]$ and $K_2[(UO_2)(MoO_4)2](H_2O)$", The Canadian Mineralogist, Vol. 40 (2002) 193-200.

[148] S.V. Krivovichev and P.C. Burns, "Crystal Chemistry of Uranyl Molybdates. 8. Crystal Strucutres of $Na_3Tl_3[(UO_2)(MoO_4)_4]$, $Na_{13-x}Tl_{3+x}[(UO_2)(MoO_4)_3(H_2O)_{6+x}$ (x=0.1), $Na_3Tl_5[(UO_2)(MoO_4)_3]_2(H_2O)_3$ and $Na_2[(UO_2)(MoO_4)_2](H_2O)_4$", The Canadian Mineralogist, Vol. 41 (2003) 707-719.

[149] S.V. Krivovichev and P.C. Burns, "Crystal Chemistry of Uranyl Molybdates. 3. New Structural Themes in $Na_6[(UO_2)_2O(MoO_4)_4]$, $Na_6[(UO_2)(MoO_4)_4]$ and $K_6[(UO_2)_2O(MoO_4)_4]$", The Canadian Mineralogist, Vol. 39 (2001) 197-206.

[150] S.V. Krivovichev, C.L. Cahill, and P.C. Burns, "Syntheses and Crystal Structures of Two Topologicaly Related Modification of $Cs_2[(UO_2)_2(MoO_4)_3]$", Journal of Inorganic Chemistry, Vol. 41 (2002) 34-39.

[151] E.V. Alekseev, S.V. Krivovichev, T. Armbruster, W. Depmeier, E.V. Suleimanov, E.V. Chuprunov, and A.V. Golubev, "Dimensional Reduction

in Alkali Metal Uranyl Molybdates: Synthesis and Structure of $Cs_2[(UO_2)O(MoO_4)]$", Zeitschrift fur anorganische und allgemeine Chemie, Vol. 633 (2007) 1979-1984.

[152] S. Yagoubi, S. Obbade, S. Saad, and F. Abraham, "From $[(UO_2)_2O(MoO_4)_4]^{6-}$ to $[(UO_2)_2(MoO_4)_3(MoO_5)]^{6-}$ Infinite Chains in $A_6U_2Mo_4O_{21}$ (A=Na, K, Rb, Cs) Compounds: Synthesis and Crystal Structure of $Cs_6[(UO_2)_2(MoO_4)_3(MoO_5)]$", Journal of Solid State Chemistry, Vol. 184 (2011) 971-981.

[153] R.A. Barry, J. Deveau, I. Korobkov, E.C. Corcoran, and J. Scott, "A facile and accurate preparation of pure $UMoO_6$ and a crystallographic study of a Na-U-Mo-O intermediate", Polyhedron, under review − submitted June 2015, manuscript number POLY-D-15-00465.

[154] http://www.sigmaplot.com/products/sigmaplot/sigmaplot-details.php Last accessed: 1 June 2015.

[155] R. Prasad, R. Agarwal, K.N. Roy, V.S. Iyer, V. Venugopal, and D.D. Sood, "Determinantion of Thermal Propteries of $Cs_2C_2O_7(s,l)$ by High Temperature Calvet Calorimetry", Journal of Nuclear Materials, Vol. 167 (1989) 261-264.

[156] V.N. Serezhkin, G.N. Ronami, L.M. Kovba, and V.K. Trunov, "New Double Oxides of Uranium and Molybdenum", Zhurnai Neorganicheskoi Khimii, Vol. 19 (1974) 1033-1039.

[157] E.H.P. Cordfunke, R.J.M. Konings, "Thermochemical Data for Reactor Materials and Fission Products", Elsevier Science Publishers, Amsterdam, 1990.

[158] http://www.crct.polymtl.ca/fact/ Last accessed: 1 June 2015.

[159] R.L. Filler, P. Lindenfeld, and G. Deutscher, "Specific heat and thermal conductivity measurements on thin films with a pulse method", Rev. Sci. Instrum. Vol. 46 Iss. 4 (1975) 439–442.

[160] I. Catarino, and G. Bonfait, "A simple calorimeter for fast adiabatic heat capacity measurements from 15 to 300 K based on closed cycle cryocooler", Cryogenics Vol. 40 Iss. 7 (2000) 425–430.

[161] S. Riegel, and G. Weber, "A dual-slope method for specific heat measurements", Journal of Physics E: Scientific Instruments Vol. 19 Iss. 10 (1886) 790.

[162] P.F. Sullivan, G. Seidel, "Steady-state, ac-temperature calorimetry" Phys. Rev. Vol. 173 Iss. 3, (1968) 679

[163] A. Yakymovych, S. Fürtauer, A. Elmahfoudi, H. Ipser, and H. Flandorfer, "Enthalpy of mixing of liquid Co–Sn alloys", Journal of Chemical Thermodynamics, Vol 74 (2014) 269-285.

[164] L.R. Bidwell, "Effusion from Knudsen Triple Cells", Journal of Chemical Physics, Vol. 52, Iss. 4, (1970) 1987-1991.

Appendices

Appendix A   MoO$_2$ Non-stoichiometry

Mode II that Ref. [19] used to explain the under-prediction of oxidation of SIMFUELs during the CT experiments was the non-stoichiometry of MoO$_2$. Molybdenum is a common fission product in nuclear fuel (accounting for ~17.52 % of all cumulative fission products in the thermal fission of ^{235}U and ~12.27 % of all cumulative fission products in the thermal fission of ^{239}Pu [1]). The relatively large quantity of Mo in a nuclear fuel, combined with its affinity to buffer oxygen, make it a factor to consider. The hyper-stoichiometric region may be larger than previously thought. Part of this thesis was to investigate the non-stoichiometry of MoO$_2$. The results were unfruitful but are included in this appendix.

A.1.   Background

A.1.1.   Ability to Buffer Oxygen

When UO$_2$ undergoes fission, the U atom is split and the oxygen is left to come to equilibrium in the complex chemical system of the nuclear fuel. Generally, the oxygen comes to equilibrium in accordance with the laws of thermodynamics. One way to visualize and evaluate this phenomenon is through the use of an Ellingham diagram. An Ellingham diagram is a plot of the change in Gibbs free energy of a reaction as a function of temperature.

Figure A-1 is an Ellingham diagram of the oxidation reactions of different elements found in nuclear fuel by one mol of O$_2$ in isolation. The oxidation of H$_2$ to form H$_2$O (Equation A-2) is used as a reference point as heavy water is the source of oxygen for oxidation in defective fuels. It is important to note that each reaction is conducted in isolation from one another with 1 mol of O$_2$.

If the oxidation reaction line in question lies below the H$_2$ oxidation line on this diagram, it indicates that the reaction is spontaneous in the direction written (oxidation of the metal to the oxide) under defective fuel conditions as the oxide form is more stable than H$_2$O (*e.g.,* UO$_2$). Conversely, if the oxidation reaction line lies above the H$_2$ oxidation line on this diagram, the reverse reaction is favoured as the oxide form is less stable than H$_2$O and the metallic form is more stable (*e.g.,* Pd). Interestingly, the water line and the Mo line cross.
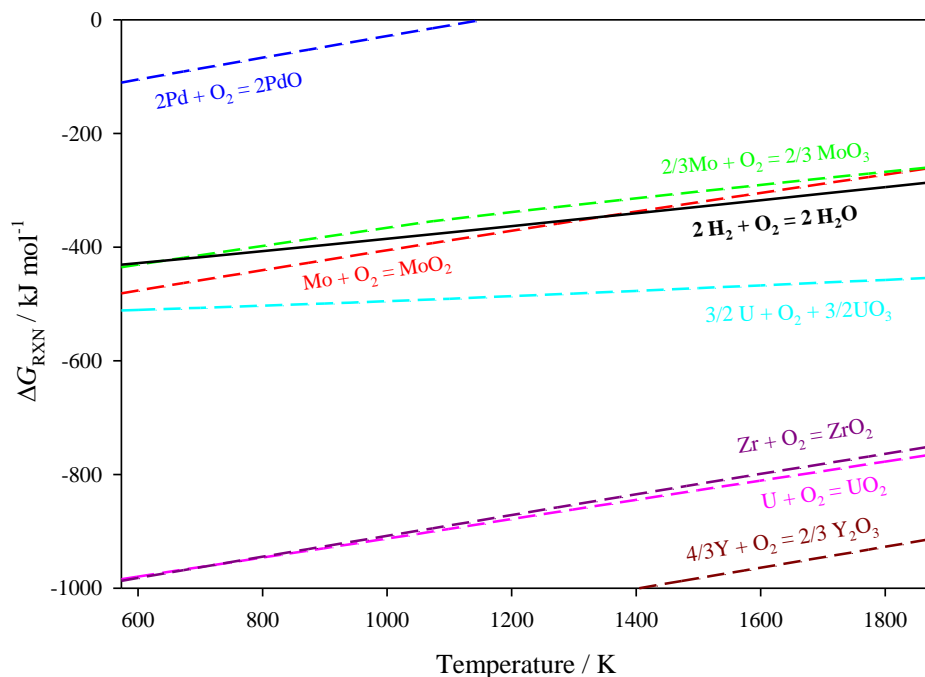
Figure A-1: Ellingham diagram of the oxidation of select elements with 1 mol O_2 in relation to H_2O [19]

Figure A-2 focuses on the intersection of the water formation line and the MoO_2 formation line. The slopes and intersection of the lines indicate that at lower temperatures Mo is more likely to be found in the oxide form, as its line lies lower on the diagram. Furthermore at higher temperatures, Mo is more likely to be found in the metallic form as its line lies higher on the diagram. Therefore, the distribution of Mo in the metallic form to Mo in the oxide form will be dependent on temperature and oxygen pressure. Thus, Mo acts as an oxygen buffer. Mo was selected for study over all other fission and activation products because of this unique characteristic.

In addition to the critical thermodynamic property described above, Mo is also suitable for experimentation because it is stable, non-toxic, and its forms of interest in this thesis are found in the solid state.
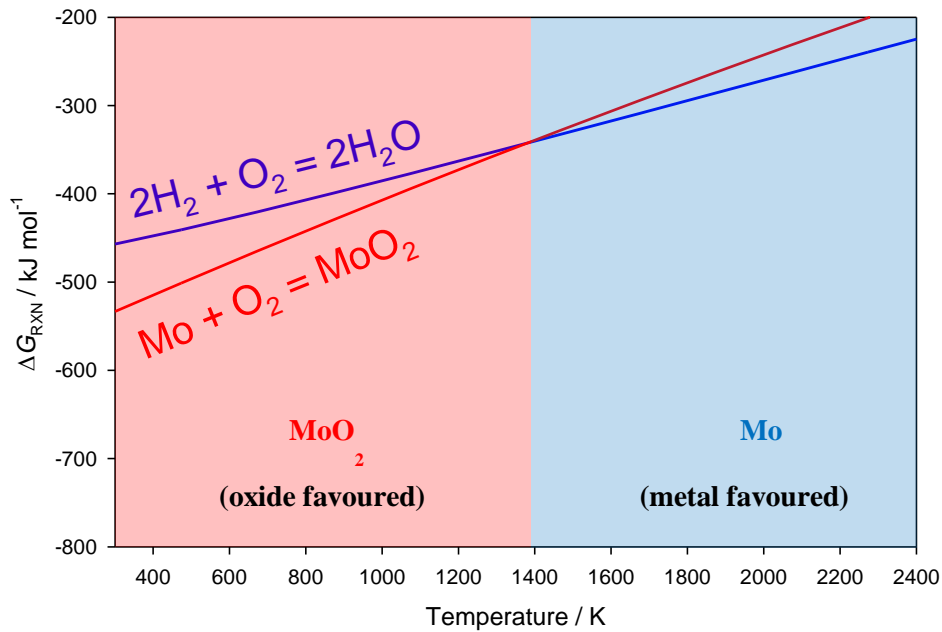
Figure A-2 Ellingham diagram comparing H$_2$O and MoO$_2$ formed with 1 mol O$_2$ [33]

A.1.2.   *Effect of Temperature on Ability to Buffer Oxygen*

The effect of temperature on the ability of molybdenum to buffer oxygen can be shown using the equations derived in Section 2.2. First consider the formation of MoO$_2$ at 800 K

$$Mo + O_2 \rightarrow MoO_2 \qquad \Delta G(800\ K) = \text{-440 kJ mol}^{-1} \qquad \text{Equation A-1}$$

This reaction is favoured in isolation because it has a negative ΔG

However, H$_2$ is competing for the O$_2$ in the fuel element as well

$$2H_2 + O_2 \rightarrow 2H_2O \qquad \Delta G(800\ K) = \text{-408 kJ mol}^{-1} \qquad \text{Equation A-2}$$

Reversing Equation A-2 and adding it to Equation A-1

$$2H_2O \rightarrow 2H_2 + O_2 \qquad \Delta G(800\ K) = +408\ \text{kJ mol}^{-1}$$

$$Mo + O_2 \rightarrow MoO_2 \qquad \Delta G(800\ K) = -440\ \text{kJ mol}^{-1}$$

$$2H_2O + Mo + O_2 \rightarrow 2H_2 + \qquad \Delta G(800\ K) = -32\ \text{kJ mol}^{-1}$$
$$O_2 + MoO_2$$
$$Mo + 2H_2O \rightarrow MoO_2 + 2H_2 \qquad \Delta G(800\ K) = -32\ \text{kJ mol}^{-1} \qquad \text{Equation A-3}$$
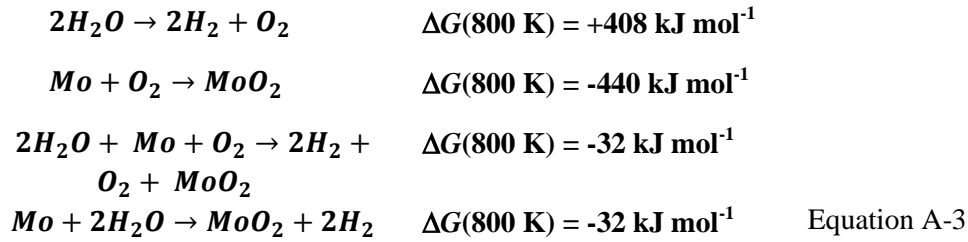
As seen in Equation A-3, the oxidation of molybdenum over hydrogen is favoured at 800 K as the ΔG_{RXN} is negative. However, at 1600 K

$$Mo + O_2 \rightarrow MoO_2 \qquad \Delta G(1600\ K) = -320\ \text{kJ mol}^{-1} \qquad \text{Equation A-4}$$

$$2H_2 + O_2 \rightarrow 2H_2O \qquad \Delta G(1600\ K) = -340\ \text{kJ mol}^{-1} \qquad \text{Equation A-5}$$

Therefore,

$$2H_2O \rightarrow 2H_2 + O_2 \qquad \Delta G(1600\ K) = +320\ \text{kJ mol}^{-1}$$

$$Mo + O_2 \rightarrow MoO_2 \qquad \Delta G(1600\ K) = -308\ \text{kJ mol}^{-1}$$

$$2H_2O + Mo + O_2 \rightarrow 2H_2 + \qquad \Delta G(1600\ K) = 12\ \text{kJ mol}^{-1}$$
$$O_2 + MoO_2$$
$$Mo + 2H_2O \rightarrow MoO_2 + 2H_2 \qquad \Delta G(1600\ K) = 12\ \text{kJ mol}^{-1} \qquad \text{Equation A-6}$$
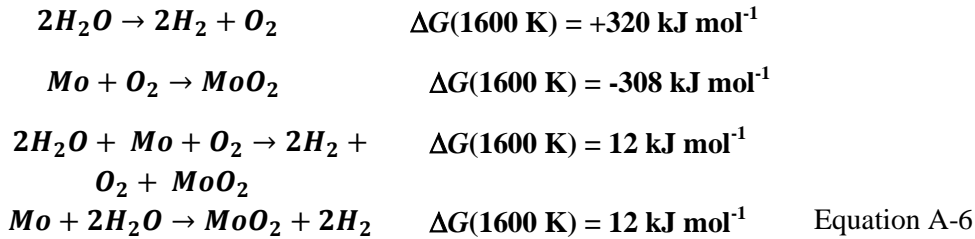
The oxidation of molybdenum over hydrogen is not favoured at 1600 K. This reaction will occur in the opposite direction and metallic Mo will be favoured. Thus, temperature has an effect on the ability of molybdenum to buffer oxygen.

A.1.3.   *Effect of Pressure on Ability to Buffer Oxygen*

The effect of temperature on the ability of molybdenum to buffer oxygen was seen in Section A.1.2. That example had 1 mol of O_2 present, but varying oxygen potential also has an effect on the ability of molybdenum to buffer oxygen. Consider the formation of MoO_2

$$Mo + O_2 \rightarrow MoO_2 \qquad \text{Equation A-7}$$
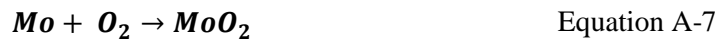
Apply Equation 26

$$\Delta G_{f,MoO_2} = \Delta G^o_{f,MoO_2} + R\,T\,ln\left(\frac{pMoO_2}{(pO_2)(pMo)}\right) \qquad \text{Equation A-8}$$

Since Mo and MoO_2 are both solids and do not have partial pressures (*i.e.,* they have an activity of one), Equation A-8 can be rewritten as

$$\Delta G_{f,MoO_2} = \Delta G^o_{f,MoO_2} - R\,T\,ln(pO_2) \qquad \text{Equation A-9}$$

$\Delta G_{f,\,MoO_2}$ is dependent on temperature and pO_2. Thus, whether Mo or MoO_2 is favoured (whether molybdenum will absorb or release oxygen) is dependent on temperature and pO_2.

For MoO_2 to form, it must be favoured thermodynamically. In a nuclear fuel, it must be more favoured than competing reactions. So now consider the competing H_2 oxidation

$$2H_2 + O_2 \rightarrow 2H_2O$$
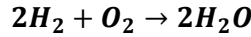
$$\Delta G_{f,H_2O} = \Delta G^o_{f,H_2O} + R\,T\,ln\left(\frac{pH_2O^2}{pO_2\,pH_2{}^2}\right) \qquad \text{Equation A-10}$$

The favourability of water is dependent on the partial pressure of O_2, H_2, and H_2O.

These two competing reactions are combined to show the oxidation of Mo by H_2O.

$$Mo + 2H_2O \rightarrow MoO_2 + 2H_2$$
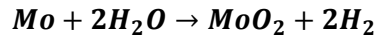
$$\Delta G_{RXN} = \Delta G^o_{RXN} + RT\,ln\left(\frac{a(MoO_2)\,pH_2{}^2}{a(Mo)\,pH_2O^2}\right)$$

$$\Delta G_{RXN} = \Delta G^o_{RXN} + RT\,ln\left(\frac{pH_2{}^2}{pH_2O^2}\right) \qquad \text{Equation A-11}$$

Equation A-11 shows that ΔG_{RXN}, the favourability of the oxidation of Mo in the presence of water, is dependent on the ratio of $H_2:H_2O$ and temperature.

A.1.4. *Non-Stoichiometry*

In addition to the complete oxidation of Mo from the metallic form to the dioxide form shown in Equation A-7, Zador [21] proposed a region of non-stoichiometry in the MoO_2 crystal structure. Figure A-3 is the binary Mo-O phase diagram published by Brewer [22] that plots the phases created by Mo and O depending on the mole fraction of O and temperature. It shows that pure MoO_2 exists only along the line where $x_o = 2/3$ exactly (shown in green), x_o being the percentage of O atoms in the Mo-O system. This line is surrounded by an area of non-stoichiometry, as seen in blue. To the left of $x_o = 2/3$ exists an area of hypo-stoichiometry, MoO_{2-x}, and to the right of $x_o = 2/3$ exists an area of hyper-stoichiometry, MoO_{2+x}.

This non-stoichiometry adds to the ability of molybdenum to buffer oxygen in a nuclear fuel, the extent of which is not well understood. Thus, this thesis attempted to measure it experimentally in order to validate its addition in the RMC-TFM.
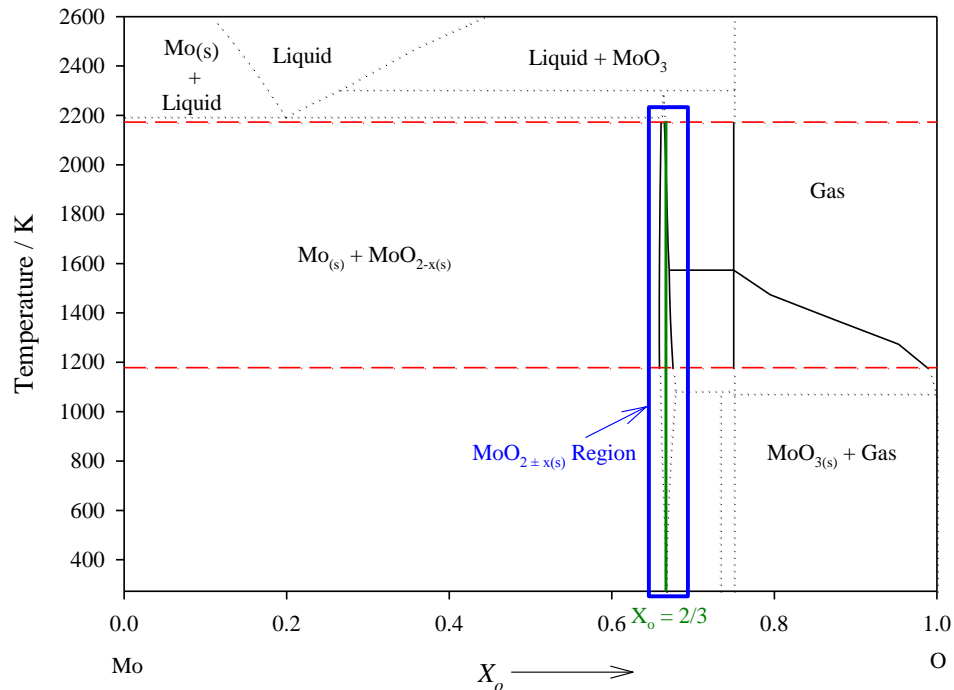
Figure A-3: Mo-O binary phase diagram by Brewer [19]

A.2.   Scope and Methodology

This section describes the original experimental methodology for the Mo-O system. As discussed later in Section A.3, this original experimental methodology was modified in order to accommodate unexpected results. Ultimately, it was determined that the experimental setup at the RMC would not be sufficient for this type of work.

The original test plan for the Mo-O system tested the non-stoichiometric region of $MoO_{2\pm x}$ using a SETARAM SETSYS Evolution 24 Thermogravimetric Analyzer / Differential Scanning Calorimeter (TGA/DSC) and a Zirox SGM5 EL semi-conductor CT cell. The experimental setup can be seen in Figure A-4. First, quality assurance of the TGA/DSC was conducted to ensure the mass and heat flow measurements were accurate and can be found in Appendix L. Next, quality assurance of the CT cell was completed to ensure accurate pO_2's were being generated and measured and can be found in Appendix M. The CT cell is the same as the one described in Section 2.5.2. Upon completing calibration of the equipment, experimentation could begin.
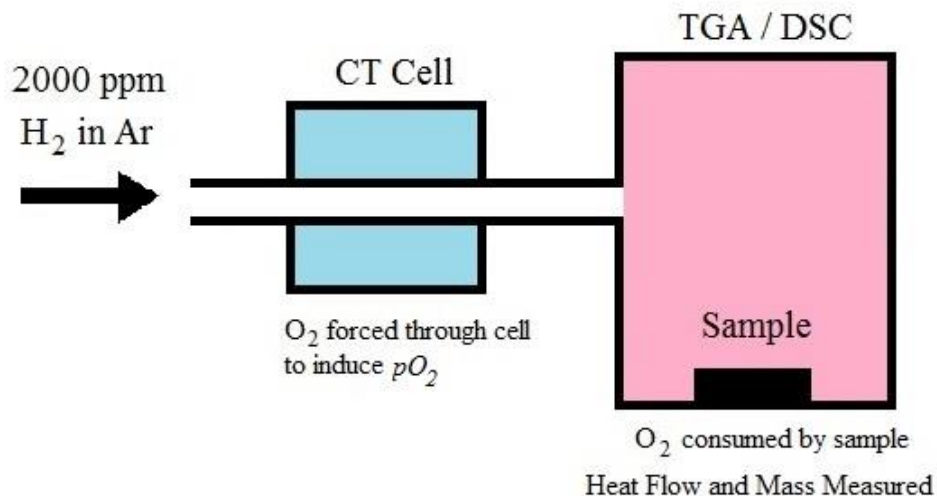
Figure A-4: TGA / DSC experimental setup

A sample of MoO_2 was placed inside the TGA/DSC and heated to 1273 K. The CT cell was used to draw oxygen into the 2000 ppm H_2 and Ar carrier gas mixture to create a pO_2 that would stabilize pure MoO_2. This ultra-high purity gas drove off

any oxygen adhered to the surface of the sample. Next a higher pO_2 was introduced that would stabilize MoO_{2+x}. Change in mass and heat flux were measured as a function of time. The sample was then reduced again to pure MoO_2 to ensure no Mo was lost in the carrier gas as volatile species during the experiment. A blank run with two empty crucibles and identical heating rates and gas mixtures was completed prior to the sample run and subtracted to account for buoyancy during heating and mass difference in the two crucibles.

The independent variable for these experiments was pO_2. The extremely small pO_2 range (10^{-19} to 10^{-10} atm) required by these experiments were made possible due to the CT cell described in Appendix B. The measured change in mass was assumed to be entirely from the gain or loss of oxygen and thus used to determine the corresponding change in stoichiometry for each new pO_2. The measured heat flow data was integrated over the time of the experiment to determine the enthalpy of reaction (ΔH_{RXN}).

Figure A-5 shows the range of oxidizing and reducing conditions that can be tested in this work. It also shows the H_2:H_2O ratios required to create those pO_2 conditions. If all tests are run at 1273 K, shown by the vertical violet line, the metallic form will be favoured under reducing conditions and the oxide form will be favoured in oxidizing conditions. This will ensure a testing range that covers all areas of interest.
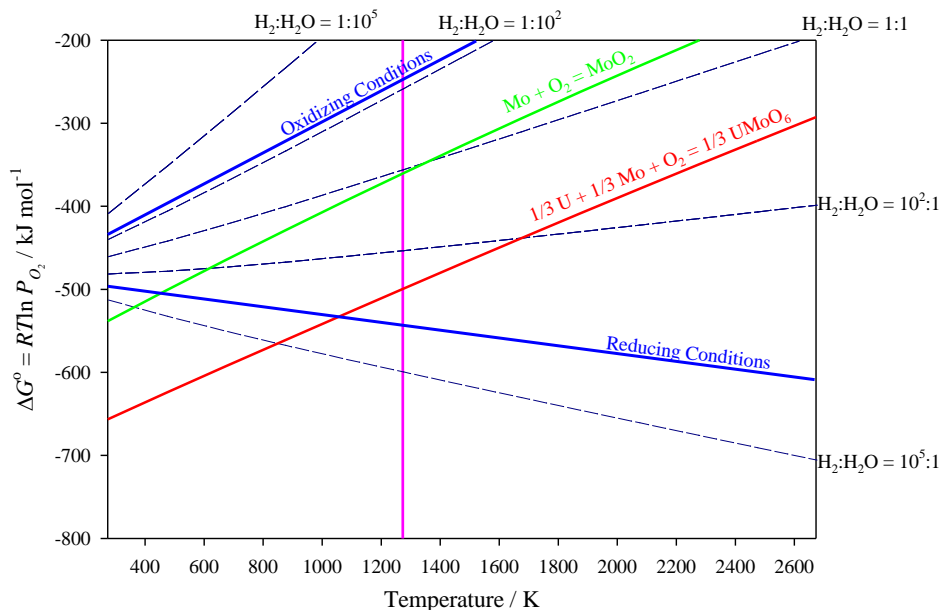
Figure A-5: Ellingham diagram illustrating the range of pO_2 to be tested and the change in ΔG in relation to MoO_2 and $UMoO_6$ [19]

A.3.   Results and Discussion

While investigating the Mo-O system, some obstacles were reached that could not be overcome in the timeframe and budget of this thesis. First, the starting stoichiometry of MoO_2 could not be determined to the accuracy needed for this thesis. Neutron activation analysis (NAA), ICP-MS, titration experiments, and gravimetric analysis were trialed and failed. Creating Mo-oxides *in situ* in the TGA/DSC to obtain a starting stoichiometry also failed. Finally, an inherent error in the ability of the TGA to measure mass was discovered and analysed.

It was postulated that if the starting stoichiometry of MoO_2 stock was known, any deviation in mass could be associated to a change in O as all Mo would remain in the reaction crucible. The expected changes in MoO_2 stoichiometry ranged from $MoO_{1.95}$ to $MoO_{2.05}$. For an average sample size of 100 mg of MoO_2, this corresponds to a change in mass of ± 0.6 mg. Given the published error of the TGA/DSC by the manufacturer of ± 0.023 µg for the large mass range setting, the changes in mass of the MoO_2 sample would be taken with enough accuracy to identify the small expected deviations from stoichiometry.

However, determining the MoO_2 stock stoichiometry proved to be a major obstacle. This is due to the fact that Mo accounts for approximately 75 % of the mass of MoO_2. This means that any small change in mass results in a large change in stoichiometry. For example, if the mass of a 1.00 g sample of perfectly stoichiometric $MoO_{2.00}$ is known accurately to $\pm$ 1 % and the mass of Mo in this sample (0.7499 g) is determined accurately to $\pm$ 1 %, the stoichiometry determined is $MoO_{2.00}$, but the associated error ranges from $MoO_{1.84}$ to $MoO_{2.16}$. A weighing accuracy of $\pm$ 0.08 % is needed in order to have an associated error range of $MoO_{1.99}$ to $MoO_{2.01}$. This is why a suitable method for determining the initial MoO_2 stoichiometry to the necessary accuracy was a great challenge.

A.3.1.   Determining MoO₂ Stoichiometry

A method to determine the starting stoichiometry of the starting MoO_2 stock had to be developed. Methods trialed included NAA, ICP-MS, titrations, and gravimetric analysis. All of these methods proved to have errors larger than required for the small stoichiometric changes expected.

A.3.2.   Neutron Activation Analysis (NAA)

NAA can be used to determine elemental concentration by irradiating a sample with neutrons, forming radioactive isotopes, and measuring the corresponding radioactive emissions. As the radioactive decay paths for the elements are well-known, the elemental concentration can be determined.

For the purposes of determining MoO_2 stoichiometry, only Mo would need to be considered. As there are many isotopes of Mo in significant quantity (^{92}Mo (14.84 %), ^{94}Mo (9.25 %), ^{95}Mo (15.92 %), ^{96}Mo (16.68 %), ^{97}Mo (9.55 %), ^{98}Mo (24.13 %) and ^{100}Mo (9.63 %) [2]) and their isotopic percentages well-known, only one needs to be measured to represent the entire sample. ^{101}Mo was selected as ^{100}Mo could be bombarded with a neutron to form this isotope and its beta decay to ^{101}Tc has a half-life of 14.61 min [2] for ease of measurement. The accuracy of the detector is $\pm$ 2.5 %. Combined with other inherent errors of NAA, such as geometry, variation in the neutron flux, and measurement of irradiation time, decay time, and counting time, push the accuracy to $\pm$ 10 % or more. It is evident this method is not suitable to determine the stoichiometry of MoO_2 to the accuracy needed for this application.

A.3.3. Inductively Coupled Plasma Mass Spectroscopy (ICP-MS)

ICP-MS can measure the concentrations of metals as low as the parts per trillion (ppt) level. It does so by ionizing a sample in an inductively coupled plasma and then measuring the mass to charge ratio of these ions with a mass spectrometer. The general error range is $\pm$ 10 %. Additionally, an error associated with the serial dilutions necessary to create a concentration of MoO_2 in solution detectable by ICP-MS would compound this error. ICP-MS is not suitable for the application of accurately determining MoO_2 stoichiometry.

A.3.4. Titration

While newer technologies allow for lower detection limits and non-destructive testing of complex materials, it is often mature analytical methods that provide the lowest errors. A titration has three sources of error that can all be minimized by larger samples. The first is the original mass of MoO_2. If a 1 g sample is used, an ordinary laboratory balance can give an associated error of $\pm$ 0.0002 g or $\pm$ 0.02 %. The second source of error is the volume of titrant needed to balance the titrand. If 100 mL of titrant is used, the accuracy is $\pm$ 0.05 mL or $\pm$ 0.05 %. Finally the last source of error is the concentration of the titrant. Given this source of error is low as the titrant is made commercially for this purpose, it is possible to obtain a starting stoichiometry in the error range necessary.

Titration experiments were completed using six different methods published by Gopala Rao *et al*. [3] [4] and Bhaskara Rao *et al*. [5]. In general, the Mo-oxide was dissolved in acid, an indicator added, and titration with a base completed. The combinations are listed in Table A-1. Unfortunately, the titrations were unsuccessful as the indicator would turn colour, indicating reaction completion, but then slowly return to the original colour. It was thought that the oxidation of the titrand is favoured over the oxidation of the indicator, however kinetically the former is a much slower reaction than the latter. This makes a definite end point impossible to achieve and the starting stoichiometry unknown.

Table A-1: Titration Methods Used

	Method 1	Method 2	Method 3
Titrand	Sulphuric acid	Hydrochloric acid[ab]	Hydrochloric acid[a]
Indicator	N-phenyl anthranilic acid	Diphenyl benzidine	Diphenyl benzidine
Titrant	Sodium vanadate	Sodium vanadate	Ceric sulphate
	Method 4	**Method 5**	**Method 6**
Titrand	Hydrochloric acid[a]	Hydrochloric acid[a]	Hydrochloric acid[a]
Indicator	Ferroin	Methyl orange	Electrode
Titrant	Ceric sulphate	Ceric sulphate	Ceric sulphate

a = Additional phosphoric acid
b = Additional oxalic acid

A.3.5. *Gravimetric Analysis (GA)*

GA is an analytical method used to determine the concentration of an element or compound in a solution by precipitating the selected element or compound from solution in a known form and weighing the precipitate in that form to determine the number of moles of element or compound originally in the solution. It has three sources of errors, two of which can be minimized by larger samples and one that is dependent on the skill of the experimentalist. The first two sources of error are the mass of starting MoO_2 and the final mass of Mo precipitate. Again, if a 1 g sample is used, an ordinary laboratory balance can give an associated error of $\pm$ 0.0002 g or $\pm$ 0.02 %. The last source of error is the skill of the technician performing the analysis. All of the precipitate must be captured in order to achieve an accurate final mass measurement. The sample must be completely dry but must also be at room temperature while being weighed.

GA was conducted using the oxine method published in [76], the same as described in section 3.2.2.1. While these methods were very accurate ($<\pm$ 1.5 %), they were still not accurate enough to determine the starting stoichiometry of the MoO_2 such that further experimentation could be conducted.

A.3.6. *Creating MoO$_2$ in situ*

It was postulated that if the starting stoichiometry of MoO_2 stock could not be determined by an external method, it could be possible to create MoO_2 *in situ* inside the TGA. The oxidation state of Mo is a function of the pO_2 of the surrounding atmosphere and the pO_2 inside the TGA could be controlled via the CT cell. The number of moles of Mo in a sample could be determined by a variety

of methods: oxidizing Mo to form MoO_2, reducing MoO_2 to form Mo, and decomposing $(NH_4)_6Mo_7O_{24}$ to form MoO_3 and then reducing to form MoO_2. Ultimately, none of these methods could provide a starting stoichiometry of MoO_2.

A.3.7. *Oxidizing Mo to Form MoO₂*

Mo metal was selected as the starting material, thus the number of moles of Mo in the sample was known and any mass gain was associated with oxidation. Mo was subjected to a stream of 10 % H_2 in Ar at 1123 K to drive off oxygen and water adhered to the surface until a stable mass of Mo was achieved. This provided the number of moles of Mo present in the sample. The sample was then subjected to a pO_2 of 1×10^{-21} atm at 823 K using the CT cell to attempt to oxidize the sample to MoO_2 *in situ*. The reaction kinetics were too slow and would require at least two weeks to oxidize one sample. A higher temperature of 973 K and a pO_2 of 1×10^{-18} atm was attempted with similar results. Temperatures higher than this would result in rapid MoO_2 volatilization, meaning MoO_2 would leave the sample crucible and the original number of moles of Mo would no longer be accurate.

A.3.8. *Reducing MoO₂ to Form Mo*

As the kinetics of the oxidation of Mo to MoO_2 were too slow for this thesis, the reduction of MoO_2 to Mo was trialed. A pO_2 of 1×10^{-21} atm at 823 K was selected using the CT cell to stabilize MoO_2 *in situ*. Changing the pO_2 to 1×10^{-14} atm at 823 K oxidized the sample to MoO_{2+x}. Finally, the sample was fully reduced in a 10 % H_2 in Ar gas mixture at 1123 K to Mo to determine the number of moles of Mo in the sample. Unfortunately, the high temperatures required for fast kinetics resulted in the volatilization of some Mo giving false stoichiometries much too large ($>MoO_{2.1}$). Lowering the reducing temperature to 923 K resulted in less volatilization, but the effect was still significant. Reduction temperatures below 923 K produced kinetics too slow for this thesis.

A.3.9. *Decomposing (NH₄)₆Mo₇O₂₄ to MoO₃ and then Reducing to MoO₂*

A final *in situ* method to determine the starting stoichiometry of MoO_2 was attempted by decomposing a known amount of $(NH_4)_6Mo_7O_{24}$ to MoO_3 and then reducing to MoO_2. Oxygen does not adhere to the surface of the salt $(NH_4)_6Mo_7O_{24}$, and thus the number of moles of Mo is known if the mass of $(NH_4)_6Mo_7O_{24}$ is known. A sample of $(NH_4)_6Mo_7O_{24}$ was dried and then slowly

heated to 623 K under argon. It decomposed to form $MoO_{3.005}$. It was then attempted to reduce MoO_3 to MoO_2 using a pO_2 of 1.4942×10^{-13} atm. Temperatures up to 873 K were used but the kinetics were too slow. Temperatures above 973 K resulted in a mass corresponding to less than MoO_2, thus Mo was again volatilizing at higher temperatures.

A.3.10.   Mass Balance Error Analysis

The mass balance was calibrated using standard reference materials according to the TGA operational manual prior to any experimentation. The published mass error of the TGA by the manufacturer was ± 0.023 µg for the large mass range setting and should have been sufficient for this experimentation. After the results above, it was deemed necessary to further investigate the sensitivity of the mass balance.

Copper sulphate pentahydrate ($CuSO_4 \cdot 5H_2O$) was selected as a testing material as it dehydrates to $CuSO_4$ at known temperatures independent of the surrounding atmosphere. Additionally, $CuSO_4$ can decompose at higher temperatures and different copper oxides produced depending on pO_2. This test could both validate the mass balance and the CT cell.

A sample of $CuSO_4 \cdot 5H_2O$ was placed in the TGA and slowly heated to 498 K at a rate of 0.5 K min^{-1}. The literature suggests two water molecules are lost at 338 K, two more lost at 363 K, and the last water molecule at 493 K [6]. The sample was then heated to 1273 K at a ramp rate of 20 K min^{-1} to decompose to Copper (II) oxide (CuO). Next, it was subjected to a pO_2 of 1.26×10^{-4} atm at 1273 K for 8 h to stabilize Copper (I) oxide (Cu_2O). Finally, the sample was subjected to 2000 ppm H_2 in Ar (pO_2 of 5.37×10^{-20} atm) at 1273 K to stabilize copper metal (Cu).

The number of moles of Cu should remain constant throughout the experiment; therefore the number of moles of Cu was determined for each species using its measured mass and molar mass. A standard deviation of 1.712 % was found. This result confirms the experimental setup is not sufficient for the data collection needed. It is higher than the 0.08 % mass error necessary for the experimentation and much higher than the published mass error of the TGA by the manufacturer.

A.3.11.   Qualitative Analysis

Since a starting stoichiometry of MoO_2 could not be determined by external or *in situ* methods, only qualitative conclusions can be drawn from the experimental data. While trying to stabilize MoO_2, oxidize to MoO_{2+x}, and then reduce to Mo, as described in section A.3.8, a small increase in mass was seen between stable MoO_2 mass and MoO_{2+x} mass. While this mass gain was within the determined mass error of the TGA and should therefore be discounted, it was observed in six separate tests and different behaviour was never observed. This suggests that this mass gain may be real and not within experimental noise. The greatest degree of hyper-stoichiometry achieved was $MoO_{2.015}$, indicating the deviation from ideal stoichiometry in MoO_2 is likely in the same region predicted by Zador [21] or smaller. Unfortunately, quantitative data confirming this hypothesis was unachievable and the qualitative observation is the only evidence supporting this argument. Section A.4 provides recommendations on how accurate quantitative data can be acquired. Ultimately, if the non-stoichiometry of $MoO_{2\pm x}$ is as small as predicted by Zador and as indicated by this qualitative data, further refinement will not have a significant impact on the RMC-TFM.

A.3.12.   Summary

It was assumed that if the starting stoichiometry of MoO_2 could be determined, changes in stoichiometry could be measured by changes in mass. NAA, ICP MS, titration experiments, and gravimetric analysis all failed to determine the starting stoichiometry of MoO_2 outside the TGA/DSC. *In situ* methods of oxidizing Mo to form MoO_2, reducing MoO_2 to form Mo, and decomposing $(NH_4)_6Mo_7O_{24}$ to MoO_3 and then reducing to MoO_2 also failed. Finally, the $CuSO_4 \cdot 5H_2O$ test showed the mass measurements in the TG had a standard deviation of 1.712 %. This means that the TGA/DSC itself is not accurate enough for the measurements required for this work. Qualitative observations indicated that the non-stoichiometric region of $MoO_{2\pm x}$ is close to that predicted by Zador [21] and further refinement will not have a significant impact on the RMC-TFM. Recommendations for how to complete this work have been given in the next section.

A.4.   Recommendations for Future Work

After experimenting on the non-stoichiometric region of MoO_2, there are two recommendations on how these experiments could best be completed. One method

can be completed by upgrading the current experimental setup at RMC. The second requires a completely different experimental setup.

The best method to complete this research at the RMC would be to purchase a second CT cell and replicate the experimental setup of [19] described in Section 2.5.2. A carrier gas would flow through an upstream CT cell, over a sample, and finally through a downstream CT cell. First, the upstream CT cell would be used to induce a pO_2 that would stabilize $MoO_{2.000}$ by FACTSage calculation and the downstream CT cell used to determine the process is at equilibrium when the downstream pO_2 matches the upstream pO_2. At this point it would be assumed the sample is $MoO_{2.000}$ unless a more accurate determination of the starting stoichiometry could be made. Next, the mass of the sample would be determined via a mass balance. The sample size would be sufficiently large to minimize the mass balance's associated weighing error. Finally, a pO_2 would be created by the upstream CT cell to induce a change in stoichiometry in the $MoO_{2.000}$ sample. The pO_2 in the downstream gas would be continually monitored by the downstream CT cell. By integrating the pO_2 difference between the upstream and downstream CT cells over time, the amount of oxygen obtained or lost by the sample would be known. Coupled with the mass of $MoO_{2.000}$, the degree of non-stoichiometry induced could be determined. This process could be replicated through a range of variables including different pO_2's and temperatures. Additionally, if the time needed to achieve equilibrium is recorded, kinetic data can also be acquired.

An alternative method to achieve this experimentation is the experimental setup used by Zador [21]. They reduced ammonium molybdate to MoO_2 at 773 K in a gas stream of $pH_2/pH_2O = 3$ and then used a high temperature galvanic cell to measure changes in stoichiometry. $9ThO_2+YO_{1.5}$ was used as an electrolyte as it has an ionic transport number very close to one in the pO_2 range investigated and the reference electrode was $FeO_{1.05}$. The electrode unit had to be enclosed and vacuum sealed before each test. By applying an external electrical potential, oxygen atoms could be transported into or out of the dioxide proportional to the current applied. This coulometric titration could only measure changes in composition and the oxygen content of the entire dioxide sample needed to be determined. This was achieved by reducing a 0.8 g sample of the dioxide to a pure metal using pure H_2 at 1073 K. This is not an option at the RMC due to the explosive nature of H_2.

[1] E.A.C. Crouch, "Fission-Product Yields from Neutron-Induced Fission", Atomic Data and Nuclear Data Tables, Vol. 19 (1977) 417-532.

[2] atom.kaeri.re.kr/ton/nuc8.html

[3] G. Gopala Rao and M. Suryanarayana, "Oxidimetric Methods for the Volumetric Determination of Molybdenum (V)", Analytical and Bioanalytical Chemistry, Vol. 169 (1959) 161-169.

[4] G. Gopala Rao and M. Suryanarayana, "A New Volumetric Method for the Determination of Molybdenum (VI)", Analytical and Bioanalytical Chemistry, Vol. 168 (1959) 177-181.

[5] K. Bhaskara Rao, "Titration of Molybdenum (V) with Ceric Sulfate, Using Methyl Orange and Methyl Red as Indicators", Recueil des Travaux Chimiques des Pays-Bas, Vol. 84 (1965) 71-73.

[6] S. El-Houte and M. El-Sayed Ali, "Dehydration of $CuCO_4·5H_2O$ Studies by Conventional and Advanced Thermal Analysis Techniques", Thermochimica Acta, Vol. 138 (1989) 107-114.

Appendix B Coulombic Titration Cells

Coulombic titration or CT cells are used in this research. It is important to understand how they work in order to understand their application in this thesis. A CT cell is used to induce a known amount of oxygen into a carrier gas. In this thesis, 2000 ppm H_2 in Ar is almost exclusively used as the carrier gas. A CT cell operates by running a current through a ZrO_2-$YO_{1.5}$ solid electrolyte. O_2 in the air is pulled across the electrolyte as O^{2-} ions to balance the charge induced by the current. As 4 electrons move from the low [O_2] side of the electrolyte to the high [O_2] side, two O^{2-} ions moves from the high [O_2] side to the low [O_2] side to balance the charge, Figure B-1. The result is an induced oxygen concentration on one side proportional to the amount of current run to the other side of the electrolyte.
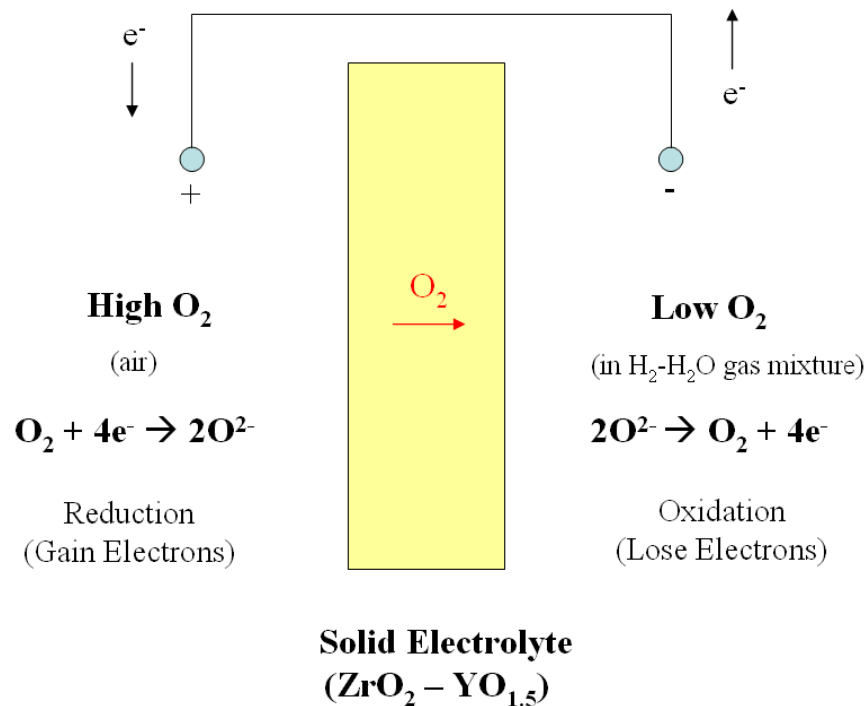
Figure B-1: CT cell function [1]

In an inert carrier gas such as Ar, the oxygen does not react and the amount of oxygen added is directly proportional to the pO_2 of the carrier gas. In a reactive

carrier gas such as one that contains H_2, the oxygen can react with the H_2 in the carrier gas to form H_2O. Due to this phenomenon, extremely small pO_2's (10^{-19} to 10^{-10} atm) can be obtained.

Consider the dissociation of H_2O at equilibrium

$$2H_2O \rightarrow 2H_2 + O_2$$
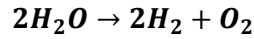
$$\Delta G_{RXN} = \Delta G^o_{RXN} + R\,T \ln\left(\frac{pO_2\,pH_2{}^2}{pH_2O^2}\right)$$

and

$$\Delta G^o_{RXN} = -2\Delta G^o_{f,H_2O}$$

as this is the opposite of the formation of H_2O.

At equilibrium conditions, $\Delta G_{RXN} = 0$ and $\Delta G^o_{RXN} = -RT\ln(K)$, where K is the equilibrium constant. Hence,

$$2\Delta G^o_{f,H_2O} = R\,T \ln\left(\frac{pO_2\,pH_2{}^2}{pH_2O^2}\right) \qquad \text{Equation B-1}$$

This can be re-arranged to give

$$pO_2 = \frac{pH_2O^2}{pH_2{}^2}e^{\left(\frac{2\Delta G^o_{f,H_2O}}{RT}\right)} \qquad \text{Equation B-2}$$

If the H_2:H_2O ratio is controlled by the CT cell, pO_2 at a given temperature can be determined as all other variables are constant and $\Delta G^o_{f,\,H_2O}$ is well-defined for the temperature range of interest. Figure B-2 shows pO_2's achievable over a range of temperature with different H_2:H_2O ratios.
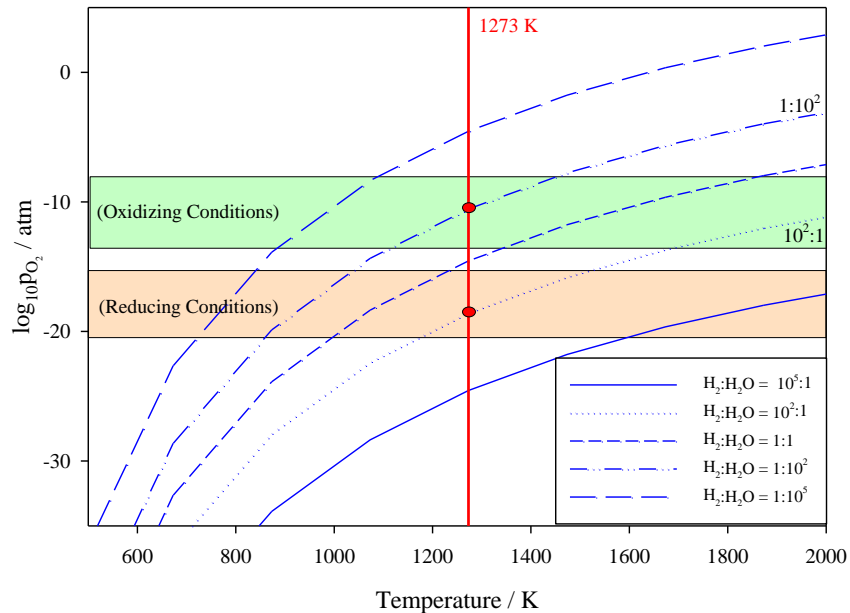
Figure B-2: Relationship between pO_2 and H_2:H_2O over a range of temperatures [19]

Inducing a small pO_2 using a H_2:H_2O ratio from a CT cell differs from small pO_2 induced in an inert gas, such as oxygen impurities in Ar. Although both are small pO_2, a H_2-H_2O gas mixture can buffer the specified pO_2 (*i.e.,* if the O_2 reacts with the sample, the H_2O in the gas mixture will dissociate to form H_2 and O_2 while the H_2:H_2O remains relatively unchanged). This means that a small pO_2 can be induced, O_2 allowed to react, and the pO_2 to remain relatively constant. O_2 in an inert gas, such as an O_2 impurity in Ar, can react with the sample, but will not be replaced by a buffering gas mixture. The pO_2 of the gas mixture will change and the sample will remain relatively unaffected by the small amount of O_2 reacted.

[1] E.C. Corcoran, "Thermochemical Modelling of Advanced CANDU Reactor Fuel", PhD Thesis, Royal Military College of Canada, March 2009.

Appendix C   Thermodynamic Equation Proofs

C.1.   <u>Derivation of Equation 12</u>

Molar heat capacity at constant pressure (C_p) can be obtained by applying a constant pressure to Equation 7,

$$C_P = \frac{dq_P}{dT}$$

Equation C-1

By taking the partial derivative of Equation 4 with respect to V at constant P,

$$dH_P = dU_P + PdV_P$$

Equation C-2

And applying Equation C-3 (the partial derivative of the equation for internal energy),

$$dU = dq - PdV$$

Equation C-3

To obtain

$$dH_P = dq_P$$

Equation C-4

Thus Equation C-1 can be extended to include

$$C_P = \frac{dq_P}{dT} = \frac{dH_P}{dT}$$

Equation C-5

and

$$\Delta H_P = \int_{T_1}^{T_2} C_p dT$$

Equation C-6

Because $\Delta H^o{}_{298K}$ is most often reported in the literature, Equation C-6 can be modified to give ΔH^o for a given temperature T

$$\Delta H^o{}_T = \Delta H^o_{298K} + \int_{298K}^{T} C_p dT$$

Equation 12

C.2.   <u>Derivation of Equation 26</u>

Rearrange Equation 15,

$$dq = TdS$$ Equation C-7

Apply Equation C-3,

$$dU = TdS - PdV$$ Equation C-8

It can be seen in Equation C-8 that internal energy has a slope $+T$ as entropy changes and a slope $-P$ as volume changes.

Next, take the first derivative of Equation 4

$$dH = dU + PdV + VdP$$ Equation C-9

and substitute in Equation C-8

$$dH = TdS + VdP$$ Equation C-10

Next take the first derivative of Equation 23,

$$dG = dH - TdS - SdT$$ Equation C-11

and substitute Equation C-10 into Equation C-11.

$$dG = VdP - SdT$$ Equation C-12

It can be seen that G is dependent on P and T. These variables are commonly experienced and measured during experimentation, showing the usefulness of G.

The pressure dependency of Gibbs free energy is useful when dealing with gases. At constant temperature

$$SdT = 0$$ Equation C-13

Applying Equation C-13 to Equation C-12 for a closed system of fixed chemical composition and constant temperature,

$$dG = VdP \qquad\qquad \text{Equation C-14}$$

Substitute in the ideal gas law

$$PV = nRT \qquad\qquad \text{Equation C-15}$$

For one mol of gas

$$dG = \frac{RT}{P}dP$$

$$\Delta G = \int_{P_1}^{P_2} \frac{RT}{P}dP$$

$$\Delta G = RT \ln\left(\frac{P_2}{P_1}\right) \qquad\qquad \text{Equation C-16}$$

We can use Equation C-16 to define ΔG at some pressure relative to ΔG^o (*i.e.*, ΔG at the standard state of 1 atm).

$$\Delta G = \Delta G^o + RT \ln\left(\frac{P}{1\ atm}\right)$$
$$\Delta G = \Delta G^o + RT \ln(P) \qquad\qquad \text{Equation 26}$$

C.3.   <u>Derivation of Equation 28</u>

The entropy of the surroundings at constant temperature and pressure can be defined by substituting the integral of Equation 9 into Equation 15.

$$\Delta S_{surroundings} = \frac{\Delta H_{P,T,surroundings}}{T}$$ Equation C-17

The change in enthalpy of the surroundings must be equal and opposite to the change in enthalpy of the system.

$$\Delta H_{P,T,surroundings} = -\Delta H_{P,T,system}$$

Therefore

$$\Delta S_{surroundings} = \frac{-\Delta H_{P,T,system}}{T}$$ Equation C-18

Substituting Equation C-18 into the inequality of Equation 14 for an irreversible process and multiplying through by T

$$\Delta H_{P,T,system} - T\Delta S_{system} < 0$$ Equation C-19

Substitute in Equation 23

$$\Delta G_{P,T,system} < 0$$ Equation 28

Appendix D Thermodynamic Data in the RMC-TFM

The following data from the RMC-TFM was used in this thesis.

Compound	Phase	T_{min} (K)	T_{max} (K)	$\Delta H^o_{298\ K}$ (J mol^{-1})	$S^o_{298\ K}$ (J K^{-1} mol^{-1})	C_p (J K^{-1} mol^{-1})	Ref.
H	Gas	298.1	6000.0	217999.00	114.606556	20.7860000	1-3
H$_2$	Gas	298.1	1200.0	0.00	130.570556	$19.8256305 + 0.307772746E\text{-}02T - 295179.899T^{-2} + 0.142984494E\text{-}05T^2 + 194.861244T^{-0.5}$	1-3
	Gas	1200.0	4100.0	-10732.25	103.241627	$14.3874604 + 0.206410759E\text{-}02T + 20833154.9T^{-2} -74353.4040T^{-1} + 2134.83456T^{-0.5}$	
	Gas	4100.0	6000.0	-1129294.58	-2303.92676	$-42.9570600 + 730731789T^{-2} - 931953.898T^{-1} + 17037.9449T^{-0.5}$	
	Aqueous	289.0	573.0	-4184.00	57.739000	$-305.311000 + 0.685703000T + 26420300.0T^{-2}$	
H$_2$O	Solid	250.0	273.0	-292816.20	44.529000	36.2460000	4
	Liquid	298.1	500.0	-285830.00	69.950000	$-203.118982 + 1.52069960T + 3848757.66T^{-2} - 0.319132464E\text{-}02T^2 + 0.247095842E\text{-}05T^3$	1-3
H$_2$O	Gas	298.1	1100.0	-241834.00	188.724556	$25.7816397 + 0.149497163E\text{-}01T - 27999.3194T^{-2} - 0.552355894E\text{-}06T^2 + 1107.27182\ T^{-1}$	1-3

Compound	Phase	T_{min} (K)	T_{max} (K)	$\Delta H^o_{298\,K}$ (J mol^{-1})	$S^o_{298\,K}$ (J K^{-1} mol^{-1})	C_p (J K^{-1} mol^{-1})	Ref.
	Gas	1100.0	4000.0	-252154.99	161.932684	$53.1457895 + 0.161080076E\text{-}03T + 24151166.4T_{-2} - 83128.2757T_{-1}$ $1486.84251T_{-0.5}$	
	Gas	4000.0	6000.0	677934.63	2175.77975	$155.190827 - 596528405T^{-2}$ $778290.990T^{-1} - 16093.085T^{-0.5}$	
HOO	Gas	298.1	2100.0	2092.00	228.996556	$62.9139746 + 0.233783178E\text{-}02T + 811278.469T^{-2} - 2663.71138T^{-1} - 499.012278T^{-0.5}$	5
	Gas	2100.0	6000.0	-69394.23	58.816277	$24.8925885 + 85794204.2T^{-2} - 231446.384T^{-1} + 5577.68739T^{-0.5}$	
HOOH	Liquid	298.0	431.0	-187300.00	109.621000	89.3280000	5
	Gas	298.1	1500.0	-136106.00	232.881556	$78.3148506 - 0.526314543E\text{-}02T + 1370452.46\ T^{-2} + 0.318179288E\text{-}05T^2 - 14710.1342T^{-1}$	
	Aqueous	298.0	473.0	-191209.00	143.930000	$-1069.64800 + 2.74468300T + 4043400.00T^{-2}$	
Mo	Solid	298.0	3000.0	0.00	28.610000	$30.8610000 - 0.729340000E\text{-}02T - 534070.000T^{-2} + 0.515090000E\text{-}05T^2$ *Sol.->Liq T=2896.0K* *ΔH=41403.0 J*	5

Compound	Phase	T_{min} (K)	T_{max} (K)	$\Delta H^o_{298\,K}$ (J mol^{-1})	$S^o_{298\,K}$ (J K^{-1} mol^{-1})	C_p (J K^{-1} mol^{-1})	Ref.
	Liquid	298.0	3000.0	41403.00	42.906616	$30.8610000 - 0.729340000E-02T - 534070.000T^{-2} + 0.515090000E-05T^2$	
	Liquid	3000.0	4919.0	-12370.27	-13.201143	55.2800000 *Liq ->Gas T=4919.2K* *ΔH=589159.8 J*	
	Gas	298.0	5000.0	738347.00	227.840000	$110.886000 - 0.263990000E-01T - 2206221.00T^{-2} + 0.486230000E-05T^2 + 41776.1000T^{-1} - 3814.35000T^{-0.5}$	
Mo$_2$	Gas	298.0	3000.0	913400.00	244.083000	$37.2710720 + 0.364008000E-03T - 244345.600T^{-2}$	5
Mo$_2$O$_6$	Gas	298.0	3000.0	-1119999.99	405.500000	$175.539720 + 0.229701600E-02T - 3929194.40T^{-2}$	5
Mo$_3$O$_9$	Gas	298.0	3000.0	-1858999.99	549.599998	$270.939104 + 0.365681600E-02T - 5595681.60T^{-2}$	5
Mo$_4$O$_{11}$	Solid	298.2	1093.0	-2845630.64	284.499656	$171.343951 + 0.186937902T - 12343957.8T^{-2} + 0.542918000E-05T^2 + 57197.4045T^{-1}$	6
Mo$_4$O$_{12}$	Gas	298.0	3000.0	-2562999.99	671.099998	$367.104160 + 0.461495200E-02T - 7409027.20T^{-2}$	5, 6

Compound	Phase	T_{min} (K)	T_{max} (K)	$\Delta H^o_{298 K}$ (J mol^{-1})	$S^o_{298 K}$ (J K^{-1} mol^{-1})	C_p (J K^{-1} mol^{-1})	Ref.
Mo_5O_{15}	Gas	298.0	3000.0	-3248999.99	788.399998	$463.767112 + 0.552706400E\text{-}02T - 9338269.60T^{-2}$	5, 6
MoO	Gas	298.1	4500.0	310959.00	241.654556	$37.6816653 + 0.194965451E\text{-}03T + 65544.6935T^{-2} - 0.163104150E\text{-}08T^2 - 731.139620T^{-1}$	1-3
	Gas	4500.0	6000.0	554758.22	761.118946	$60.4567789 - 151463147.0T^{-2} + 189284.444T^{-1} - 3801.77963T^{-0.5}$	
MoO_2	Solid	298.2	3000.0	-589500.00	46.459000	$65.6689658 + 0.115585211E\text{-}01T - 1217745.10T^{-2} + 0.542917580E\text{-}05T^2$ *Sol.->Gas T=2963.2K* *ΔH=462341.1 J*	1-3
	Gas	298.2	1600.0	-8314.00	276.880556	$73.6139217\ 0.953584726E\text{-}02T + 1052563.34T^{-2} + 0.222292099E\text{-}05T^2 - 11520.5654T^{-1}$	
	Gas	1600.0	3500.0	37536.12	389.218294	$124.652977 - 69348272.2T^{-2} + 230000.383T^{-1} - 7362.23998T^{-0.5}$	

Compound	Phase	T_{min} (K)	T_{max} (K)	$\Delta H^o_{298\,K}$ (J mol^{-1})	$S^o_{298\,K}$ (J K^{-1} mol^{-1})	C_p (J K^{-1} mol^{-1})	Ref.
MoO$_2$	Gas	3500.0	6000.0	-529513.68	-858.844434	$42.3513685 + 340909034.0T^{-2} - 410307.467T^{-1} + 6348.64860T^{-0.5}$	1-3
MoO$_2$H$_2$ Mo(OH)$_2$	Gas	298.0	3000.0	-183000.00	295.000000	$79.7100986 + 0.138622470E\text{-}01T + 148545.030T^{-2} - 0.956156000E\text{-}06T^2 + 115.699585T^{-0.5} - 2976.23000T^{-1}$	7-10
MoO$_3$	Solid	298.1	1074.0	-751222.10	79.060000	$35.3345099 + 0.583978385E\text{-}01T - 3699475.75T^{-2} + 19007.7514T^{-1}$	1-3, 6
						Sol.->Liq. T=1073.2K ΔH= 48495.6J	
	Liquid	1074.0	1500.0	-702726.45	124.249654	$35.2249951 + 0.584597937E\text{-}01T - 3708737.55T^{-2} + 19065.8015T^{-1}$	
						Liq.>Gas T=2908.4K ΔH= 248470.6J	
	Gas	1500.0	3000.0	-346435.00	283.787556	$83.2016240 - 4656791.25T^{-2} - 2.58607131T^{-0.5} + 762783924.0T^{-3}$	

Compound	Phase	T_{min} (K)	T_{max} (K)	$\Delta H^{o}_{298\,K}$ (J mol^{-1})	$S^{o}_{298\,K}$ (J K^{-1} mol^{-1})	C_p (J K^{-1} mol^{-1})	Ref.
MoOH	Gas	298.0	3000.0	300000.00	263.000000	$56.3352547 + 0.383404300E\text{-}02T + 181470.352T^{-2} + 0.171200000E\text{-}05T^{2} + 57.8497927T^{0.5} - 2976.23000T^{-1}$	7-10
$O_2Mo(OH)_2$	Gas	298.1	1500.0	-851026.00	355.510556	$153.963477 + 0.195375644E\text{-}02T + 1878941.75T^{-2} - 27012.1669T^{-1} + 329.150584T^{-0.5}$	1-3
	Gas	1500.0	6000.0	-848772.08	360.382068	$153.064010 + 3144938.46T^{-2} - 42577.3784T^{-1} + 857.589861T^{-0.5}$	

Compound	Phase	T_{min} (K)	T_{max} (K)	$\Delta H^o_{298\,K}$ (J mol^{-1})	$S^o_{298\,K}$ (J K^{-1} mol^{-1})	C_p (J K^{-1} mol^{-1})	Ref.
O	Gas	298.1	2200.0	249173.00	160.948556	$19.9649683 + 0.263898925E\text{-}03T + 58654.8778\ T^{-2} - 0.369535916E\text{-}07T^2 + 20.9524641T^{-0.5}$	1-3
	Gas	2200.0	6000.0	268898.71	208.033777	$38.0506692 - 24241478.3T^{-2} + 70811.4364T^{-1} - -2082.71338T^{-0.5}$	
O_2	Gas	298.1	1000.0	0.00	205.037556	$26.9240574 + 0.169786815E\text{-}01T + 229329.255T^{-2} - 0.676616525E\text{-}05T^2 - 79.1616586T^{-0.5}$	1-3
	Gas	1000.0	4000.0	6939.76	223.155758	$89.6813271 - 0.144744488E\text{-}02T - 18682685.9T^{-2} - 4126.53721T^{-0.5} + 95803.9595T^{-1}$	
O_2	Gas	4000.0	6000.0	1758559.65	4020.39315	$249.173117 - 0.118497842E\text{+}10T^{-2} - 34935.6696T^{-0.5} + 1674792.24T^{-1}$	1-3
	Aqueous	298.1	400.0	-11715.00	110.876000	$162.230000 + 0.321250000E\text{-}01T + 3161400.00T^{-2}$	

Compound	Phase	T_{min} (K)	T_{max} (K)	$\Delta H^o_{298\,K}$ (J mol^{-1})	$S^o_{298\,K}$ (J K^{-1} mol^{-1})	C_p (J K^{-1} mol^{-1})	Ref.
O$_3$	Gas	298.1	1900.0	142674.00	238.822556	$76.5557641 - 0.922313946E\text{-}02T + 1643688.91T^{-2} + 0.193603005E\text{-}05T^2 - 15871.0065T^{-1}$	1-3
	Gas	1900.0	6000.0	156956.66	273.333592	$73.7136240 - 18640342.9\ T^{-2} + 47079.5829\ T^{-1} - 1534.58525\ T^{-0.5}$	
OH	Gas	298.1	1300.0	38987.00	183.598556	$20.5632667 + 0.725248255E\text{-}02T - 378224.166T^{-2} - 0.205193933E\text{-}06T^2 + 3436.31385T^{-1}$	1-3
	Gas	1300.0	4000.0	29570.28	159.642345	$20.4153782 + 0.924306352E\text{-}03T + 19252666.5T^{-2} - 69526.5184T^{-1} + 1894.25149T^{-0.5}$	
OH	Gas	4000.0	6000.0	274790.98	697.406748	$73.0053619 - 159793237.0T^{-2} + 230246.826T^{-1} - 5230.08972T^{-0.5}$	1-3
U	α-Solid	298.0	942.0	0.00	50.291680	$26.9198560 - 0.250203200E\text{-}02T - 76985.6000T^{-2} + 0.265579400E\text{-}04T^2$	5
	α-Solid	942.0	5000.0	-4316.85	40.478249	42.9278400	

Compound	Phase	T_{min} (K)	T_{max} (K)	$\Delta H^{o}_{298\,K}$ (J mol^{-1})	$S^{o}_{298\,K}$ (J K^{-1} mol^{-1})	C_p (J K^{-1} mol^{-1})	Ref.
	β-Solid	298.0	942.0	2790.73	53.254236	$\alpha \rightarrow \beta$ T= 942.00K ΔH= 2790.728 J 26.9198560 – 0.250203200E-02T – 76985.6000T^{-2} + 0.265579400E-04T^2	
	β-Solid	942.0	1049.0	-1526.12	43.440805	42.9278400	
	β-Solid	1049.0	5000.0	1961.00	49.283240	38.2836000	
	γ-Solid	298.1	1049.0	3231.08	47.975798	$\beta \rightarrow \gamma$ T=1049.00K ΔH=4757.208 J 42.9278400	
	γ-Solid	1049.0	1405.0	6718.21	53.818233	38.2836000	
	Liquid	1405.0	4407.0	4375.22	44.239695	$\gamma \rightarrow$ Liq. T=1405.00K ΔH=9142.04 J 48.6599200	
	Gas	4407.0	5000.0	486669.77	161.473384	Liq.>Gas T=4407.0K ΔH=464106.01 J 44.2332480	4
U_3O_7	Solid	298.0	800.0	-3435454.31	250.194300	250.000000	11
U_3O_8	Solid	298.0	1950.0	-3601658.31	271.675091	265.423470 + 0.493810000E-01T – 0.299931000E-05T^2 – 3537016.40T^{-2}	4
U_4O_9	Solid	298.0	850.0	-4522317.41	334.492400	319.163000 + 0.496910000E-01 – 3960200.00T^{-2}	12
	Solid	850.0	1397.5	-4519997.64	338.612645	281.500000 + 0.888360000E-01T –	

Compound	Phase	T_{min} (K)	T_{max} (K)	$\Delta H^o_{298\,K}$ (J mol^{-1})	$S^o_{298\,K}$ (J K^{-1} mol^{-1})	C_p (J K^{-1} mol^{-1})	Ref.
	Solid	1397.5	3500.0	-4130863.48	864.782995	1175737.60T^{-2} 20.0000000T^{-1}	
UO	Gas	298.0	1400.0	43600.00	248.855998	47.9862960 + 0.511284800E-02T − 2020872.00T^{-2}	5
UO$_2$	α-Solid	298.2	3120.0	-1084910.99	77.821998	52.1743000 + 0.879510000E-01T − 0.842411000E-04T^2 + 0.315420000E-07T^3 − 0.263340000E-11T^4 − 713910.000T^{-2} *α >β T= 298.15K ΔH=0.000 J* *α >β T= 366.56K ΔH=15.130 J* *α >β T=2109.91K ΔH=- 3614.772J*	4
	β-Solid	298.0	3121.0	-1084910.99	77.821998	81.1172000 + 0.453050000E-02T − 1719076.82T^{-2} *β >Liq. T=143.15K ΔH=- 22039.667 J* *β >Liq. T=2892.52K ΔH=123443.6 J*	13
	Liquid	298.2	3120.0	-1092237.91	-3.743554	136.757000	14
	Liquid	3120.0	4500.0	-4737959.07	-7089.09547	0.251360000 + 0.132880000E+10T^{-2} *Liq.>Gas T=4078.87K*	

Compound	Phase	T_{min} (K)	T_{max} (K)	$\Delta H^o_{298\ K}$ (J mol^{-1})	$S^o_{298\ K}$ (J K^{-1} mol^{-1})	C_p (J K^{-1} mol^{-1})	Ref.
						ΔH=413156.6 J	
UO_2	Gas	298.2	2000.0	-466600.00	270.206000	62.3876240 + 0.700820000E-02T − 1459797.60T^{-2}	14
UO_2H_2 $U(OH)_2$	Gas	298.0	3000.0	-343000.00	338.000000	73.6695439 + 0.175543770E-01T − 142836.244T^{-2} + 0.212216000E-04T^2 + 115.699585T$^{-0.5}$	7-10
UO_3	α-Solid	298.0	3500.0	-1229524.51	96.106488	88.7000000 + 0.144900000E-01T − 1009000.00T^{-2}	5
	β-Solid	298.0	3100.0	2008769.34	7737.47360	-12888.6925 + 4.81843298T − 0.593746420E+10T^{-2} − 0.629699000E-03T^2 + 14739079.0T^{-1}	11
						β >γ T=10895.97K ΔH=-7152656 J	
	γ-Solid	298.0	3120.0	-1790740.82	937.198000	-492.405379	13
$UO_3(H_2O)$	Solid	298.0	800.0	-1537620.00	134.306400	123.428000 + 0.648520000E-01T − 2259360.00T^{-2}	4

Compound	Phase	T_{min} (K)	T_{max} (K)	$\Delta H^o_{298 K}$ (J mol^{-1})	$S^o_{298 K}$ (J K^{-1} mol^{-1})	C_p (J K^{-1} mol^{-1})	Ref.
UO$_3$(H$_2$O)	Gas	298.1	1000.0	-1199941.91	369.894888	$101.089624 + 0.489779040\text{E-}01T - 1178632.80T^{-2} - 0.179075200\text{E-}04T^2$	15
	Gas	1000.0	3000.0	-1194761.56	382.717305	$127.072264 + 0.118951120\text{E-}01T - 6168471.20T^{-2} - 0.181167200\text{E-}05T^2$	
UOH	Gas	298.0	3000.0	86000.00	272.000000	$50.2947000 + 0.752617200\text{E-}02T - 109910.922T^{-2} + 0.238898000\text{E-}04T^2 + 57.8497927T^{-0.5}$	7-10

MoO$_{2\pm x}$ Solution File:

TYPE 1 SOLUTION (Kohler/Toop Polynomial)

Energy in JOULES

COMPONENT NUMBER		PARTICLES PER MOLE	EQ. FRAC. PARAM	GROUP	COMPOSITION LIMIT
1	Mo*O2	1.000	1.0000	1	1.000
2	Mo*O	1.000	1.0000	1	1.000
3	Mo*O3	1.000	1.0000	1	1.000

G0 = G0(reference phase from main F*A*C*T file)
+ (A + B*T + C*T**2 + D*T**U + E*T**V + F*T*ln(T) + G/T
  + H*T**W + I*T**X)

COMP. NO.	REF. PHASE (if any)	A	B	C	D
		E	F	G	H
		I	U	V	W	X
1	S1 <---	0.0000000E+00	0.0000000E+00	0.0000000E+00	0.0000000E+00
		0.0000000E+00	0.0000000E+00	0.0000000E+00	0.0000000E+00
		0.0000000E+00	3.0000	4.0000	0.0000	0.0000
2		-0.2933834E+06	0.2367876E+03	0.0000000E+00	0.0000000E+00
		0.0000000E+00	-0.4000000E+02	0.0000000E+00	0.0000000E+00
		0.0000000E+00	3.0000	4.0000	0.0000	0.0000
3	S1 <---	0.2000000E+05	0.0000000E+00	0.0000000E+00	0.0000000E+00
		0.0000000E+00	0.0000000E+00	0.0000000E+00	0.0000000E+00
		0.0000000E+00	3.0000	4.0000	0.0000	0.0000

LIST COMPONENTS WHICH MAY BE GROUPED TOGETHER
 NO.

- no lists, all components can be grouped together

Ge term = (XM**I)(XN**J)(XQ**K)(XR**L)*(A + B*T + C*T*ln(T))
  "R-K" indicates a binary Redlich-Kister term:
    XM*XN*(XN-XM)**J)*(A + B*T + C*T*(ln(T))
  "LEG" indicates a binary Legendre term:
    XM*XN*P(J,(XN-XM))*(A + B*T + C*T*ln(T))
  "T" indicates magnetic TC(K) term in Red-Kister format
  "B" indicates magnetic moment term in Red-Kister format

PARAM. M N Q R   I J K L   A   B   C

UO$_{2\pm x}$ Solid with Dilute Fission Products Solution File:

TYPE 1 SOLUTION (Kohler/Toop Polynomial)

Energy in JOULES

COMPONENT NUMBER		PARTICLES PER MOLE	EQ. FRAC. PARAM	GROUP	COMPOSITION LIMIT
1	U*O2	1.000	1.0000	1	1.000
2	U*O3	1.000	1.0000	1	1.000
3	U*O	1.000	1.0000	1	1.000
4	Cs2O	2.000	1.0000	1	1.000
5	Sr*O	1.000	1.0000	1	1.000
6	Ce*O2	1.000	1.0000	1	1.000
7	Ba*O	1.000	1.0000	1	1.000
8	La2O3	2.000	1.0000	1	1.000
9	Pr2O3	2.000	1.0000	1	1.000
10	Nd2O3	2.000	1.0000	1	1.000
11	Y2O3	2.000	1.0000	1	1.000
12	Nb*O2	1.000	1.0000	1	1.000
13	Mo*O2	1.000	1.0000	1	1.000
14	Te*O2	1.000	1.0000	1	1.000
15	Zr*O2	1.000	1.0000	1	1.000
16	Ce2O3	2.000	1.0000	1	1.000
17	Dy2O3	2.000	1.0000	1	1.000
18	Pu*O2	1.000	1.0000	1	1.000
19	Np*O2	1.000	1.0000	1	1.000
20	Rb2O	2.000	1.0000	1	1.000
21	Ho2O3	2.000	1.0000	1	1.000

G0 = G0(reference phase from main F*A*C*T file)
+ (A + B*T + C*T**2 + D*T**U + E*T**V + F*T*ln(T) + G/T
  + H*T**W + I*T**X)

COMP. NO.	REF. PHASE (if any)	A E I	B F U	C G V	D H W	X
1	S1 <---	0.0000000E+00 0.0000000E+00 0.0000000E+00	0.0000000E+00 0.0000000E+00 3.0000	0.0000000E+00 0.0000000E+00 4.0000	0.0000000E+00 0.0000000E+00 0.0000	0.0000
2	S2 <---	0.0000000E+00 0.0000000E+00 0.0000000E+00	0.0000000E+00 0.0000000E+00 3.0000	0.0000000E+00 0.0000000E+00 4.0000	0.0000000E+00 0.0000000E+00 0.0000	0.0000
3		-0.5165843E+06 0.0000000E+00 0.0000000E+00	0.6029652E+03 -0.9493200E+02 3.0000	0.0000000E+00 0.0000000E+00 4.0000	0.0000000E+00 0.0000000E+00 0.0000	0.0000
4	S1	0.2300000E+03	0.0000000E+00	0.0000000E+00	0.0000000E+00	

```
                    0.0000000E+00  0.0000000E+00  0.0000000E+00  0.0000000E+00
                    0.0000000E+00   3.0000   4.0000   0.0000   0.0000
   5    S1          0.3100000E+05  0.0000000E+00  0.0000000E+00  0.0000000E+00
                    0.0000000E+00  0.0000000E+00  0.0000000E+00  0.0000000E+00
                    0.0000000E+00   3.0000   4.0000   0.0000   0.0000
   6    S1          0.0000000E+00  0.0000000E+00  0.0000000E+00  0.0000000E+00
                    0.0000000E+00  0.0000000E+00  0.0000000E+00  0.0000000E+00
                    0.0000000E+00   3.0000   4.0000   0.0000   0.0000
   7    S1          0.9700000E+05  0.0000000E+00  0.0000000E+00  0.0000000E+00
                    0.0000000E+00  0.0000000E+00  0.0000000E+00  0.0000000E+00
                    0.0000000E+00   3.0000   4.0000   0.0000   0.0000
   8    S1          0.1026712E+05  0.0000000E+00  0.0000000E+00  0.0000000E+00
                    0.0000000E+00  0.0000000E+00  0.0000000E+00  0.0000000E+00
                    0.0000000E+00   3.0000   4.0000   0.0000   0.0000
   9    S1          0.8685115E+04  0.0000000E+00  0.0000000E+00  0.0000000E+00
                    0.0000000E+00  0.0000000E+00  0.0000000E+00  0.0000000E+00
                    0.0000000E+00   3.0000   4.0000   0.0000   0.0000
  10    S1          0.5239115E+04  0.0000000E+00  0.0000000E+00  0.0000000E+00
                    0.0000000E+00  0.0000000E+00  0.0000000E+00  0.0000000E+00
                    0.0000000E+00   3.0000   4.0000   0.0000   0.0000
  11       S1  <---   0.1420185E+05    0.0000000E+00    0.0000000E+00    0.0000000E+00
                                      0.0000000E+000.0000000E+00
0.0000000E+00  0.0000000E+00
                    0.0000000E+00   3.0000   4.0000   0.0000   0.0000
  12    S3          0.6305600E+05  0.0000000E+00  0.0000000E+00  0.0000000E+00
                    0.0000000E+00  0.0000000E+00  0.0000000E+00  0.0000000E+00
                    0.0000000E+00   3.0000   4.0000   0.0000   0.0000
  13    S1 <---  0.5880000E+06 -0.2900000E+03  0.0000000E+00  0.0000000E+00
                    0.0000000E+00  0.0000000E+00  0.0000000E+00  0.0000000E+00
                    0.0000000E+00   3.0000   4.0000   0.0000   0.0000
  14    S1         -0.4990000E+06  0.0000000E+00  0.0000000E+00  0.0000000E+00
                    0.0000000E+00  0.0000000E+00  0.0000000E+00  0.0000000E+00
                    0.0000000E+00   3.0000   4.0000   0.0000   0.0000
  15    S1          0.1096360E+06 -0.4413300E+02  0.0000000E+00  0.0000000E+00
                    0.0000000E+00  0.0000000E+00  0.0000000E+00  0.0000000E+00
                    0.0000000E+00   3.0000   4.0000   0.0000   0.0000
  16    S1          0.0000000E+00  0.0000000E+00  0.0000000E+00  0.0000000E+00
                    0.0000000E+00  0.0000000E+00  0.0000000E+00  0.0000000E+00
                  0.0000000E+00   3.0000   4.0000   0.0000   0.0000
  17    S1 <---  0.0000000E+00  0.0000000E+00  0.0000000E+00  0.0000000E+00
                    0.0000000E+00  0.0000000E+00  0.0000000E+00  0.0000000E+00
                    0.0000000E+00   3.0000   4.0000   0.0000   0.0000
  18    S1          0.0000000E+00  0.0000000E+00  0.0000000E+00  0.0000000E+00
                    0.0000000E+00  0.0000000E+00  0.0000000E+00  0.0000000E+00
                    0.0000000E+00   3.0000   4.0000   0.0000   0.0000
  19    S1 <---  0.0000000E+00  0.0000000E+00  0.0000000E+00  0.0000000E+00
                    0.0000000E+00  0.0000000E+00  0.0000000E+00  0.0000000E+00
```

```
                    0.0000000E+00   3.0000   4.0000   0.0000   0.0000
 20   S1          0.2300000E+03  0.0000000E+00  0.0000000E+00  0.0000000E+00
                    0.0000000E+00  0.0000000E+00  0.0000000E+00  0.0000000E+00
                    0.0000000E+00   3.0000   4.0000   0.0000   0.0000
 21   S1          0.0000000E+00  0.0000000E+00  0.0000000E+00  0.0000000E+00
                    0.0000000E+00  0.0000000E+00  0.0000000E+00  0.0000000E+00
                    0.0000000E+00   3.0000   4.0000   0.0000   0.0000
```

LIST   COMPONENTS WHICH MAY BE GROUPED TOGETHER
 NO.
 1   1 2 3 4 5 6 7 8 9 10 11 12 13 14 15 16 17 18 19 20

Ge term = (XM**I)(XN**J)(XQ**K)(XR**L)*(A + B*T + C*T*ln(T))
    "R-K" indicates a binary Redlich-Kister term:
        XM*XN*(XN-XM)**J)*(A + B*T + C*T*(ln(T))
    "LEG" indicates a binary Legendre term:
        XM*XN*P(J,(XN-XM))*(A + B*T + C*T*ln(T))
    "T" indicates magnetic TC(K) term in Red-Kister format
    "B" indicates magnetic moment term in Red-Kister format

```
PARAM.  M  N  Q  R    I J K L       A           B           C
 1     1  2  0  0    1 1 0 0    0.0000000E+00 -0.7151486E+03  0.0000000E+00
 2     1  2  0  0    1 2 0 0    0.0000000E+00 -0.7058900E+03  0.0000000E+00
 3     1  2  0  0    1 3 0 0    0.0000000E+00 -0.6033030E+03  0.0000000E+00
 4     1 17  0  0    1 3 0 0    0.4200000E+05  0.0000000E+00  0.0000000E+00
 5     1  2  0  0    1 4 0 0    0.0000000E+00 -0.9630000E+03  0.0000000E+00
 6     1 21  0  0    1 3 0 0    0.4200000E+05  0.0000000E+00  0.0000000E+00
```

UO$_{2\pm x}$ Liquid with Dilute Fission Products Solution File:

TYPE 1 SOLUTION (Kohler/Toop Polynomial)

Energy in JOULES

COMPONENT NUMBER		PARTICLES PER MOLE	EQ. FRAC. PARAM	GROUP	COMPOSITION LIMIT
1	U*O2	1.000	1.0000	1	1.000
2	U*O3	1.000	1.0000	1	1.000
3	U*O	1.000	1.0000	1	1.000
4	Pu*O2	1.000	1.0000	1	1.000
5	Np*O2	1.000	1.0000	1	1.000
6	U	1.000	1.0000	1	1.000
7	Zr*O2	1.000	1.0000	1	1.000
8	Ce2O3	2.000	1.0000	1	1.000
9	Nd2O3	2.000	1.0000	1	1.000
10	Sr*O	1.000	1.0000	1	1.000
11	Ba*O	1.000	1.0000	1	1.000
12	La2O3	2.000	1.0000	1	1.000
13	Y2O3	2.000	1.0000	1	1.000
14	Mo*O3	1.000	1.0000	1	1.000
15	Cs2O2	1.000	1.0000	1	1.000
16	Sr	1.000	1.0000	1	1.000
17	Sr(O*H)2	1.000	1.0000	1	1.000
18	Zr	1.000	1.0000	1	1.000
19	Ru*O4	1.000	1.0000	1	1.000
20	Cs	1.000	1.0000	1	1.000
21	Cs*O*H	1.000	1.0000	1	1.000
22	Ba	1.000	1.0000	1	1.000
23	La	1.000	1.0000	1	1.000
24	Ce	1.000	1.0000	1	1.000
25	Nd	1.000	1.0000	1	1.000
26	I2	2.000	1.0000	1	1.000
27	Cs*I	1.000	1.0000	1	1.000
28	Ba*I2	1.000	1.0000	1	1.000
29	La*I3	1.000	1.0000	1	1.000
30	Ce*I3	1.000	1.0000	1	1.000
31	Pr*I3	1.000	1.0000	1	1.000
32	Nd*I3	1.000	1.0000	1	1.000
33	U*I4	1.000	1.0000	1	1.000
34	Pu*I3	1.000	1.0000	1	1.000
35	Rb*I	1.000	1.0000	1	1.000
36	Sr*I2	1.000	1.0000	1	1.000
37	Zr*I2	1.000	1.0000	1	1.000

G0 = G0(reference phase from main F*A*C*T file)

+ (A + B*T + C*T**2 + D*T**U + E*T**V + F*T*ln(T) + G/T
  + H*T**W + I*T**X)

COMP. NO.	REF. PHASE (if any)	A E I	B F U	C G V	D H W	X
1	S1 <---	0.6935000E+05	-0.2200000E+02	0.0000000E+00	0.0000000E+00	
		0.0000000E+00	0.0000000E+00	0.0000000E+00	0.0000000E+00	
		0.0000000E+00	3.0000	4.0000	0.0000	0.0000
2	S1 <---	0.1754967E+06	-0.7142900E+02	0.0000000E+00	0.0000000E+00	
		0.0000000E+00	0.0000000E+00	0.0000000E+00	0.0000000E+00	
		0.0000000E+00	3.0000	4.0000	0.0000	0.0000
3		-0.9001395E+05	-0.7430215E+03	0.0000000E+00	0.0000000E+00	
		0.0000000E+00	0.5487040E+02	0.0000000E+00	0.0000000E+00	
		0.0000000E+00	3.0000	4.0000	0.0000	0.0000
4	L1	0.0000000E+00	0.0000000E+00	0.0000000E+00	0.0000000E+00	
		0.0000000E+00	0.0000000E+00	0.0000000E+00	0.0000000E+00	
		0.0000000E+00	3.0000	4.0000	0.0000	0.0000
5	L1 <---	0.0000000E+00	0.0000000E+00	0.0000000E+00	0.0000000E+00	
		0.0000000E+00	0.0000000E+00	0.0000000E+00	0.0000000E+00	
		0.0000000E+00	3.0000	4.0000	0.0000	0.0000
6	L1	0.0000000E+00	0.0000000E+00	0.0000000E+00	0.0000000E+00	
		0.0000000E+00	0.0000000E+00	0.0000000E+00	0.0000000E+00	
		0.0000000E+00	3.0000	4.0000	0.0000	0.0000
7	L1	0.0000000E+00	0.0000000E+00	0.0000000E+00	0.0000000E+00	
		0.0000000E+00	0.0000000E+00	0.0000000E+00	0.0000000E+00	
		0.0000000E+00	3.0000	4.0000	0.0000	0.0000
8	L1	0.0000000E+00	0.0000000E+00	0.0000000E+00	0.0000000E+00	
		0.0000000E+00	0.0000000E+00	0.0000000E+00	0.0000000E+00	
		0.0000000E+00	3.0000	4.0000	0.0000	0.0000
9	L1	0.0000000E+00	0.0000000E+00	0.0000000E+00	0.0000000E+00	
		0.0000000E+00	0.0000000E+00	0.0000000E+00	0.0000000E+00	
		0.0000000E+00	3.0000	4.0000	0.0000	0.0000
10	L1	0.0000000E+00	0.0000000E+00	0.0000000E+00	0.0000000E+00	
		0.0000000E+00	0.0000000E+00	0.0000000E+00	0.0000000E+00	
		0.0000000E+00	3.0000	4.0000	0.0000	0.0000
11	L1	0.0000000E+00	0.0000000E+00	0.0000000E+00	0.0000000E+00	
		0.0000000E+00	0.0000000E+00	0.0000000E+00	0.0000000E+00	
		0.0000000E+00	3.0000	4.0000	0.0000	0.0000
12	L1	0.0000000E+00	0.0000000E+00	0.0000000E+00	0.0000000E+00	
		0.0000000E+00	0.0000000E+00	0.0000000E+00	0.0000000E+00	
		0.0000000E+00	3.0000	4.0000	0.0000	0.0000
13	L1 <---	0.0000000E+00	0.0000000E+00	0.0000000E+00	0.0000000E+00	
		0.0000000E+00	0.0000000E+00	0.0000000E+00	0.0000000E+00	
		0.0000000E+00	3.0000	4.0000	0.0000	0.0000
14	L1 <---	0.0000000E+00	0.0000000E+00	0.0000000E+00	0.0000000E+00	
		0.0000000E+00	0.0000000E+00	0.0000000E+00	0.0000000E+00	
		0.0000000E+00	3.0000	4.0000	0.0000	0.0000

```
15  L1 <---   0.0000000E+00  0.0000000E+00  0.0000000E+00  0.0000000E+00
              0.0000000E+00  0.0000000E+00  0.0000000E+00  0.0000000E+00
              0.0000000E+00   3.0000    4.0000    0.0000    0.0000
16  L1        0.0000000E+00  0.0000000E+00  0.0000000E+00  0.0000000E+00
              0.0000000E+00  0.0000000E+00  0.0000000E+00  0.0000000E+00
              0.0000000E+00   3.0000    4.0000    0.0000    0.0000
17  L1        0.0000000E+00  0.0000000E+00  0.0000000E+00  0.0000000E+00
              0.0000000E+00  0.0000000E+00  0.0000000E+00  0.0000000E+00
              0.0000000E+00   3.0000    4.0000    0.0000    0.0000
18  L1        0.0000000E+00  0.0000000E+00  0.0000000E+00  0.0000000E+00
              0.0000000E+00  0.0000000E+00  0.0000000E+00  0.0000000E+00
              0.0000000E+00   3.0000    4.0000    0.0000    0.0000
19  L1        0.0000000E+00  0.0000000E+00  0.0000000E+00  0.0000000E+00
              0.0000000E+00  0.0000000E+00  0.0000000E+00  0.0000000E+00
              0.0000000E+00   3.0000    4.0000    0.0000    0.0000
20  L1        0.0000000E+00  0.0000000E+00  0.0000000E+00  0.0000000E+00
              0.0000000E+00  0.0000000E+00  0.0000000E+00  0.0000000E+00
                    0.0000000E+00   3.0000    4.0000    0.0000    0.0000
21  L1        0.0000000E+00  0.0000000E+00  0.0000000E+00  0.0000000E+00
              0.0000000E+00  0.0000000E+00  0.0000000E+00  0.0000000E+00
              0.0000000E+00   3.0000    4.0000    0.0000    0.0000
22  L1        0.0000000E+00  0.0000000E+00  0.0000000E+00  0.0000000E+00
              0.0000000E+00  0.0000000E+00  0.0000000E+00  0.0000000E+00
              0.0000000E+00   3.0000    4.0000    0.0000    0.0000
23  L1        0.0000000E+00  0.0000000E+00  0.0000000E+00  0.0000000E+00
              0.0000000E+00  0.0000000E+00  0.0000000E+00  0.0000000E+00
              0.0000000E+00   3.0000    4.0000    0.0000    0.0000
24  L1        0.0000000E+00  0.0000000E+00  0.0000000E+00  0.0000000E+00
              0.0000000E+00  0.0000000E+00  0.0000000E+00  0.0000000E+00
              0.0000000E+00   3.0000    4.0000    0.0000    0.0000
25  L1        0.0000000E+00  0.0000000E+00  0.0000000E+00  0.0000000E+00
              0.0000000E+00  0.0000000E+00  0.0000000E+00  0.0000000E+00
              0.0000000E+00   3.0000    4.0000    0.0000    0.0000
26  L1        0.0000000E+00  0.0000000E+00  0.0000000E+00  0.0000000E+00
              0.0000000E+00  0.0000000E+00  0.0000000E+00  0.0000000E+00
              0.0000000E+00   3.0000    4.0000    0.0000    0.0000
27  L1        0.0000000E+00  0.0000000E+00  0.0000000E+00  0.0000000E+00
              0.0000000E+00  0.0000000E+00  0.0000000E+00  0.0000000E+00
              0.0000000E+00   3.0000    4.0000    0.0000    0.0000
28  L1        0.0000000E+00  0.0000000E+00  0.0000000E+00  0.0000000E+00
              0.0000000E+00  0.0000000E+00  0.0000000E+00  0.0000000E+00
              0.0000000E+00   3.0000    4.0000    0.0000    0.0000
29  L1        0.0000000E+00  0.0000000E+00  0.0000000E+00  0.0000000E+00
              0.0000000E+00  0.0000000E+00  0.0000000E+00  0.0000000E+00
              0.0000000E+00   3.0000    4.0000    0.0000    0.0000
30  L1        0.0000000E+00  0.0000000E+00  0.0000000E+00  0.0000000E+00
              0.0000000E+00  0.0000000E+00  0.0000000E+00  0.0000000E+00
```

```
                              0.0000000E+00   3.0000   4.0000   0.0000   0.0000
  31   L1      0.0000000E+00 0.0000000E+00 0.0000000E+00 0.0000000E+00
               0.0000000E+00 0.0000000E+00 0.0000000E+00 0.0000000E+00
               0.0000000E+00   3.0000   4.0000   0.0000   0.0000
  32   L1      0.0000000E+00 0.0000000E+00 0.0000000E+00 0.0000000E+00
                   0.0000000E+00          0.0000000E+00          0.0000000E+00
0.0000000E+00
               0.0000000E+00   3.0000   4.0000   0.0000   0.0000
  33   L1      0.0000000E+00 0.0000000E+00 0.0000000E+00 0.0000000E+00
               0.0000000E+00 0.0000000E+00 0.0000000E+00 0.0000000E+00
               0.0000000E+00   3.0000   4.0000   0.0000   0.0000
  34   L1      0.0000000E+00 0.0000000E+00 0.0000000E+00 0.0000000E+00
               0.0000000E+00 0.0000000E+00 0.0000000E+00 0.0000000E+00
               0.0000000E+00   3.0000   4.0000   0.0000   0.0000
  35   L1      0.0000000E+00 0.0000000E+00 0.0000000E+00 0.0000000E+00
               0.0000000E+00 0.0000000E+00 0.0000000E+00 0.0000000E+00
               0.0000000E+00   3.0000   4.0000   0.0000   0.0000
  36   L1      0.0000000E+00 0.0000000E+00 0.0000000E+00 0.0000000E+00
               0.0000000E+00 0.0000000E+00 0.0000000E+00 0.0000000E+00
               0.0000000E+00   3.0000   4.0000   0.0000   0.0000
  37   L1      0.0000000E+00 0.0000000E+00 0.0000000E+00 0.0000000E+00
               0.0000000E+00 0.0000000E+00 0.0000000E+00 0.0000000E+00
               0.0000000E+00   3.0000   4.0000   0.0000   0.0000
```

LIST   COMPONENTS WHICH MAY BE GROUPED TOGETHER
 NO.

- no lists, all components can be grouped together

Ge term = (XM**I)(XN**J)(XQ**K)(XR**L)*(A + B*T + C*T*ln(T))
   "R-K" indicates a binary Redlich-Kister term:
       XM*XN*(XN-XM)**J)*(A + B*T + C*T*(ln(T))
   "LEG" indicates a binary Legendre term:
       XM*XN*P(J,(XN-XM))*(A + B*T + C*T*ln(T))
   "T" indicates magnetic TC(K) term in Red-Kister format
   "B" indicates magnetic moment term in Red-Kister format

```
PARAM.  M N Q R   I J K L        A            B            C
  1    1 2 0 0   1 1 0 0    -0.5010000E+05  0.0000000E+00  0.0000000E+00
  2    1 6 0 0   1 1 0 0     0.9088440E+06 -0.2260000E+03  0.0000000E+00
  3    3 6 0 0   1 1 0 0     0.6500000E+05  0.0000000E+00  0.0000000E+00
  4    1 3 0 0   1 1 0 0    -0.6000000E+03  0.0000000E+00  0.0000000E+00
```

UO₃-MoO₃ Liquid Solution File:

TYPE 1 SOLUTION (Kohler/Toop Polynomial)

Energy in JOULES

COMPONENT NUMBER		PARTICLES PER MOLE	EQ. FRAC. PARAM	GROUP	COMPOSITION LIMIT
1	U*O3	1.000	1.0000	1	1.000
2	Mo*O3	1.000	1.0000	1	1.000

G0 = G0(reference phase from main F*A*C*T file)
+ (A + B*T + C*T**2 + D*T**U + E*T**V + F*T*ln(T) + G/T
  + H*T**W + I*T**X)

COMP. NO.	REF. PHASE (if any)	A	B	C	D
		E	F	G	H
		I	U	V	W	X
1	S1 -> L1	17.54967E+04	-71.429E+00	0.0000000E+00	0.0000000E+00
		0.0000000E+00	0.0000000E+00	0.0000000E+00	0.0000000E+00
		0.0000000E+00	3.0000	4.0000	0.0000	0.0000

LIST COMPONENTS WHICH MAY BE GROUPED TOGETHER
NO.

- no lists, all components can be grouped together

Ge term = (XM**I)(XN**J)(XQ**K)(XR**L)*(A + B*T + C*T*ln(T))
  "R-K" indicates a binary Redlich-Kister term:
    XM*XN*(XN-XM)**J)*(A + B*T + C*T*(ln(T))
  "LEG" indicates a binary Legendre term:
    XM*XN*P(J,(XN-XM))*(A + B*T + C*T*ln(T))
  "T" indicates magnetic TC(K) term in Red-Kister format
  "B" indicates magnetic moment term in Red-Kister format

PARAM.	M N Q R	I J K L	A	B	C
1	1 2 0 0	1 1 0 0	-2.25250E+05	5.0E+01	0.0000000E+00

[1] US Department of Commerce, "JANAF Thermochemical Tables", National Bureau of Standards/Institute for Applied Technology, Washington, D.C., USA. June 1971, supplements 1974, 1975.
[2] M.W. Chase, Jr., C.A. Davies, J.R. Downey, Jr., D.J. Frurip, R.A. McDonald, and A.N. Syverud, "JANAF Thermochemical Tables: 3rd Edition", J. of Phys. and Chem. Ref. / National Bureau of Standards, US Department of Commerce, Washington D.C., USA (1985).

[3] M.W. Chase, Jr., "JANAF Thermochemical Tables: 4rd Edition", J, of Phys, and Chem. Ref, National Bureau of Standards, US Department of Commerce, Washington D.C., USA, (1998).

[4] I. Barin, O. Knacke, and O. Kubaschewski, "Thermochemical Properties of Inorganic Substances", Springer-Verlag, Berlin, 1973 and Supplement 1977.

[5] E.H.P. Cordfunke and R.J.M. Konings, "Thermochemical Data for Reactor Materials and Fission Products", Elsevier Science Publishers, Amsterdam, 1990.

[6] B. Phillips, Transactions of the Metallurgical Society, Vol. 233 (1965) 1433-1436.

[7] D. Cubicciotti, "A Model for Release of Fission Gases and Volatile Fission Products from Irradiated UO_2 in Steam Environment", Nuclear Technology, Vol. 53 (1981) 5-7.

[8] D. Cubicciotti, "Vaporization Thermodynamics of Fission Products from Fuel Under Nuclear-Accident Conditions", Advances in Ceramics, Vol. 17 (1986) 211-222.

[9] D. Cubicciotti, B.R. Sehgal, "Vapour Transport of Fission Products in Postulated Severe Light Water Reactor Accidents", Nuclear Technology, Vol. 65 (1984) 266-291.

[10] D. Cubicciotti, "Vapour Transport of Fission Products Under Nuclear-Accident Conditions", Journal of Nuclear Materials, Vol. 154 (1988) 53-61.

[11] J.D. Higgs, "Modelling Oxidation Behaviour in Operating Defective Nuclear Reactor Fuel Elements", Doctoral Thesis, The Royal Military College of Canada, Kingston, Ontario, (2006).

[12] D. Labroche, O. Dugne, and C. Chatillon, "Thermodynamics of the O-U System. I - Oxygen Chemical Potential Critical Assessment in the UO_2-U_3O_8 Composition Range", Journal of Nuclear Materials, Vol. 312 (2003) 21-49.

[13] Private Communication, M.H. Kaye to E.C. Corcoran, 2006.

[14] J.K. Fink, "Thermophysical Properties of Uranium Dioxide- A Review", Journal of Nuclear Materials, Vol. 279 (2000) 1-18.

[15] Private Communication, M. Adamson to M.H. Kaye, Lawrence Livermore Laboratories, 1994.

Appendix E   Example Input and Output of RMC-TFM

Initial Product Inventory:
0.56849E-02 mol U
0.11667E-06 mol Zr
0.14263E-04 mol Mo
0.75956E-07 mol Ce
0.42121E-05 mol Ru
0.86762E-07 mol Sr
0.99634E-07 mol Ba
0.38310E-07 mol La
0.18974E-06 mol Nd
0.10003E-04 mol Pd
0.73875E-06 mol Rh
0.12584E-08 mol Cs
0.57078E-02 mol O_2
0 mol H_2

Temperature:
1173 K

Pressure:
1 atm

Databases Selected:
RMC compound database
RMC solution database

Figure E-1: Example input required to represent a SIMFUEL 1 at 1173 K and 1 atm exposed to an oxygen partial pressure of 0.61414E-12 atm

0 mol Ideal Gas

5.6848E-03 mol Fluorite
0.99717	UO_2
2.7777E-03	UO_3
2.6130E-15	UO
3.8732E-10	Cs_2O
1.0863E-07	SrO
1.3007E-05	CeO_2
2.5807E-10	BaO
3.3695E-06	La_2O_3
1.6688E-05	Nd_2O_3
1.0237E-09	MoO_2
2.0523E-05	ZrO_2
1.7728E-07	Ce_2O_3

$UO_{2\pm x}$ and Dilute Soluble Fission Products

1.0645E-05 mol FCCN
1.5215E-02	Mo
0.87909	Pd
8.9139E-02	Ru
1.6557E-02	Rh

Face Centred Cubic Noble Metals

4.5307E-06 mol HCPN
1.3291E-02	Mo
0.14233	Pd
0.72023	Ru
0.12415	Rh

Hexagonal Close Packed Noble Metals

0 mol BCCN

0 mol Liquid

0 mol Rhombohedral

1.3440E-05 mol $MoO_{2(s)}$
4.1396E-07 mol $UMoO_{6(s)}$
9.9633E-08 mol $BaMoO_{4(s)}$
8.6144E-08 mol $MoSrO_{4(s)}$
6.2700E-10 mol $Cs_2MoO_{4(l)}$

Insoluble Oxides

Figure E-2: Example output representing a SIMFUEL 1 at 1173 K and 1 atm exposed to an oxygen partial pressure of 0.61414E-12 atm

Appendix F   Quality Assurance of the C_p Method

The C_p of known standard materials was determined using the method published in ASTM E1269-11 [1] to ensure the experimental setup at the RMC could accurately measure the C_p of materials. The C_p of aluminum metal and MoO_3 powder was determined using the same experimental setup and procedure as used for the unknown material C_p determination. An accuracy of $\pm$ 5 % was determined as seen in Figures F-1 and F-2.
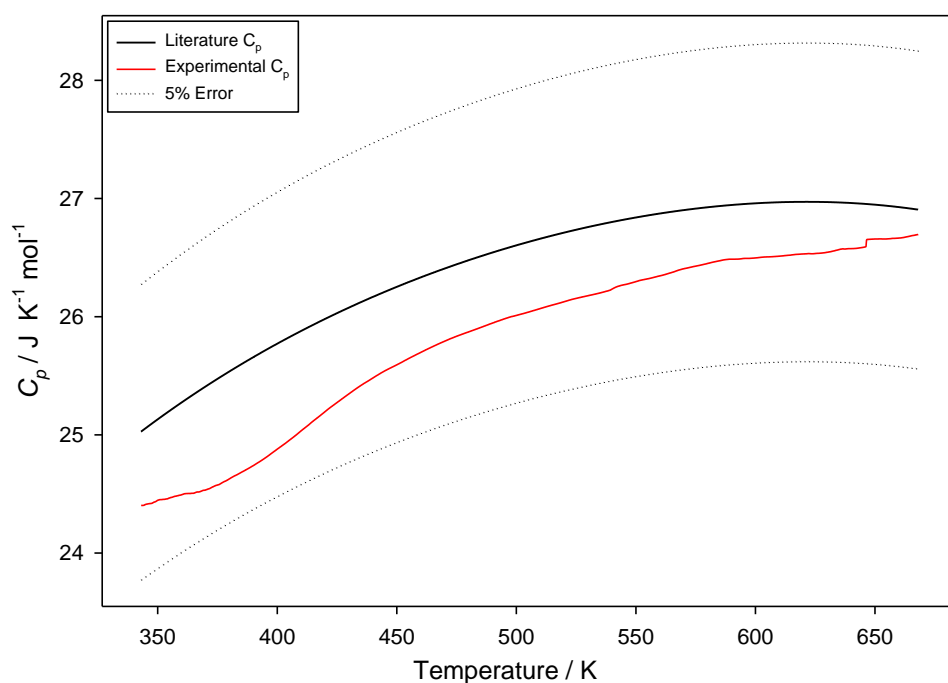
Figure F-1: C_p of aluminium for quality assurance compared against literature [2]
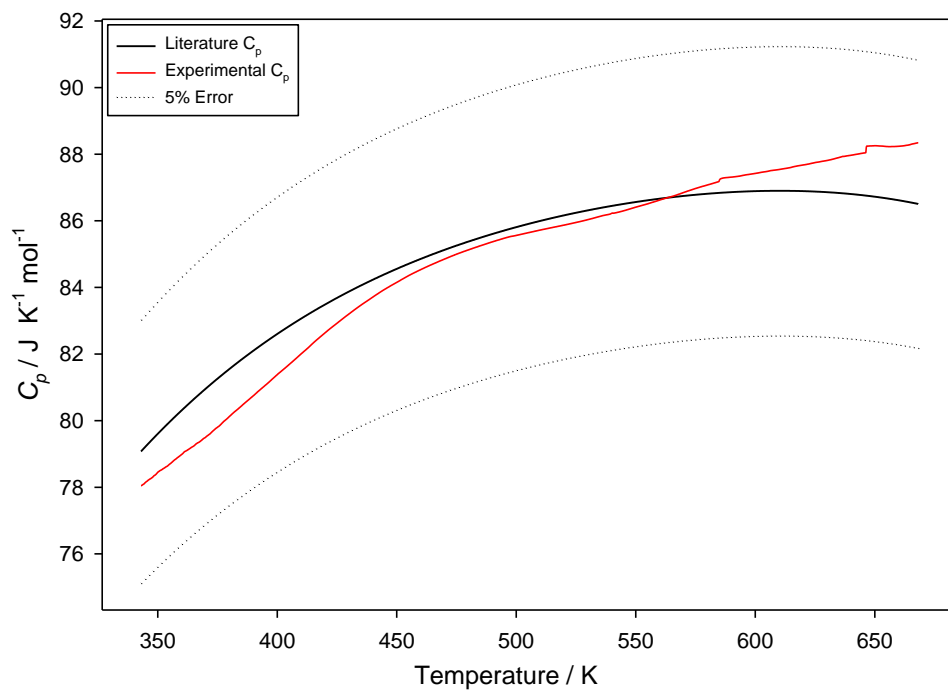
Figure F-2: C_p of MoO$_3$ for quality assurance compared against literature [3]

[1] ASTM E1269-11, "Standard Test Method for Determining Specific Heat Capacity by Differential Scanning Calorimetry".

[2] D.A. Ditmars, C.A. Plint, and R.C. Shukla, "Aluminium 1. Measurement of the Relative Enthalpy from 273 to 929 K and Derivation of Thermodynamic Functions for Al(s) from 0 K to its Melting Point", International Journal of Thermophysics, Vol 6. No. 5 (1985) 499-515.

[3] D.R. Stull and H. Prophet, "JANAF Thermochemical Table," Second Edition, National Bureau of Standards, 1971.

Appendix G C_p of Wet and Damp Sample

The experimental heat capacity results were found to be highly dependent on water content. To demonstrate this dependency, the resulting $C_p(T)$ functions of: (i) wet sample (compound **2**), (ii) damp sample (compound **2**), and (iii) dry sample (compound **3**), were determined and are listed in Table G-1, with the form seen in Equation G-1.

$$C_p^{\circ}(T(K))\ (J\ mol^{-1}K^{-1}) = k_o + k_1T + k_2T^2 + k_{-2}T^{-2} \qquad \text{Equation G-1}$$

Table G-1: Coefficients for the UMoO$_6$ $C_p(T)$ functions of wet, damp, and dry sample valid for the temperature range of 343-668 K

Sample	k_o	k_1	k_2	k_{-2}	Error
Wet	161.26	-9.8243E-03	3.6934E-05	-2.8251E06	20 %
Damp	255.0472	-0.3129	3.4708E-04	-2.63164E06	40 %
Dry	**223.0844**	**-0.1945**	**2.2965E-04**	**-2.51549E06**	**5 %**
Dash [23]	158.65	0.004288	-2.361E-04	-1.40770E+06	5 %*

* Assumed uncertainty range based on [155].

G.1.   Wet Sample

Wet sample is compound **2** that was synthesized and filtered via a water aspirator. This sample is classified as 'wet' because water aspirators tend not to have as much suction power as a vacuum pump and the sample is left with an excess of water. As seen in Figure G-1, three sequential tests were completed on wet sample that was originally characterized as UMoO$_6$·1.84 H$_2$O, however, each sample contained less water with each subsequent test. This is because a full day was required to complete a test and the remaining sample was stored in an oven at 393 K during testing. This resulted in each sequential test having slightly less water content in the sample than the previous test.
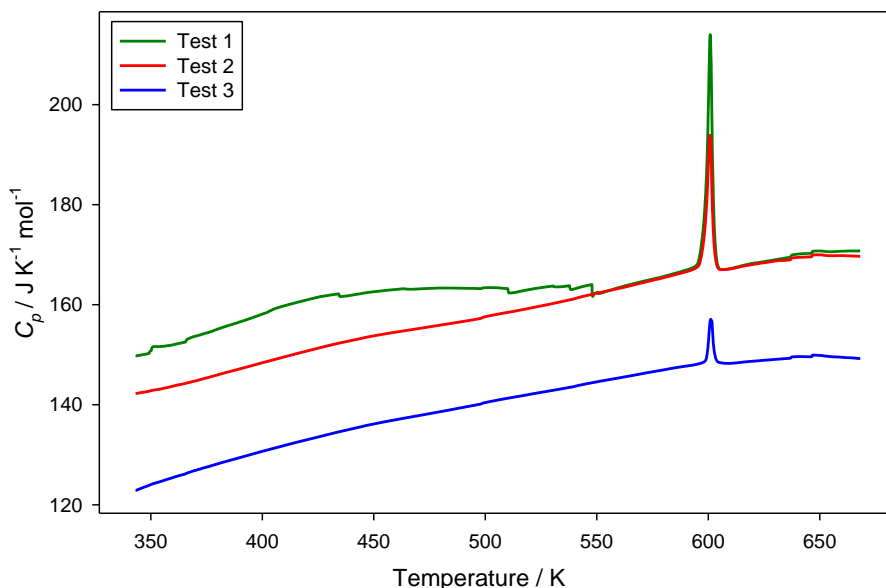
Figure G-1: Specific heat capacity of three wet C_p tests

There is a large peak around 600 K, which corresponds to water leaving the crystal structure as a stable mass is seen in the TGA experiments beyond this temperature, Figure 45. The association of this peak with water loss is supported by the magnitude of this peak decreasing with each subsequent test. Test 1 (green) had the wettest sample and the highest peak at 600 K. Meanwhile, Test 3 (blue) had the smallest peak at 600 K as its sample spent two more days in the drying oven than the Test 1 sample. Therefore, less water in the sample correlates to a decrease in magnitude of the 600 K peak.

The high water content variability among the three tests caused a large error when averaged and fitted with a $C_p(T)$ function. The three separate tests produced an average $C_p(T)$ function (J K^{-1} mol^{-1}) of $161.26 - 9.8243 \times 10^{-3} T(\text{K}) + 3.6934 \times 10^{-5} T^2(\text{K}) - 2.8251 \times 10^6 T^{-2}(\text{K})$ with an associated error of $\pm 20 \%$ over a temperature range of 343-668 K. As seen in Figure G-2, the average $C_p(T)$ function lies below that of Dash *et al.* [23].
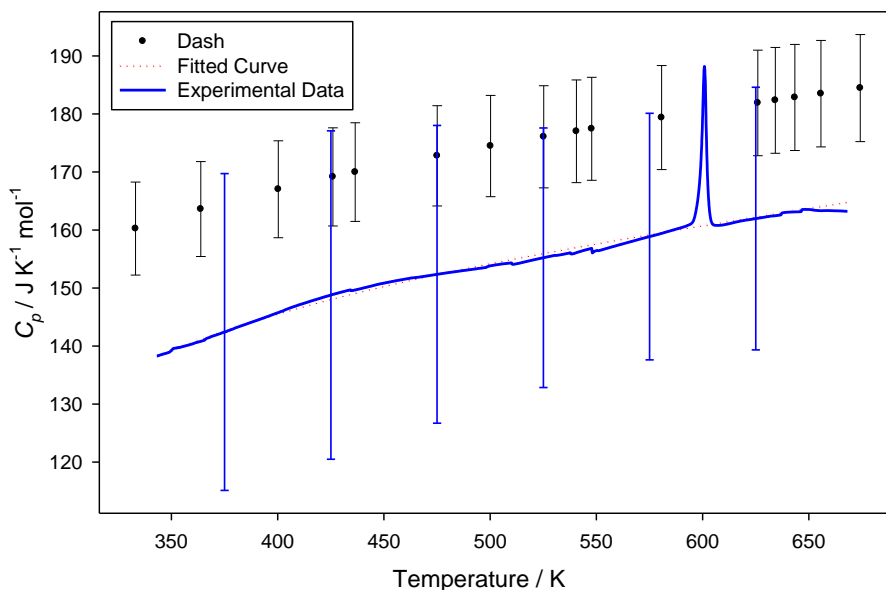
Figure G-2: Specific heat capacity of wet UMoO$_6$ in relation to Dash *et al.* [23]

G.2. <u>Damp Sample</u>

Damp sample is compound **2** that was synthesized and filtered via a vacuum pump. It is drier than wet sample because of the greater suction power of a vacuum pump over a water aspirator. The damp sample was originally characterized as UMoO$_6$·1.14 H$_2$O, but similar to the wet sample, it became drier with each sequential test as the sample was stored in an oven at 393 K. There was a greater water content variability among damp samples than wet samples and thus a larger error associated with the fitted $C_p(T)$ function. Three separate samples produced a $C_p(T)$ function (J K^{-1} mol^{-1}) of 255.0472 − 0.3129T(K) + 3.4708x10$^{-4}T^2$(K) − 2.63164x10$^6T^{-2}$(K) with an associated error of ± 40 % over a temperature range of 343-668 K.
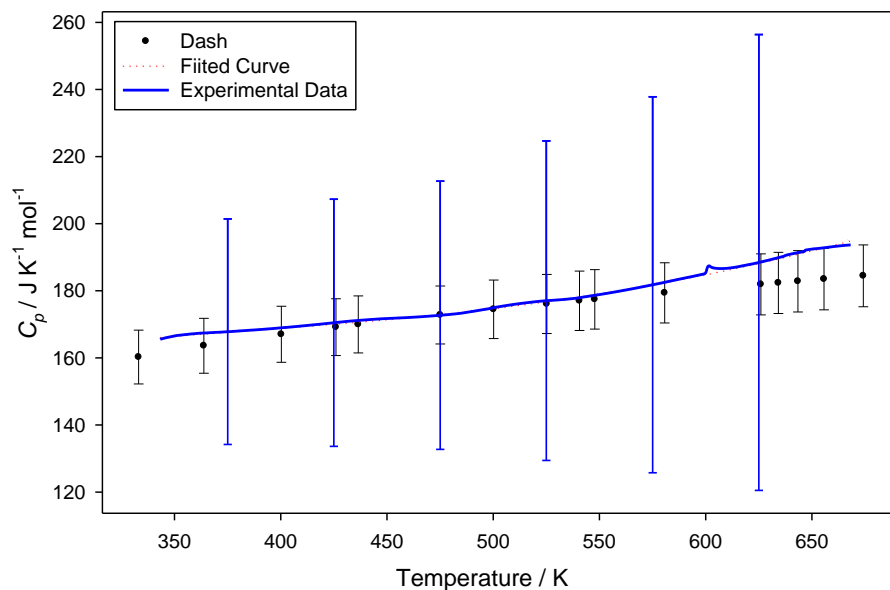
Figure G-3: Specific heat capacity of damp UMoO$_6$ in relation to Dash *et al.* [23]

As seen in Figure G-3, the $C_p(T)$ function becomes closer to that determined by Dash *et al.* [23] as less water is present. Also, the peak around 600 K has been significantly reduced as a result of less water content. Like the wet sample, the magnitude of this peak decreased with each subsequent test due to a longer time in the storage drying oven.

Appendix H   Calisto Software

Calisto is a software package made by AKTS Thermokinetics for use with Setaram scientific instruments [1]. It has two independent parts, Calisto Acquisition and Calisto Processing. Calisto Acquisition is used to program experimental runs for the TGA/DSC. A heating profile including hold times is pre-programmed along with carrier gas selection and flow rates, cooling water flow, PID values, and calibration coefficients selection. Once programmed, an experiment can be started and left to run until competition.

Calisto Processing is the user operated data manipulation module used to extract information from the raw experimental data files. The software will subtract baseline blank data from the experimental data when both files are selected. It exports images in .png, .gif, .bmp, .jpg, and .emf file types and can export data in .xls, .ascii, .html, and .xml file types for further data manipulation in another program. It will integrate the area under peaks from baselines of different types including sigmoidal, tangential sigmoidal, linear, horizontal, staged, spline, and Bezier. These baseline types can be selected by the software or can be user-defined. This software has a variety of other options for data manipulation that were not utilized by this thesis as they were not applicable and will therefore not be described here.

[1] http://www.setaram.com/CALISTO.htm

Appendix I   Exemption Quantities

Ref. [1] states the CNSC exemption quantity for uranium of 10^4 Bq. In order to ensure safety and abide by regulations, the quantity of compound outside the SLOWPOKE facility had to be kept under this limit. To determine the mass of sample 10^4 Bq corresponds to, all the isotopes of each element in the sample of interest must be known including their mass, half-life, and percent abundance.

Assume the sample compound has a mass of m_c. Using the molar mass of the compound (M_c), the number of molecules of compound (N_c) is found.

$$N_c = \frac{m_c}{M_c}$$

Equation I-1

The number of atoms of each isotope (i) in the compound (N_i) can be found using the percent abundance of the isotope ($\%a_i$), and the stoichiometric number of the element in the compound (v) according to Equation I-2.

$$N_i = \%a_i \cdot v \cdot N_c$$

Equation I-2

Next, the half-life ($t_{1/2\ i}$) in s of each isotope is converted to a decay constant (λ_i) in s^{-1} using Equation I-3.

$$\lambda_i = \frac{ln\,(2)}{t_{\frac{1}{2}i}}$$

Equation I-3

λ and N are related to radioactivity (A) by Equation I-4. The units of λ are s^{-1}, and as a Bq is a decay per second, A is given in Bq.

$$A = \lambda\,N$$

Equation I-4

The activity of the compound (A_c) is the sum of the activity of all the individual isotopes.

$$A_c = \sum_i A_i$$

Equation I-5

$$A_c = \sum_i \lambda_i\,N_i$$

Equation I-6

$$A_c = \sum_i \lambda_i = \%a_i \cdot v \cdot N_c \qquad \text{Equation I-7}$$

$$A_c = N_c \cdot \sum_i \lambda_i = \%a_i \cdot v \qquad \text{Equation I-8}$$

If $A_c = 10^4$ Bq, N_c can be determined. Using Equation I-1, we can obtain m_c.

An example calculation of UO_2 is given in Table I-1.

Table I-1: Activity Calculation of UO_2

Isotope	%a_i	v	N_i	$t_{1/2}$ (years)	λ (s^{-1})
U-234	0.000055	1	0.000055 N_c	245500	8.94685E-14
U-235	0.0072	1	0.0072 N_c	703800000	3.12085E-17
U-238	0.992745	1	0.992745 N_c	4468000000	4.91596E-18
O-16	0.99762	2	1.99524 N_c	stable	
O-17	0.00038	2	0.00076 N_c	stable	
O-18	0.002	2	0.004 N_c	stable	

A_c (Bq)	N_c (atoms)	m_c (g)
1000	9.974E20	0.447

[1] Canadian Nuclear Safety Commission Radiation Safety Data Sheet, Uranium, revised 19 September 2011.

Appendix J   Safety Precautions for Radioactive Materials

The following appendix is the safety proposal outlining the safety precautions followed when working with radioactive materials.

J.1.   Radioactivity of Uranium

Natural uranium is an alpha emitting element, making it weakly radioactive. It has an annual limit on intake (ALI) of 2.5×10^6 Bq by ingestion and 3.2×10^3 Bq by inhalation. The exemption quantity as set by the Canadian Nuclear Safety Commission (CNSC) is 1×10^4 Bq [1]. For the purposes of these experiments, this means that no more than 440 mg of UO_2 or 710 mg of $UMoO_6$ can be used under the definition of an "exemption quantity", as seen in Appendix I. These experiments intend to only take exemption quantities out of the SLOWPOKE-2 facility at any given time. This ensures that no additional safeguards have to be amended to the existing RMC licence. It also allows for free transport to other areas of the building (*i.e.,* the XRD and SEM).

J.2.   Experimental Setup

The experimental setup involves testing a variety of uranium compounds in the TGA/DSC, SEM, and P-XRD. The temperature range of the testing can be 123 K to 2673 K, but will normally be room temperature to 1473 K. Sample sizes will normally range from 50-100 mg. Samples to be tested include a variety of molybdenum oxides, uranium oxides, and U-Mo-O compounds, particularly $UMoO_6$ created via wet chemistry. Later testing will try to create U-Mo-O compounds (particularly $UMoO_6$) *in situ* inside the TGA/DSC using molybdenum oxides and uranium oxides. All samples containing uranium will be natural uranium dioxide.

It is expected that 10 g of sample will be used during the course of this experiment (100 runs of 100 mg). This equates to approximately 5.536 g of uranium metal. All uranium will be accounted for at all times throughout the experiment and upon completion, returned to the SLOWPOKE-2 facility. Some small losses of uranium will occur (*e.g.*, effusing gas, surface adhesion, etc.), it will be the expectation of this work to minimize these losses and avoid laboratory contamination.

J.3.   Experimental Procedure

Each run will last approximately the course of one work day. The sample will be weighed in the morning in the SLOWPOKE-2 facility and returned to a waste container within this facility before the end of the working day, when possible. The experimenter will wear latex gloves and eye protection and will work within a fume hood whenever possible. They will log the quantity of uranium at all points during the experiment using a tracking log.

J.3.1.   TGA/DSC

The mass of a new/clean Al_2O_3 crucible will be measured using the TGA/DSC in lab S2508. The crucible will be filled with a 50-100 mg sample inside the SLOWPOKE-2 facility. It will then be returned to lab S2508 and the mass measured again. The difference will be assumed to be the mass of the sample. The sample will be subjected to a variety of temperatures and partial pressures of oxygen and mass and enthalpy data measured. The change in mass during the TGA/DSC experimentation will be applied to the original sample mass. As the mass of the sample is not expected to change during further experimentation, the mass of the sample after TGA/DSC analysis will be used as the baseline for the amount of sample that must be accounted for at all times.

J.3.2.   SEM

A carbon SEM pad will be prepared with a small amount of sample, 5-10 mg, in lab S2508. The crucible mass will be measured again and the loss of uranium to the carbon SEM pad will be logged. The carbon SEM pad will be transported to the SEM (S4503) in a sealed container and the remaining sample left in the crucible in lab S2508. The carbon SEM pad will be transported back to S2508 in a sealed container, weighed to confirm no loss of uranium, and placed in the solid waste container.

J.3.3.   P-XRD

The remainder of the sample will be transferred from the crucible to a pre-weighed plastic P-XRD pad in lab S2508. The empty crucible will be measured to determine the amount left in the crucible and the amount on the plastic P-XRD pad. The plastic P-XRD pad will be transferred to and from the P-XRD (S3510) in a sealed container. The mass of the plastic P-XRD pad will be measured before and

after transferring its contents to the dry waste container to determine the mass of uranium placed in the solid waste container and the amount left on the plastic P-XRD pad. The plastic P-XRD pad will be cleaned according to the procedure in the Containment and Cleanup section.

J.4.   Containment and Cleanup

J.4.1.   Solid Containment

The solid waste, both the SEM carbon pads and post-P-XRD solid waste, will be collected in a 60 mL Nalgene container marked "Solid Waste Containing Low Amounts of Uranium Dioxide". This solid waste container will be stored in the SLOWPOKE-2 facility until disposal. Disposal of this waste container will occur when 10 g of waste accumulates or experimentation on all uranium compounds is complete. When the waste container is to be disposed, A. Barry will contact the RadSO to start the proper waste disposal procedure for low-level radioactive waste.

J.4.2.   Gaseous Containment

For the TGA/DSC experimentation, a cold trap is fixed to the exhaust system of the TGA/DSC to capture any effusing uranium compounds that could have aerosolized during the experiment. Cleaning the cold trap will occur once a week or more frequently if required. It is expected that waste will form as a thin film inside the cold trap. The procedure will be to don gloves and eye protection at a minimum and rinse the cold trap with methanol and wipe with a Kimwipe in the fume hood. The Kimwipes and gloves containing trace uranium will be collected in a Ziploc bag in the fume hood to be disposed of upon completion of experimentation. The plastic P-XRD pads will be cleaned in the same manner and the Kimwipes and gloves placed in the same Ziploc bag. The bag will be labelled "Solid Waste Containing Trace Amounts of Uranium Dioxide".

J.4.3.   Aqueous Waste

The crucibles will need to be cleaned in an acid bath. The first wash of this process, containing the majority of the uranium, will be collected and stored in a 950 mL glass container marked "Liquid Waste Containing Low Amounts of Uranium Dioxide" in the fume hood. The mass of sample dissolved from the crucibles into the acid bath will be logged.

J.4.4.   Swab Testing

The following areas will need to have a 10" x 10" area swab test after use to ensure no contamination:
1) Fume hood
2) The sample loading area of the TGA/DSC
3) The sample location of the SEM
4) The sample location of the P-XRD
5) The S2508 lab bench (if required)

J.5.   <u>Accounting for All Uranium</u>

By the end of experimentation, all uranium will be in one of the following places:
1) The solid waste container (transferred from the plastic P-XRD pad)
2) A carbon SEM pad (in the solid waste container)
3) Dissolved in the acid wash (from the crucible)
4) The Kimwipes and gloves used to clean the cold trap and plastic P-XRD pads

The mass of uranium left on the Kimwipes and gloves is expected to be negligible. The mass on the carbon SEM pad, in the solid waste container and in the acid wash is expected to be equivalent to the amount of sample post-TGA/DSC. If this is not the case, the RadSO will be contacted immediately.

[1] Canadian Nuclear Safety Commission Radiation Safety Data Sheet, Uranium, revised 19 September 2011.

Appendix K   Atomic Coordinates and Select Bond Lengths of Compound 1

Table K-1: Atomic coordinates (x10⁴) of compound 1

	x	y	z	U(eq)
Na(1)	6591(17)	4909(13)	5142(9)	30(5)
Na(2)	3780(20)	5589(13)	2577(10)	36(5)
Na(3)	3060(30)	730(20)	3861(16)	26(8)
U(1)	4521(1)	2403(1)	5126(1)	18(1)
U(2)	1307(1)	5387(1)	3796(1)	19(1)
U(3)	2332(1)	2677(1)	2624(1)	25(1)
Mo(1)	6692(1)	2532(1)	3981(1)	16(1)
Mo(2)	2315(1)	3752(1)	4767(1)	16(1)
Mo(3)	0	6432(1)	2500	21(1)
Mo(4)	-86(1)	3578(1)	3375(1)	21(1)
O(1)	4020(15)	1749(9)	4639(6)	33(4)
O(2)	5019(17)	3048(9)	5628(8)	44(5)
O(3)	5574(13)	2906(9)	4364(7)	35(4)
O(4)	7829(12)	2480(11)	4419(7)	41(4)
O(5)	6345(15)	1656(8)	3823(6)	33(3)
O(6)	6917(13)	2948(8)	3302(6)	26(3)
O(7)	3483(12)	3277(8)	4624(7)	31(4)
O(8)	2463(12)	4246(8)	5422(6)	26(3)
O(9)	1213(12)	3189(8)	4819(6)	25(3)
O(10)	2038(14)	4335(8)	4187(7)	32(4)
O(11)	262(13)	5353(9)	4338(7)	33(4)
O(12)	2330(12)	5405(8)	3260(6)	28(3)
O(13)	32(13)	5893(8)	3136(7)	33(4)
O(14)	426(13)	4439(8)	3302(6)	29(3)
O(15)	-1098(18)	6950(10)	2552(8)	52(6)
O(16)	-571(12)	3463(8)	4095(6)	25(3)
O(17)	-1142(13)	3464(9)	2870(7)	33(4)
O(18)	883(14)	2930(10)	3263(7)	36(4)
O(19)	3053(14)	3404(11)	2938(8)	44(5)
O(20)	1635(19)	1927(11)	2322(12)	70(8)
O(21)	2400(40)	1990(30)	3570(20)	64(12)
O(22)	7140(30)	3838(19)	4157(15)	49(8)
O(23)	4660(40)	4680(30)	5790(20)	44(11)

Table K-2: Selected bond lengths and angles for compound 1

Bond lengths (Å)					
U1-O1	1.763(16)	U2-O11	1.793(15)	U3-O19	1.781(17)
U1-O2	1.771(17)	U2-O12	1.764(15)	U3-O20	1.79(2)
U1-O4	2.362(14)	U2-O10	2.344(16)	U3-O6	2.356(14)
U1-O3	2.367(15)	U2-O14	2.370(14)	U3-O18	2.366(16)
U1-O7	2.378(13)	U2-O5	2.376(15)	U3-O17	2.375(15)
U1-O9	2.390(14)	U2-O13	2.384(15)	U3-O15	2.393(19)
U1-O16	2.400(14)	U2-O8	2.387(14)	U3-O21	2.50(5)
Mo1-O5	1.734(16)	Mo2-O9	1.738(14)	Mo4-O18	1.732(17)
Mo1-O4	1.737(14)	Mo2-O7	1.738(15)	Mo4-O14	1.742(14)
Mo1-O6	1.747(15)	Mo2-O10	1.743(15)	Mo4-O16	1.753(13)
Mo1-O3	1.789(17)	Mo2-O8	1.760(15)	Mo4-O17	1.760(16)
Mo3-O15	1.684(19)	Na2-O12	2.41(3)	Na3-O21	2.59(6)
Mo3-O13	1.760(15)	Na2-O20	2.57(3)	Na3-O1	2.86(4)

Bond angles (°)					
O1-U1-O2	178.9(8)	O12-U2-O11	179.0(8)	O19-U3-O20	178.1(12)
O4-U1-O7	69.9(6)	O10-U2-O14	74.4(6)	O6-U3-O17	72.2(5)
O7-U1-O3	71.4(5)	O14-U2-O13	71.9(6)	O17-U3-O18	71.7(5)
O3-U1-O9	74.4(5)	O13-U2-O5	68.4(6)	O18-U3-O21	66.7(12)
O9-U1-O16	72.0(5)	O5-U2-O8	71.4(5)	O21-U3-O15	74.9(12)
O16-U1-O4	72.5(6)	O8-U2-O10	74.1(5)	O15-U3-O6	74.6(6)
O4-Mo1-O5	105.6(9)	O9-Mo2-O7	111.6(7)	O18-Mo4-O14	112.1(8)
O5-Mo1-O6	106.3(7)	O9-Mo2-O10	105.8(7)	O18-Mo4-O16	107.0(7)
O5-Mo1-O3	106.0(8)	O9-Mo2-O8	110.1(7)	O18-Mo4-O17	110.1(9)
O4-Mo1-O6	113.4(8)	O7-Mo2-O10	110.3(7)	O14-Mo4-O16	109.2(7)
O4-Mo1-O3	112.5(8)	O7-Mo2-O8	109.7(8)	O14-Mo4-O17	109.0(8)
O6-Mo1-O3	112.3(7)	O8-Mo2-O10	109.2(7)	O16-Mo4-O17	109.3(7)

O15(#10)-Mo3-O15	109.7(15)		O12-Na2-O20	85.9(9)
O15(#10)-Mo3-O13(#10)	106.9(9)		O21-Na3-O1	71.3(14)
O15(#10)-Mo3-O13	111.6(8)		O21-Na3-O13	91.7(16)
O15-Mo3-O13	107.0(9)		O1-Na3-O13	85.8(11)
O13-Mo3-O13(#10)	110.0(11)			

Appendix L   Quality Assurance of the TGA/DSC

The TGA/DSC was calibrated for quality assurance in three ways. A TG calibration was performed to ensure the mass measured by the TGA/DSC was correct. A temperature calibration was conducted to quantify the difference in the furnace temperature and the sample temperature. Finally, a regression calibration was completed to create sensitivity coefficients used to convert the raw heat flow signal to a real measurement of heat.

L.1.   TG Calibration

The TGA/DSC measures mass by using electromagnets to hold the sample holding rod in place. The amount of electricity needed to keep the rod in place is directly proportional to the mass placed on the rod. The calibration module of Calisto was opened and the empty rod allowed to stabilize for 3 h. A 50 mg standard calibration mass was then added and allowed to stabilize for 3 h. The amount of electricity needed to hold the rod in place was correlated to 50 mg. As additional confirmation, 20 mg and 100 mg standard calibration masses were added to the empty rod to ensure the calibration accurately measured their mass to < 1 % error.

L.2.   Temperature Calibration

The furnace of the TGA/DSC induces heat upon the sample. The temperature of the furnace and the sample can be different at any given temperature. A calibration was required to correlate the temperature of the furnace and the temperature of the sample. To accomplish this, standard reference materials of calibration grade were heated at a variety of heating rates past their melting temperatures and then cooled and re-solidified. Each sample was melted and re-solidified three times and only the latter two serials accepted to account for air pockets initially within the solid samples. Calibration runs were conducted on gold, silver, tin, zinc, and aluminium to cover a large temperature range of interest. Corresponding blank runs were completed and subtracted.

A peak occurs in the DSC heat flow data during a melting or re-solidification at the real melting temperature of the sample. The temperature of the furnace at that peak is then correlated to the sample temperature by the melting temperature of the sample. A series of sample temperatures and their corresponding furnace temperatures and heat rates are fitted by the Calisto calibration software to produce

a calibration function that could accurately measure the sample temperature to ± 4 K, Figure L-1.
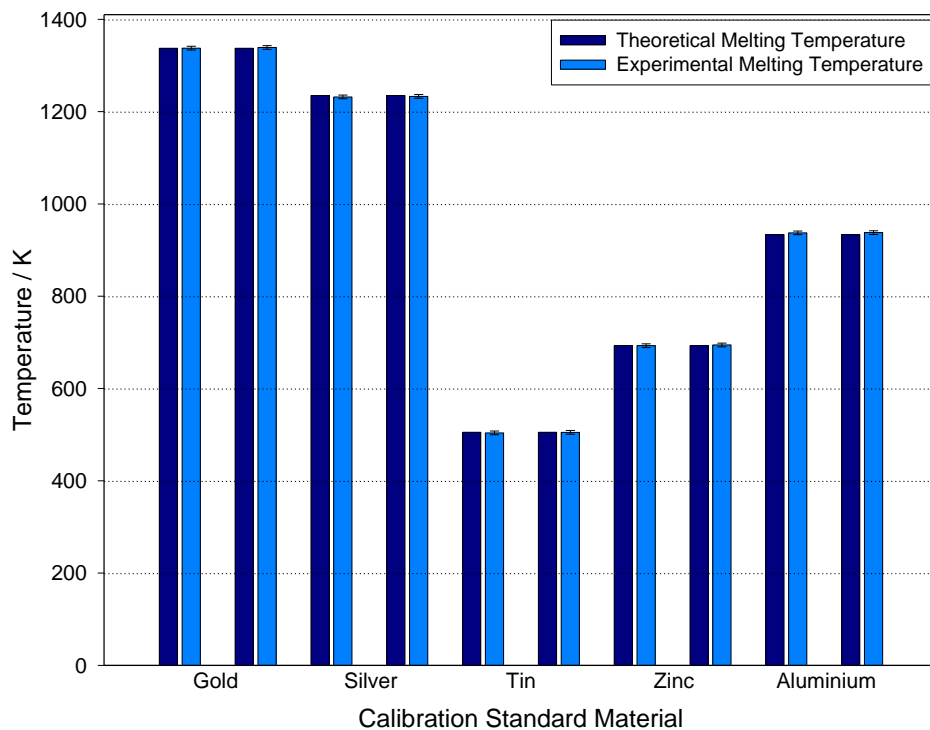
Figure L-1: Temperature calibration of the TGA/DSC

L.3. Regression Calibration

A thermocouple measures the difference in heat flow between the empty crucible and sample crucible. The raw electrical signal generated needs sensitivity coefficients unique to the system and thermocouple to convert to a heat measurement. This was done by integrating the area under the peaks described above using the same calibration runs. The Calisto calibration software fit a function to correlate peak area to the theoretical heats of fusion of the calibration standard materials. Figure L-2 shows the function gives heat values within ± 7.5 % of the theoretical value.
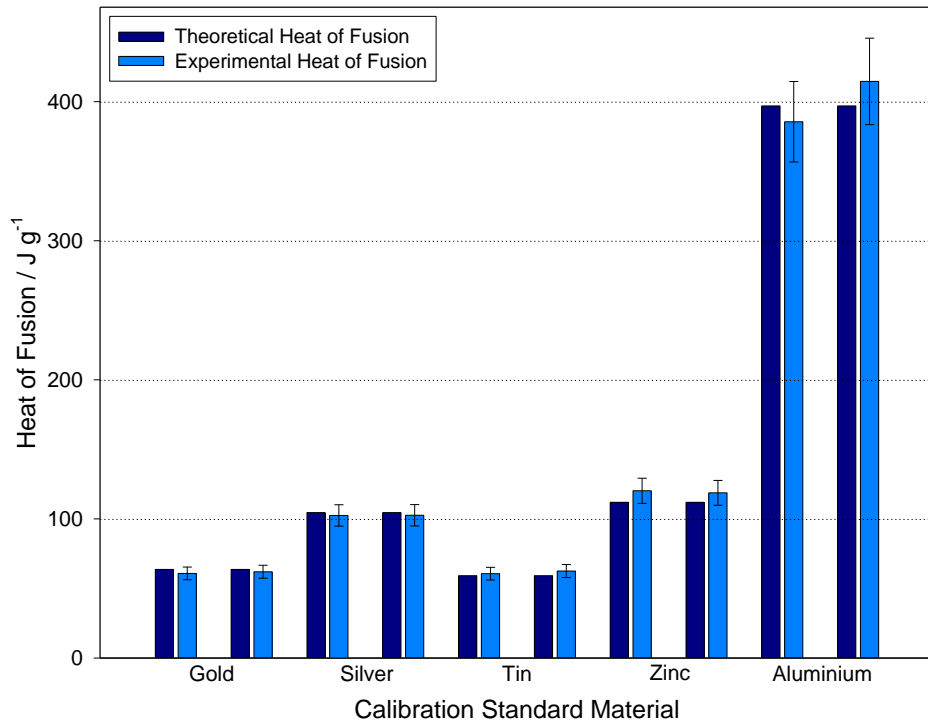
Figure L-2: Heat calibration of the TGA/DSC

Appendix M Quality Assurance of the CT Cell

A quality assurance check was performed on the CT Cell to ensure pO_2 values read from the display were correct. A 2000 ppm H_2 in Ar gas mixture was allowed to bubble through water in a cold trap at 273.2 K and 297.8 K. This gas mixture then entered the CT Cell at an operating condition of 1023 K and the pO_2 measured. This value was compared to that calculated by FACTSage.

The calculation of the pO_2 expected for the 297.8 K water will be used as an example. The following overall reaction mixture was assumed:

      1 000 000 mol Ar

      2 000 mol H_2

      3 000 000 mol H_2O

For these calculations, only relative ratios of gases are necessary as pO_2 is a function of the relative ratios of gases only and not the total amount of gas. Enough H_2O was added such that liquid H_2O still remained at equilibrium, as observed during the quality assurance check.

Using the overall reaction mixture above, the following mixture is obtained at equilibrium at 297.8 K:

      1.0336×10^6 mol of gas with the following partial pressures

            0.96745 atm   Ar

            3.06E-02 atm H_2O

            1.93E-03 atm H_2

            9.48E-38 atm   H

            5.26E-47 atm   OH

            9.60E-63 atm H_2O_2

      and 2.9684×10^6 mol of liquid H_2O.

It is assumed that this gas mixture represents the gas that forms after bubbling through the water and the liquid H_2O remains in the cold trap. If this gas mixture with a Ar:H_2O:H_2 ratio of $0.96745:3.06 \times 10^{-2}:1.93 \times 10^{-3}$ is allowed to flow into the CT Cell at its operating temperature of 1023 K and come to equilibrium, the following gas mixture is obtained and measured by the CT Cell:

      0.96745 atm   Ar

      3.06E-02 atm H_2O

1.93E-03 atm   H$_2$
1.82E-10 atm   H
7.87E-12 atm   OH
7.22E-18 atm   O$_2$
8.36E-19 atm   O
3.01E-19 atm   H$_2$O$_2$
1.15E-21 atm   HO$_2$
2.51E-37 atm   O$_3$

It is this pO_2 that is compared to that measured during the quality assurance check. The following table summarizes the results. The CT Cell is in line with expected results.

Table M-1: Results of the CT Cell Quality Assurance Check

Water Temperature (K)	297.8	273.2
FACTSage pO_2 (atm)	7.22×10^{-18}	2.69×10^{-19}
Measured pO_2 (atm)	8.28×10^{-18}	6.52×10^{-19}

A possible reason for discrepancy is the room temperature of the lab affecting the temperature of the gas before it reaches the CT Cell. A change in temperature would cause a change in the Ar:H$_2$O:H$_2$ ratio before it reaches the CT Cell, thus affecting the measured pO_2. As the temperature of the lab was above 297.8, more H$_2$O would dissociate than calculated and create more O$_2$, resulting in a higher pO_2. This effect would increase with greater deviation below the room temperature as observed.

In addition to this quality assurance check, gas checks were completed before the start of any experiment. This involved selecting PID values to achieve the pO_2 of interest quickly and with minor oscillation such to not affect the experiment.

Appendix N   Raw C_p Data

Below is the raw test data of dry $UMoO_6$ used to fit the $C_p(T)$ function

Test 1		Test 2		Test 3		Average	
Temp (K)	C_p (J mol^{-1} K^{-1})	Temp (K)	C_p (J mol^{-1} K^{-1})	Temp (K)	C_p (J mol^{-1} K^{-1}))	Temp (K)	C_p (J mol^{-1} K^{-1})
343.0152	161.2042	343.0585	166.2681	343.0301	160.647	343.0346	162.7064
343.9452	161.1583	343.9907	166.4064	343.9618	160.7236	343.9659	162.7627
344.8754	161.15	344.9233	166.5832	344.8933	160.8338	344.8973	162.8557
345.8063	161.1402	345.8557	166.758	345.8256	160.9489	345.8292	162.949
346.7376	161.1143	346.7882	166.907	346.7574	161.0641	346.7611	163.0285
347.6689	161.0711	347.7212	167.0314	347.6896	161.1742	347.6932	163.0923
348.6007	161.0436	348.6545	167.1707	348.6224	161.3073	348.6259	163.1739
349.5326	161.0074	349.5877	167.2954	349.5546	161.4357	349.5583	163.2462
350.4649	161.0023	350.5205	167.4447	350.4871	161.5961	350.4908	163.3477
351.3968	160.9488	351.4538	167.5433	351.4201	161.7043	351.4235	163.3988
352.3291	160.8694	352.3871	167.6096	352.3535	161.784	352.3565	163.421
353.2616	160.7895	353.3202	167.6694	353.2863	161.8602	353.2894	163.4397
354.1937	160.7217	354.2543	167.7315	354.2196	161.9449	354.2225	163.466
355.1267	160.6856	355.1872	167.8194	355.1526	162.0486	355.1555	163.5179
356.0601	160.6399	356.1211	167.8891	356.086	162.134	356.0891	163.5543
356.9929	160.5954	357.0545	167.9531	357.0196	162.2134	357.0224	163.5873
357.9263	160.5473	357.988	168.0061	357.953	162.2797	357.9558	163.6111
358.859	160.5046	358.9214	168.0584	358.8862	162.3416	358.8888	163.6349

Test 1		Test 2		Test 3		Average	
Temp (K)	C_p (J mol^{-1} K^{-1})	Temp (K)	C_p (J mol^{-1} K^{-1})	Temp (K)	C_p (J mol^{-1} K^{-1}))	Temp (K)	C_p (J mol^{-1} K^{-1})
359.7922	160.469	359.8554	168.1106	359.8199	162.4035	359.8225	163.661
360.7262	160.4477	360.7896	168.1703	360.7539	162.4719	360.7566	163.6966
361.6592	160.4303	361.7225	168.2247	361.6871	162.5389	361.6896	163.7313
362.5922	160.3914	362.6562	168.251	362.6206	162.5752	362.623	163.7392
363.5253	160.3459	363.5904	168.2651	363.5543	162.5934	363.5567	163.7348
364.4592	160.3123	364.524	168.2851	364.4882	162.6149	364.4905	163.7374
365.3926	160.2755	365.458	168.2967	365.4216	162.6294	365.4241	163.7339
366.3263	160.2876	366.3921	168.3538	366.3556	162.689	366.358	163.7768
367.2596	160.2692	367.3255	168.3769	367.2898	162.7119	367.2916	163.786
368.1929	160.2683	368.2593	168.4135	368.2227	162.7453	368.225	163.809
369.1267	160.2899	369.1936	168.4647	369.1572	162.7953	369.1592	163.8499
370.0603	160.2798	370.1274	168.4777	370.0905	162.8067	370.0927	163.8547
370.9939	160.2938	371.061	168.5104	371.0245	162.8378	371.0265	163.8807
371.9273	160.3114	371.9946	168.5457	371.9583	162.8677	371.96	163.9083
372.8611	160.3576	372.9287	168.6066	372.8923	162.9218	372.894	163.962
373.7952	160.3979	373.8626	168.6563	373.826	162.9686	373.8279	164.0076
374.7288	160.4381	374.7965	168.7036	374.7596	163.0137	374.7616	164.0518
375.6623	160.4612	375.7306	168.7331	375.6936	163.0382	375.6955	164.0775
376.596	160.514	376.6647	168.7912	376.6274	163.0879	376.6294	164.131
377.53	160.5796	377.598	168.8566	377.5614	163.148	377.5631	164.1947
378.4642	160.6356	378.5325	168.9082	378.4955	163.1997	378.4974	164.2478

Test 1		Test 2		Test 3		Average	
Temp (K)	C_p (J mol^{-1} K^{-1})	Temp (K)	C_p (J mol^{-1} K^{-1})	Temp (K)	C_p (J mol^{-1} K^{-1}))	Temp (K)	C_p (J mol^{-1} K^{-1})
379.3978	160.6907	379.4663	168.9577	379.4293	163.2485	379.4311	164.2989
380.3312	160.7629	380.3998	169.0237	380.3633	163.311	380.3647	164.3659
381.2654	160.8349	381.3342	169.0873	381.2971	163.3694	381.2989	164.4305
382.1992	160.9025	382.2681	169.146	382.2309	163.4218	382.2327	164.4901
383.1328	160.96	383.2017	169.1932	383.1651	163.4632	383.1665	164.5388
384.0665	161.025	384.1358	169.246	384.098	163.5117	384.1001	164.5942
385.0003	161.0923	385.0694	169.301	385.0324	163.5631	385.034	164.6522
385.9348	161.1599	386.0038	169.356	385.9663	163.6143	385.9683	164.7101
386.8679	161.2274	386.9374	169.4127	386.9001	163.6654	386.9018	164.7685
387.8021	161.2993	387.8716	169.4718	387.8345	163.7189	387.8361	164.83
388.7364	161.3733	388.8055	169.5315	388.7678	163.7742	388.7699	164.893
389.6698	161.4497	389.7397	169.5931	389.702	163.8315	389.7038	164.9581
390.6035	161.5278	390.6732	169.6544	390.6356	163.8878	390.6374	165.0234
391.5379	161.6119	391.6074	169.72	391.5695	163.9492	391.5716	165.0937
392.4714	161.6924	392.5411	169.7828	392.504	164.0071	392.5055	165.1608
393.4058	161.7736	393.4755	169.8474	393.4375	164.0651	393.4396	165.2287
394.3398	161.858	394.4092	169.9171	394.3714	164.1263	394.3734	165.3005
395.2735	161.9449	395.3432	169.9887	395.3059	164.1901	395.3075	165.3746
396.2078	162.0334	396.2774	170.0587	396.2396	164.256	396.2416	165.4494
397.1414	162.127	397.2113	170.133	397.1732	164.3269	397.1753	165.529
398.0754	162.2224	398.1448	170.2082	398.1074	164.3995	398.1092	165.61

Test 1		Test 2		Test 3		Average	
Temp (K)	C_p (J mol^{-1} K^{-1})	Temp (K)	C_p (J mol^{-1} K^{-1})	Temp (K)	C_p (J mol^{-1} K^{-1}))	Temp (K)	C_p (J mol^{-1} K^{-1})
399.009	162.3139	399.0791	170.2792	399.0413	164.468	399.0431	165.687
399.9425	162.4062	400.0131	170.3513	399.9754	164.5366	399.977	165.7647
400.877	162.4968	400.9467	170.4224	400.909	164.6025	400.9109	165.8406
401.8107	162.5862	401.8809	170.4926	401.8431	164.6668	401.8449	165.9152
402.7446	162.6776	402.815	170.5649	402.7772	164.7321	402.7789	165.9915
403.6786	162.7685	403.7487	170.6368	403.711	164.797	403.7128	166.0674
404.6124	162.8637	404.6828	170.7133	404.645	164.8666	404.6467	166.1479
405.5467	162.9601	405.6169	170.7904	405.5787	165.0339	405.5808	166.2614
406.4806	163.0537	406.5506	170.8652	406.5124	165.1284	406.5145	166.3491
407.4149	163.1499	407.485	170.9435	407.4473	165.2053	407.4491	166.4329
408.3482	163.2471	408.4188	171.0228	408.3806	165.2791	408.3825	166.5163
409.2821	163.3495	409.3523	171.108	409.3147	165.3554	409.3164	166.6043
410.2163	163.4534	410.2866	171.1959	410.2487	165.4314	410.2506	166.6936
411.1501	163.5518	411.2206	171.2779	411.1824	165.5007	411.1844	166.7768
412.0836	163.6487	412.1543	171.3597	412.1164	165.5678	412.1181	166.8587
413.0178	163.7474	413.0878	171.4428	413.0498	165.6354	413.0518	166.9419
413.9515	163.8526	414.0224	171.5326	413.984	165.71	413.986	167.0317
414.8862	163.9612	414.9565	171.6257	414.9183	165.7897	414.9203	167.1255
415.8197	164.0616	415.8903	171.7105	415.8518	165.8687	415.8539	167.2136
416.7535	164.1602	416.8243	171.7933	416.7862	165.9461	416.788	167.2999
417.6877	164.2597	417.7585	171.8774	417.72	166.0237	417.7221	167.3869

Test 1		Test 2		Test 3		Average	
Temp (K)	C_p (J mol^{-1} K^{-1})	Temp (K)	C_p (J mol^{-1} K^{-1})	Temp (K)	C_p (J mol^{-1} K^{-1}))	Temp (K)	C_p (J mol^{-1} K^{-1})
418.6219	164.3617	418.6929	171.9648	418.6542	166.1027	418.6563	167.4764
419.5557	164.466	419.6266	172.0541	419.5883	166.1827	419.5902	167.5676
420.4894	164.573	420.5602	172.1459	420.5219	166.2645	420.5238	167.6611
421.4234	164.681	421.4944	172.2387	421.456	166.3462	421.4579	167.7553
422.3573	164.7863	422.4285	172.3284	422.3897	166.4242	422.3919	167.8463
423.291	164.8894	423.3625	172.4165	423.3237	166.5002	423.3257	167.9354
424.225	164.9917	424.2966	172.5046	424.2573	166.5753	424.2596	168.0239
425.1589	165.0959	425.2299	172.5947	425.1915	166.6521	425.1934	168.1142
426.0929	165.1995	426.1642	172.6851	426.1259	166.7282	426.1277	168.2043
427.0268	165.3028	427.0982	172.7763	427.0597	166.8041	427.0616	168.2944
427.9608	165.4064	428.0323	172.8681	427.9931	166.8814	427.9954	168.3853
428.8948	165.5094	428.966	172.9596	428.9271	166.9591	428.9293	168.476
429.8286	165.609	429.9007	173.0488	429.862	167.0348	429.8638	168.5642
430.7628	165.7072	430.8339	173.1361	430.7958	167.1096	430.7975	168.6509
431.6968	165.8056	431.7683	173.2245	431.7295	167.1851	431.7315	168.7384
432.6307	165.9032	432.702	173.3124	432.6635	167.2601	432.6654	168.8252
433.5648	165.9962	433.6362	173.3956	433.5972	167.3308	433.5994	168.9075
434.4988	166.0868	434.5702	173.4772	434.5312	167.3994	434.5334	168.9878
435.4322	166.175	435.5036	173.5568	435.4646	167.4659	435.4668	169.0659
436.3663	166.2608	436.4378	173.6343	436.399	167.5304	436.401	169.1418
437.3005	166.3413	437.372	173.7073	437.3334	167.5896	437.3353	169.2127

Test 1		Test 2		Test 3		Average	
Temp (K)	C_p (J mol^{-1} K^{-1})	Temp (K)	C_p (J mol^{-1} K^{-1})	Temp (K)	C_p (J mol^{-1} K^{-1}))	Temp (K)	C_p (J mol^{-1} K^{-1})
438.2344	166.4206	438.3062	173.7796	438.2672	167.6476	438.2693	169.2826
439.1683	166.5028	439.2403	173.8551	439.2011	167.7086	439.2032	169.3555
440.1022	166.586	440.1737	173.9323	440.1355	167.7719	440.1372	169.4301
441.0368	166.6679	441.1087	174.0083	441.0697	167.8344	441.0717	169.5036
441.9705	166.7471	442.0425	174.0808	442.0031	167.8943	442.0053	169.5741
442.9042	166.825	442.9758	174.1521	442.9369	167.9531	442.939	169.6434
443.8378	166.9027	443.9102	174.2234	443.8712	168.0117	443.8731	169.7126
444.7719	166.9777	444.8443	174.2913	444.805	168.0658	444.8071	169.7782
445.7057	167.0552	445.7782	174.3625	445.7389	168.1192	445.7409	169.8457
446.6392	167.1278	446.7114	174.429	446.6723	168.169	446.6743	169.9086
447.5731	167.1966	447.6459	174.4913	447.6069	168.2157	447.6086	169.9679
448.508	167.2616	448.5796	174.5493	448.5411	168.2588	448.5429	170.0232
449.4417	167.325	449.514	174.6065	449.475	168.3014	449.4769	170.0776
450.3755	167.3879	450.4481	174.6636	450.409	168.3442	450.4109	170.1319
451.3092	167.4506	451.3822	174.722	451.3425	168.3888	451.3447	170.1871
452.2441	167.514	452.3165	174.7814	452.2769	168.4348	452.2792	170.2434
453.1776	167.578	453.2501	174.8419	453.2109	168.4824	453.2128	170.3008
454.1112	167.6422	454.1841	174.9031	454.1447	168.5313	454.1466	170.3589
455.0454	167.7047	455.1178	174.9629	455.0786	168.579	455.0806	170.4155
455.9792	167.7649	456.0519	175.0204	456.0126	168.6243	456.0145	170.4699
456.9133	167.8238	456.9859	175.0767	456.9466	168.6687	456.9486	170.5231

Test 1		Test 2		Test 3		Average	
Temp (K)	C_p (J mol^{-1} K^{-1})	Temp (K)	C_p (J mol^{-1} K^{-1})	Temp (K)	C_p (J mol^{-1} K^{-1}))	Temp (K)	C_p (J mol^{-1} K^{-1})
457.8468	167.8815	457.9197	175.1331	457.8804	168.7131	457.8823	170.5759
458.7808	167.939	458.854	175.1908	458.8143	168.7582	458.8163	170.6293
459.7148	167.9954	459.7878	175.2481	459.7484	168.8031	459.7503	170.6822
460.6489	168.0531	460.7217	175.3066	460.6822	168.8507	460.6843	170.7368
461.5831	168.1116	461.6562	175.3664	461.616	168.8992	461.6184	170.7924
462.5165	168.1694	462.5901	175.4272	462.55	168.9482	462.5522	170.8483
463.4508	168.2246	463.5237	175.4873	463.484	168.9967	463.4861	170.9029
464.3845	168.2783	464.4579	175.5469	464.4181	169.0452	464.4202	170.9568
465.3186	168.3316	465.3917	175.6066	465.3521	169.0937	465.3542	171.0106
466.252	168.3842	466.3256	175.666	466.2864	169.1423	466.288	171.0642
467.1862	168.4367	467.2601	175.7254	467.22	169.1911	467.2221	171.1177
468.1199	168.4885	468.194	175.7844	468.154	169.2396	468.156	171.1708
469.0538	168.5403	469.1276	175.8431	469.0879	169.2879	469.0897	171.2238
469.9882	168.5929	470.0618	175.9018	470.0218	169.336	470.0239	171.2769
470.9216	168.6461	470.9953	175.9606	470.956	169.3835	470.9576	171.33
471.8556	168.7004	471.9297	176.0203	471.8894	169.4306	471.8916	171.3838
472.7895	168.755	472.8633	176.0805	472.8233	169.4779	472.8254	171.4378
473.7239	168.8096	473.7977	176.1405	473.7581	169.5239	473.7599	171.4913
474.6579	168.8647	474.7314	176.1992	474.6919	169.5682	474.6937	171.5441
475.5913	168.921	475.6653	176.2577	475.6255	169.6123	475.6273	171.597
476.5256	168.9795	476.5991	176.316	476.5595	169.6568	476.5614	171.6508

Test 1		Test 2		Test 3		Average	
Temp (K)	C_p (J mol^{-1} K^{-1})	Temp (K)	C_p (J mol^{-1} K^{-1})	Temp (K)	C_p (J mol^{-1} K^{-1}))	Temp (K)	C_p (J mol^{-1} K^{-1})
477.4591	169.0394	477.5334	176.3739	477.4937	169.7014	477.4954	171.7049
478.3929	169.1007	478.4669	176.4324	478.4276	169.7462	478.4291	171.7598
479.3271	169.163	479.4007	176.491	479.3615	169.7912	479.3631	171.8151
480.261	169.2262	480.3349	176.5501	480.2955	169.8369	480.2971	171.8711
481.1948	169.2914	481.269	176.6101	481.229	169.8839	481.2309	171.9284
482.1289	169.3583	482.2028	176.6708	482.1632	169.9314	482.165	171.9869
483.0627	169.4272	483.1365	176.7326	483.0974	169.9795	483.0988	172.0464
483.9965	169.4981	484.0707	176.7961	484.031	170.0289	484.0328	172.1077
484.9301	169.571	485.0047	176.8613	484.965	170.0799	484.9666	172.1707
485.8645	169.6464	485.9385	176.9286	485.8989	170.1326	485.9006	172.2359
486.7979	169.7244	486.8725	176.9987	486.8328	170.1871	486.8344	172.3034
487.7324	169.8054	487.8066	177.0718	487.7668	170.2427	487.7686	172.3733
488.6664	169.8887	488.7405	177.1484	488.7007	170.3018	488.7025	172.4463
489.5998	169.9747	489.6746	177.2292	489.6349	170.3629	489.6364	172.5223
490.5338	170.0631	490.6091	177.3135	490.5688	170.4245	490.5706	172.6004
491.4676	170.1535	491.5426	177.4005	491.5028	170.4859	491.5044	172.6799
492.4018	170.245	492.4769	177.4903	492.4366	170.5474	492.4384	172.7609
493.3355	170.3378	493.4106	177.5827	493.3708	170.6095	493.3723	172.8433
494.2693	170.4328	494.3446	177.6793	494.3047	170.673	494.3062	172.9284
495.2033	170.528	495.2782	177.7775	495.2382	170.7358	495.2399	173.0138
496.1369	170.6237	496.2124	177.8766	496.1722	170.7981	496.1738	173.0994

Test 1		Test 2		Test 3		Average	
Temp (K)	C_p (J mol^{-1} K^{-1})	Temp (K)	C_p (J mol^{-1} K^{-1})	Temp (K)	C_p (J mol^{-1} K^{-1}))	Temp (K)	C_p (J mol^{-1} K^{-1})
497.0709	170.719	497.1467	177.9764	497.1066	170.8591	497.108	173.1848
498.005	170.8144	498.0808	178.0768	498.0406	170.9191	498.0421	173.2701
498.9392	170.9598	499.0147	178.2297	498.9746	170.9986	498.9762	173.396
499.8729	171.0672	499.9487	178.3433	499.9088	171.0632	499.9101	173.4912
500.8068	171.1693	500.8828	178.4516	500.843	171.1256	500.8442	173.5822
501.7406	171.2674	501.8168	178.5567	501.7767	171.1858	501.778	173.67
502.6747	171.3629	502.7508	178.6593	502.7106	171.2443	502.712	173.7555
503.6088	171.4566	503.6849	178.76	503.6444	171.3012	503.646	173.8393
504.5429	171.5508	504.6188	178.8614	504.5785	171.3582	504.58	173.9235
505.4767	171.6469	505.5531	178.966	505.5125	171.4157	505.5141	174.0095
506.4106	171.7414	506.4868	179.0697	506.4471	171.4724	506.4481	174.0945
507.3447	171.834	507.4206	179.1725	507.3806	171.5283	507.3819	174.1783
508.2789	171.924	508.3549	179.2744	508.3147	171.5836	508.3162	174.2607
509.2128	172.0104	509.2891	179.3742	509.2488	171.6376	509.2502	174.3407
510.1465	172.0934	510.223	179.4712	510.1826	171.6898	510.184	174.4181
511.0805	172.173	511.1567	179.565	511.1164	171.7398	511.1178	174.4926
512.0145	172.2485	512.0909	179.6556	512.0508	171.7881	512.052	174.5641
512.9489	172.3203	513.0256	179.7436	512.9849	171.8356	512.9864	174.6332
513.8826	172.3886	513.9591	179.8291	513.9189	171.8821	513.9202	174.7
514.8167	172.4536	514.8931	179.9121	514.8529	171.9267	514.8542	174.7641
515.7507	172.5162	515.8274	179.992	515.787	171.9692	515.7884	174.8258

Test 1		Test 2		Test 3		Average	
Temp (K)	C_p (J mol^{-1} K^{-1})	Temp (K)	C_p (J mol^{-1} K^{-1})	Temp (K)	C_p (J mol^{-1} K^{-1}))	Temp (K)	C_p (J mol^{-1} K^{-1})
516.6848	172.5767	516.7614	180.0697	516.7208	172.0096	516.7223	174.8853
517.6193	172.6349	517.6957	180.1454	517.6552	172.0484	517.6567	174.9429
518.5533	172.6915	518.6303	180.219	518.5896	172.0863	518.5911	174.999
519.4877	172.7466	519.5644	180.2911	519.5238	172.1233	519.5253	175.0537
520.4224	172.7996	520.4987	180.3614	520.4576	172.1584	520.4595	175.1064
521.3559	172.8499	521.4332	180.429	521.3924	172.1914	521.3938	175.1568
522.2907	172.8969	522.3675	180.4932	522.3264	172.2219	522.3282	175.204
523.2248	172.9404	523.3016	180.5543	523.261	172.2498	523.2625	175.2481
524.1592	172.9799	524.2366	180.6121	524.1953	172.275	524.197	175.289
525.0931	173.0152	525.1701	180.6659	525.1297	172.2974	525.131	175.3262
526.0275	173.0465	526.1042	180.7159	526.0637	172.3177	526.0651	175.36
526.9616	173.0747	527.0387	180.7635	526.9977	172.3364	526.9993	175.3915
527.8957	173.1005	527.9731	180.8097	527.9323	172.3538	527.9337	175.4213
528.8294	173.126	528.9073	180.8559	528.8659	172.371	528.8675	175.451
529.7636	173.1543	529.841	180.9037	529.8002	172.3905	529.8016	175.4828
530.6979	173.1853	530.7754	180.953	530.7344	172.412	530.7359	175.5168
531.6319	173.219	531.7092	181.0038	531.6681	172.4358	531.6697	175.5529
532.5667	173.2552	532.6441	181.0564	532.6028	172.4616	532.6045	175.5911
533.5004	173.2962	533.578	181.1128	533.5366	172.4901	533.5383	175.633
534.4344	173.3419	534.5117	181.1733	534.4704	172.5216	534.4721	175.6789
535.3683	173.39	535.4459	181.2358	535.4046	172.5549	535.4062	175.7269

Test 1		Test 2		Test 3		Average	
Temp (K)	C_p (J mol^{-1} K^{-1})	Temp (K)	C_p (J mol^{-1} K^{-1})	Temp (K)	C_p (J mol^{-1} K^{-1}))	Temp (K)	C_p (J mol^{-1} K^{-1})
536.3022	173.4405	536.3798	181.3004	536.3384	172.5894	536.3402	175.7768
537.2354	173.4935	537.3131	181.3673	537.2718	172.6248	537.2734	175.8285
538.17	173.5492	538.2476	181.4376	538.2063	172.662	538.208	175.883
539.1042	173.6073	539.1821	181.5107	539.1405	172.7009	539.1422	175.9397
540.0384	173.6882	540.1167	181.6076	540.0749	172.7616	540.0766	176.0192
540.9725	173.7862	541.0504	181.7229	541.0086	172.8393	541.0105	176.1162
541.9064	173.8778	541.9841	181.8323	541.9429	172.9108	541.9445	176.207
542.8411	173.964	542.9189	181.9367	542.8776	172.976	542.8792	176.2922
543.7744	174.0455	543.8526	182.0366	543.8108	173.0368	543.8126	176.373
544.7087	174.1251	544.7867	182.1358	544.745	173.096	544.7468	176.4523
545.6425	174.2019	545.7207	182.2324	545.6786	173.152	545.6806	176.5288
546.5764	174.2792	546.6544	182.3289	546.613	173.2071	546.6146	176.6051
547.5102	174.3573	547.5883	182.4258	547.5465	173.2616	547.5483	176.6816
548.4443	174.4351	548.5227	182.5223	548.4806	173.3157	548.4825	176.7577
549.3786	174.5137	549.4566	182.6202	549.4148	173.3701	549.4167	176.8346
550.3124	174.5917	550.3908	182.7178	550.349	173.4242	550.3507	176.9112
551.2465	174.6712	551.325	182.8179	551.283	173.4802	551.2848	176.9898
552.1807	174.7515	552.2589	182.9191	552.2169	173.5375	552.2189	177.0693
553.1144	174.8337	553.1927	183.0215	553.1508	173.5959	553.1526	177.1504
554.0483	174.9175	554.1271	183.1243	554.085	173.6553	554.0868	177.2324
554.982	175.0012	555.0614	183.2274	555.0187	173.7146	555.0207	177.3144

Test 1		Test 2		Test 3		Average	
Temp (K)	C_p (J mol^{-1} K^{-1})	Temp (K)	C_p (J mol^{-1} K^{-1})	Temp (K)	C_p (J mol^{-1} K^{-1}))	Temp (K)	C_p (J mol^{-1} K^{-1})
555.9163	175.0858	555.9951	183.3314	555.9526	173.775	555.9547	177.3974
556.8501	175.1731	556.9292	183.4379	556.887	173.8384	556.8887	177.4832
557.7842	175.2609	557.8633	183.5443	557.8209	173.9017	557.8228	177.5689
558.7182	175.3491	558.7974	183.65	558.7549	173.9647	558.7568	177.6546
559.6523	175.4409	559.7312	183.7595	559.6889	174.031	559.6908	177.7438
560.5856	175.5319	560.6652	183.8696	560.6231	174.097	560.6246	177.8328
561.5197	175.6213	561.5992	183.9785	561.5566	174.1615	561.5585	177.9204
562.4542	175.7115	562.5332	184.0884	562.4908	174.2262	562.4927	178.0087
563.3879	175.8026	563.4673	184.1992	563.4248	174.2913	563.4266	178.0977
564.3221	175.8975	564.4013	184.3132	564.3589	174.3596	564.3607	178.1901
565.2557	175.9924	565.3354	184.4268	565.2926	174.4276	565.2945	178.2823
566.19	176.0898	566.269	184.5424	566.2267	174.4976	566.2286	178.3766
567.1233	176.1912	567.2034	184.6622	567.1607	174.5712	567.1625	178.4749
568.0576	176.2933	568.1375	184.7826	568.0948	174.6457	568.0966	178.5739
568.9919	176.3937	569.0714	184.9016	569.0289	174.7188	569.0307	178.6714
569.9255	176.4941	570.0055	185.0211	569.9628	174.792	569.9646	178.7691
570.8599	176.5969	570.9394	185.1436	570.8968	174.8671	570.8987	178.8692
571.7934	176.6989	571.8732	185.2654	571.8302	174.9413	571.8323	178.9685
572.7275	176.8015	572.8077	185.3869	572.7645	175.0154	572.7666	179.0679
573.6616	176.9017	573.7418	185.5059	573.699	175.0869	573.7008	179.1649
574.5956	177.0011	574.6758	185.6244	574.6324	175.1573	574.6346	179.2609

Test 1		Test 2		Test 3		Average	
Temp (K)	C_p (J mol^{-1} K^{-1})	Temp (K)	C_p (J mol^{-1} K^{-1})	Temp (K)	C_p (J mol^{-1} K^{-1}))	Temp (K)	C_p (J mol^{-1} K^{-1})
575.529	177.1015	575.6094	185.7448	575.5664	175.228	575.5682	179.3581
576.4631	177.2028	576.5435	185.8667	576.5006	175.2989	576.5024	179.4561
577.397	177.3027	577.4775	185.9878	577.4344	175.3681	577.4363	179.5529
578.3308	177.4041	578.4115	186.1112	578.3681	175.4382	578.3701	179.6512
579.2646	177.5083	579.3454	186.2377	579.302	175.5096	579.304	179.7519
580.1992	177.6178	580.2795	186.3687	580.2364	175.5845	580.2383	179.857
581.1329	177.7279	581.2134	186.4995	581.1704	175.6581	581.1722	179.9618
582.0667	177.8414	582.1472	186.6335	582.1042	175.7346	582.106	180.0698
583.0008	177.9558	583.0814	186.7678	583.038	175.8113	583.04	180.1783
583.9341	178.0674	584.0145	186.899	583.9711	175.8848	583.9732	180.2838
584.8683	178.179	584.9487	187.0291	584.906	175.957	584.9077	180.3884
585.8023	178.2875	585.8831	187.1549	585.84	176.0249	585.8418	180.4891
586.736	178.3946	586.8171	187.28	586.774	176.0924	586.7757	180.589
587.6703	178.503	587.7514	187.4066	587.708	176.1615	587.7099	180.6904
588.6042	178.6128	588.6855	187.5349	588.6417	176.2333	588.6438	180.7937
589.538	178.7232	589.6194	187.6639	589.5756	176.3064	589.5777	180.8978
590.4721	178.8301	590.5533	187.7899	590.5094	176.3763	590.5116	180.9988
591.406	178.9345	591.4869	187.9144	591.4435	176.4435	591.4454	181.0975
592.3396	179.0353	592.4208	188.0353	592.3772	176.5068	592.3792	181.1925
593.2735	179.1374	593.3549	188.1562	593.3112	176.57	593.3132	181.2879
594.2081	179.2445	594.2896	188.281	594.2459	176.6375	594.2479	181.3877

Test 1		Test 2		Test 3		Average	
Temp (K)	C_p (J mol^{-1} K^{-1})	Temp (K)	C_p (J mol^{-1} K^{-1})	Temp (K)	C_p (J mol^{-1} K^{-1}))	Temp (K)	C_p (J mol^{-1} K^{-1})
595.1413	179.3561	595.2232	188.4104	595.1795	176.7093	595.1813	181.4919
596.0749	179.4647	596.1565	188.5367	596.113	176.7781	596.1148	181.5932
597.009	179.5684	597.0909	188.657	597.0469	176.841	597.0489	181.6888
597.9427	179.6703	598.0246	188.7738	597.9809	176.9013	597.9827	181.7818
598.8759	179.7715	598.9577	188.8882	598.9141	176.9594	598.9159	181.873
599.8103	179.873	599.8919	189.0014	599.8481	177.0175	599.8501	181.964
600.7448	179.973	600.8266	189.1121	600.7825	177.0731	600.7846	182.0527
601.6779	180.0751	601.7605	189.2245	601.7165	177.1314	601.7183	182.1437
602.6121	180.1826	602.6946	189.344	602.6503	177.1969	602.6523	182.2412
603.5463	180.2942	603.628	189.4687	603.5842	177.2671	603.5862	182.3433
604.4802	180.4065	604.5626	189.595	604.5188	177.3388	604.5205	182.4468
605.4142	180.5167	605.4963	189.7206	605.4525	177.4101	605.4543	182.5491
606.3479	180.6283	606.4298	189.8497	606.3862	177.4844	606.388	182.6541
607.2817	180.7403	607.3641	189.982	607.3198	177.5601	607.3219	182.7608
608.2155	180.8483	608.2979	190.1122	608.2536	177.6325	608.2557	182.8643
609.1493	180.9554	609.2315	190.2409	609.1879	177.7025	609.1896	182.9663
610.0831	181.0628	610.1657	190.3701	610.1213	177.7729	610.1234	183.0686
611.017	181.17	611.0992	190.4993	611.0552	177.8443	611.0571	183.1712
611.9505	181.2778	612.0331	190.6278	611.989	177.9167	611.9909	183.2741
612.8849	181.3845	612.9676	190.7542	612.9234	177.9884	612.9253	183.3757
613.8189	181.4964	613.9017	190.8853	613.857	178.0646	613.8592	183.4821

Test 1		Test 2		Test 3		Average	
Temp (K)	C_p (J mol^{-1} K^{-1})	Temp (K)	C_p (J mol^{-1} K^{-1})	Temp (K)	C_p (J mol^{-1} K^{-1}))	Temp (K)	C_p (J mol^{-1} K^{-1})
614.7518	181.6103	614.835	191.0171	614.7916	178.1427	614.7928	183.59
615.6885	181.7409	615.77	191.1647	615.724	178.236	615.7275	183.7139
616.6191	181.8644	616.7035	191.3049	616.6593	178.3232	616.6606	183.8308
617.5547	181.9817	617.6376	191.4381	617.5929	178.399	617.5951	183.9396
618.4881	182.0937	618.5717	191.5658	618.5269	178.4724	618.5289	184.044
619.4222	182.201	619.5056	191.6877	619.4609	178.5423	619.4629	184.1436
620.3562	182.3035	620.4402	191.8031	620.3951	178.6086	620.3971	184.2384
621.2907	182.4026	621.3738	191.9138	621.3293	178.6722	621.3313	184.3295
622.2251	182.508	622.3084	192.0298	622.2633	178.7422	622.2656	184.4267
623.1589	182.6246	623.2424	192.1571	623.1973	178.8488	623.1996	184.5435
624.0932	182.7455	624.1768	192.2897	624.1318	178.9466	624.1339	184.6606
625.0271	182.8683	625.1106	192.4258	625.0657	179.1321	625.0678	184.8087
625.9611	182.9917	626.0445	192.5636	625.9999	179.2422	626.0018	184.9325
626.8951	183.1113	626.9789	192.6971	626.9338	179.3411	626.9359	185.0498
627.8292	183.2363	627.913	192.8367	627.8678	179.4435	627.87	185.1721
628.7629	183.3606	628.8467	192.9775	628.8016	179.5449	628.8037	185.2943
629.697	183.4878	629.7814	193.1222	629.7361	179.6475	629.7381	185.4192
630.6307	183.6154	630.7151	193.2673	630.6699	179.7491	630.6719	185.5439
631.5647	183.752	631.6485	193.4195	631.6035	179.8568	631.6056	185.6761
632.4985	183.8873	632.5828	193.5704	632.5372	179.962	632.5395	185.8065
633.4323	184.0219	633.5166	193.7207	633.4712	180.0667	633.4733	185.9365

Test 1		Test 2		Test 3		Average	
Temp (K)	C_p (J mol^{-1} K^{-1})	Temp (K)	C_p (J mol^{-1} K^{-1})	Temp (K)	C_p (J mol^{-1} K^{-1}))	Temp (K)	C_p (J mol^{-1} K^{-1})
634.3664	184.1505	634.4511	193.8631	634.4053	180.1662	634.4076	186.0599
635.3002	184.2752	635.3853	193.9998	635.3395	180.2621	635.3417	186.1791
636.2342	184.4007	636.3192	194.1366	636.2735	180.3589	636.2756	186.2987
637.1679	184.6099	637.2527	194.3589	637.2071	180.4901	637.2092	186.4863
638.1018	184.775	638.1867	194.5337	638.141	180.6012	638.1432	186.6366
639.0357	184.8969	639.1207	194.6637	639.0744	180.6965	639.0769	186.7523
639.9683	185.0051	640.0537	194.7828	640.0075	180.7848	640.0098	186.8576
640.9022	185.1058	640.9885	194.8985	640.9419	180.8718	640.9442	186.9587
641.8364	185.1959	641.9227	195.0016	641.8757	180.9537	641.8783	187.0504
642.7703	185.2818	642.8564	195.0998	642.8092	181.0371	642.8119	187.1396
643.7037	185.3738	643.79	195.202	643.7431	181.1353	643.7456	187.237
644.638	185.4674	644.7249	195.304	644.6773	181.2413	644.68	187.3376
645.5716	185.5641	645.6583	195.407	645.6108	181.3565	645.6136	187.4426
646.5053	185.7219	646.592	195.5704	646.5445	181.5396	646.5472	187.6106
647.4385	186.1918	647.5261	196.0592	647.478	182.0297	647.4809	188.0936
648.3722	186.2722	648.4599	196.1518	648.4118	182.1846	648.4146	188.2029
649.3057	186.3373	649.3935	196.2282	649.3457	182.2921	649.3483	188.2859
650.2398	186.4005	650.3274	196.3025	650.2794	182.3701	650.2822	188.3577
651.1733	186.4547	651.2614	196.3667	651.2129	182.4369	651.2159	188.4194
652.1069	186.4905	652.1949	196.4084	652.1466	182.4941	652.1495	188.4643
653.0407	186.5355	653.1288	196.4616	653.0807	182.5555	653.0834	188.5175

Test 1		Test 2		Test 3		Average	
Temp (K)	C_p (J mol^{-1} K^{-1})	Temp (K)	C_p (J mol^{-1} K^{-1})	Temp (K)	C_p (J mol^{-1} K^{-1}))	Temp (K)	C_p (J mol^{-1} K^{-1})
653.9741	186.5839	654.0627	196.5214	654.0139	182.6152	654.0169	188.5735
654.9078	186.6308	654.9961	196.5809	654.9477	182.6703	654.9505	188.6273
655.8417	186.6855	655.9302	196.6457	655.8817	182.7279	655.8845	188.6863
656.7755	186.7474	656.8644	196.7222	656.8156	182.7879	656.8185	188.7525
657.7089	186.8106	657.7984	196.8046	657.7489	182.8434	657.7521	188.8195
658.643	186.8705	658.7325	196.8899	658.6826	182.897	658.6861	188.8858
659.5765	186.9312	659.6665	196.9782	659.6165	182.9506	659.6198	188.9533
660.5106	186.9901	660.5999	197.0645	660.5499	182.9992	660.5534	189.0179
661.4436	187.0521	661.534	197.1517	661.4836	183.0445	661.487	189.0828
662.3777	187.119	662.468	197.2449	662.4172	183.0939	662.421	189.1526
663.3112	187.1926	663.4021	197.3481	663.3511	183.1546	663.3548	189.2318
664.2447	187.2573	664.3354	197.4451	664.2849	183.2137	664.2883	189.3054
665.1789	187.3329	665.2698	197.5549	665.2189	183.283	665.2225	189.3903
666.1125	187.4163	666.2032	197.663	666.1522	183.3518	666.1559	189.477
667.0462	187.4948	667.137	197.763	667.0859	183.4108	667.0897	189.5562
667.9796	187.5749	668.0706	197.8617	668.02	183.4704	668.0234	189.6357
668.0465	187.5802	668.1371	197.8683	668.0862	183.4742	668.0899	189.6409